XMM-Newton

XMM-Newton Users' Handbook

Issue 2.0
Edited by: M. Ehle, M. Breitfellner, M. Dahlem,
M. Guainazzi, P. Rodriguez, M. Santos-Lleo,
N. Schartel, L. Tomas

Based on input from the entire **XMM-Newton** SOC Team

15.08.2001

Extensive contributions from the members of the **XMM-Newton** Science Working Team, the SSC, the Instrument Teams and NASA's **XMM-Newton** Guest Observer Facility are gratefully acknowledged.

Revision history

Revision number	Date	Revision author	Comments
Draft 3.0	August 1998	M. Dahlem	Complete draft
Issue 1.0	23.09.1998	M. Dahlem	Official release
Issue 1.1	19.01.1999	M. Dahlem	Release of Cal/PV/GT target tables
Issue 1.2	31.03.2000	M. Ehle	Minor updates
Issue 2.0	15.08.2001	M. Ehle	Release for AO2

Contents

List of Figures

List of Tables

1 Glossary

For more information on frequently used technical terms, see also the **XMM-Newton** Glossary.

Acronym	Explanation
ACIS	*Chandra* CCD Imaging Spectrograph
AHF	Attitude History File
AMA	Absolute Measurement Accuracy
AO	Announcement of Opportunity
AOCS	Attitude and Orbit Control and Measurement Subsystem
AMS	Archive Management Subsystem
CAL	Calibration Access Layer
CCD	Charge Coupled Device
CCF	Current Calibration File
Chandra	Chandra X-Ray Observatory
CTE	Charge Transfer Efficiency
CVZ	Continuous Viewing Zone
DEC	Declination, δ(J2000)
DPU	Digital Processing Unit
EPIC	European Photon Imaging Camera
ERMS	EPIC Radiation Monitor Subsystem
ESTEC	European Space Research and Technology Centre
EW	Equivalent Width
FAQ	Frequently Asked Question
FITS	Flexible Image Transport System
FM	Flight Module
FOV	Field Of View
FWHM	Full Width at Half Maximum
GO	Guest Observer
GSFC	Goddard Space Flight Center
GT(O)	Guaranteed Time (Observer)
GTI	Good Time Interval
GUI	Graphical User Interface
HEASARC	(NASA) High Energy Astrophysics Science Archive Research Center
HED	High Energy Detector (of the ERMS)
HER	RGS high event rate (selectable mode)
HETG	(*Chandra*) High Energy Transmission Grating
HEW	Half Energy Width
HRC	(*Chandra*) High Resolution Camera
HTR	High Time Resolution (mode of the RGS)
LED	Low Energy Detector (of the ERMS)
LETG	(*Chandra*) Low Energy Transmission Grating
LSF	Line-spread Function
METG	(*Chandra*) Medium Energy Transmission Grating

MOC	**XMM-Newton** Mission Operation Centre
MOS	Metal Oxide Semi-conductor
OBDH	Onboard Data Handler
OCB	On-Chip Binning
ODF	Observation Data File
ODS	Observation Data Subsystem
OGIP	(NASA's) Office of the Guest Investigator Program
OM	Optical Monitor
OTAC	Observatory Time Allocation Committee
PHA	Pulse Height Analyser
PHS	Proposal Handling Subsystem
PI	Principal Investigator
PIMMS	Portable, Interactive Multi-Mission Simulator
PPS	Pipeline Processing Subsystem
PSF	Point-Spread Function
PV	Performance Verification
QE	Quantum Efficiency
RA	Right Ascension, α(J2000)
RAF	Raw Attitude File
RFC	RGS Focal Camera
RFS	Refreshed Frame Store mode of EPIC MOS
RGA	Reflection Grating Assembly (of the RGS)
RGS	Reflection Grating Spectrometer
RPE	Relative Pointing Error
SAS	Science Analysis Subsystem
SciSim	**XMM-Newton** Science Simulator
SDF	Slew Data File
SER	RGS split event reconstruction (selectable mode)
SES	RGS single event selection (selectable mode)
SGS	Sequence Generator Subsystem
SMP	Science Management Plan
SOC	**XMM-Newton** Science Operations Centre
SSC	Survey Science Centre
SSD	Software Specification Document
TBC	To Be Confirmed
TBD	To Be Determined
TOC	Table of contents
ToO	Target of Opportunity
UHB	**XMM-Newton** Users' Handbook
URD	User Requirements Document
URL	Unique Resource Location
W90	90% energy width
WWW	World Wide Web
XID	X-ray source identification (by the SSC)

XMM-Newton	X-ray Multi-Mirror Mission
XRPS	Remote Proposal Submission
XSA	**XMM-Newton** Science Archive

2 Introduction

2.1 Scope of this document

This document is designed to be the starting point for **XMM-Newton** users in the search for information on the instrumentation on board of the satellite. Users working with a printed (postscript or PDF) version of this document, please note that the online **XMM-Newton** Users' Handbook (UHB) is full of links to other components of our web-based information system (and other, external servers). Also, most of the figures are colour based and some do not reproduce well in black and white. Various appendices also provide introductions and links to other online services of the **XMM-Newton** Science Operations Centre (SOC) and the Survey Science Centre (SSC).

The **XMM-Newton** UHB is primarily intended to serve as a proposal preparation document, based on which potential **XMM-Newton** users will be able to assess the technical feasibility of their planned observations and the expected data quality. Details on how to fill out the proposal submission forms of the **XMM-Newton** Remote Proposal Submission (XRPS) software are described in a separate document, the XRPS Users' Manual. An updated version of the XRPS Users' Manual will be available in time for each Announcement of Opportunity (AO).

In addition, this document provides an overview of **XMM-Newton** data calibration and analysis (the Science Analysis Subsystem, SAS) mainly specifying links to related documents for further reading.

2.2 Structure and contents of the Users' Handbook

This document contains, in the order listed here:

1. A concise summary of **XMM-Newton**'s properties and the instruments onboard, intended for use as a guideline for observers writing **XMM-Newton** proposals, and a short description of how to conduct observations with **XMM-Newton**. Most of the information needed for this purpose is contained in § 3 and § 4 and in some of the appendices (the necessary links are provided in § 3 and 4, as well).

2. The next chapter (§ 5) describes the **XMM-Newton** Guest Observer (GO) program.

3. A brief description of the data calibration and analysis (§ 6, which also introduces the **XMM-Newton** Science Analysis Subsystem SAS) and of the **XMM-Newton** Science Archive (§ 6.4).

4. Appendices on related issues, like e.g., the **XMM-Newton** Science Simulator (SciSim; Appendix A) and the **XMM-Newton** Survey Science Centre (SSC; Appendix B).

CAVEAT: **This version of the UHB is the first one to reflect the experience acquired in-orbit with the satellite and the instruments. It is therefore much more complete and accurate than previous versions which should be discarded. The information contained in this document represents the best *current* understanding of XMM-Newton at the time of release. Updates, if necessary, will be made as soon as possible after evaluation of incoming new information.**

The information contained in § 3, 4 and 5 and appendix A should supply sufficient detail to enable the reader to prepare the submission of an XMM-Newton observing proposal via the XMM-Newton Remote Proposal Submission software (XRPS).

2.3 Location

This document forms part of the online **XMM-Newton** SOC documentation server on the WWW, at the URL `http://xmm.vilspa.esa.es`. The URL of the interface document leading to the **XMM-Newton** Users' Handbook is

`http://xmm.vilspa.esa.es/user/uhb_top.html`.

2.4 Sources of information

Whenever possible information presented in this document comes from in-flight observations. As the analysis of calibration data is still ongoing, some plots are still based on model simulations using the **XMM-Newton** Science Simulator (SciSim) though.

Information on flux to count rate conversions comes from the HEASARC *PIMMS* software provided by the **XMM-Newton** Guest Observer Facility at NASA's Goddard Space Flight Center. The SOC will supply updated information to HEASARC so that *PIMMS* reflects the latest EPIC effective area in time for AO–2.

2.5 Updates on this document

It is intended not to update this document during a call for proposals. If, however, new information which is significant for the proposal preparation becomes available, the user will be informed via the **XMM-Newton** News Mailing List.
The version number of the latest release of the UHB is always visible in the **XMM-Newton** Users' Handbook introduction page leading to this document.

2.6 How to obtain further help and information

The Users' Handbook is an integral part of the SOC's web-based online information system and it contains lots of links to other components of the web server. All links can also always be reached via the SOC home page.
Additionally, in order to facilitate the search for more information, § 7 of this document contains a compilation of relevant links and references.
The contact address for users who need help or additional information, or who want to send suggestions on how to improve our system, is **xmmhelp@xmm.vilspa.esa.es**. All questions relating to AO and observing matters should be directed to this account. The SOC is collecting users' questions which can be accessed via the **XMM-Newton** helpdesk at `http://xmm.vilspa.esa.es/xmmhelp`.

2.7 Acknowledgements

Extensive contributions to several sections of the Users' Handbook are gratefully acknowledged, especially from

- B.Aschenbach and P.Gondoin (§ 3.2, X-ray Telescopes),
- D.Lumb, U.Briel, A.De Luca, K.Dennerl, P.Ferrando, M.Freyberg, G.Griffiths, F.Haberl, E.Kenziorra, M.Kirsch, S.Molendi and S.Sembay (§ 3.3, EUROPEAN PHOTON IMAGING CAMERA (EPIC)),
- C.Erd, J.W.den Herder, M.Audard, C.Gabriel, F.Paerels, A.Rasmussen, M.Sako and T.Tamura (§ 3.4, REFLECTION GRATING SPECTROMETER (RGS)),
- A.Breeveld, B.Cheng, I.Antokhin, K.O.Mason, R.Much and A.Talavera (§ 3.5, OPTICAL MONITOR (OM)),
- M.Watson (Appendix B, **XMM-Newton** Survey Science Centre (SSC)).

3 XMM-Newton – a concise overview

XMM-Newton is the second of ESA's four "cornerstone" missions defined in the Horizon 2000 Programme. It was launched on December 10th, 1999 and carries two distinct types of telescopes: three Wolter type-1 X-ray telescopes, with different X-ray detectors in their foci (which are described in this chapter), and a 30-cm optical/UV telescope with a microchannel-plate pre-amplified CCD detector in its focal plane (see also below). Thus, **XMM-Newton** offers simultaneous access to two windows of the electromagnetic spectrum: X-ray and optical/UV.

XMM-Newton provides the following three types of science instruments:

1. European Photon Imaging Camera (EPIC)

   3 CCD cameras for X-ray imaging, moderate resolution spectroscopy, and X-ray photometry; the two different types of EPIC cameras, MOS and pn, are described in § 3.3. **XMM-Newton** carries 2 MOS cameras and one pn.

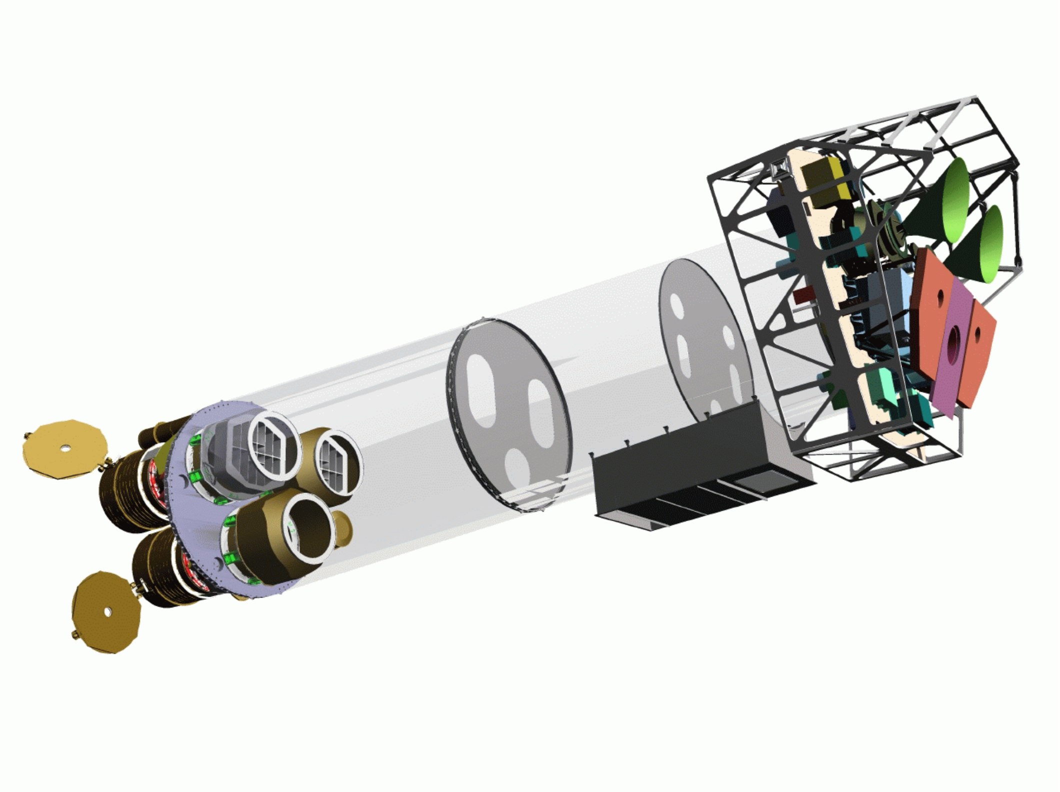

Figure 1: *Sketch of the* **XMM-Newton** *payload. The mirror modules, two of which are equipped with Reflection Grating Arrays, are visible at the lower left. At the right end of the assembly, the focal X-ray instruments are shown: The EPIC MOS cameras with their radiators (black/green "horns"), the radiator of the EPIC pn camera (violet) and those of the (light blue) RGS detectors (in pink). The OM telescope (orange) is obscured by the lower mirror module. Figure courtesy of Dornier Satellitensysteme GmbH.*

2. Reflection Grating Spectrometer (RGS)

   2 essentially identical spectrometers for high-resolution X-ray spectroscopy and spectro-photometry (§ 3.4).

3. Optical Monitor (OM)

   for optical/UV imaging and grism spectroscopy; § 3.5 provides an overview.

The three EPIC cameras and the two detectors of the RGS spectrometers reside in the focal planes of the X-ray telescopes, while the OM has its own telescope. A sketch of the **XMM-Newton** payload is displayed in Fig. 1. **There are in total six science instruments onboard XMM-Newton, which are operated simultaneously** (unless prohibited by constraints, like e.g., excessive target brightness). The instruments can be operated independently and each in different modes of data acquisition. Observers will receive data from all science instruments.

3.1 Basic characteristics

The most important characteristics of **XMM-Newton** are compiled in Table 1. More detailed numbers will follow in the chapters on the individual instruments (below) and a comparison with other X-ray satellites is provided in § 3.7. The basic characteristics of **XMM-Newton** are:

- Simultaneous operation of all science instruments

  If not prohibited, e.g. by target brightness constraints, all six **XMM-Newton** science instruments operate simultaneously. They work independently (i.e., exposures of the individual instruments do not necessarily start and end at the same time).

- High sensitivity

  XMM-Newton carries the X-ray telescopes with the largest effective area of a focusing telescope ever: the total mirror geometric effective area at 1.5 keV energy is ca. 1550 cm^2 for each telescope, i.e., 4650 cm^2 in total.

- Good angular resolution

  XMM-Newton's high sensitivity is achieved by using 58 thin nested mirror shells in each X-ray telescope. The achieved point-spread function (PSF) has a full width at half maximum (*FWHM*) on the order of $6''$ and a *HEW*, at which 50% of the total energy are encircled, of ca. $15''$.

- Moderate and high spectral resolution

  The EPIC CCD cameras have moderate spectral resolution (with a resolving power, $E/\Delta E$, of ca. 20–50). The RGS spectrometers offer much higher spectral resolution, with a resolving power in the range of 200–800.

- Simultaneous optical/UV observations

  Observations with the co-aligned OM optical/UV telescope render possible the monitoring and identification of optical/UV counterparts of X-ray sources seen by the X-ray telescopes as well as imaging of the surrounding field.

Table 1: **XMM-Newton** *characteristics – an overview*

Instrument	**EPIC MOS**	**EPIC pn**	**RGS**	**OM**
Bandpass	0.15–12 keV	0.15–15 keV	0.35–2.5 keV[1]	160–600 nm
Orbital target vis.[2]	5–135 ks	5–135 ks	5–145 ks	5–145 ks
Sensitivity[3]	$\sim 10^{-14}$ (4)	$\sim 10^{-14}$ (4)	$\sim 8 \times 10^{-5}$ (14)	24 mag[12]
Field of view (FOV)	30′ [5]	30′ [5]	$\sim$ 5′	17′
PSF (*FWHM/HEW*)[6]	5″/14″	6″/15″	N/A	$\sim$ 1″
Pixel size	40 μm (1.1″)	150 μm (4.1″)	81 μm (9×10^{-3} Å)[13]	0.5″ [7]
Timing resolution[8]	1.5 ms	0.03 ms	16 ms	500 ms
Spectral resolution[9]	$\sim$ 70 eV	$\sim$ 80 eV	0.04/0.025 Å[10]	0.5/1.0 nm[11]

Notes to Table 1:
1) In the –1. grating order (wavelength range: 5–35 Å; λ [Å] × E [keV] = 12.3984).
2) Total time available for science per orbit; minimum of 5 ks (excl. overheads, see § 4.5.2) in order to ensure observatory efficiency. EPIC observations can only be performed outside the Earth's radiation belts (see § 4.2.1).
3) After 10 ks; cf. overview tables on the individual instruments.
4) In the range 0.15–15.0 keV, in units of erg s^{-1} cm^{-2}, see § 3.3.8 for details.
5) See Figs. 16, 17 and 18 for the detailed shape of the FOV.
6) See Fig. 4 for an in-flight point source measurement.
7) 1″ with default 2 × 2 binning. A higher resolution is achieved with the OM magnifier (not available in AO2)
8) In fast data acquisition mode (i.e., fast mode for OM and timing mode for EPIC, high time resolution mode for RGS, reading out only one of nine CCDs). The EPIC pn burst mode offers an even higher timing resolution of 7μs, but has a very low duty cycle of 3%.
9) At 1 keV energy. At the energy of Fe Kα (6.4 keV), the energy resolution of both EPIC cameras is ca. 150 eV.
10) In –1. and –2. order, resp.; at 1 keV, this corresponds to 3.2/2.0 eV (*HEW*).
11) With grism 1 (UV) and grism 2 (optical), respectively.
12) For a 1000 s white light filter observation of a B0 star; dependent on pointing direction (celestial background).
13) In spectroscopy mode (standard 3 × 3 pixel on-chip binning applied).
14) O VII 0.57 keV line flux in photons cm^{-2} s^{-1}, for an integration time of 10 ks and a background of 10^{-4} photons cm^{-2} s^{-1} keV^{-1}. More details are provided in § 3.4.6.

- Long continuous target visibility

  A highly elliptical orbit offers continuous target visibility of up to about 40 hours, with a minimum height for science observations of 46,000 km. This is very favourable for studies of source variability and also in order to achieve a high overall observatory efficiency.

For a comparison of these basic characteristics with those of other past or contemporaneous X-ray satellite missions, see § 3.7.

More detailed information on the mirrors and on the instruments listed in Table 1 and their observing modes is provided in the following sections (§§ 3.2–3.5).

3.2 X-ray Telescopes

XMM-Newton's three X-ray telescopes are co-aligned with an accuracy of better than about 1′. One telescope has a light path as shown in Fig. 2; the two others have grating assemblies in their light paths, diffracting part of the incoming radiation onto their secondary focus. Fig. 3 shows the light path in the latter two X-ray telescopes onboard **XMM-Newton**. Ca. 44% of the incoming light focused by the multi-shell grazing incidence mirrors is directed onto the camera at the prime focus, while 40% of the radiation is dispersed by a grating array onto a linear strip of CCDs. The remaining light is absorbed by the support structures of the RGAs.
The focal instruments are described in §§ 3.3, 3.4 and 3.5. First we explain the most important properties of the mirror assemblies.

The performance of each X-ray telescope is characterised by:

1. the image quality,
2. the effective area and
3. the straylight rejection efficiency,

which will be described in the following.

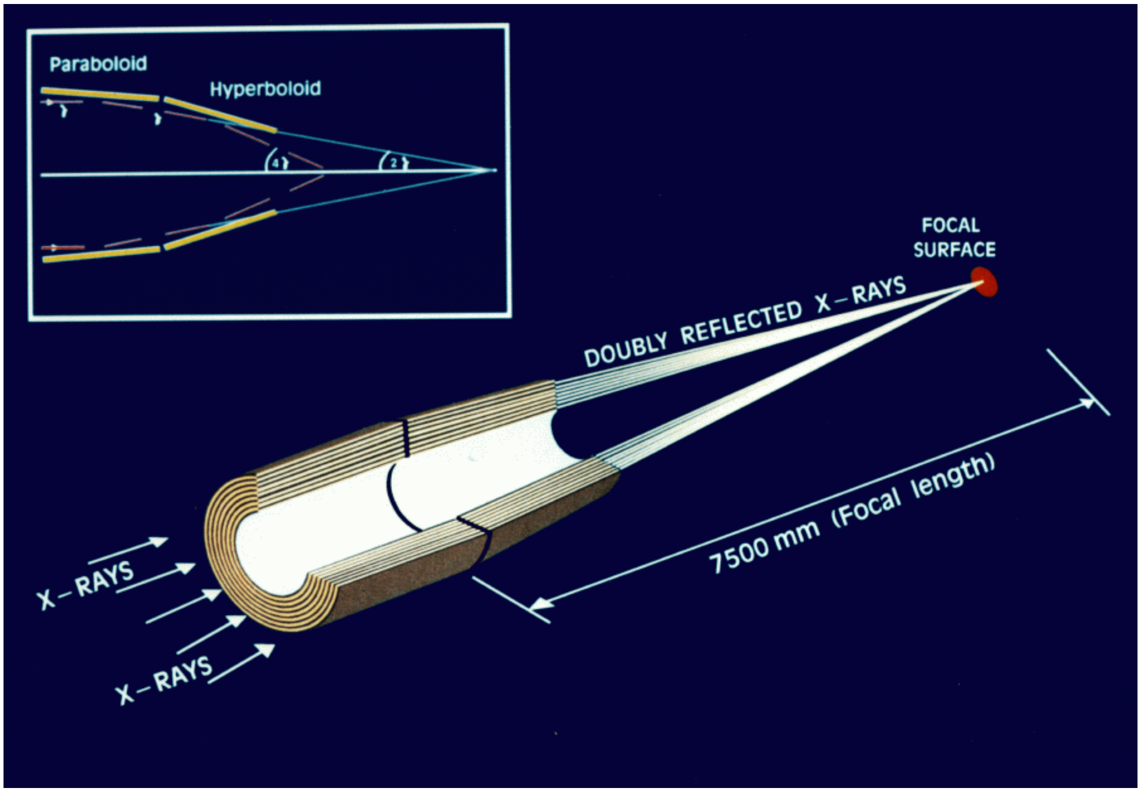

Figure 2: *The light path in* **XMM-Newton's** *open X-ray telescope with the pn camera in focus (not to scale).*

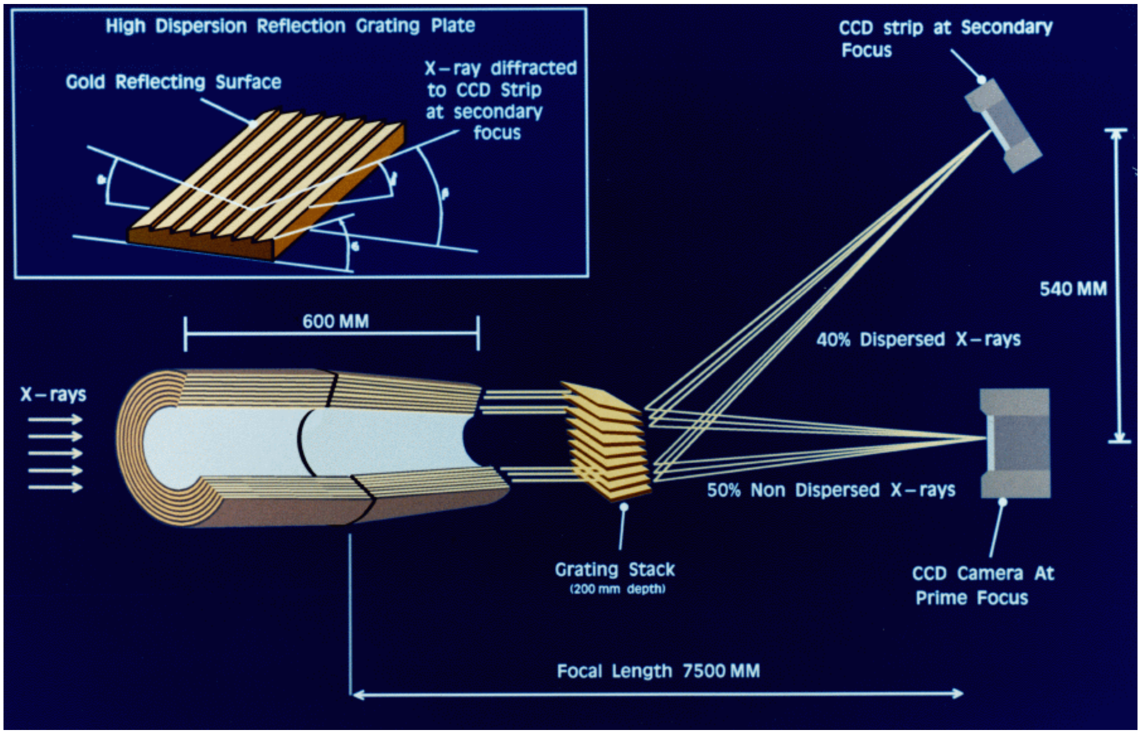

Figure 3: *The light path in the two* **XMM-Newton** *telescopes with grating assemblies (not to scale). Note that the actual fraction of the non-intercepted light that passes to the primary MOS focus is 44%, while 40% of the incident light is intercepted by grating plates of the RGA.*

3.2.1 X-ray point-spread function

The first critical parameter determining the quality of an X-ray mirror module is its ability to focus photons. Here lies one of **XMM-Newton**'s major strong points: the core of its on-axis point-spread function (PSF) is narrow and varies little over a wide energy range (0.1–4 keV). Above 4 keV, the PSF becomes only slightly more energy dependent.

3.2.1.1 On-axis PSF

Each of the three Wolter-type X-ray telescopes onboard **XMM-Newton** has its own point-spread function (PSF). As an example, Fig. 4 shows the in orbit on-axis PSF of the MOS1, MOS2 and pn X-ray telescopes, registered on the same source. This figure is primarily provided to show the shape of the PSF, with for example the radial substructures caused by the spiders holding the mirror shells. Values for the full width at half maximum ($FWHM$) and half energy width (HEW) of the PSFs (both in-orbit and ground measurements) are listed in Table 2.
Fig. 5 displays the azimuthally averaged profile of the PSF of one X-ray telescope together with the best-fit King profile [1].
Figs. 6 and 7 show the fractional encircled energy as a function of radius from the centre

---

[1] A King profile has the form $A(1/([1+(r/r_c)^2]^\alpha))$, where r is the radial distance from the centre of the PSF, r_c is the core radius and α is the slope of the King model.

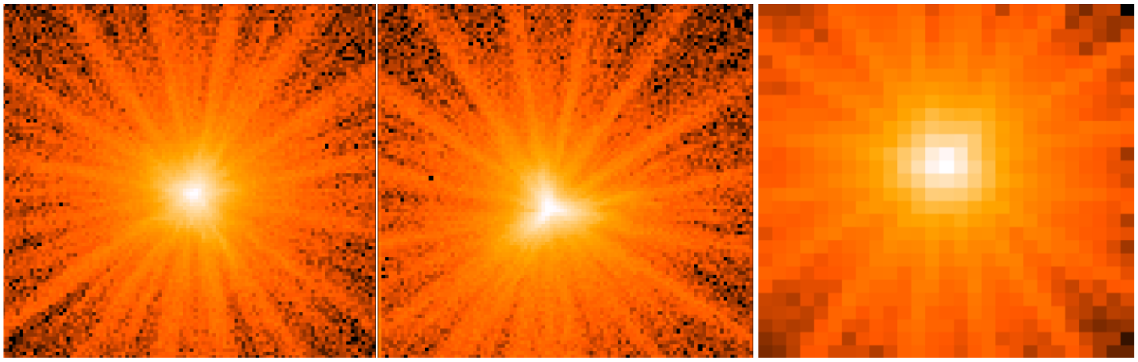

Figure 4: *On axis point spread function of the MOS1, MOS2 and pn X-ray telescopes (left to right) registered on the same source with each MOS camera in Small Window Mode, and the pn camera in Large Window mode. The pixel size is 1.1 arcsec square for the MOS, and 4.1 arcsec square for the pn. The images are 110 arcsec wide. A logarithmic scale has been used to visualize the wings of the point spread function. The core of the PSF is piled-up for this source, with a different factor for the MOS and the pn. The star-like pattern is created by the spider which supports the 58 co-axial Wolter I mirrors of the telescope. The shape of the point spread function core is slightly different for all cameras, with MOS2 having a somewhat triangular shape.*

of the PSF for several different energies. For on-axis sources, high energy photons are reflected and focused predominantly by the inner shells of the X-ray telescope. The inner shells apparently give better focus than the average of all shells, hence the fractional encircled energy increases with increasing photon energy. Above 12 keV, the effective area, A_e, is very small, which makes simulations and the calibration of the PSF at such high energies unreliable.

Please note that the PSF measurements by the EPIC cameras might depend on the instrument readout mode, through combinations of out-of-time event smearing and/or pile-up. The PSF can be severely affected by pile-up effects when the count rate exceeds a few counts per frame. Depending on the selection of event types in the EPIC event analysis

Table 2: *The on-axis in orbit and on ground 1.5 keV PSFs of the different X-ray telescopes*

Mirror module	**2**	**3**	**4**
Instr. chain[a]	**pn** orbit/ground	**MOS-1+RGS-1** orbit/ground	**MOS-2+RGS-2** orbit/ground
FWHM [$''$]	$< 12.5^b/6.6$	4.3/6.0	4.4/4.5
HEW [$''$]	15.2/15.1	13.8/13.6	13.0/12.8

Notes to Table 2:

a) The instruments located behind the mirror module.

b) The core of mirror module 2 cannot be resolved in orbit because of the large pn-CCD pixel size, but studies are under way to deduce a maximum value of the width of the PSF core.

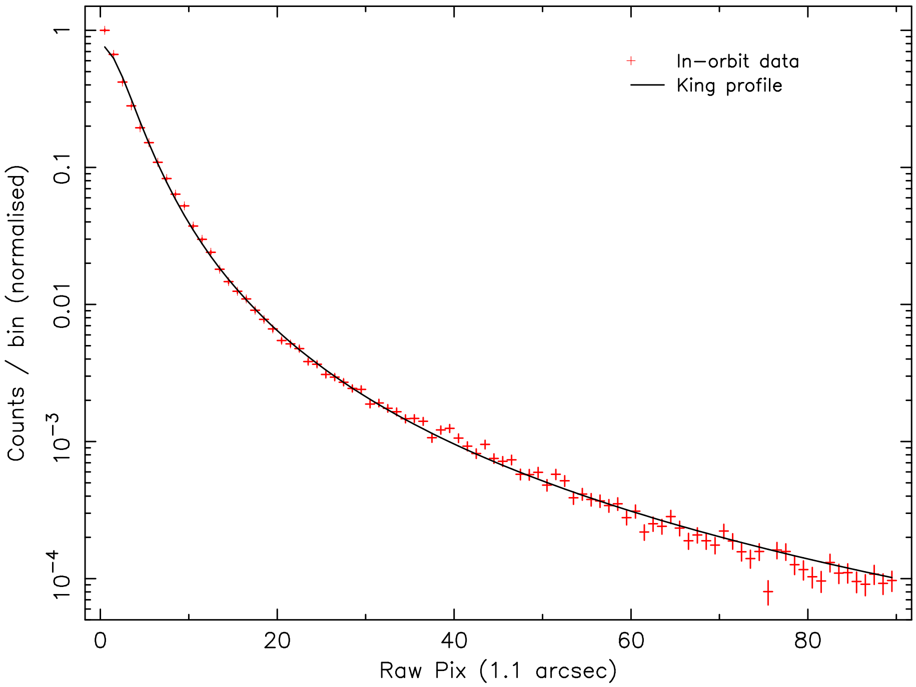

Figure 5: *Radial count distribution for the on-axis PSF of the MOS1 X-ray telescope in the 0.75-2.25 keV energy range. A King profile (solid black line) best fit to the in-orbit measurement (red crosses) is shown for comparison.*

process, a hole can even appear in the core of the PSF due to the lack of isolated events under high flux conditions (see § 3.3.9).

3.2.1.2 Off-axis PSF

The PSF of the X-ray telescopes depends on the source off-axis angle, i.e., its distance from the centre of the field of view (FOV). It also depends slightly on the source azimuth within the FOV. In Fig. 8 the dependence of the shape of the **XMM-Newton** X-ray PSF on the position within the FOV is presented, based on measurements during ground calibration. One can see that the PSF at large off-axis angles is elongated due to off-axis aberration (astigmatism). The reader is also referred to Figs. 16, 17 and 18 for an impression of the in-orbit appearance of the off-axis PSF.
For the two EPIC MOS cameras, the PSF is also affected at a level of a few times 10^{-4} (integral relative intensity) by scattering off the RGA rib structures. This contribution, however, is negligible in the vast majority of cases.

It is important to know the encircled energy fraction at different positions in the FOV, e.g., to use the correct extraction areas for source photons. In Fig. 9 we show the dependence of the radius at which 90% of the total energy is encircled ($W90$) on the off-axis angle. Note that as the off-axis angle increases the energy dependence of the PSF changes as focusing of high energy photons is no longer confined to the inner shells. A large fraction of these high energy photons are redistributed into the wings of the PSF by X-ray scattering hence $W90$ is larger at high energies than at soft energies for large off-axis angles.

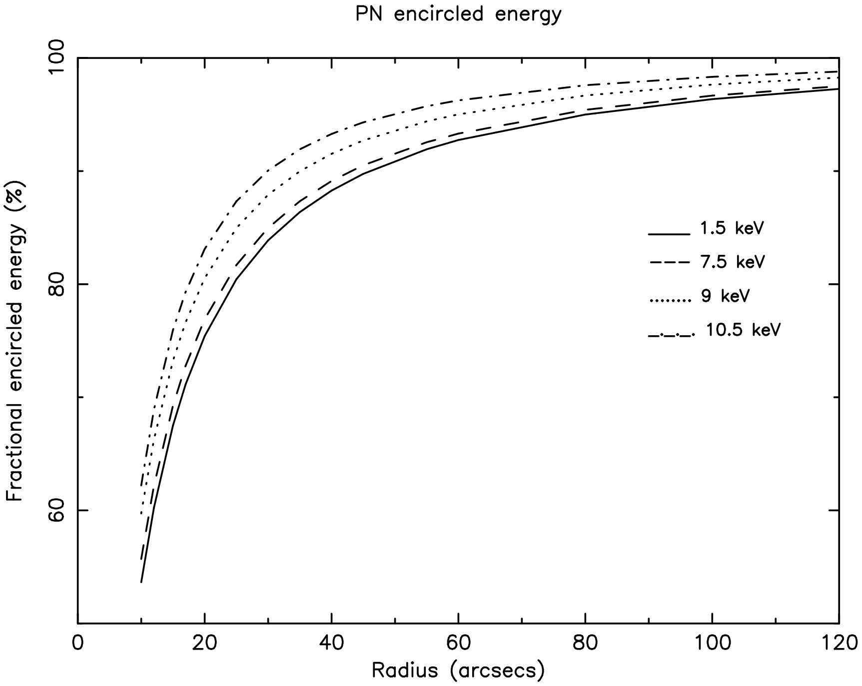

Figure 6: *The pn fractional encircled energy as a function of angular radius (on-axis) at different energies. The curves were calculated assuming a fractional encircled energy of 100% at a radial distance of 5 arcmin.*

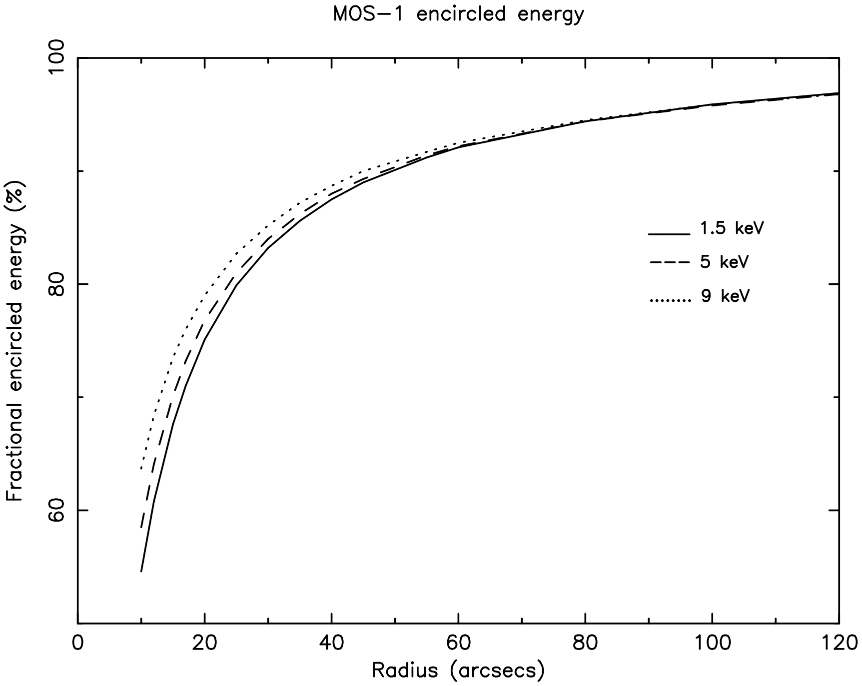

Figure 7: *The MOS1 fractional encircled energy as a function of angular radius (on-axis) at different energies. The curves were calculated assuming a fractional encircled energy of 100% at a radial distance of 5 arcmin.*

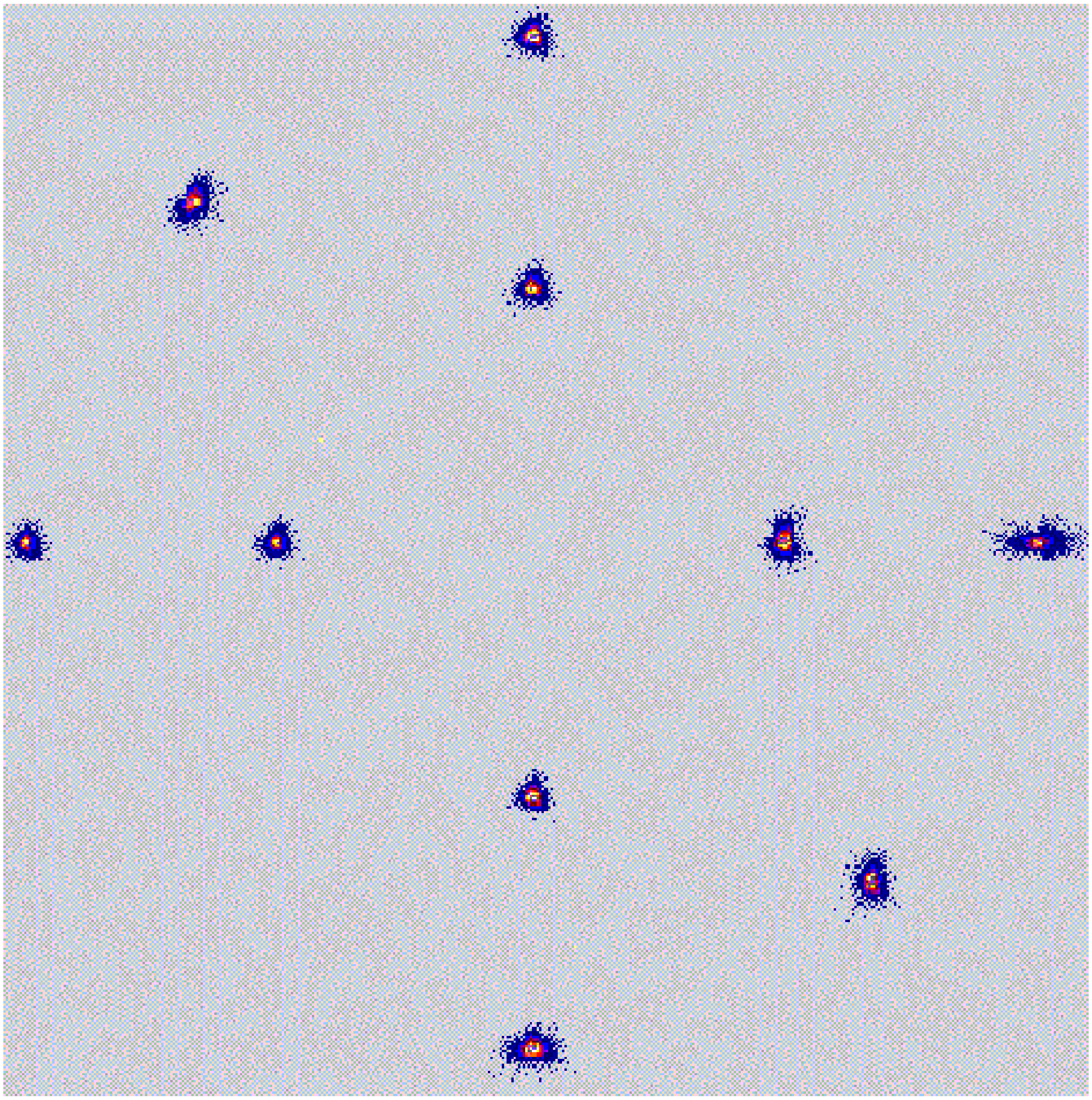

Figure 8: *The dependence of the X-ray PSF's shape on the position in the field of view. This image was made from Panter measurements, thus not under flight conditions, but the PSFs are representative. Measurements were taken at off-axis angles of* 7′ *and* 14′, *at 4 (6) different azimuthal positions. The intensity scale is logarithmic.*

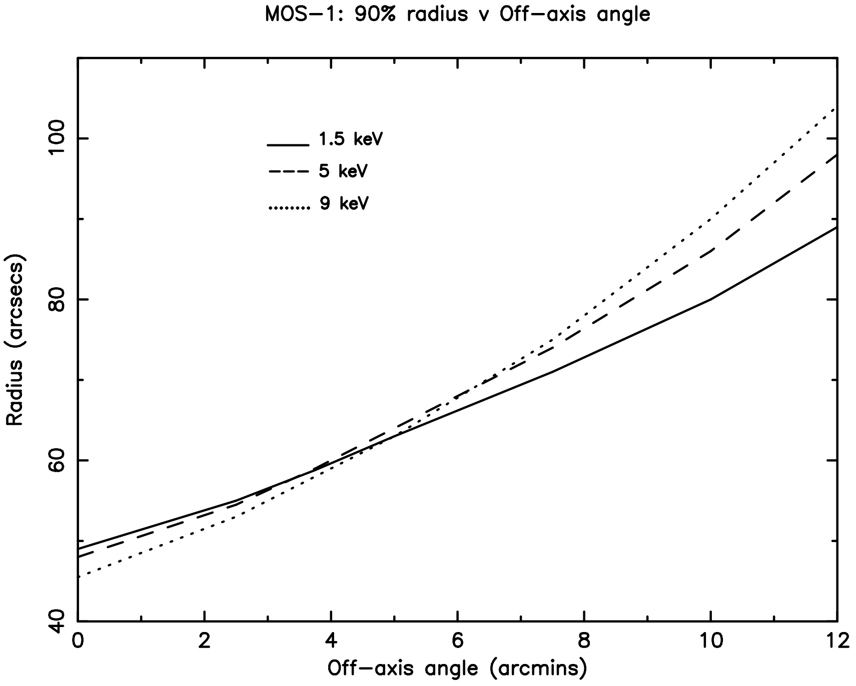

Figure 9: *The W90 radius of a point source as a function of off-axis angle at different energies. The curves were calculated assuming a fractional encircled energy of 100% at a radial distance of 5 arcmin, independent of the off-axis angle.*

3.2.2 X-ray effective area

The second important characteristic of the mirror performance is their effective area, A_e, which reflects the ability of the mirrors to collect radiation at different photon energies.

3.2.2.1 On-axis effective area

The most important information for **XMM-Newton** users is the mirror effective area, folded through the response of the different focal instruments. These are shown in Figs. 10 and 11. The effective areas have been extracted from the ready-made EPIC response matrices (full-frame mode, thin filter) and from response matrices created with the SAS task rgsrmfgen in case of the RGS's. One can see that the **XMM-Newton** mirrors are most efficient in the energy range from 0.1 to 10 keV, with a maximum at about 1.5 keV and a pronounced edge near 2 keV (the Au M edge). The effective areas of the two MOS cameras are lower than that of the pn, because only part of the incoming radiation falls onto these detectors, which are partially obscured by the RGAs (Fig. 3).

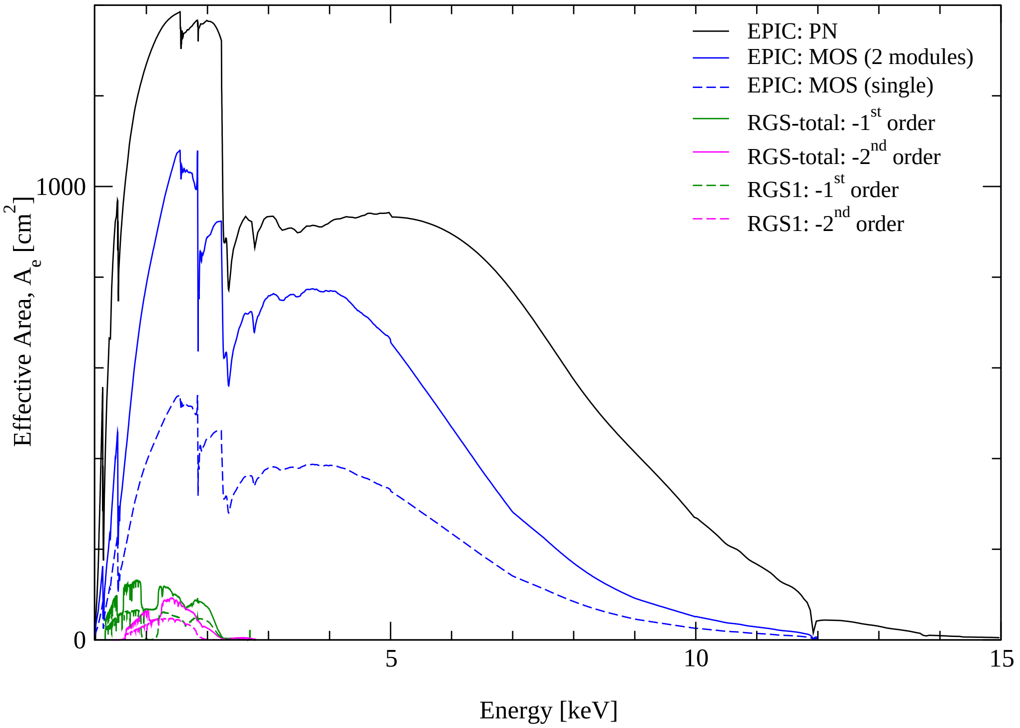

Figure 10: *The net effective area of all* **XMM-Newton** *X-ray telescopes, combined with the response characteristics of the focal X-ray instruments, EPIC and RGS (linear scale).*

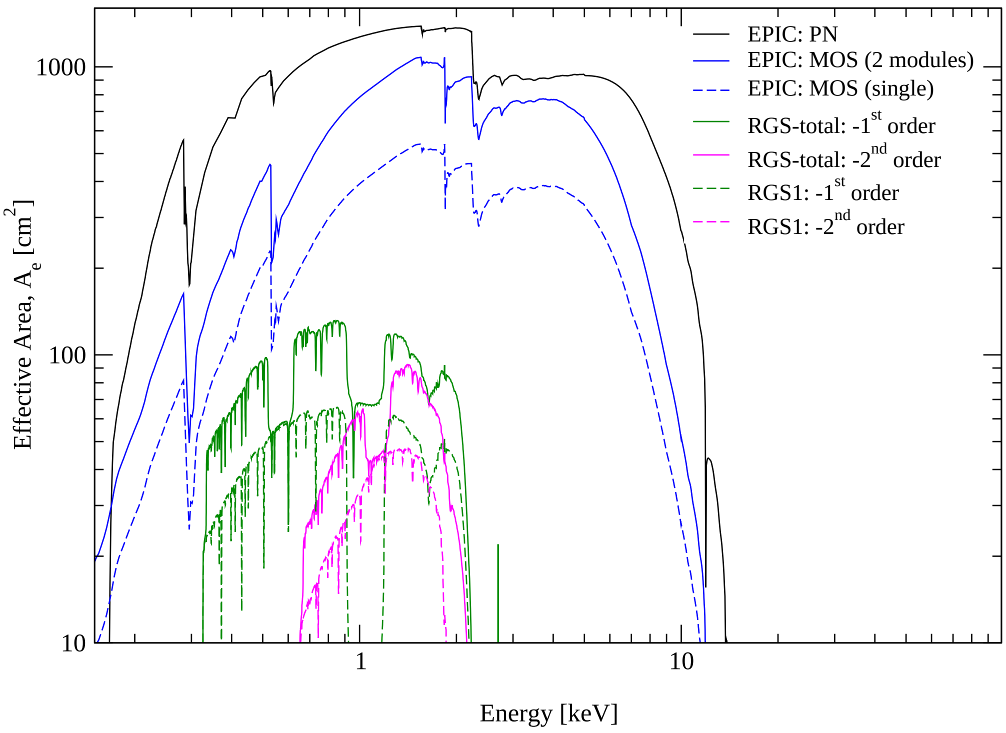

Figure 11: *The net effective area of all* **XMM-Newton** *X-ray telescopes, combined with the response characteristics of the focal X-ray instruments, EPIC and RGS (logarithmic scale).*

3.2.2.2 Off-axis effective area

Not only the shape of the X-ray PSF, but also the effective area of the mirrors is a function of off-axis angle within the mirrors' 30′ FOV. With increasing off-axis angle, less of the photons entering the telescopes actually reach the focal plane. This effect is called "vignetting". The vignetting of the **XMM-Newton** telescopes, which is reflected by the decline of the X-ray telescope's effective area as a function of off-axis angle, is displayed for a few energies for the X-ray telescope 2 in Fig. 12.

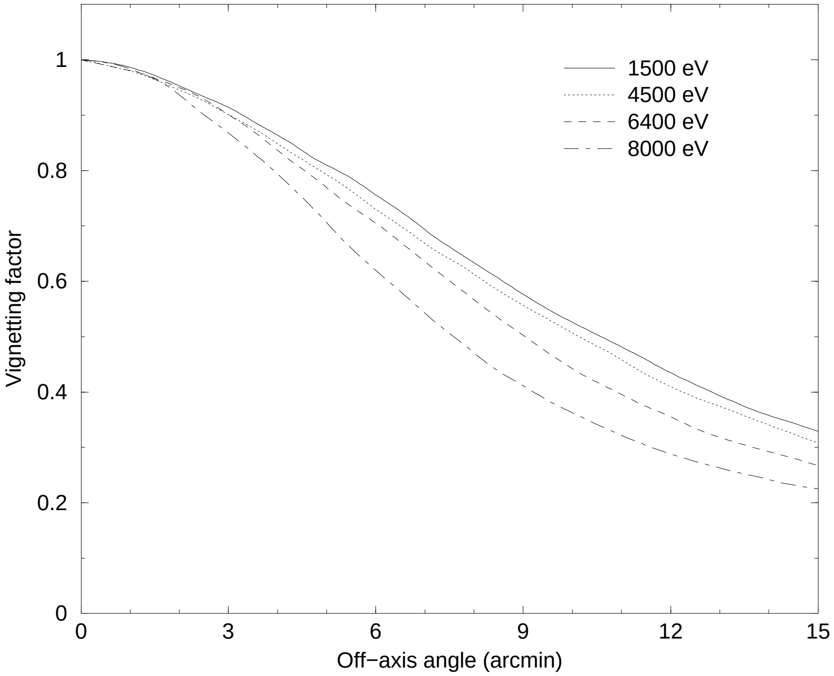

Figure 12: *Vignetting function as a function of off-axis angle (0′–15′, based on simulations), at a few selected energies, of the X-ray telescope 2 in front of the pn camera*

The off-axis vignetting in the two telescopes with an RGA has a dependence on angle with respect to the RGAs' dispersion direction. A source at an off-axis position perpendicular to the dispersion direction will be vignetted by a different amount to one at a position parallel to the dispersion direction. This azimuthal dependency of the vignetting is shown in Fig. 13.

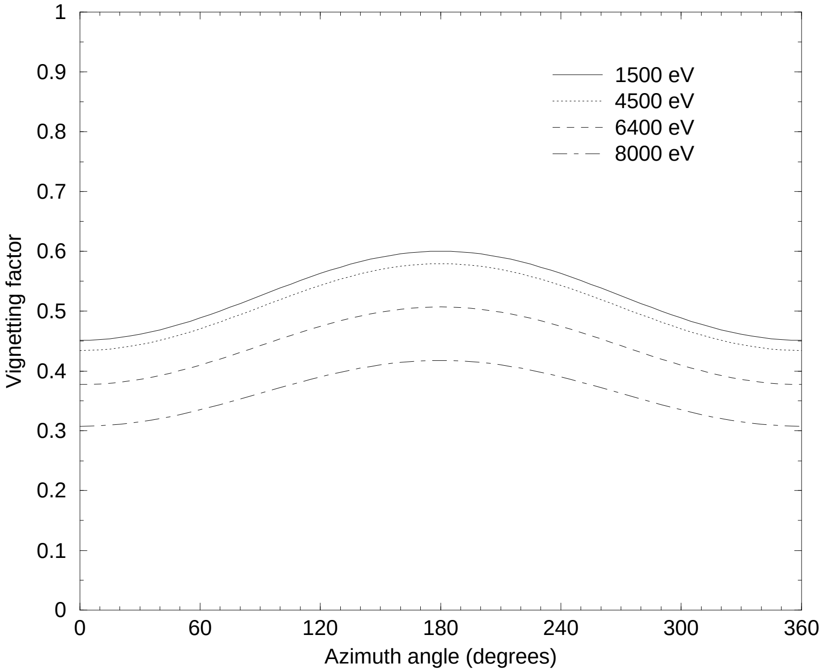

Figure 13: *Vignetting function as a function of azimuth angle of the X-ray telescope 3 in front of the MOS1 camera. The curves are given for an off-axis angle of 10 arcmin. Due to the presence of reflection grating assemblies in the exit beams of the X-ray telescopes 3 and 4, the vignetting functions measured in the MOS cameras are modulated azimuthally.*

3.2.3 Response matrices used in the SAS data analysis

The EPIC and RGS response matrices generated by the SAS tasks 'rmfgen' and 'rgsrmfgen' already include the effective area of the telescopes together with the vignetting or the diffraction efficiency of the gratings, the transmissions of the filters and the quantum efficiency of the detectors.

Depending on the selected source extraction window in EPIC and on the spectrum extraction region in RGS, the SAS tasks 'rmfgen' and 'rgsrmfgen' apply additional corrections for count losses out of these windows. In the case of EPIC, this is performed using encircled energy fractions of the point spread function calibrated for the different telescopes. The illustration of telescopes effective area and encircled energy functions are provided in this section only for general information. These graphs shall not be used for the purpose of effective area correction. This is normally done by the SAS tasks by the generation of the RGS and EPIC instrument response matrices. In particular situations, the user could produce tabulated values of the telescope effective area and encircled energy fraction using the SAS task 'calview'. Should this be the case, the **XMM-Newton** SAS User's Guide and the **XMM-Newton** Calibration Access and Data Handbook should imperatively be consulted.

3.2.4 Straylight rejection

The third important performance characteristic of the X-ray telescope, as listed above, is the efficiency of the straylight rejection.

Without X-ray baffles, the **XMM-Newton** mirror modules would suffer from X-ray straylight entering the tubes. The effect is that the image of a $30'$ area of the sky (the EPIC FOV) would be contaminated by a diffuse light background produced by X-ray sources located outside this field. X-ray straylight in EPIC is produced by rays which are singly reflected by the mirror hyperbolas and which reach the sensitive area of the camera. An X-ray baffle was implemented to shadow those singly reflected rays. It consists of two sieve plates made of concentric annular aperture stops located in front of the mirrors at 85 mm and 145 mm, respectively. The design is such that the entrance annular aperture of each mirror remains unobstructed for on-axis rays. Most of the rays with large off-axis angle are vignetted and cannot reach the detectors anymore via a single hyperbola reflection.

The straylight collecting area in the EPIC detector as a function of off-axis angle for a point source is about 3 cm^2 for stray sources located between $20'$ and 1.4° from the optical axis. At higher off-axis angles it is completely negligible. The ratio of the X-ray straylight collecting area to the on-axis effective area is smaller than 0.2% at 1.5 keV for a point source located at off-axis angles of 0.4–1.4° and negligible at higher off-axis angles. This ratio, expressed in surface brightness values, is even smaller since the stray-image is unfocused at detector position.

Assuming a 10 counts/s source, for EPIC MOS on-axis observations half of the incoming photon flux is distributed over ca. 150 pixels (adopting a $15''$ *HEW*), with a central peak. The light of the same source, observed at a large off-axis angle, is distributed over about 1/4 or 1/5 of the total EPIC FOV (of order 10^6 pixels), leading to a *mean* count rate of 10^{-5} counts s^{-1} pixel^{-1} of diffuse straylight. However, this is only a rough approximation, because the stray radiation due to an off-axis point source is not uniformly distributed in the EPIC FOV, but produces near-annular structures in the image, as for example seen in Fig. 14.

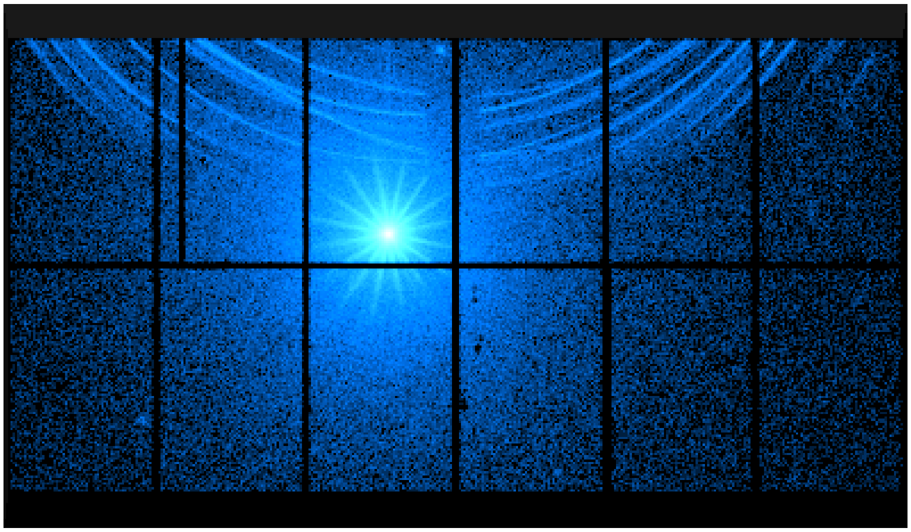

Figure 14: *EPIC pn image of GRS1758-258 (a black hole candidate near the Galactic center) observed in the large window readout mode demonstrating the effect of straylight: in the upper part of the image, sharp arcs appear that are caused by single mirror reflections of photons possibly from GX 5-1 which is* ~ 40 *arcmin offaxis to the north and outside the FOV.*

This illustrates the high straylight rejection efficiency of the **XMM-Newton** mirror modules. EPIC observations of isolated sources and RGS spectra are hardly affected. For bright extended sources (which are larger than the EPIC FOV, such as some supernova remnants, clusters of galaxies, stellar clusters and star forming regions), on the contrary, there might be a degradation in the ability to perform spatially resolved spectroscopy.

Simulations using SciSim (Appendix A) are strongly recommended prior to proposing observations in case the target is within 1.5° of a bright X-ray source, or in case imaging is foreseen of an extended object that is larger than the EPIC $30'$ FOV. Which level of straylight is problematic for a given proposal depends largely on the scientific objectives and on the ratio of the flux of the off-axis source and the required minimum detectable source flux within the FOV.

3.3 EUROPEAN PHOTON IMAGING CAMERA (EPIC)

Two of **XMM-Newton**'s X-ray telescopes are equipped with EPIC MOS (Metal Oxide Semi-conductor) CCD arrays, the third carries a different CCD camera called EPIC pn. In a nutshell, the **XMM-Newton** EPIC cameras offer the possibility to perform extremely sensitive imaging observations over a field of view of $30'$ and the energy range from 0.15 to 15 keV, with moderate spectral ($E/\Delta E \sim 20-50$) and angular resolution ($6''$ *FWHM*; $15''$ *HEW*). The pn type camera can be operated with very high time resolution down to 0.03 ms in the timing mode and 0.007 ms (but with a very low duty cycle) in the burst mode. Note however that the absolute timing accuracy is determined by the process which correlates the on-board time to the universal time.
The detector layout and the baffled X-ray telescope FOV of both types of EPIC cameras are shown in Figs. 15 (which is just a rough sketch), 16, 17 and 18. For all cameras the sensitive area of the detector is about $30'$ across. The following details should be noted:

- The pn chip array is slightly offset with respect to the optical axis of its X-ray telescope so that the nominal, on-axis observing position does not fall on the central chip boundary (see boresight positions for pn marked in Fig. 18). This ensures that $\geq 90\%$ of the energy of an on-axis point source are collected on one pn CCD chip.
- Onboard **XMM-Newton** there are two EPIC MOS cameras, rotated by 90° with respect to each other.
- The dead spaces between the MOS chips are not gaps, but unusable areas due to detector edges (the MOS chips physically overlap each other, the central one being located slightly behind the ones in the outer ring).

All EPIC CCDs operate in photon counting mode with a fixed, mode dependent frame read-out frequency, producing event lists.[2] This allows for simultaneous imaging and non-dispersive spectroscopy due to the intrinsic energy resolution of the pixels.

Note: If for any reason a user should decide to observe a target with EPIC **not on-axis, but instead off-axis**, then for off-axis angles in excess of $2.5'$ the grating spectrum might slip off the RGS detector array (because the RGS FOV is about $5'$ across in the cross-dispersion direction). Observing off-axis can be complicated if the observer wants to avoid all the MOS and pn inter-chip gaps – very careful position angle and off axis angle compromises should be made.

3.3.1 Two types of EPIC cameras: MOS and pn

The two types of EPIC cameras are fundamentally different. This does not only hold for the geometry of the MOS chip array and the pn chip array (Figs. 16, 17 and 18), but other properties as well, like e.g., their readout times. The readout of the pn chips is much faster than that of the MOS cameras, because each pixel column has its own readout node. Another important difference is that the MOS chips are front-illuminated, while the pn CCDs are back-illuminated, which affects the detector quantum efficiencies decisively (§ 3.3.5).

---

[2] An event list is a table with one line per received event, listing (among others) attributes of the events such as the x and y position at which they were registered, their arrival time and their energy.

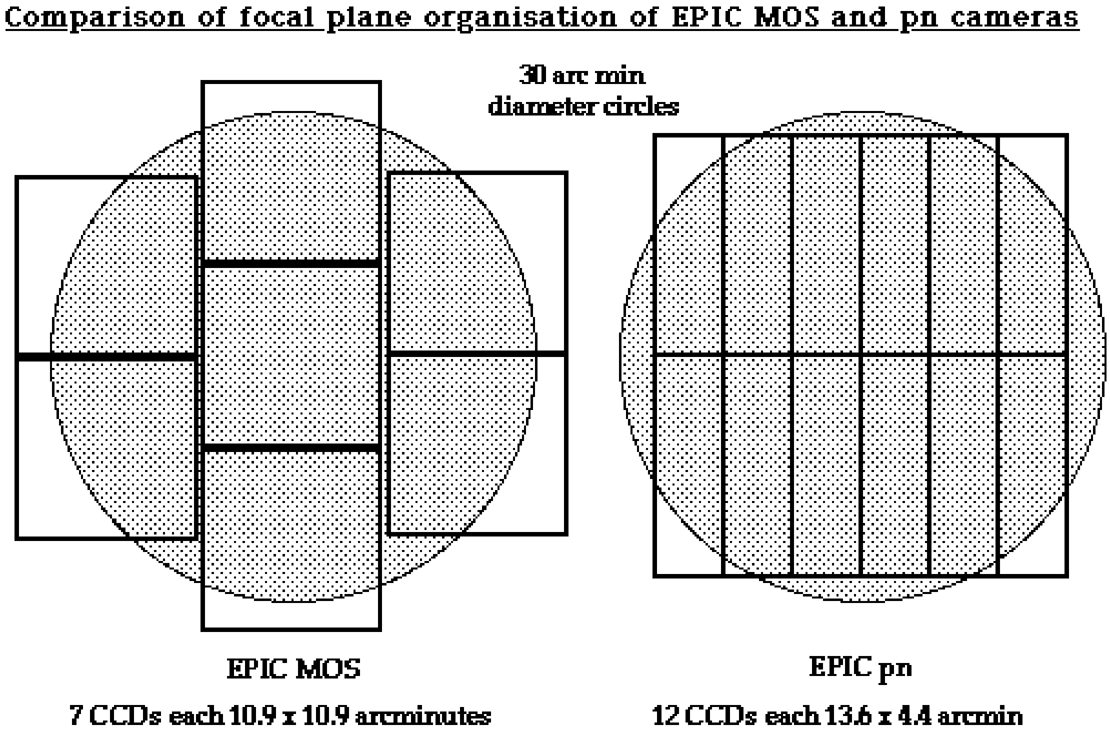

Figure 15: *A rough sketch of the field of view of the two types of EPIC cameras; MOS (left) and pn (right). The shaded circle depicts a* $30'$ *diameter area. For the alignment of the different cameras with respect to each other in the* **XMM-Newton** *focal plane refer to the text.*

3.3.1.1 EPIC MOS chip geometry

The MOS chip arrays consist of 7 individual identical, front-illuminated chips. The individual CCDs are not co-planar, but offset with respect to each other, following closely the slight curvature of the focal surface of the Wolter telescopes. Technically, this leaves space for the connections to the central CCD. The numbering scheme for the EPIC MOS chip array, the individual chip coordinate frames and the directions of the detector coordinates are displayed in Figs. 19 and 20. Not visible in the figures is that the MOS chips have a frame store region which serves as a data buffer for storage before they are read out through the readout nodes, while the rest of the chip is obtaining the next exposure.
As indicated above, the MOS cameras are mounted on those X-ray telescopes that also carry RGS instruments. Therefore, they receive only 44% of the reflected light.

3.3.1.2 EPIC pn chip geometry

The heart of the pn camera is a single Silicon wafer with 12 CCD chips integrated. The pn chip array numbering scheme, the individual chip coordinate frames and the directions of the detector coordinates are displayed in Fig. 21.

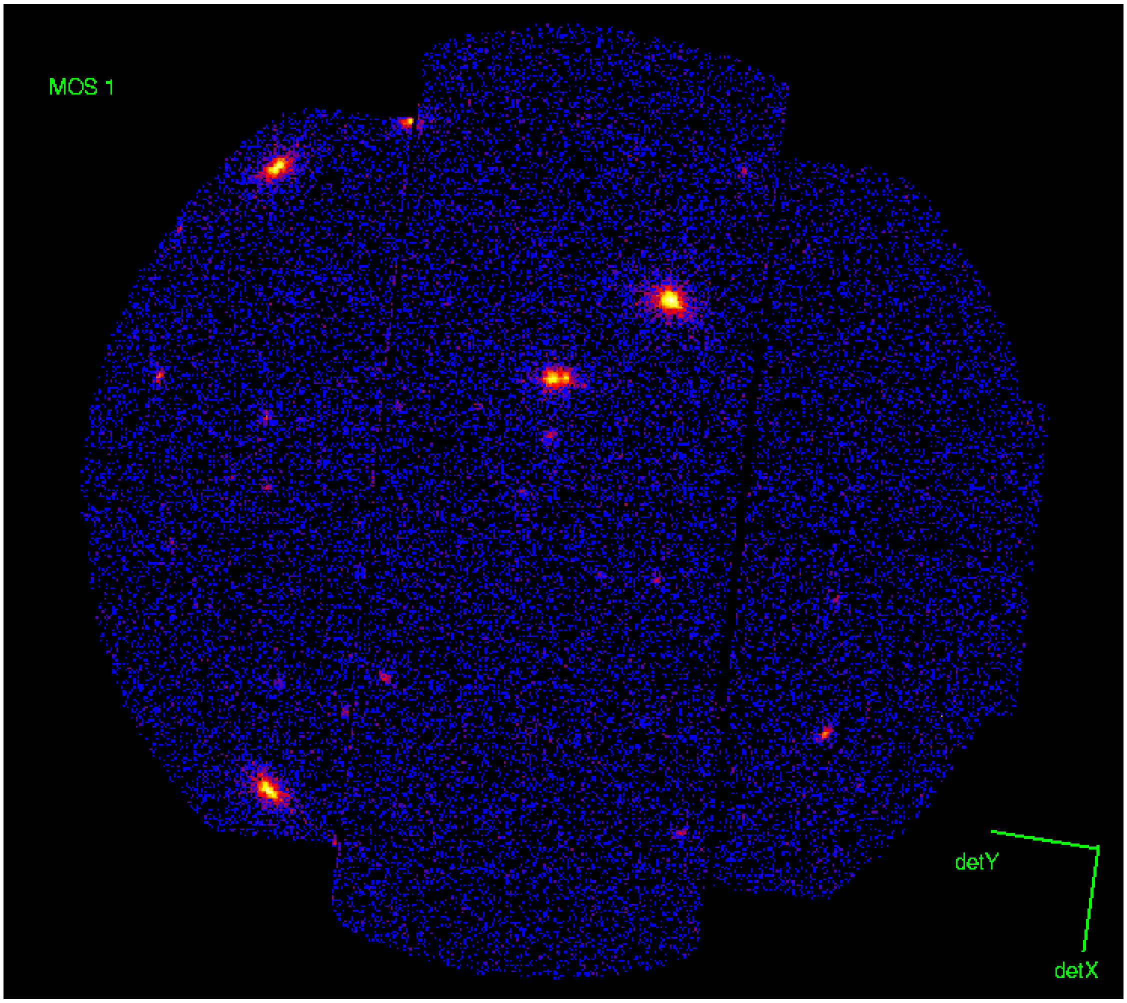

Figure 16: *The field of view of the EPIC MOS cameras: MOS1 (here) and MOS2 (next figure). The two MOS cameras view the same field as displayed in sky co-ordinates. In each case the camera detector co-ordinate frames are noted.*

3.3.2 Science modes of the EPIC cameras

The EPIC cameras allow several modes of data acquisition. Note that in the case of MOS the outer ring of 6 CCDs remain in standard imaging mode while the central MOS CCD can be operated separately. Thus all CCDs are gathering data at all times, independent of the choice of operating mode. The pn camera CCDs can be operated in common modes in all quadrants for full frame, extended full frame and large window mode, or just with one single CCD (CCD number 4 in Fig. 21) for small window, timing and burst mode.

1. “full frame” and “extended full frame” (pn only)

   In this mode, all pixels of all CCDs are read out and thus the full FOV is covered.

2. “partial window”

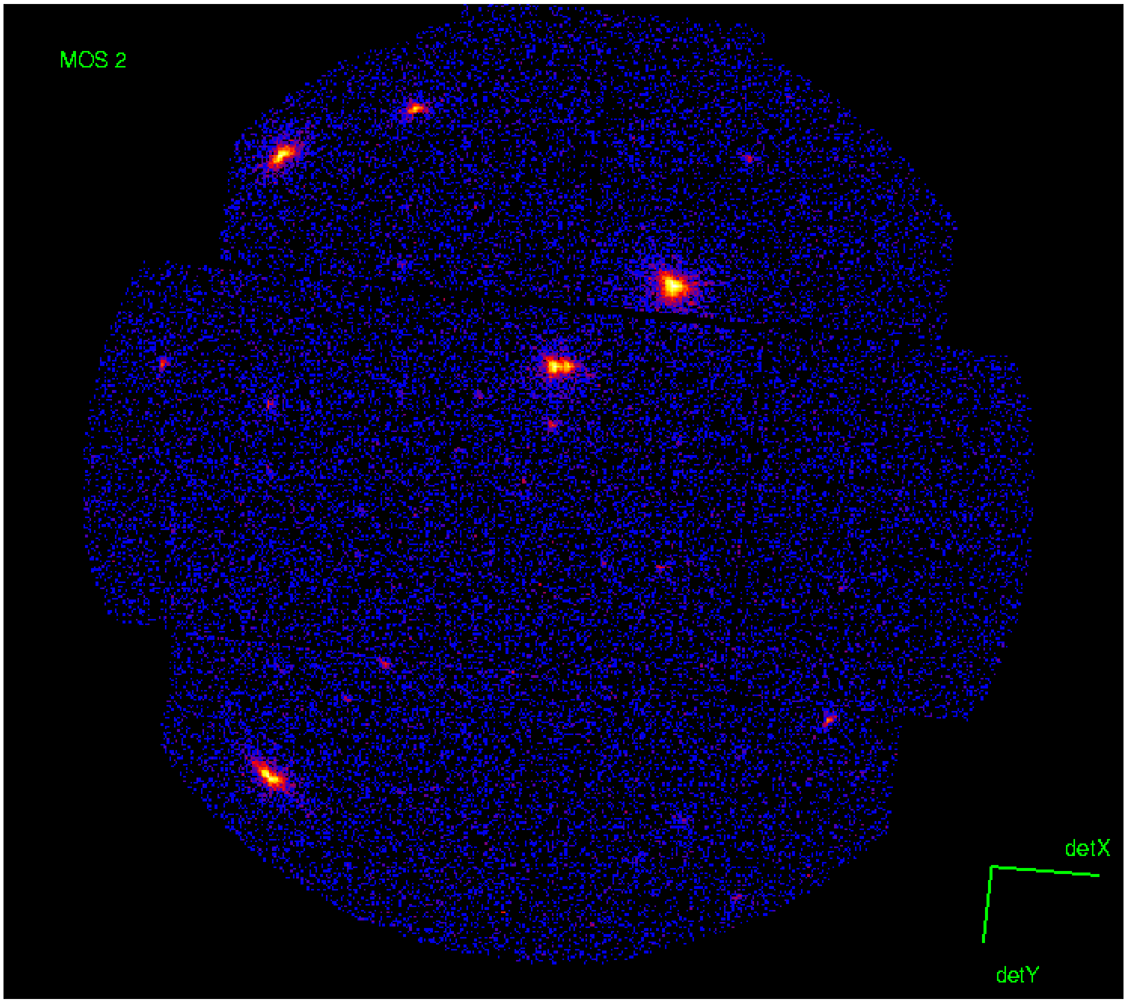

Figure 17: *The field of view of the EPIC MOS cameras (cntd. from previous figure): MOS2.*

a) MOS

In a partial window mode the central CCD of both MOS cameras can be operated in a different mode of science data acquisition, reading out only part of the CCD chip.

b) pn

In large window mode only half of the area in all 12 CCDs is read out, whereas in small window mode only a part of CCD number 4 is used to collect data.

3. “timing”

a) MOS + pn

In the timing mode, imaging is made only in one dimension, along the column (RAWX) axis. Along the row direction, data from a predefined area on one CCD chip are collapsed into a one-dimensional row to be read out at

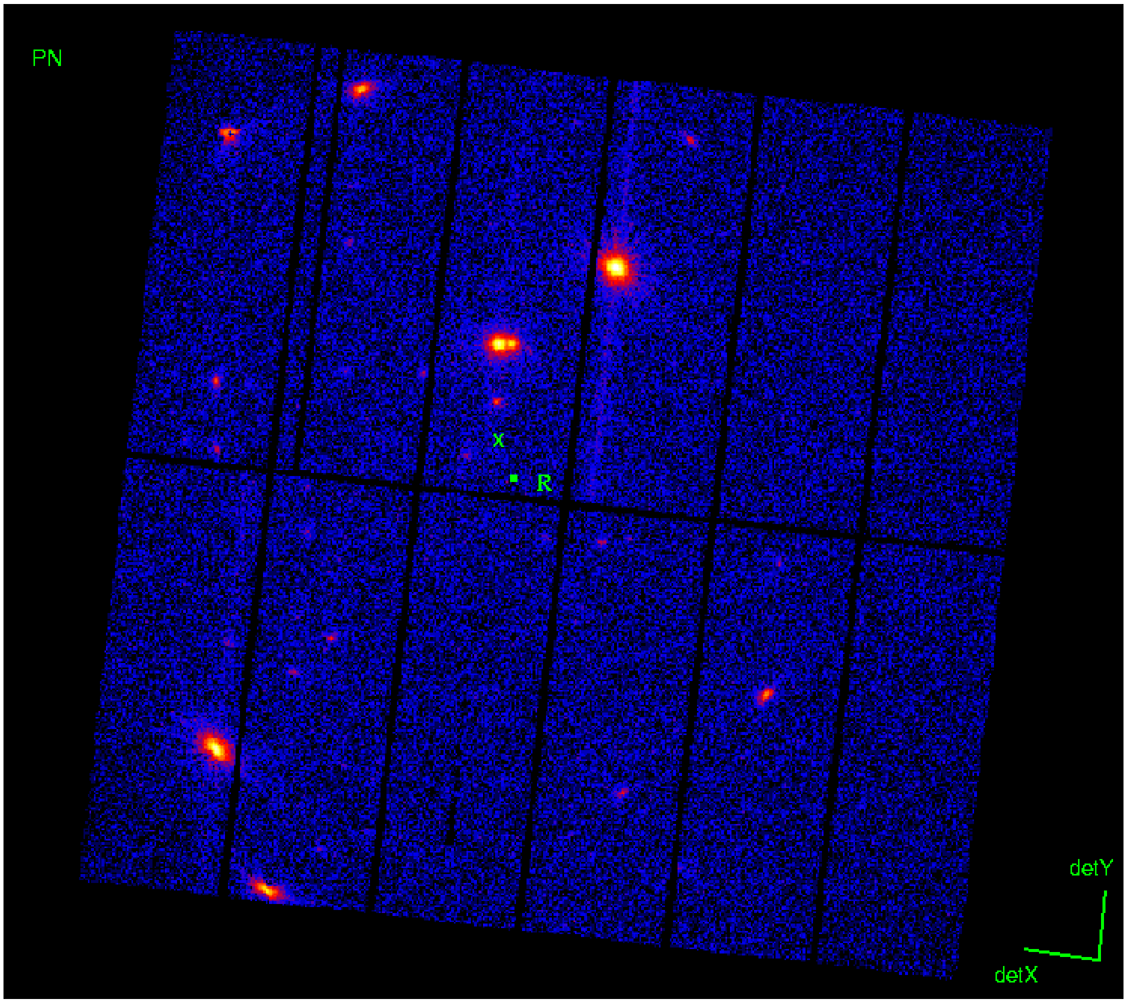

Figure 18: *The field of view of the EPIC pn camera; The pn camera views the same field as displayed in Fig. 16 in sky co-ordinates. Again the camera detector co-ordinate frame is noted. The current prime boresight is marked with a small box. Position 'X' shows the preferred location to centre on an object in the pn small window mode, however, the user is advised that this requires a knowledge of the position angle of the observation, and will also place the target outside the EPIC MOS small window. In the time frame of AO-2, it is intended to move the boresight towards position 'R' in order to maximize the coverage of important emission lines in RGS while EPIC is the prime instrument. A compromise boresight is expected to be used which will be located close to the geometric centre of the three locations marked on this figure.*

high speed. Since the 2 MOS cameras orientation differ by 90 degrees, the "imaging" directions in the 2 MOS are perpendicular to each other.

b) pn only

A special flavour of the timing mode of the EPIC pn camera is the "burst" mode, which offers very high time resolution, but has a very low duty cycle of 3%.

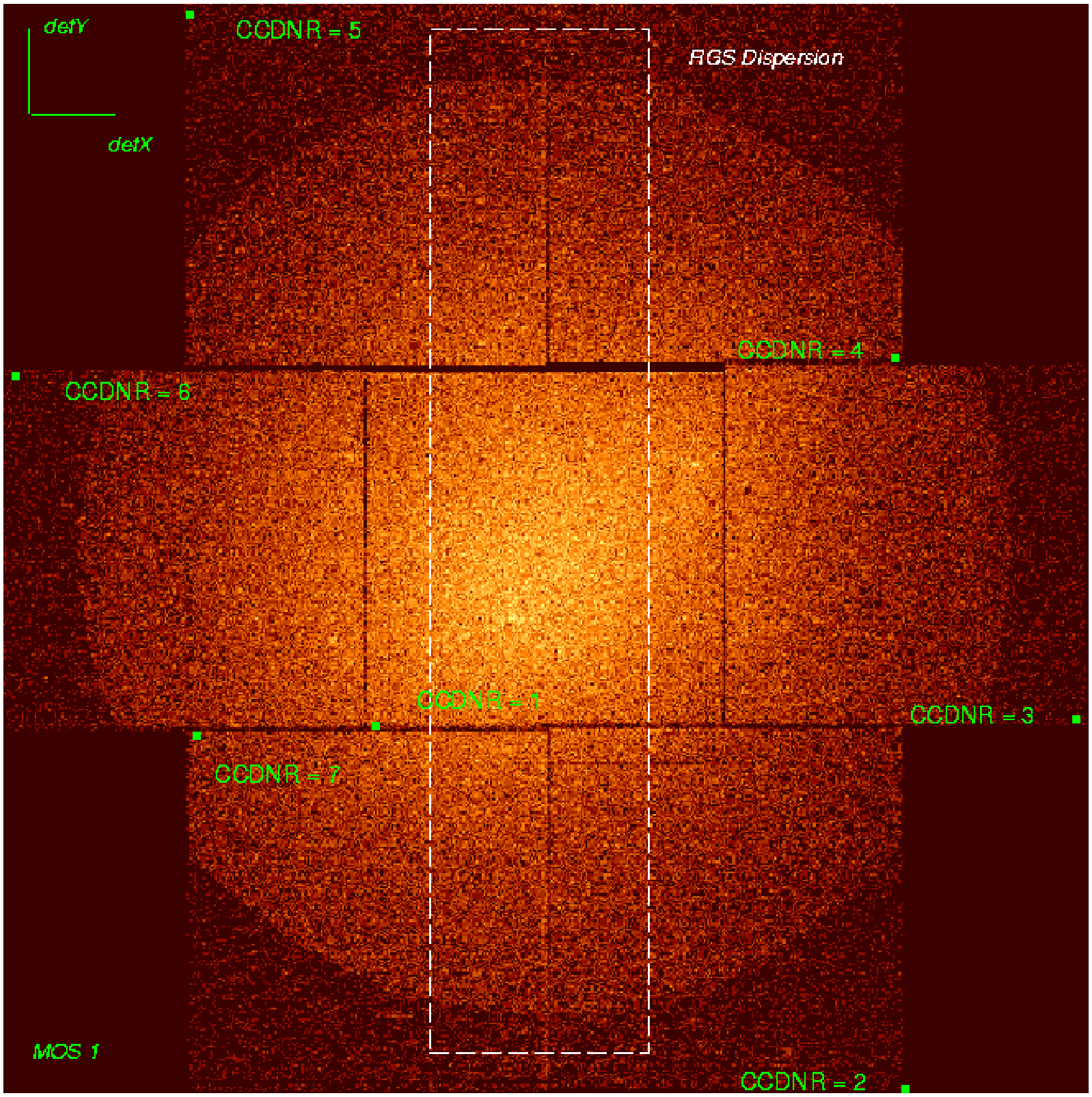

Figure 19: *The layout of the EPIC MOS cameras as presented in SAS: MOS1 (here) and MOS2 (next figure). The orientation of the detX/detY axes are shown, to highlight that the RGS dispersion axes are parallel within spacecraft physical co-ordinates, but the EPIC MOS cameras are orthogonally aligned. The readout node of each CCD is located with a small box, the rawY co-ordinate in each CCD decreases from the centre towards the node with the 3 CCDs on each side of the focal plane being read in the same direction. The rawX then decreases towards the readout node in the orthogonal direction.*

The most important characteristics of the EPIC science modes (time resolution and count rate capability) are tabulated in Table 3. Fig. 22 and Fig. 23 show the active CCD areas for the different pn and MOS readout modes, respectively.
The count rate limitations are defined for a 1% pile-up case (see § 3.3.9 for details on pile-up), which occurs at about 2 photons per MOS CCD frame, and 0.5 photons per pn CCD frame in case of an on-axis source. Early estimates of spectral fitting errors without

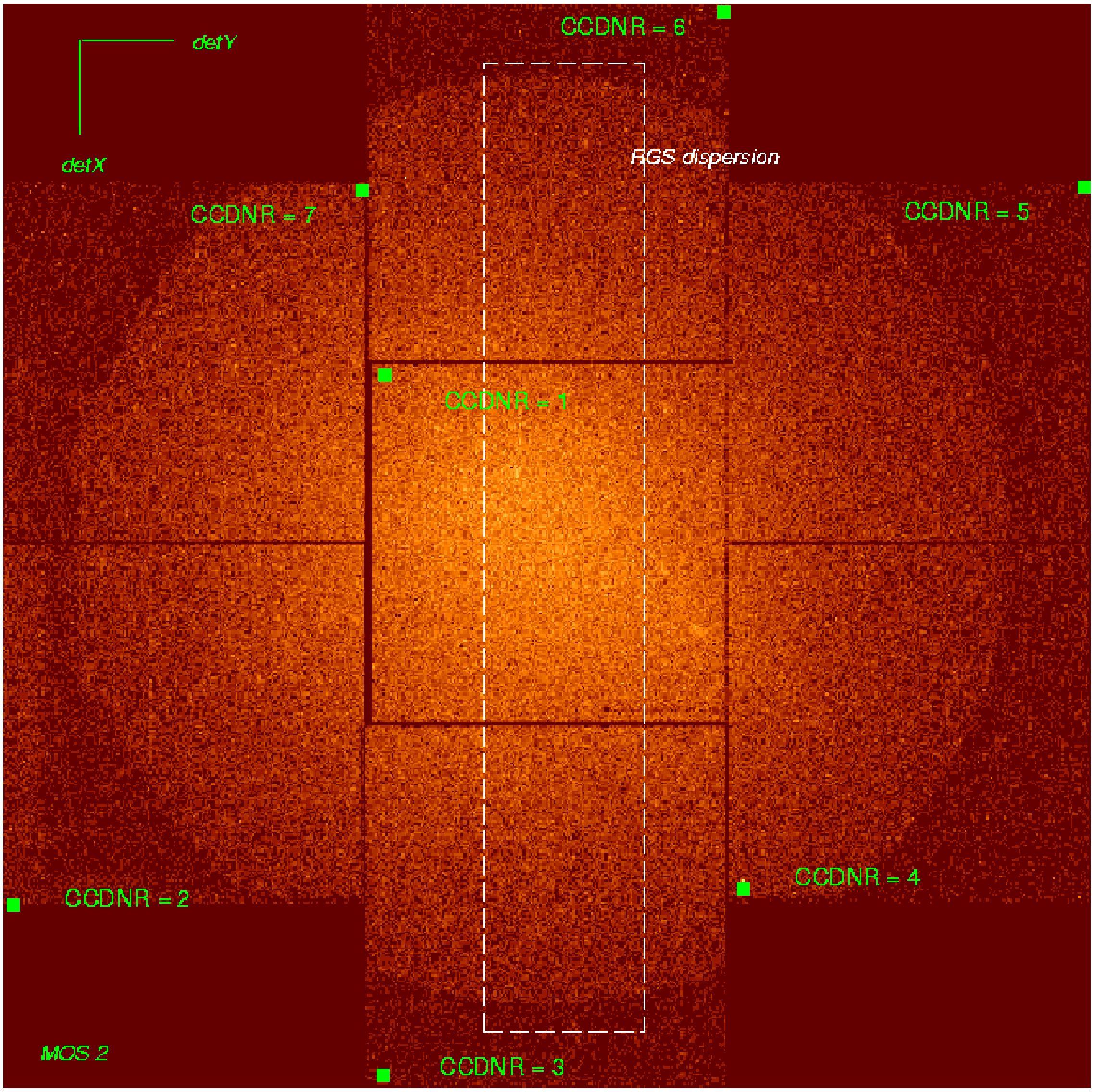

Figure 20: *The layout of the EPIC MOS cameras as presented in SAS (cntd. from previous figure): MOS2.*

any response matrix corrections show that a doubling of these count rates could lead to systematic errors greater than the nominal calibration accuracies. The SOC Team intends to develop tools to alleviate this pile-up effect, but GOs are advised that this will be a long-term effort. For the time being the pile-up can be alleviated by excising the PSF core at the penalty of losing overall flux, but retaining spectral fitting integrity.

For sources with very soft spectra a factor of 2–3 lower maximum count rate limits are recommended, see § 3.3.9. For the pn camera also for point sources with hard spectra (power law photon index alpha < 2) lower count rate limits should be applied, in order to avoid possible print through of X-ray photons during the offset map calculation. For alpha $= 1.5$ and 1.0 the maximum count rate limits given in Table 3 should be reduced by factors 2 and 4, respectively.

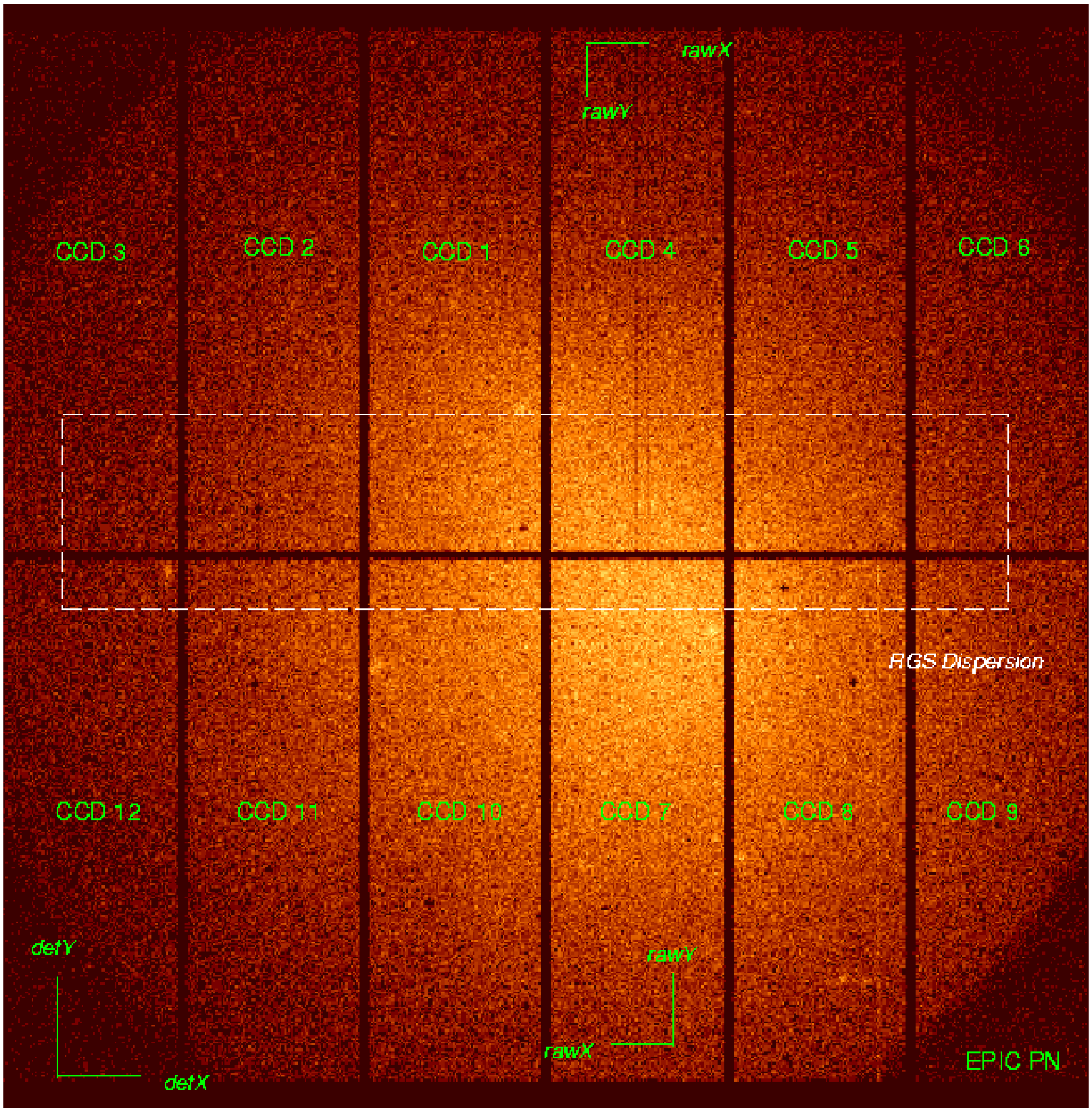

Figure 21: *The layout of the EPIC pn camera as presented in SAS. The orientation of the rawX/rawY (CCD specific) and of the detX/detY axes are shown, to highlight that the RGS dispersion axes are parallel within spacecraft physical co-ordinates. The readout CAMEX of each CCD is located at rawY = 0, i.e. at the top (for CCDs 1 – 6) or bottom (for CCDs 7 – 12) of the displayed array.*

One of the major differences between the two types of cameras is the high time resolution of the pn chip array. With this camera high-speed photometry of rapidly variable targets can be conducted, down to a minimum integration time of 30 (7) μs in the timing (burst) mode.

Table 3: *Basic numbers for the science modes of EPIC*

MOS (central CCD; pixels)	**Time resolution**	**Max. count rate[1] diffuse[2] (total) [s^{-1}]**	**Max. count rate[1] (flux) point source [s^{-1}] ([mCrab])**
Full frame (600×600)	2.6 s	150	0.70 (0.24)
Full frame two nodes (600×600)	1.4 s	285	1.30 (0.45)
Small window (100×100)[3,7]	0.3 s	37	5 (1.7)
Large window (300×300)[3,7]	0.9 s	110	1.8 (0.6)
Refreshed frame store[4]	2.9 s	2000	
Timing uncompressed	1.5 ms	N/A	100 (35)

pn (array or 1 CCD; pixels)	**Time resolution**	**Max. count rate[1] diffuse[2] (total) [s^{-1}]**	**Max. count rate[1] (flux) point source [s^{-1}] ([mCrab])**
Full frame[5] (378×384)	73.4 ms	1000(total)	8 (0.9)
Extended full frame[5,6] (378×384)	200 ms	370	3 (0.39)
Large window (198×384)	48 ms	1500	12 (1.3)
Small window (63×64)	6 ms	12000	130 (14)
Timing	0.03 ms	N/A	1500 (160)
Burst	7 μs	N/A	60000 (6300)

Notes to Table 3:
1) “Maximum” to avoid deteriorated response due to photon pile-up, see § 3.3.9. Note that telemetry limitations are in some cases more stringent than the pile-up constraints. For the MOS cameras the maximum count rates are about 150 counts/s for full window imaging and 300 counts/s for partial window imaging and timing mode. The pn telemetry limit is approximately 1150 counts/s in all modes and is triggered for each quadrant separately. See also the count rate limitations given in the text of § 3.3.2.
2) Values are representative of bright objects that are extended on scales much larger than the PSF core. In case of assumed homogeneous illumination on the CCD, the 1% pile-up limit for MOS is reached for a flux of 1 event per 900 pixels per frame.
3) 1 node readout.
4) This mode is designed for the case where the user requires to collect data from the whole of the inner CCD (600×600), but knows that the photon flux rate is so high as to lead to significant pile-up. Then the refreshed frame store (RFS) mode can be invoked, in which the frame integration time is defined as 0.2 seconds, but the data which collects during the remainder of the normal readout of 2.7 seconds must be discarded. In this case the live time is only 6.9%. There are very few bright extended objects that can be considered to require this facility, rather than a normal windowed selection, and therefore it is **not recommended for normal GO usage**.
5) The first 12 rows at the readout-node are not transmitted to ground (are set to “bad”, equivalent to “bad pixels”).
6) “Extended” means that the image collection time (i.e. the frame time) is longer than in the normal full frame mode.
7) There may be minor changes in the time resolution values as a result of the new boresight modified windows.

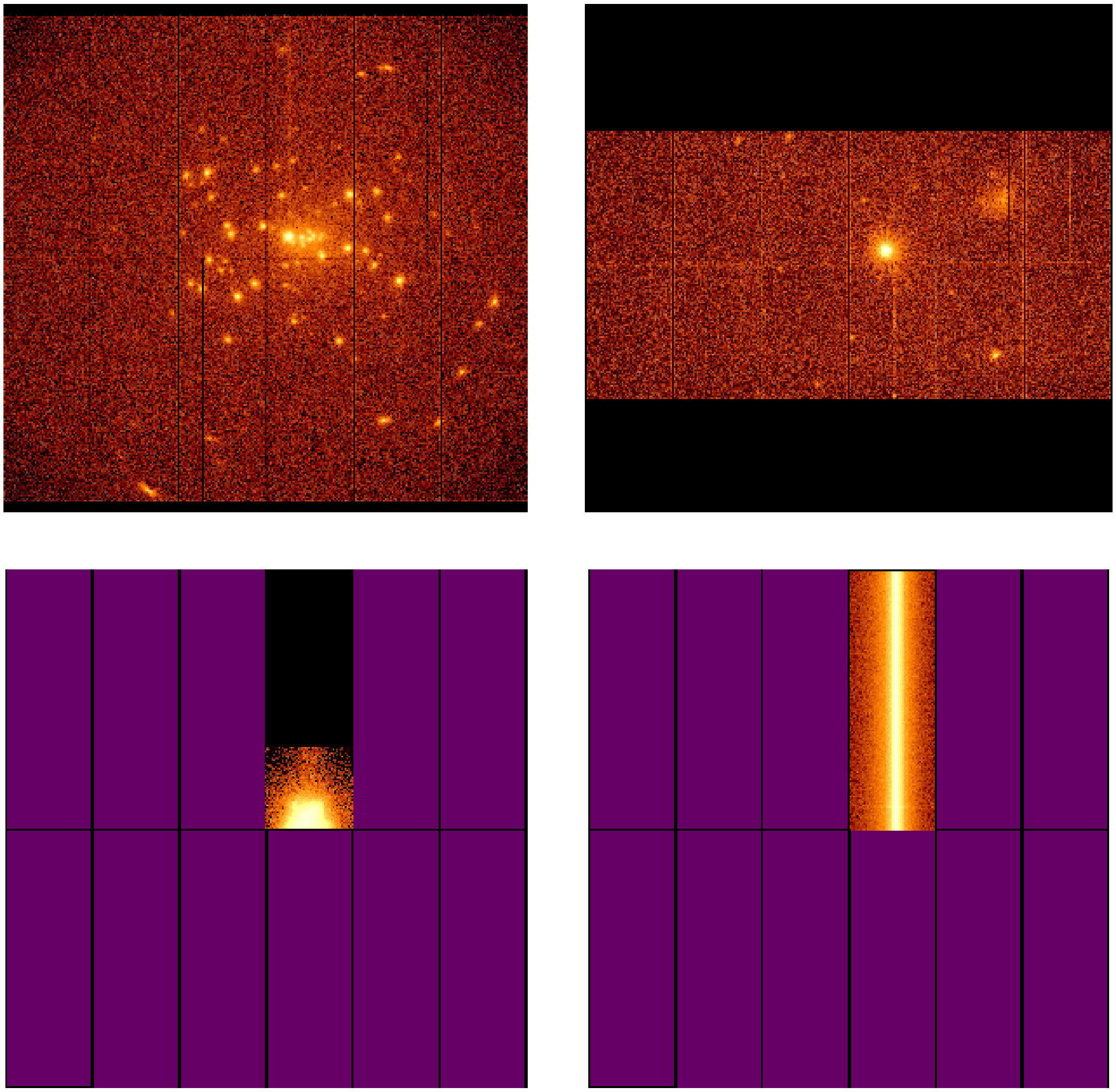

Figure 22: *Operating modes for the pn-CCD camera: top left: Full frame and extended full frame mode, top right: Large window mode, bottom left: Small window mode and bottom right: Timing mode. The burst mode is different from the timing mode as the source position is not read out, i.e. rows 181-200 will be dark.*

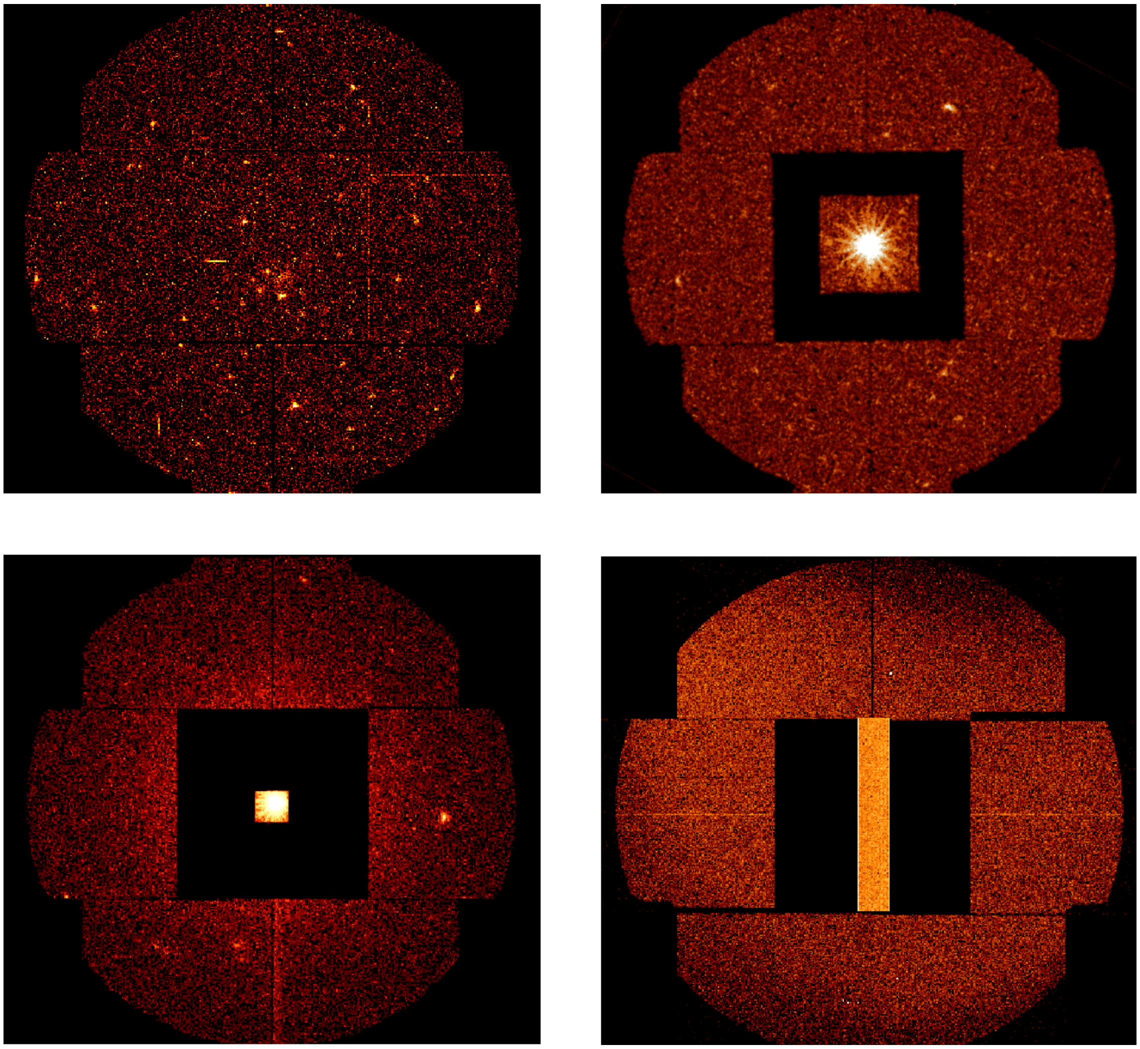

Figure 23: *Operating modes for the MOS-CCD cameras: top left: Full frame mode, top right: Large window mode, bottom left: Small window mode and bottom right: Timing mode. In timing mode, the X axis of the central CCD is the projected image of the source, and has thus true spatial information; the Y axis does not carry any spatial information, but is a measure of time, with roll-over of 1024 time-units in the figure shown.*

3.3.3 EPIC imaging – angular resolution

EPIC's angular resolution is basically determined by the PSF of the mirror modules. This is due to the fact that the EPIC MOS and pn cameras have pixels with sizes of 40 and 150 μm, respectively. For the focal length of the X-ray telescopes (7.5 m), this corresponds to $1.1''$ ($4.1''$) on the sky. Given the $FWHM$ of the PSF of ca. $6''$ (Table 2), the Nyquist theorem is thus fulfilled for the MOS cameras and images are fully sampled. The pixel size of the pn camera slightly undersamples the core of the PSF.

There is one notable exception to the above, namely when the count rate of an X-ray source is so high that photon pile-up on the EPIC chips plays an important role. This is described in § 3.3.9.

3.3.4 Intrinsic energy resolution of EPIC

The CCD pixels of the EPIC cameras are energy sensitive, enabling non-dispersive spectroscopy. The resolving power of these cameras is determined by the intrinsic energy resolution of the individual pixels. The spectral resolution for a point source located at the nominal pointing position of both the EPIC MOS and pn CCDs, as a function of energy, is displayed in Figs. 24 and 25. Also plotted in Fig. 24 are the measured in-flight $FWHM$ of the Al Kα and Mn Kα on-board calibration lines, after correction for charge transfer inefficiency (CTI) by the SAS, during orbits 85, 166 and 262. This shows a degradation of approximately 13% in the energy resolution of the MOS since the launch of **XMM-Newton**. The degradation is due to an increase in the CTI of the CCDs with time in orbit. Work is currently being carried out to improve the CTI correction technique and hence the energy resolution.
For the pn camera, no significant degradation of the $FWHM$ has been found.

3.3.5 EPIC quantum efficiencies

One of the factors to be taken into account when determining the effective area of the EPIC cameras is their quantum efficiency (QE). The QE of both types of EPIC CCD chips as a function of photon energy is displayed in Fig. 26 and 27. It is the QE of the EPIC MOS chips that in practice limits the energy passband at its high end, while the pn camera can detect photons with high efficiency up to 15 keV. The event selection strategies can be important in modifying the overall detection efficiency.

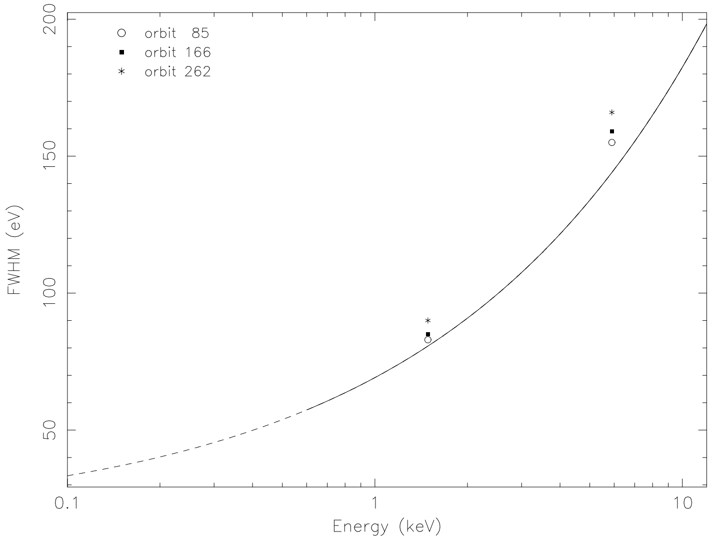

Figure 24: *The EPIC MOS energy resolution (FWHM) as a function of energy. The solid curve is a best-fit* $E^{0.5}$ *function to ground calibration data between 0.1 – 12.0 keV, all events with pattern 0 – 12 were included in the analysis (EPIC patterns are similar to Chandra "event grades", see § 3.3.10). Below around 0.6 keV (shown by the dotted region) surface charge loss effects distort the main photopeak significantly from a Gaussian form and, hence the effective energy resolution. Also plotted is the measured in-flight FWHM of the Al Kα (1.487 keV) and Mn Kα (5.893 keV) lines (using an extraction radius of 130 arcsec) during orbits 85, 166 and 262.*

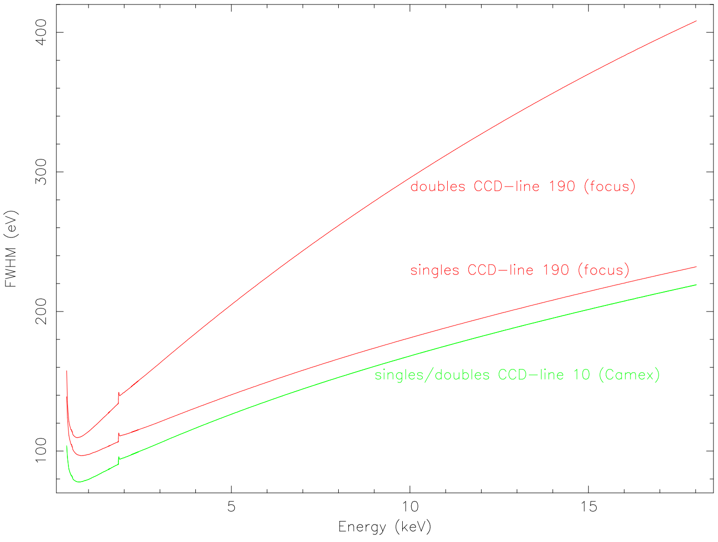

Figure 25: *The EPIC pn energy resolution (FWHM) as a function of energy as present in the most recent version of the response matrices. Curves are given for singles and double events (full frame mode) at the focus position as well as at a position 10 pixels away from the readout node. In the case of line 190 the FWHM of the double events diverges from that of the singles because their CTI correction is still insufficient. This will be improved in a later version of the correction programs.*

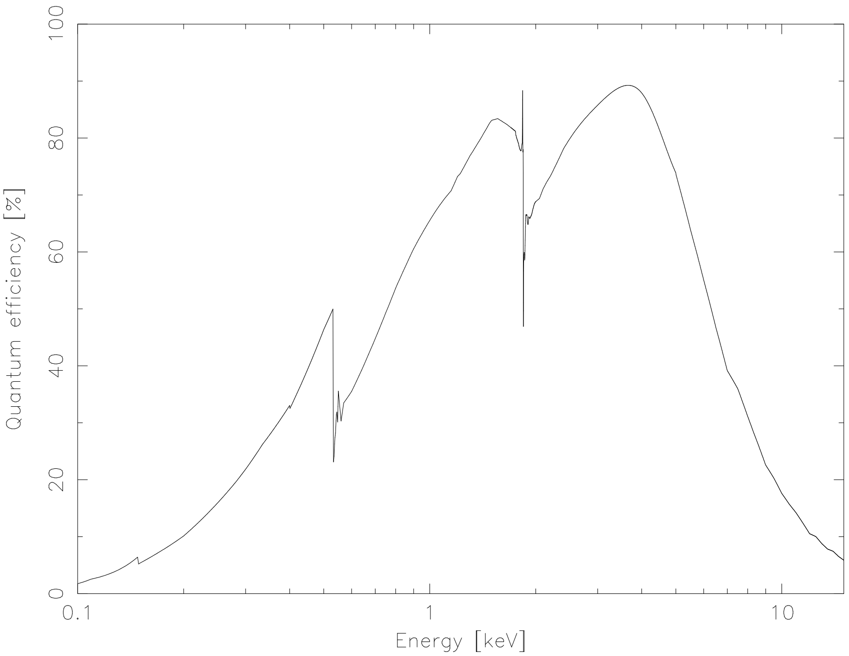

Figure 26: *Quantum efficiency of the EPIC MOS CCD chips as a function of photon energy (Turner et al., 2001, A&A 365, L27, Fig. 6).*

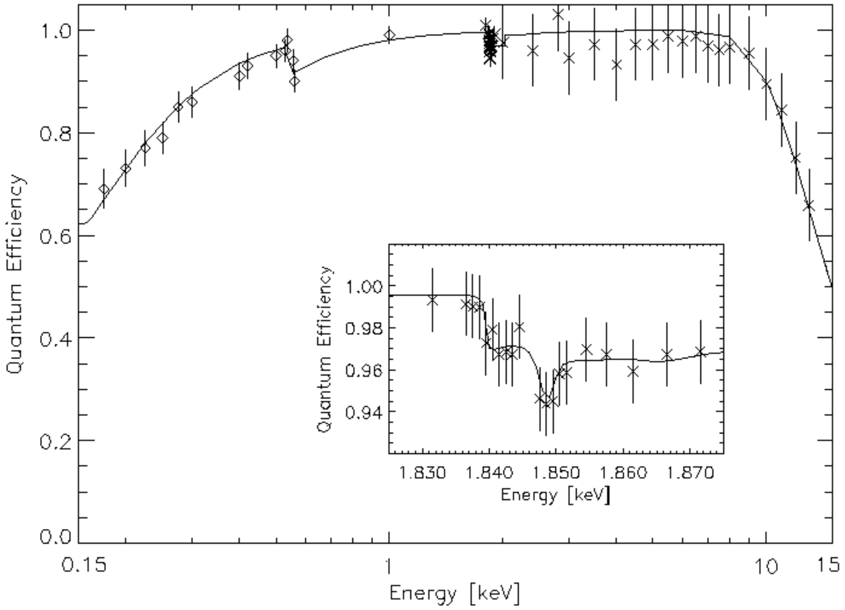

Figure 27: *Quantum efficiency of the EPIC pn CCD chips as a function of photon energy (Strüder et al., 2001, A&A 365, L18, Fig. 5).*

3.3.6 EPIC filters and effective area

The next factor influencing the EPIC effective area, specifically in the low energy part of the passband, is the choice of the optical blocking filter. These filters are used, because the EPIC CCDs are not only sensitive to X-ray photons, but also to IR, visible and UV light. Therefore, if an astronomical target has a high optical to X-ray flux ratio, there is a possibility that the X-ray signal becomes contaminated by those photons. The resulting analysis of data would be impeded in three ways:

1. Shot noise on the optically-generated photo electrons will increase the overall system noise, and hence lower the energy resolution. Spectral fitting will be inaccurate, because the calibration files will assume narrower spectral lines than observed.
2. The energy scale will be incorrectly registered, because a nominally zero signal pixel will have a finite offset. For each optically generated photo electron which is registered, the energy scale shifts by about 3.6 eV. This is comparable with the accuracy with which we expect brightest emission line features can be centroided. Consequently, contamination by visible light plays a crucial role in defining the proper energy scale. For the MOS this effect can in principle be reduced by ground processing taking into account the information on the zero level around the event which is also sent to the ground. Note, however, that although the background light can be subtracted the additional noise affects both the energy resolution and changes the distribution of the patterns and relative detection efficiencies.
3. Excess signal and noise fluctuations can affect the detection efficiency as well, by disguising single pixel X-ray events as events split between pixels.
4. Optically-generated photo electrons can lead to a saturation of electron traps, improving the CTI.

To prevent this, the EPIC cameras include aluminised optical blocking filters, and also an internal "offset table" to subtract the constant level of (optical) light or other systematic shifts of the zero level of charge measurements. For MOS the offset table values are now fixed and the SAS task emchain/emproc are used to calculate the local changes in offset. If these measures work perfectly, the above problems are minimised. The use of a thick blocking filter capable of minimising the optical light contamination for *all* scenarios will necessarily limit the softest X-ray energy response. Each EPIC camera is therefore equipped with a set of 3 separate filters, named **thick**, **medium** and **thin**. It is necessary for the observer to select the filter which maximises the scientific return, by choosing the optimum optical blocking required for the target of interest.

The following guidelines apply to point sources of optical light. Extended objects are not expected to be a significant problem (the optical loading is only important where a bright source is within < 2 arcmin of the target or along the read-out direction). At the GO's discretion a thinner filter could be used. Due to the peaked optical response, the same PSF core excising as used in pile-up cases (see § 3.3.2) might be applied to recover the desired spectra.

It should be noted that also an off-axis bright optical object will leak through the filters generating false X-ray events, which could contribute to degrading the effective telemetry bandwidth (see § 4.2.2).

The calculations have been performed for a worst case, i.e., for the brightest pixel within the core of the PSF. Therefore, averaging the brightness of an extended object over a scale of one PSF (say, $20''$) should provide a corresponding estimate with a significant margin of safety. Note that these data apply to full frame modes only, and that a change to a partial window mode with an order of magnitude faster readout rate can allow suppression of optical contamination at 2–3 visible magnitudes brighter for *ALL* filters. The GO can make an estimate on optical contamination improvement based on the mode time resolution compared with full window mode (Table 3).

- Thick filter

  This filter should be used if the expected visible brightness of the target would degrade the energy scale and resolution of EPIC. It should be able to suppress efficiently the optical contamination for all point source targets up to m_V of 1–4 (MOS) or m_V of 0–3 (pn). The range depends on the spectral type, with only extremely red (M stars for example) or blue colours causing the change to 3 magnitudes fainter level.

- Medium filter

  The optical blocking is expected to be about 10^3 less efficient than the thick filter, so it is expected that this filter will be useful for preventing optical contamination from point sources as bright as $m_V = 8$–10.

- Thin filter

  The optical blocking is expected to be about 10^5 less efficient than the thick filter, so the use of this filter will be limited to point sources with optical magnitudes about 14 magnitudes fainter than the corresponding thick filter limitations.

Figs. 28 and 29 display the impact of the different filters on the soft X-ray response of both types of EPIC cameras, whereas Fig. 30 displays the combined effective area of all **XMM-Newton** X-ray telescopes.
The user might also want to take note of the SOC document XMM-SOC-CAL-TN-0001 (available from `http://xmm.vilspa.esa.es/docs/documents/CAL-TN-0001-1-0.ps.gz`) which explains in detail the PHS tools, used to determine if the correct optical blocking filter has been chosen for a particular exposure.

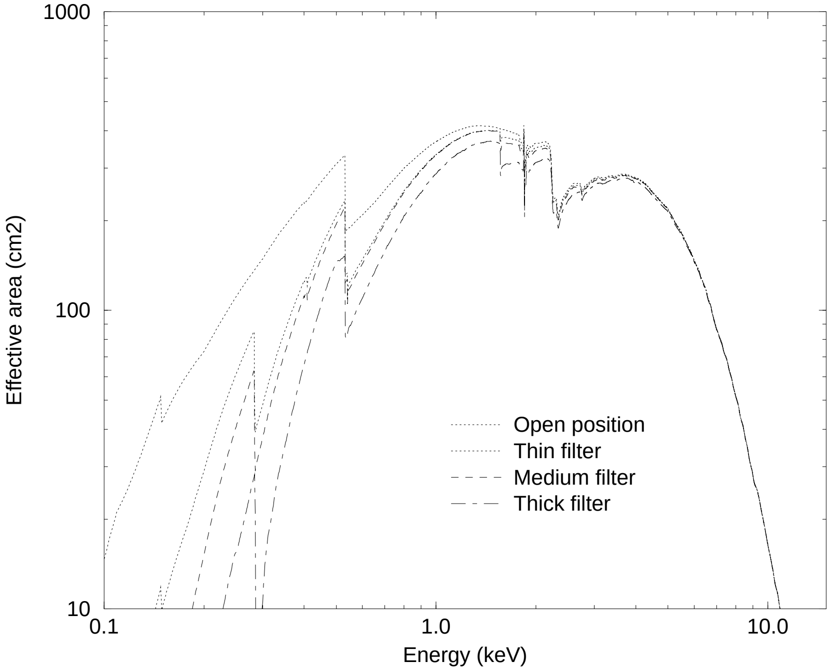

Figure 28: *The EPIC MOS effective area for each of the optical blocking filters and without a filter.*

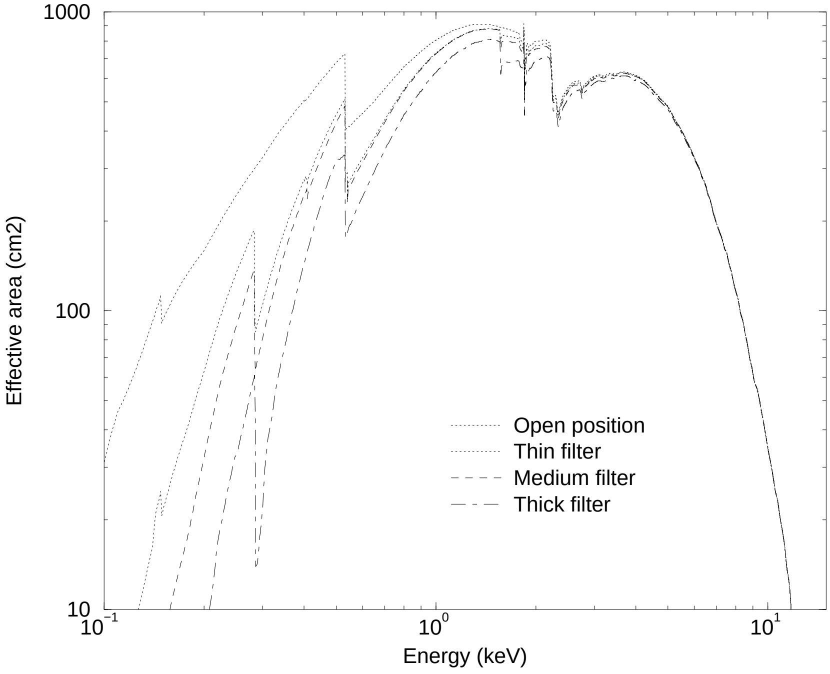

Figure 29: *The EPIC pn effective area for each of the optical blocking filters and without a filter.*

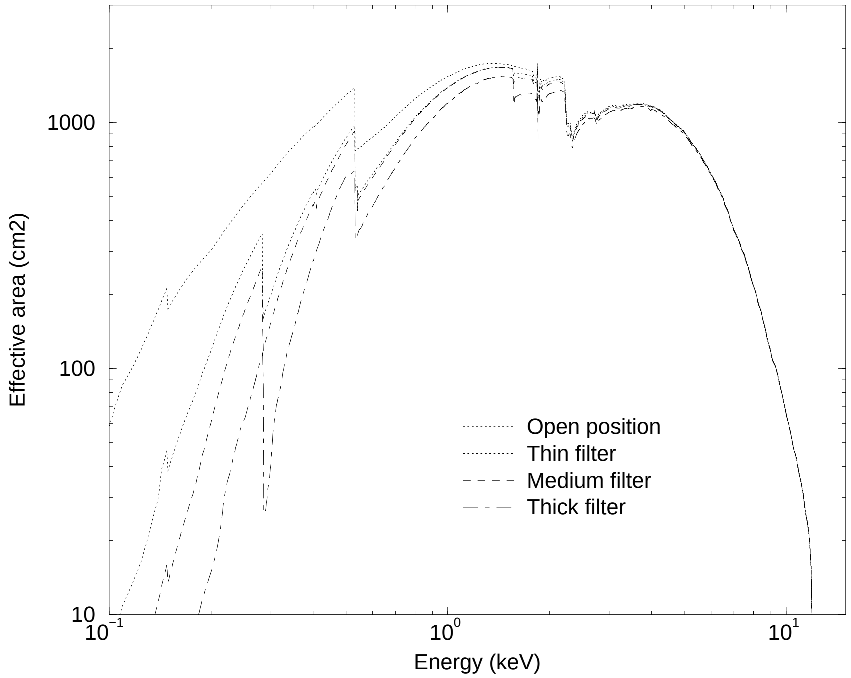

Figure 30: *Combined effective area of all telescopes assuming that all cameras operate with the same filters, either open, thin, medium or thick. As above, the curve uses the detector quantum efficiency associated with mono-pixel events in case of the MOS camera. Depending on the pattern selection, the overall effective area could increase by as much as 30 percents when multi-pixels events are also included.*

3.3.7 EPIC background

The EPIC background can be divided into two parts: a cosmic Xray background (CXB), and an instrumental background. The latter component may be further divided into a detector noise component, which becomes important at low energies (i.e. below 200 eV) and a second component which is due to the interaction of particles with the structure surrounding the detectors and the detectors themselves. This component is characterized by a flat spectrum and is particularly important at high energies (i.e. above a few keV).
The particle induced background can be divided into 2 components: an external 'flaring' component, characterized by strong and rapid variability, which is often totally absent and a second more stable internal component. The flaring component is currently attributed to soft protons (E_p smaller than a few 100 keV), which are presumably funneled towards the detectors by the Xray mirrors. The stable component is due to the interaction of high-energy particles (E larger than some 100 MeV) with the structure surrounding the detectors and possibly the detectors themselves. In the following we describe some of the main properties of both components.
The user should take note of the SOC document XMM-SOC-CAL-TN-0016 (available from `http://xmm.vilspa.esa.es/docs/documents/CAL-TN-0016-1-0.ps.gz`) which also explains the origin of the EPIC background in detail together with giving recipes on how to handle these effects in the SAS.

3.3.7.1 EPIC external 'flaring' background

This component is produced by protons with energies less than a few 100 keV which are funneled towards the detectors by the Xray mirrors. In Fig. 31 we show an image of the MOS2 detector during an observation which was badly affected by soft proton flares. The intensity of the background within the field of view is much larger than outside because of the soft proton component.
In Fig. 32 we show the background lightcurve for the MOS1 unit for another observation (the Lockman Hole Science Validation data) where rapid and strong variability is clearly present.
While the MOS1 and MOS2 cameras show almost identical lightcurves the pn camera can yield substantially different results, in the sense that some flares appear to be much more intense in the pn than in the MOS cameras.
The spectra of soft proton flares are variable and no clear correlation is found between intensity and spectral shape. The current understanding is that soft protons are most likely organized in clouds populating the Earth's magnetosphere. The number of such clouds encountered by XMM in its orbit depends upon many factors, such as the altitude of the satellite, its position with respect to the magnetosphere, and the amount of solar activity.
At the present time we are not capable of predicting the time and intensity of soft proton flares. The impact of the soft proton flares on EPIC observations is highly variable. During the Lockman hole observations about 40% of the observing time was lost because of soft proton flares. During the first half of the year 2000 soft proton flares have been quite common and have caused the almost complete loss of some observations. During the last months of the year 2000 and the first months of the year 2001 soft proton flares have become much rarer.

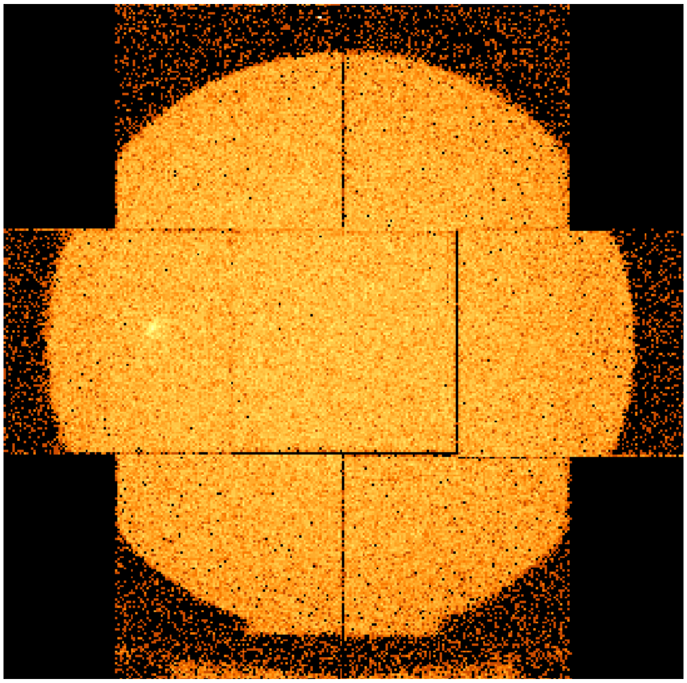

Figure 31: *Image from a MOS2 observation badly affected by soft proton flares.*

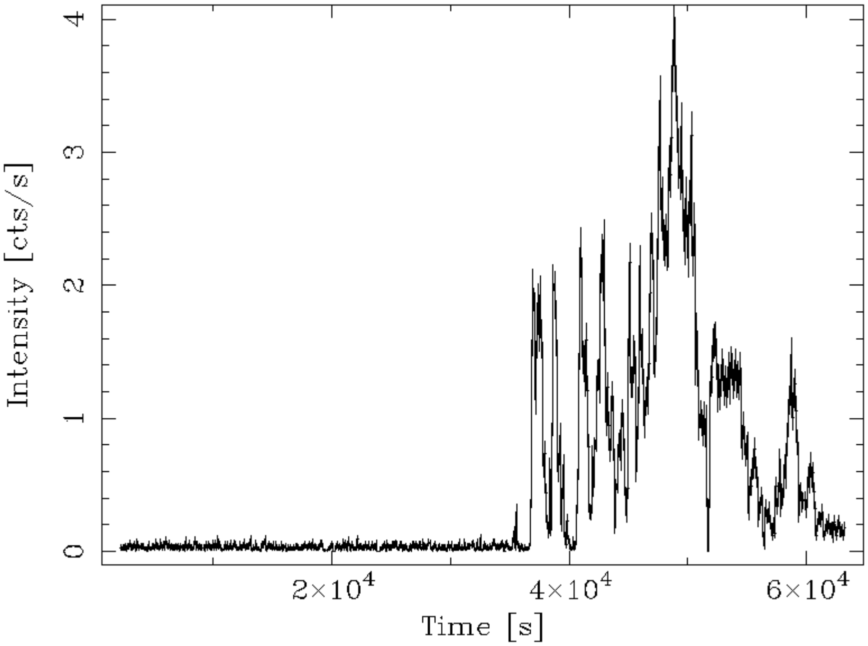

Figure 32: *Lightcurve from a MOS1 observation badly affected by soft proton flares. During the first part of the observation the background is constant. The second half, however, is heavily affected by a proton flare.*

3.3.7.2 EPIC internal 'quiescent' background

This quiescent component is associated with high energy particles interacting with the structure surrounding the detectors and the detectors themselves. The component shows only small intensity variations in time which are typically observed on long timescales. A detailed analysis (Pizzolato 2001, for full reference see § 7) of the MOS1 and MOS2 cameras conducted over timescales of a few months shows that the intensity of this component during any given observation is within ∼ 10% of the mean. The intensity observed in one MOS camera is usually well correlated with the intensity measured in the other, although some exceptions have been observed (Pizzolato 2001). In Figs. 33 and 34 we show the spectrum of the quiescent component for the MOS1 and pn camera respectively.

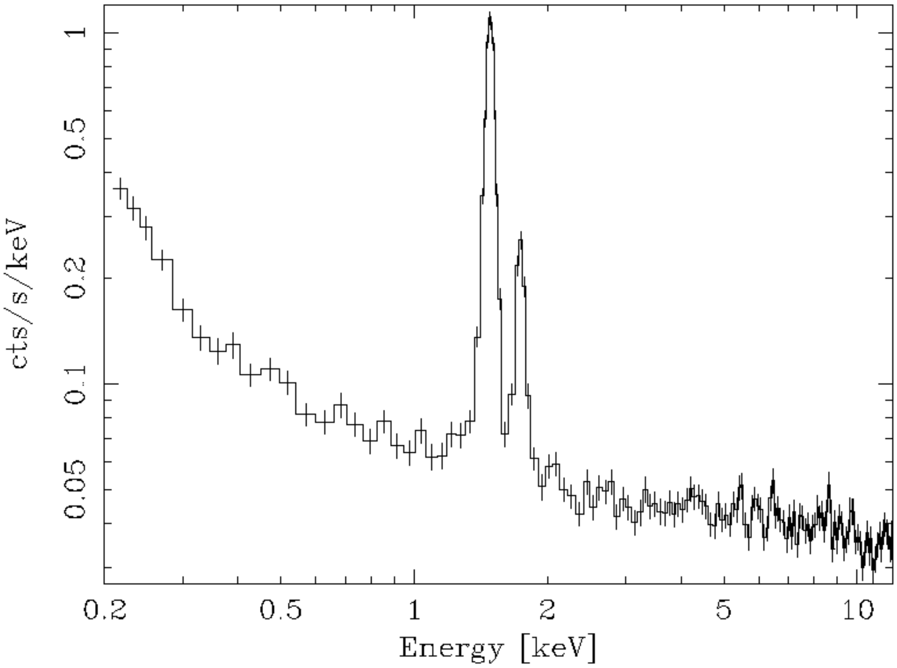

Figure 33: *Background spectrum for the MOS1 camera during an observation with the filter wheel in the closed position. The prominent features around 1.5 and 1.7 keV are respectively Al-K and Si-K fluorescence lines. The rise of the spectrum below 0.5 keV is due to the detector noise.*

The spectra are quite flat and present a number of spectral features due to fluorescence from the detectors and the structure surrounding them. Al–K and Si–K lines are clearly visible in the MOS spectrum. In case of the pn Al–K and an intense complex due to Cu–K, Ni–K and Z–K lines around 8 keV is visible. An important point is that the intensity of this complex is not constant over the pn detector. More specifically there exists a central circular region (see Fig. 35) where the complex is virtually absent.

The intensity of the quiescent component has been measured for both MOS and pn cameras during CLOSED filter observations. In the case of the MOS cameras the intensity in the 2–7 keV range (which is free of the most prominent fluorescent lines) is found to be $\sim 2.2 \cdot 10^{-3}$ cts cm^{-2} s^{-1} keV^{-1}. For the pn camera, the intensity in the same energy range is $\sim 5 \cdot 10^{-3}$ cts cm^{-2} s^{-1} keV^{-1}.

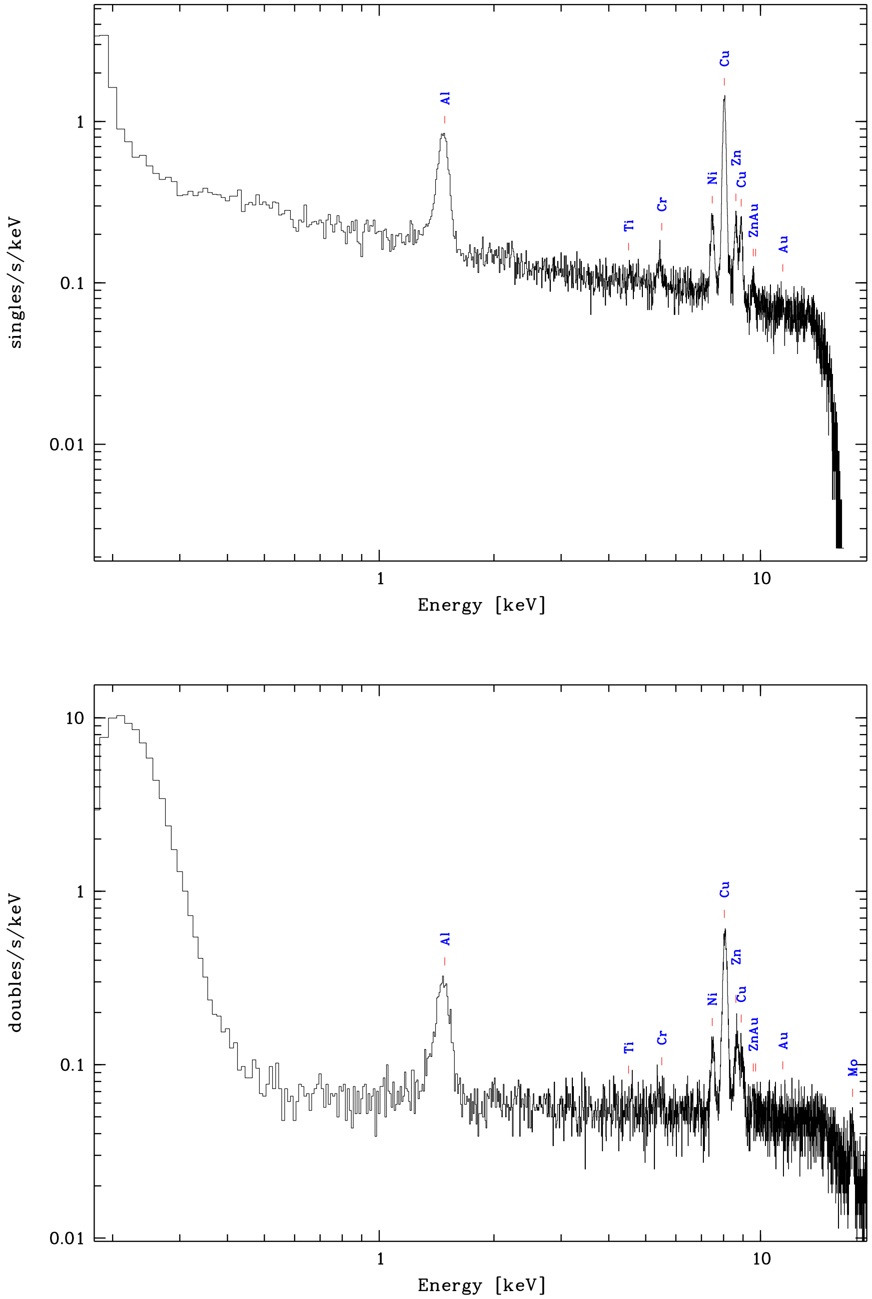

Figure 34: *Background spectrum for the pn camera during an observation with the filter wheel in the CLOSED position (top: single events, bottom: double events) in the energy range* 0.2 − 18 *keV. The prominent features around* 1.5 *keV are Al–K, at 5.5 keV Cr–K, at 8 keV Ni–K, Cu–K, Zn–K and at 17.5 keV (only in doubles) Mo–K fluorescence lines. The rise of the spectrum below 0.3 keV is due to the detector noise. The relative line strengths depend on the (variable) incident particle spectrum.*

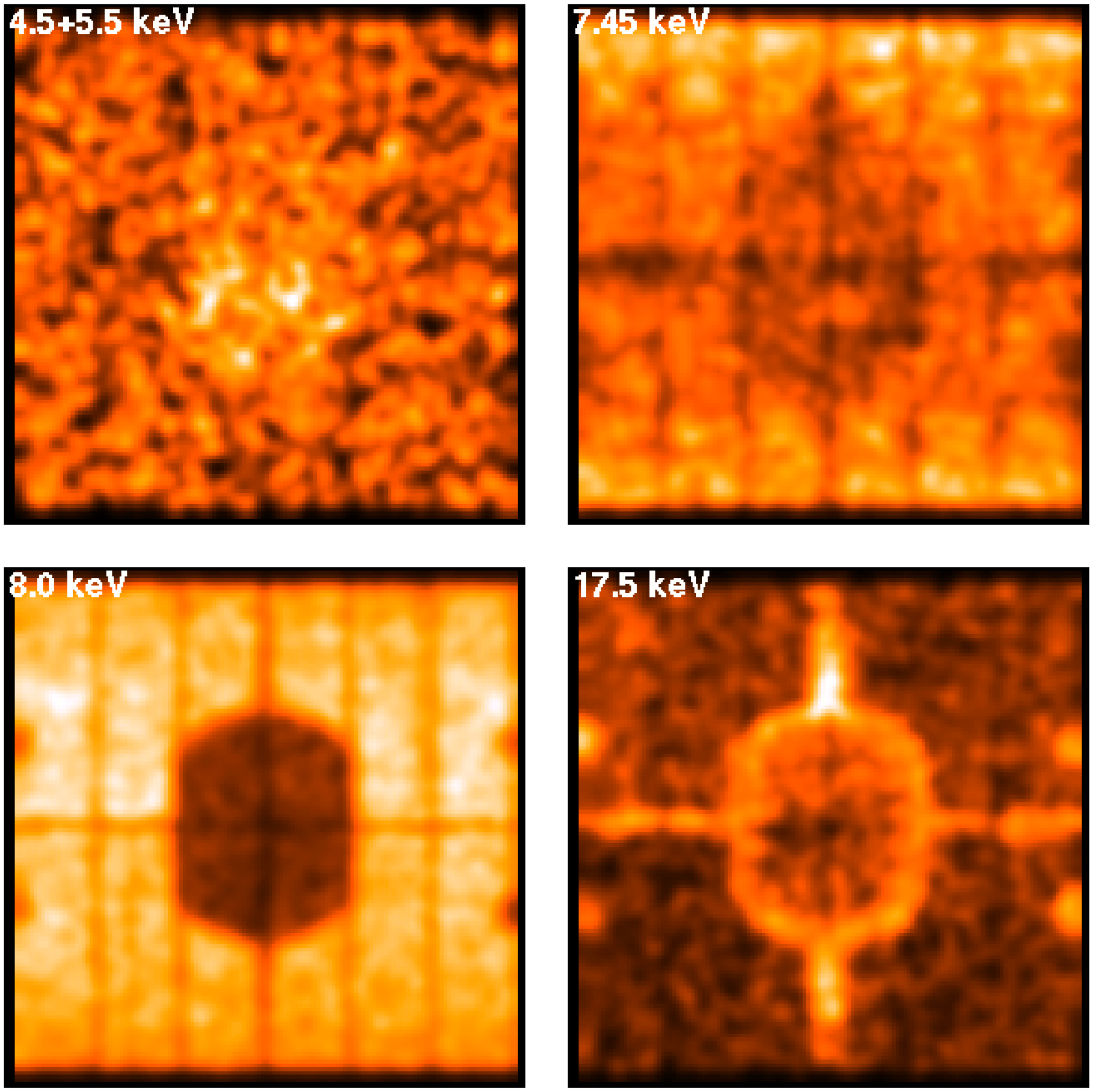

Figure 35: *Background images for the pn camera with spatially inhomogeneous fluorescent lines: Ti–K + Cr–K (top left), Ni–K (top right), Cu–Kα (bottom left) and Mo–Kα (bottom right). The inhomogeneity is mainly caused by the electronics board mounted below the CCDs.*

3.3.7.3 EPIC Detector Noise

The dark currents of both types of EPIC CCDs are negligible sources of background noise under nominal operating conditions.

In MOS there are low level 'flickerings' of a small number of pixels at an occurrence rate $< 1\%$. In pn occasional (mainly during high particle background) the offset calculation leads in some pixels to a slightly under estimate of the offset, which can result in blocks of approx. 4×4 pixels with enhanced low energy signal.

3.3.8 EPIC's sensitivity limits

The EPIC sensitivity limits depend on the sky area, i.e. the true X-ray background and on the 'space weather' as described in § 3.3.7.
As the sensitivity limits also depend on the angular structure and the spectral characteristics of the source that is observed, it is strongly recommended to use SciSim to get a feeling on the signal to noise which can be achieved with a certain instrument setup and exposure time.
Currently the best statistical results on the EPIC sensitivity limits are based on the Lockman Hole data (Hasinger et al., 2001, A&A 365, L45) and the simulations performed by Watson et al., 2001, A&A 365, L51.
The major uncertainty in predicting the EPIC sensitivity prelaunch was the background levels which would be encountered inorbit. The actual inorbit background levels measured in the first part of the Lockman Hole observation (representative of quiescent background) are $\sim (2.1, 2.9)10^{-3}$ cts s^{-1} $arcmin^{-2}$ for the pn camera in the soft (0.5 – 2 keV) and hard (2 – 10 keV) bands respectively. Very similar values: $\sim (2.0, 2.6)10^{-3}$ cts s^{-1} $arcmin^{-2}$ are found for the two MOS cameras combined.
Source detections on the Lockman hole data were accepted with likelihood values above 10 (about 4σ) and inside an off-axis angle of 10 arcmin. The resulting detection statistics are given in Tab. 4 (for further details see Hasinger et al. (2001)).

Table 4: *Detection limits for different energy bands, based on data from the Lockman hole (Hasinger et al. (2001), Tab. 2)*

Band^a	Γ^b	ECF^c	S_{lim} ^{d}
0.2 – 0.5	2.0 ± 0.5	7.16 ± 1.01	4.0
0.5 – 2.0	2.0 ± 0.5	10.20 ± 0.04	3.1
2 – 10	2.0 ± 0.5	1.79 ± 0.40	14
5 – 10	1.6 ± 0.5	1.28 ± 0.11	24

Notes to Table 4:
[a] Energy band in keV in which the flux is given.
[b] Assumed range in photon index.
[c] Energy conversion factor in cts s^{-1} per 10^{-11} erg cm^{-2} s^{-1}.
[d] Minimum detected flux in 10^{-16} erg cm^{-2} s^{-1}.

Watson et al. (2001) used the nominal quiescent background values together with the measured **XMM-Newton** PSF to compute an EPIC point source sensitivity based on a simple 5σ source detection criterion against assumed purely Poissonian background fluctuations, as shown in Fig. 36 [3].
Empirical data from analysis of several **XMM-Newton** fields using the source detection software in the SAS are broadly consistent with these plots. The actual background in an observation depends critically on the fraction of background flares removed, i.e. the tradeoff between net background levels and net exposure time. An investigation of a few

---

[3] The 5σ value represents a relatively conservative limit which crudely takes into account the fact that there are additional systematic background effects which have yet to be characterised in detail. For the effective beam area of **XMM-Newton**, the appropriate limit for purely Poissonian background fluctuations to yield ≤ 1 spurious source per field is about $3.5 - 4\sigma$.

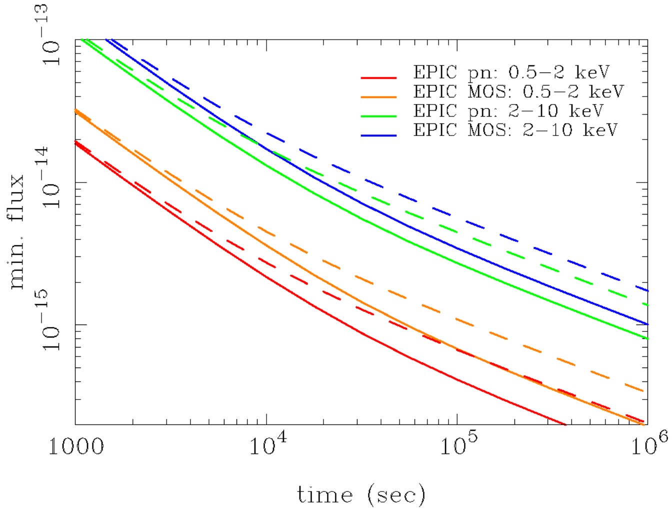

Figure 36: *EPIC sensitivity (5σ minimum detectable flux in erg cm^{-2} s^{-1} in respective bands) as a function of exposure time (from Watson et al., 2001). Sensitivity is computed for an assumed $\alpha = 1.7$ powerlaw spectrum with a column density $N_H = 3\,10^{20}$ cm^{-2}. Solid curves are for the nominal background rates. Dashed curves are for background levels enhanced by a factor 3. The EPIC MOS curves correspond to the combination of the two cameras.*

example fields demonstrates that the effective sensitivity of typical observations is within a factor 2 of the values plotted in Fig. 36. A few observations are affected by enhanced background throughout; here the average background can be several times higher than the nominal values even after the removal of the largest flares.

At very faint fluxes the effective sensitivity is limited by confusion effects. Although a detailed study of source confusion has not yet been carried out, the long **XMM-Newton** observations of the Lockman Hole (Hasinger et al., 2001) demonstrate that source confusion is not a significant problem in either the soft (0.5–2 keV) or hard (2–10 keV) X-ray bands for an observation duration of about 100 ksec which reaches flux limits $f_X \sim 3.1$ and $\sim 14\,10^{-16}$ erg cm^{-2} s^{-1} in the soft and hard bands respectively.

3.3.9 EPIC photon pile-up

Photon pile-up, i.e., the arrival of more than one X-ray photon in one camera pixel or in adjacent pixels before it is read out, can affect both the PSF and the spectral response of EPIC.

Table 3 provides estimates of count rates for the different EPIC instrument modes for which pile-up should not be a problem. For the MOS full imaging mode, e.g., ca. 0.7 counts/s should not be exceeded.

The PSF is influenced by pile-up, because in the core of the PSF many photons arrive at almost the same time (within one readout frame), creating multi-pixel photon patterns which, for the MOS camera, are then rejected by the onboard event reconstruction software (which suppresses large size events, such as that induced by most of the cosmic rays). For the pn camera, event reconstruction is performed offline in the SAS. The pile-up effect leads, in the most extreme case, to a PSF with an artificial "hole" at its centre, as displayed in Fig. 37.

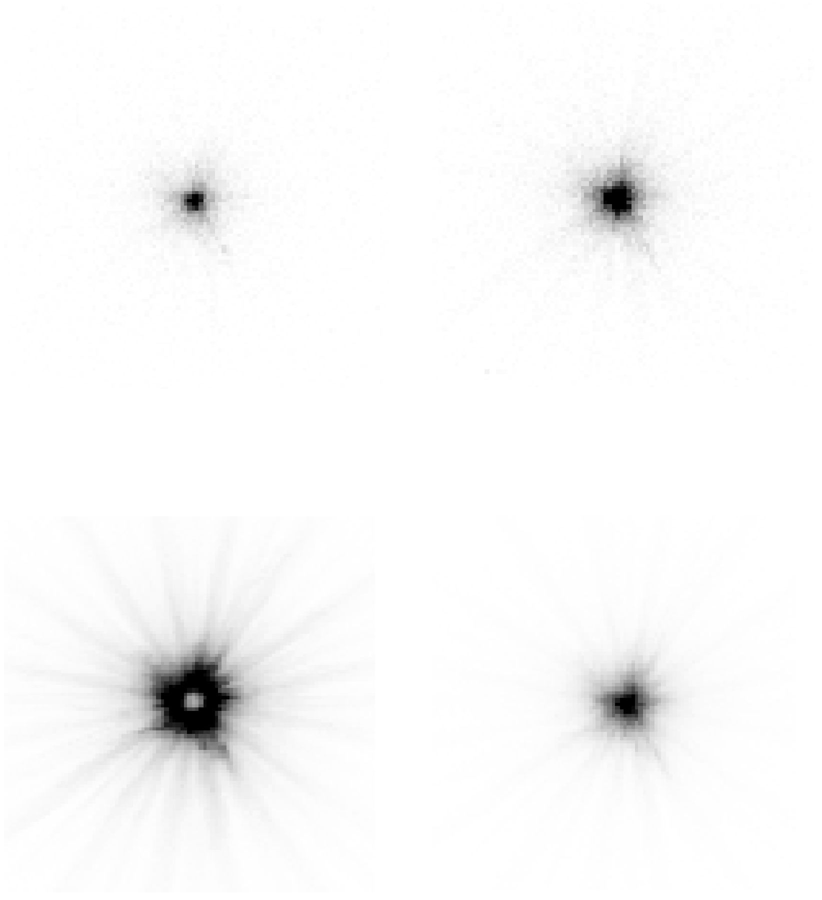

Figure 37: *In-orbit observations performed with EPIC MOS showing the increase of pile-up with increasing photon count rate per frame. The panels are arranged clockwise, with the lowest count rate (and thus pile-up rate) in the upper left and the highest in the lower left. The observed count rates are 2, 5, 12 and 16 counts/frame, respectively.*

The spectral response is compromised, because the charge deposited by more than one photon is added up before being read out, thus creating artificial "hard" photons where there have actually been two or more soft photons.
Pile-up effects on the spectral shape are very much reduced by selection of mono-pixel events. The effect of pile-up in this case is then essentially a loss of flux. Also, in case of very strong pile-up, building spectra and calculating absolute fluxes is still possible with a good accuracy by excising the heavily piled-up core (see below) from the analysis.
To get an idea on how important the pile-up effect can be for spectral analyses, a kT = 1 keV Raymond-Smith model spectrum with $N_H = 3 \times 10^{20}$ cm^{-2} has been fed into SciSim and the fit to the resulting "observed" spectrum compared with the input for EPIC MOS observations in the full window mode (Tab. 5).

Table 5: *The effect of pile-up on spectral fits*

Input flux[1]	**Output count rate [s^{-1}]**	**Counts per MOS frame**	**N$_\mathrm{H}$ [10^{20} cm^{-2}]**	**kT [keV]**	**Norm./ expect**
4.05	1.08	0.22	3.0	0.967	1
13.4	3.56	0.71	3.05	0.972	1
40.5	10.5	2.1	3.2	0.979	0.98
134	33.3	6.65	3.5	1.010	0.95
405	85.4	17.1	4.1	1.022	0.80

Notes to Table 5:
1) 0.15–10 keV flux in units of [10^{-12} erg s^{-1} cm^{-2}].

One can see how the best-fitting N_H, kT and normalisation vary as a function of input source flux (and thus count rate per frame). Note that, because of the photon pile-up, one apparently loses soft photons (whose charge combines and is then seen at higher energies), thus requiring a higher N_H and also a higher kT to reach the minimum χ^2 for the fit. The peculiarity that for low fluxes the fitted kT is a bit lower than the input value is explained by the fact that the SciSim simulation was performed without event reconstruction. What is important to note is the relative change in kT. A similar change is also caused in the best-fitting slope of a power law, as displayed in Fig. 38. The effect of pile-up on the PSF has been taken into account in these simulations by choosing an appropriately large photon extraction region for the spectral analysis.
Note: No error bars are provided in Tab. 5, because the input spectrum is a numerical model spectrum without noise. Differences in the output "fit" spectrum with respect to the noise-free input occur only because of re-grouping of photons due to pile-up. The relevance of the effect depends on the scientific goal of the observing programme. For up to 2 counts per MOS frame, the error in N$_H$ stays below 10%, that of kT and the normalisation at a level of 2%, which in many cases will be below the uncertainty of the spectral fit anyway.

The SAS task eppatplot can be used as diagnostic tool for pile-up in the pn camera. It utilizes the relative ratios of single- and double-pixel events which deviate from standard values in case of pile-up. Fig. 39 shows the produced plot for a source with a countrate of

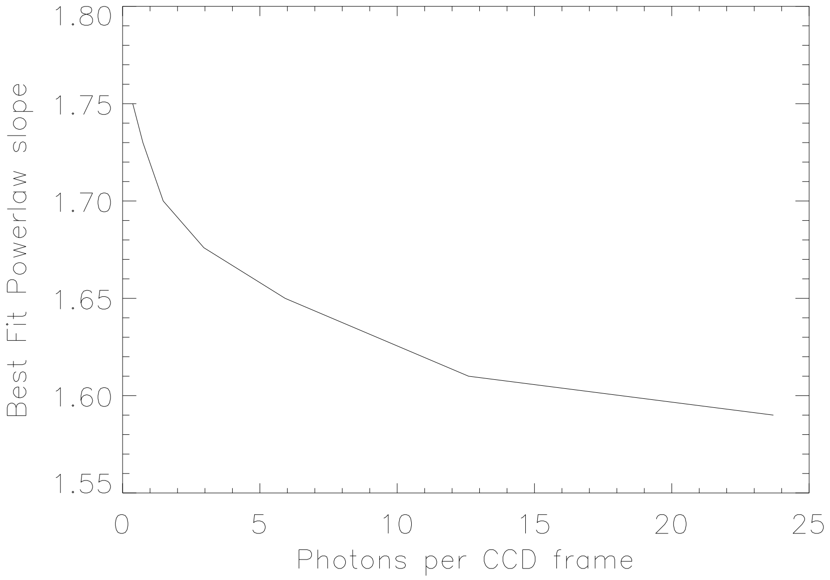

Figure 38: *The best-fitting power law slope, α, for an $\alpha = 1.7$ input spectrum into SciSim, with different input count rates, leading to different levels of pile-up.*

~ 13 cts/s in full window mode.
As input an eventfile was used which contains all events extracted from a circle with radius 30 arcsec around the source position. In the upper panel the spectral distributions as function of PI channel for single-, double-, triple- and quadruple-events (these are the four types of valid events which can be created by an X-ray photon) are plotted. Doubles can only be produced when the energy of both events is above the event threshold. Similarly triples and quadruples start at 3 and 4 times the threshold, respectively. In the lower panel the fraction of the four event types are plotted (relative to the sum). The ratios are energy dependent with higher energy photons producing less singles due to the increasing size of the electron cloud. As long as the count rate is below the pile-up limit the energy dependence follows standard curves. These are plotted for singles (1.0 at energies below twice the threshold and then decreasing with energy) and doubles. The curves are also used in the detector response matrices to correct for the pattern selection used in the spectrum to be analyzed. In the case of pile-up the ratios deviate from the standard curves as the example shows. Due to 'pattern pile-up' more doubles (which are actually two neighboring singles) are produced.

At the time of writing, the effects of pile-up are not yet investigated enough to update this section with values based on real data. The principles remain, but the quantitative estimates will need to be revised.
A quantitative comparison of both types of EPIC cameras with the *Chandra* ACIS-I instrument in this respect is provided in § 3.7.1.3.

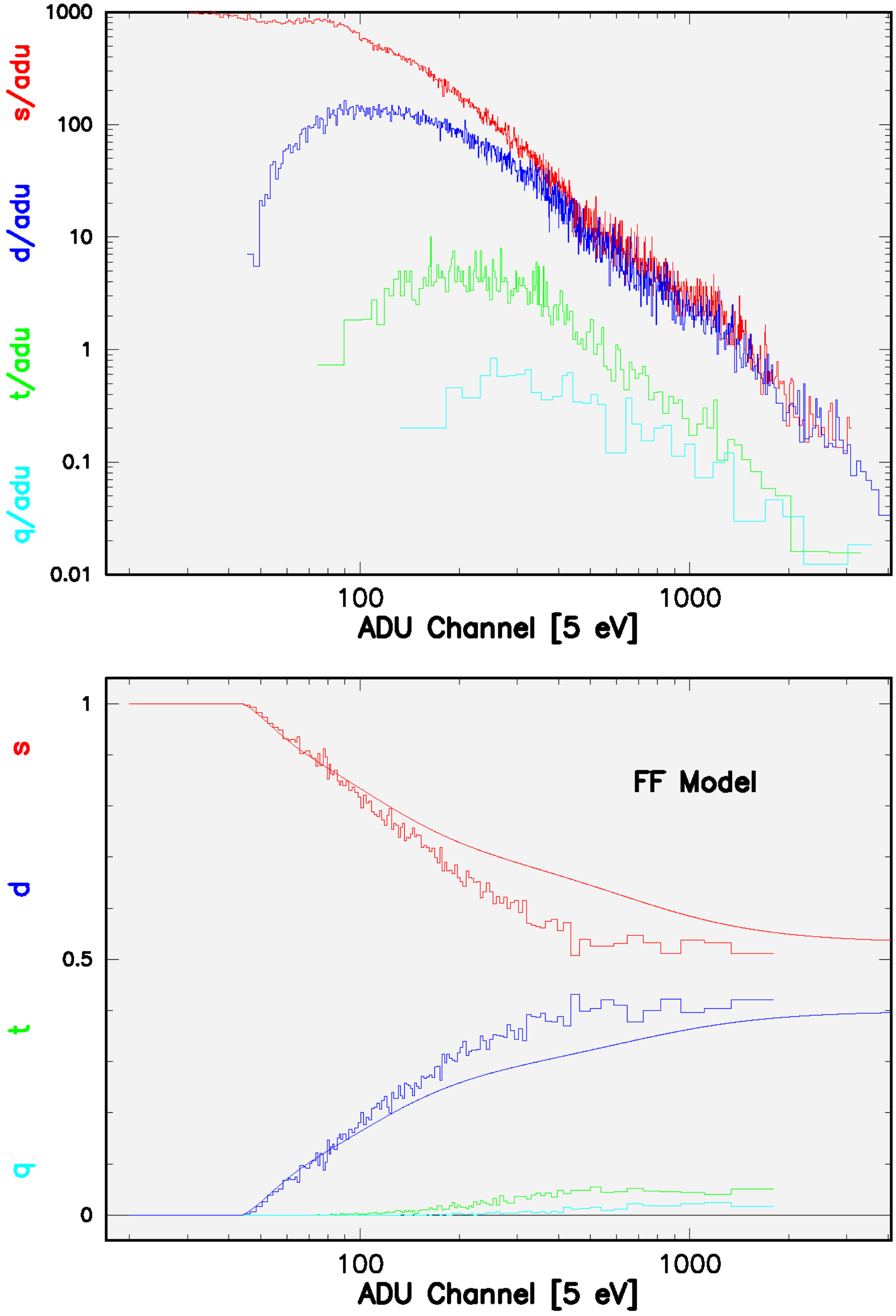

Figure 39: *Plot of the pn pattern distribution with energy as produced by the SAS task eppatplot (see text for further details).*

3.3.10 EPIC event grade selection

Users should be aware of the different methods of processing events that are present in the EPIC MOS and pn cameras. Event selection is performed on-board in order to allow transmission of useful data only (i.e., removal of empty pixels from the data stream). Also a significant number of X-ray events are expected to be split between pixels, and these must be recognised as such.

The MOS camera uses an event pattern recognition scheme. All detected events are transmitted to ground with a pattern identification [4] (similar to the *Chandra* or *ASCA* "event grades") and a number of energy data. The Science Analysis Subsystem (SAS) software allows these data to be reconstructed to a single energy value in an event list. However, the user has the possibility to select sub-sets of pattern types because optimal energy resolution may be obtained from a sub-set of events (one and two pixels in size). If maximum source detection efficiency is required all patterns might be selected. Therefore, users must choose carefully the dataset for the science of interest, and further beware that not all pattern combinations may be calibrated as well as some default sets.

The pn camera conversely telemeters all pixels above a certain threshold, and the X-ray event selection and processing is performed wholly on-ground, e.g., through the use of the SAS. However, we emphasise that default processing should be followed, because the details of events carried in the event list are crucial to performing proper processing (energy correction, pattern recognition, etc.).

A host of secondary effects of event processing is foreseen (for example the amount of pile-up in the PSF may depend on event pattern selection, particle background rejection is heavily dependent on event selection criteria), but the scope may not fully be appreciated until further reduction of ground calibrations is performed by the instrument PI teams, or after in-orbit experience further accumulates.

---

[4] The definition of EPIC patterns is given e.g. in the descriptions of the SAS tasks emevents and epevents.

3.3.11 EPIC-specific proposal submission information

In the preparation of EPIC observing proposals, the following information should be taken into account in order to assess the technical feasibility of intended **XMM-Newton** observations; see § 4 for additional, more general information.

3.3.11.1 EPIC spectral quality

In Figs. 40–44 we display a series of Mekal model spectra at different energies, ranging from 0.1 to 10.0 keV, with successively increasing total photon numbers (from 500 to 20000 counts). These show which data quality can be reached for a given total number of counts. All model spectra have been produced with *XSPEC*, faking a Mekal model spectrum and using the ready-made response matrices for MOS1 and pn for the thin filter and full window mode. Photon statistics was allowed and the faked spectra were rebinned in a way such that the 5 sigma significance criterion is fulfilled. For the 2.0 keV model, the MOS1 and pn cameras are compared directly (Figs. 42 and 43), while for all other energies only the MOS1 model spectra are displayed.
Note: These simulated spectra have been produced with the response matrices for MOS1 and pn as they were available at the time of writing. Some changes are expected if simulations are repeated with updated versions (for latest info: check the **XMM-Newton** Calibration Page).

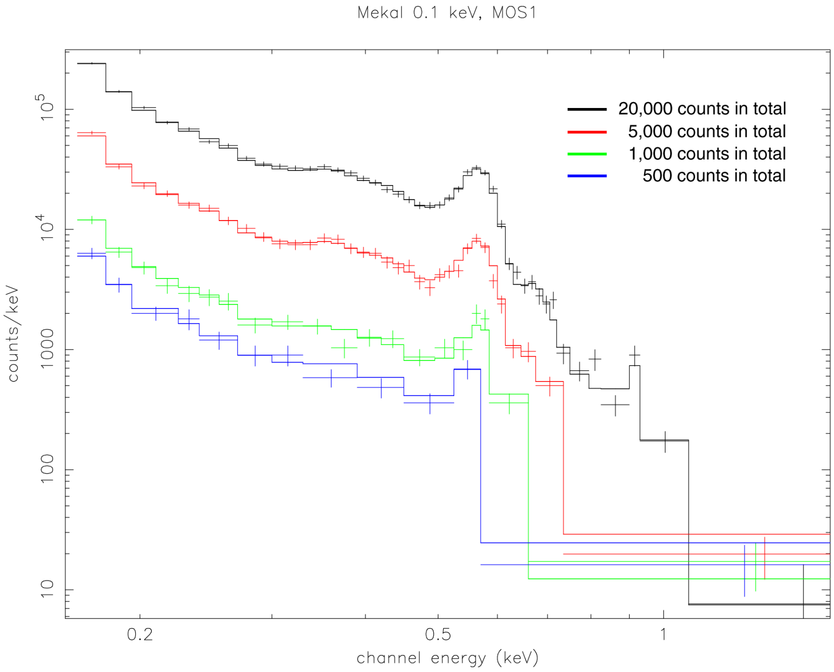

Figure 40: *Series of EPIC MOS1 model spectra of a Mekal thermal plasma with a temperature of 0.1 keV. From the bottom to the top, the total number of counts in the* **XMM-Newton** *passband (0.15–15 keV) increases from 500 to 20000.*

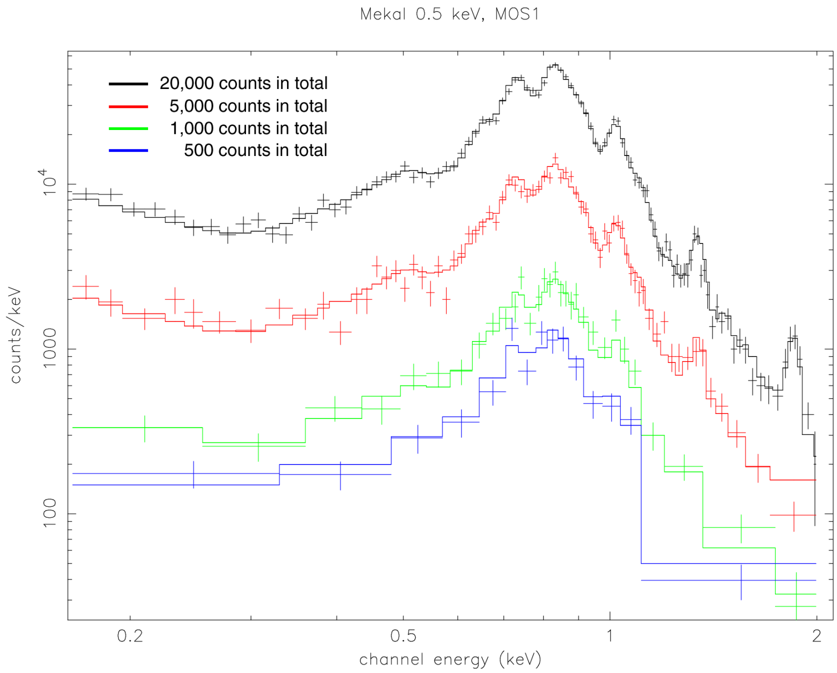

Figure 41: *Series of EPIC MOS1 model spectra of a Mekal thermal plasma with a temperature of 0.5 keV. From the bottom to the top, the total number of counts in the* **XMM-Newton** *passband (0.15–15 keV) increases from 500 to 20000.*

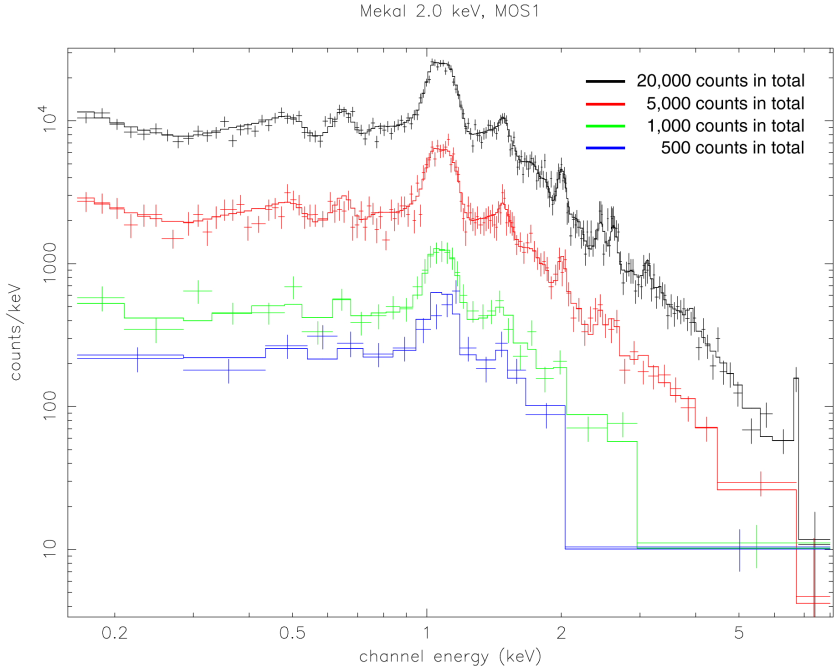

Figure 42: *Series of EPIC MOS1 model spectra of a Mekal thermal plasma with a temperature of 2.0 keV. From the bottom to the top, the total number of counts in the* **XMM-Newton** *passband (0.15–15 keV) increases from 500 to 20000.*

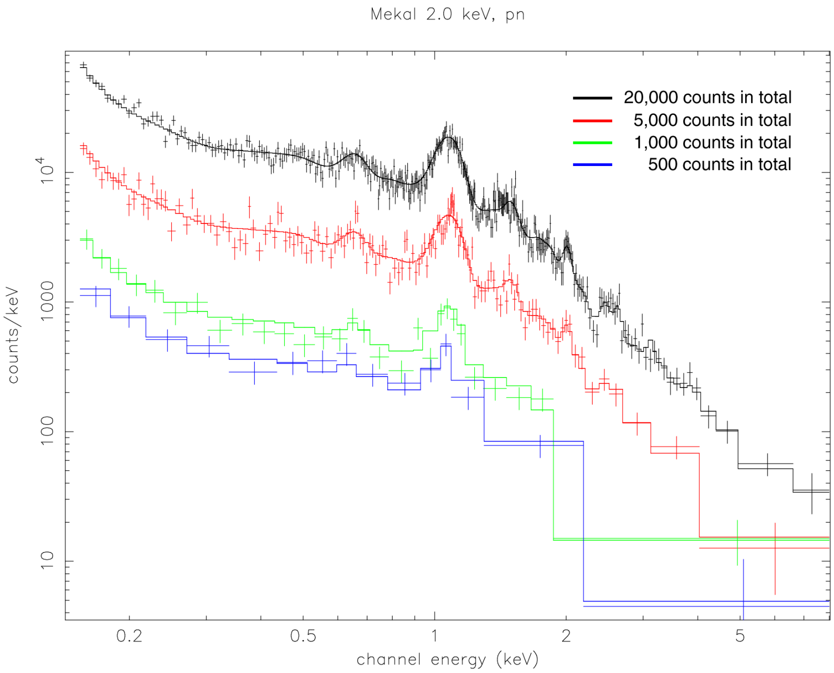

Figure 43: *Series of EPIC pn model spectra of a Mekal thermal plasma with a temperature of 2.0 keV. From the bottom to the top, the total number of counts in the* **XMM-Newton** *passband (0.15–15 keV) increases from 500 to 20000.*

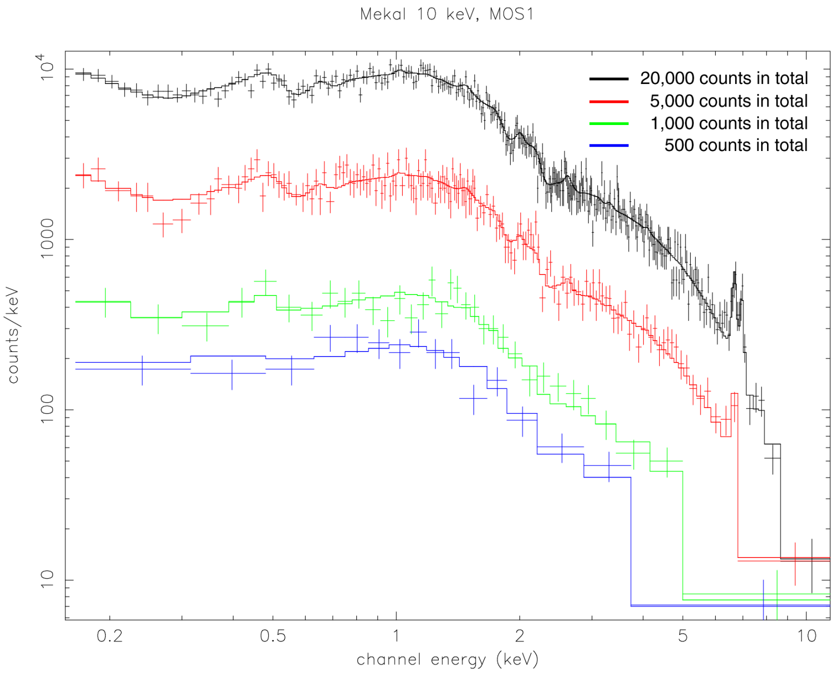

Figure 44: *Series of EPIC MOS1 model spectra of a Mekal thermal plasma with a temperature of 10.0 keV. From the bottom to the top, the total number of counts in the* **XMM-Newton** *passband (0.15–15 keV) increases from 500 to 20000.*

3.3.11.2 EPIC flux to count rate conversion

The following set of figures (Figs. 45–56) provides EPIC flux to count rate conversion factors for a variety of standard spectral models, for each camera type (pn and MOS), with the thin and medium optical blocking filters. Families of curves for various values of the foreground absorbing column density, N_H, are plotted. Both the (unabsorbed) fluxes (i.e., after taking into account the attenuation by the foreground gas) and the count rates are calculated for the 0.1–12 keV band.
Note that these plots are based on pre-launch simulations and some minor changes may apply. The conversion factors for the MOS cameras refer to **one MOS camera only**.
The order of the plots is:

1. Power law models
2. Thermal plasma (Raymond-Smith) models with solar metallicities
3. Black body models

For each model type, two pn camera plots are shown first (thin and medium filter, in that order), then two MOS plots.

3.3.11.3 Count rate conversion from other X-ray satellite missions

For the conversion of count rates from other X-ray satellites to count rates expected for the different **XMM-Newton** detectors, we recommend the use of the *PIMMS* software from NASA's HEASARC (at the URL `http://heasarc.gsfc.nasa.gov/Tools/w3pimms.html`).

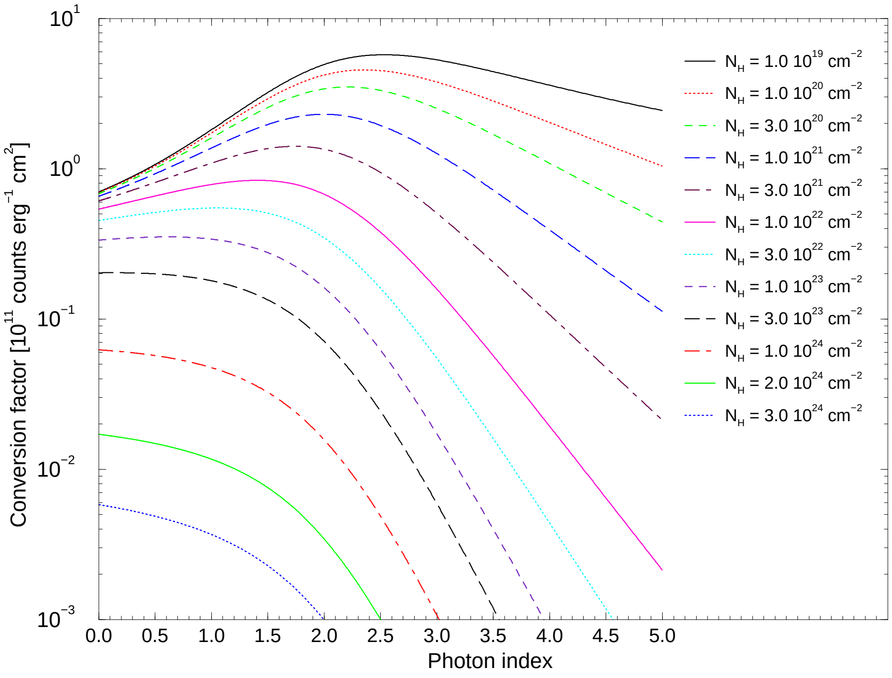

Figure 45: *EPIC pn flux to count rate conversion factors for various power law spectra and different values for the absorbing column density, N_H (thin filter).*

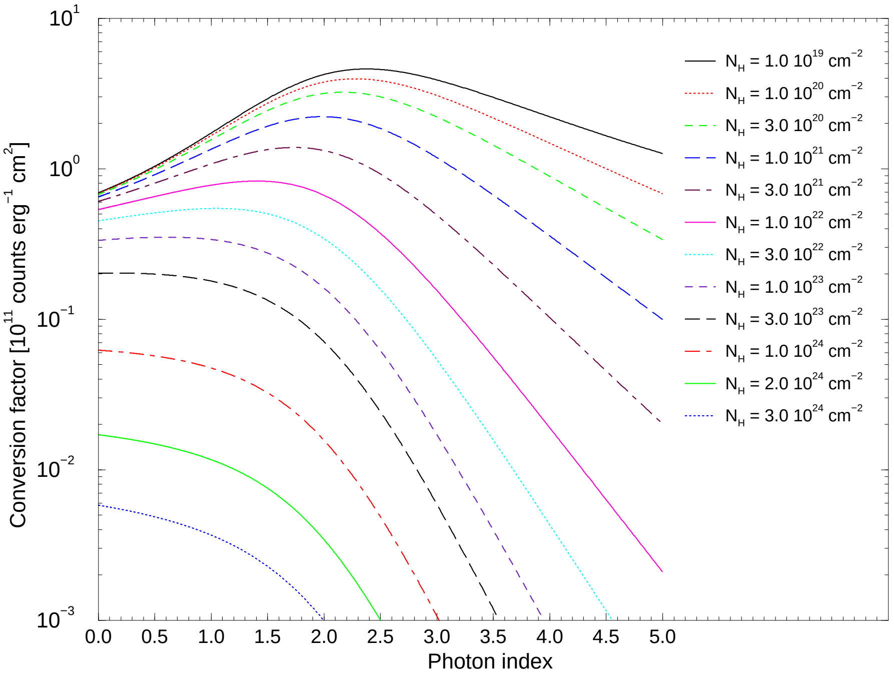

Figure 46: *EPIC pn flux to count rate conversion factors for various power law spectra and different values for the absorbing column density,* N_H *(medium filter).*

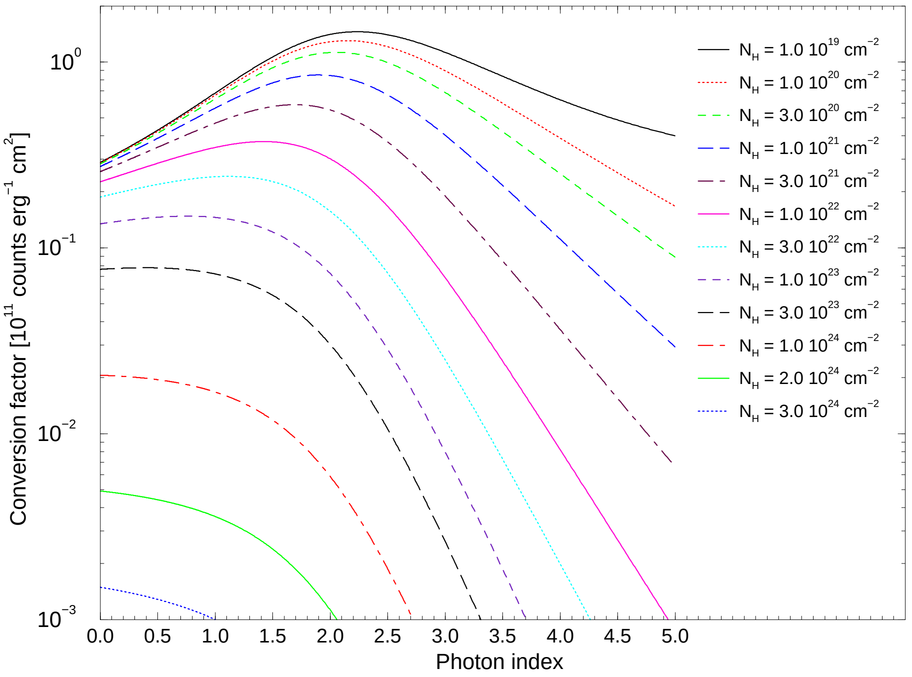

Figure 47: *EPIC flux to count rate conversion factors for one MOS camera for various power law spectra and different values for the absorbing column density,* N_H *(thin filter).*

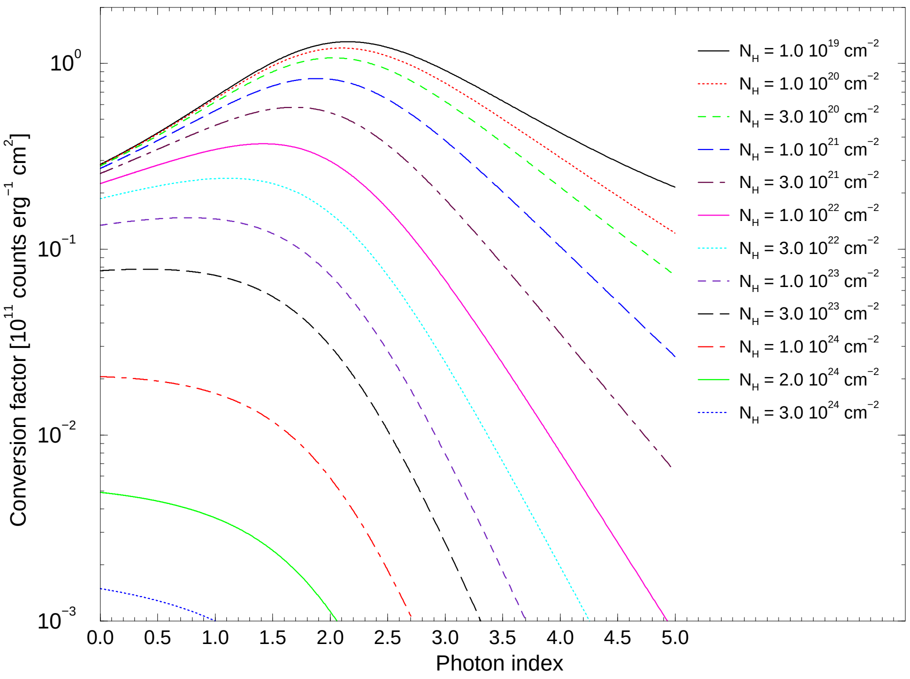

Figure 48: *EPIC flux to count rate conversion factors for one MOS camera for various power law spectra and different values for the absorbing column density, N_H (medium filter).*

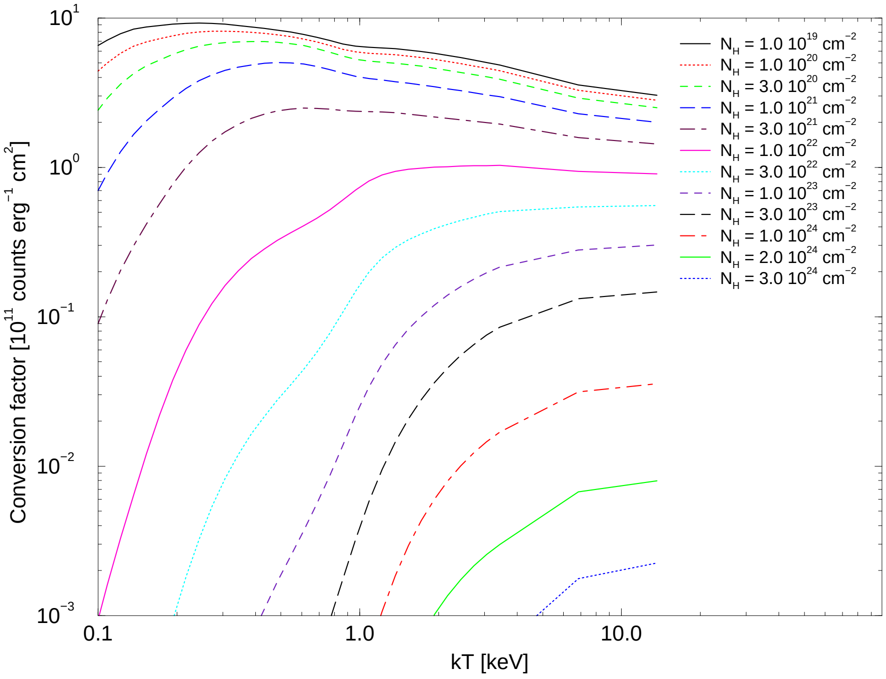

Figure 49: *EPIC pn flux to count rate conversion factors for various Raymond-Smith spectra and different values for the absorbing column density, N_H (thin filter).*

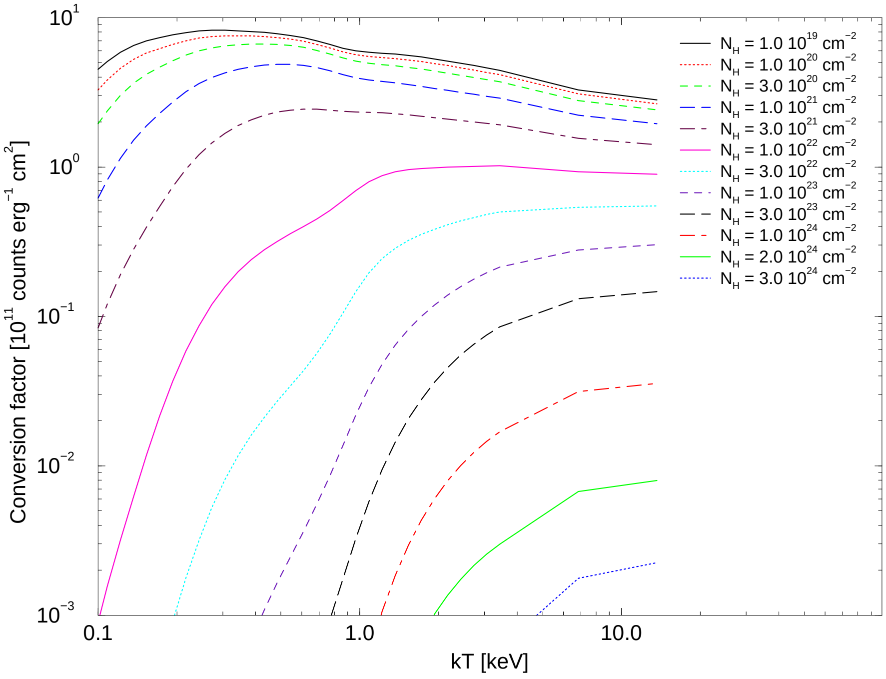

Figure 50: *EPIC pn flux to count rate conversion factors for various Raymond-Smith spectra and different values for the absorbing column density, N_H (medium filter).*

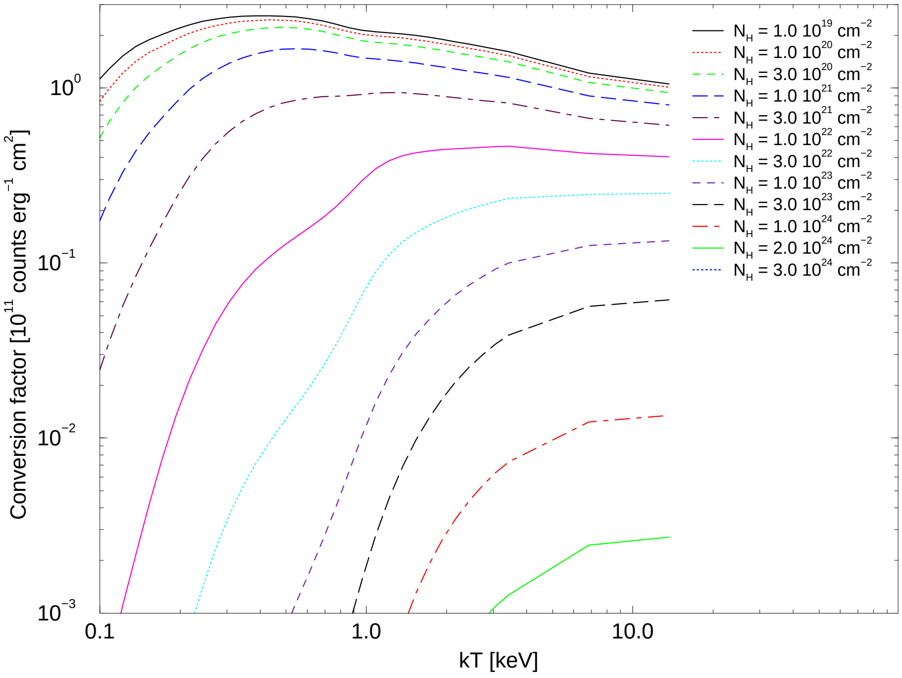

Figure 51: *EPIC flux to count rate conversion factors for one MOS camera for various Raymond-Smith spectra and different values for the absorbing column density, N_H (thin filter).*

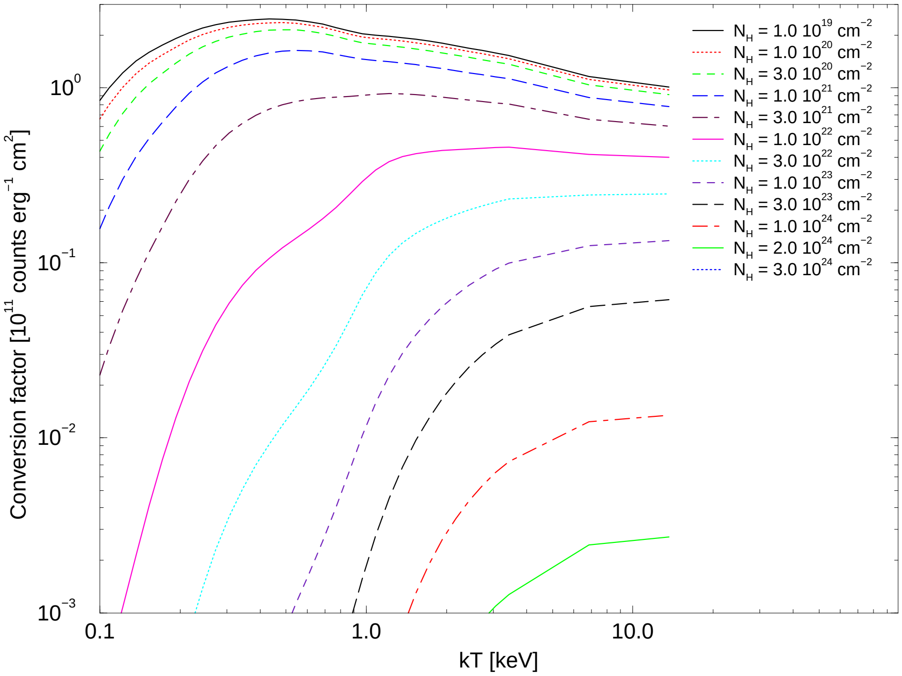

Figure 52: *EPIC flux to count rate conversion factors for one MOS camera for various Raymond-Smith spectra and different values for the absorbing column density, N_H (medium filter).*

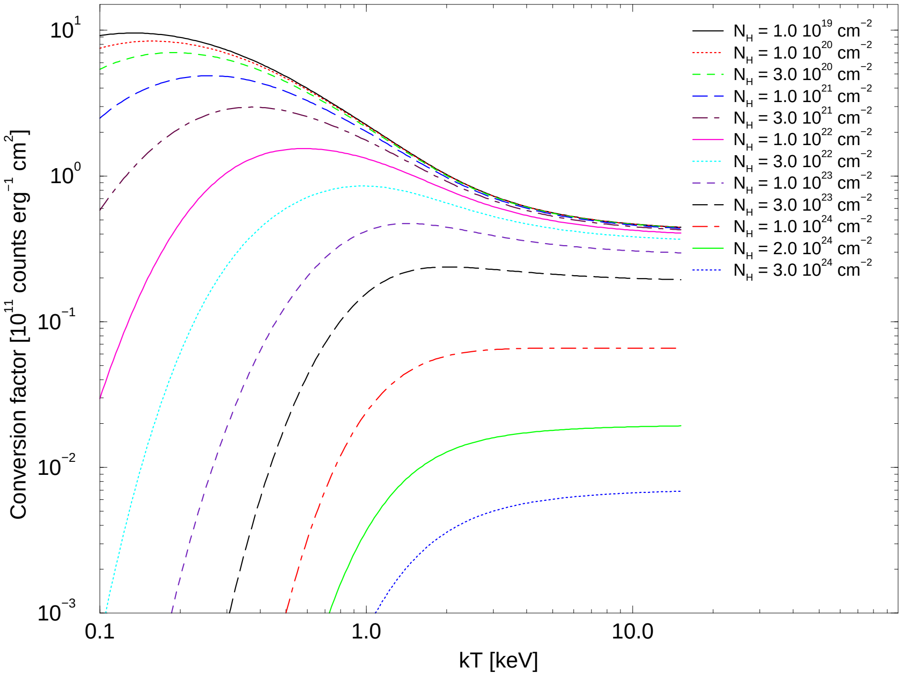

Figure 53: *EPIC pn flux to count rate conversion factors for various black body spectra and different values for the absorbing column density, N_H (thin filter).*

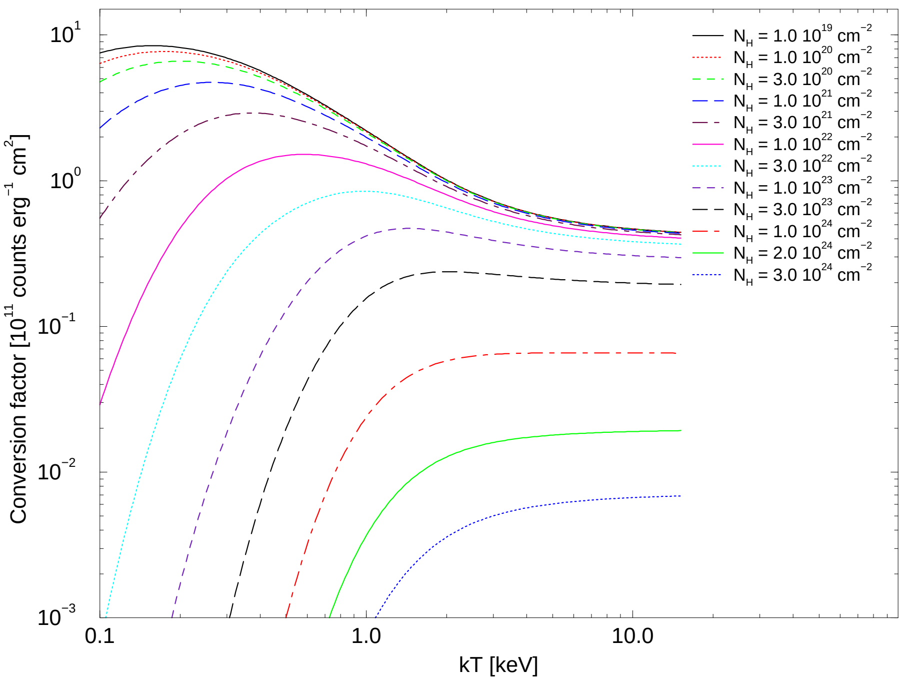

Figure 54: *EPIC pn flux to count rate conversion factors for various black body spectra and different values for the absorbing column density,* N_H *(medium filter).*

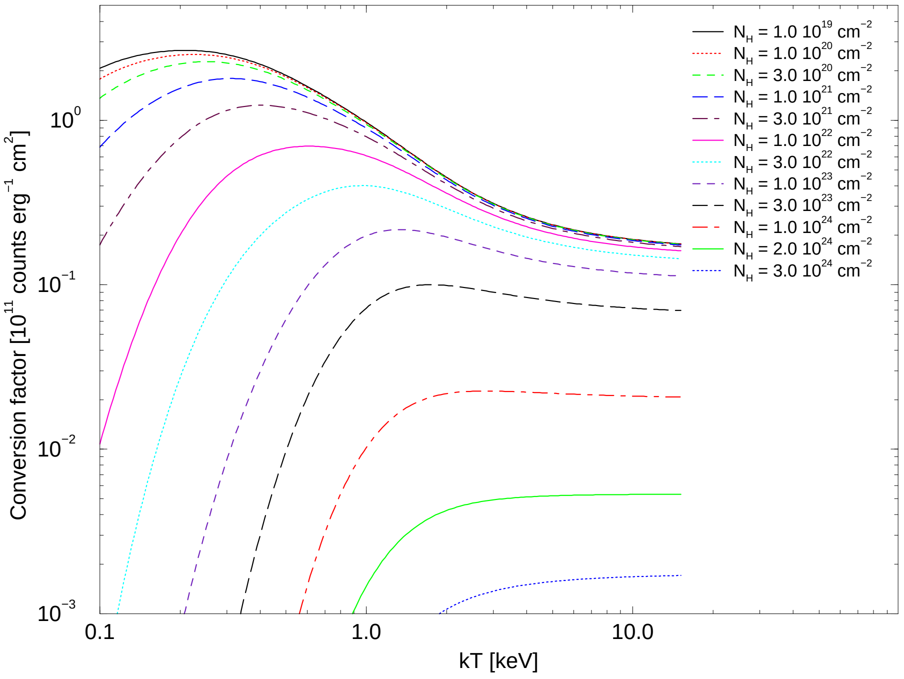

Figure 55: *EPIC flux to count rate conversion factors for one MOS camera for various black body spectra and different values for the absorbing column density,* N_H *(thin filter).*

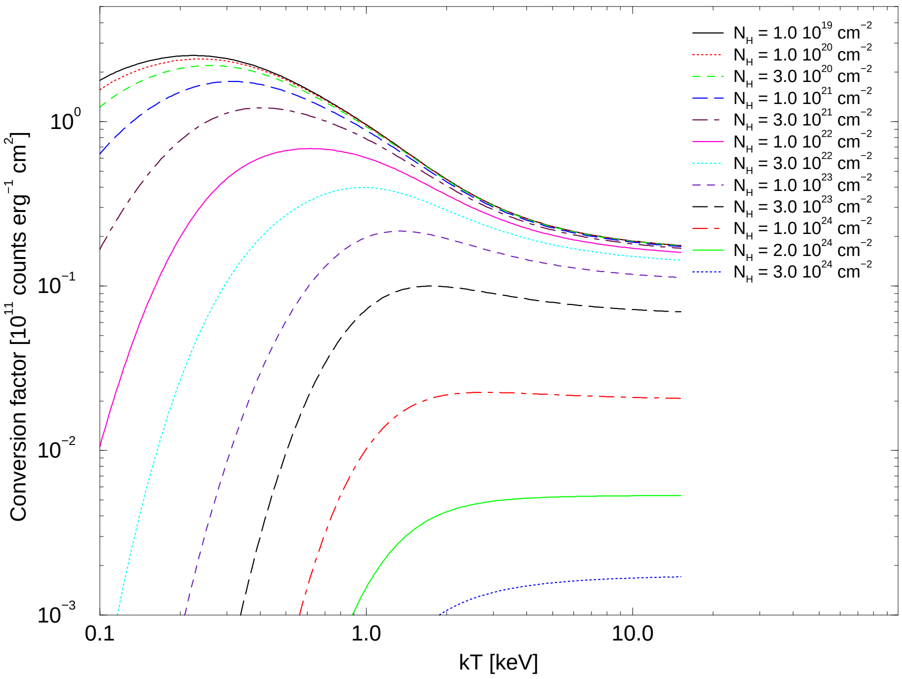

Figure 56: *EPIC flux to count rate conversion factors for one MOS camera for various black body spectra and different values for the absorbing column density, N_H (medium filter).*

3.4 REFLECTION GRATING SPECTROMETER (RGS)

Two of the three **XMM-Newton** X-ray telescopes are equipped with RGS units. These consist of Reflection Grating Assemblies (RGAs) and RGS Focal Cameras (RFCs), see Fig. 3. Among the science instruments of **XMM-Newton**, RGS is best suited for high spectral resolution ($E/\Delta E$ from 100 to 500, *FWHM*, or 100 to 800, *HEW*) X-ray spectroscopy in the energy range 0.33–2.5 keV (5–38 Å).[5] The energy range covered by the RGS has a particularly high density of X-ray emission lines, thus offering a large number of diagnostic tools to investigate the physical conditions in, and the composition of, the emitting material, e.g., the L shell transitions of heavy elements like Fe and Ni, and K shell transitions of lighter elements, such as N, O, Ne, Mg, and Si.

The grating plates in the RGAs have mean groove densities of ca. 645.6 lines mm^{-1}. The dispersion of the instrument is a slowly varying function of dispersion angle, and is equal to approximately 8.3 and 12.7 mm $\mathrm{Å}^{-1}$ at 15 Å, in first and second order, respectively. The RGAs are mounted in the light path of the two X-ray telescopes with EPIC MOS cameras in their primary focus. Each RGA intercepts about 58% of the total light focused by the mirror module.

The RFCs consist of linear arrays of 9 MOS CCD chips (similar to those in the EPIC MOS cameras), which are located along the dispersion direction of the RGAs. The RGS MOS chips are back-illuminated in order to maximize their soft energy response and aluminium-coated on the exposed side in order to suppress optical/UV light. They have 1024×768 $(27\mu\mathrm{m})^2$ pixels, half of which (1024×384) are exposed to the sky, while the other half is used as a storage area. During readout, 3×3 pixel on-chip binning (OCB) is performed in the default spectroscopy mode, leading to a bin-size of $(81\ \mu\mathrm{m})^2$, which is sufficient to fully sample the RGS line-spread function (LSF). For an on-axis source the zeroth order image of the gratings is not visible on the detector array. The size of one bin (3×3 pixels) projected onto the sky is about $2''.5$ in the cross-dispersion. In the dispersion direction one bin corresponds to about 7, 10, and 14 mÅ for wavelengths of 5, 15 and 38 Å and first order, respectively. The correspondence for the second order for the same wavelengths is about 4, 6, and 10 mÅ. Alternatively, for slightly extended sources, and given wavelengths of 5, 15, and 38 Å, the size of one detector bin in the dispersion direction on the sky is 3, 5 and 7 arcsec, respectively for first order, and 4, 6, and 9 arcsec for second order.

The field of view in the cross-dispersion direction is determined by the width of the CCDs ($5'$), and the spatial resolution in this direction is largely determined by the imaging properties of the mirror. Note that RGS is optimized for best imaging properties of the dispersed spectrum, whereas the cross-dispersion image is out of focus. In the dispersion direction the aperture of RGS covers the entire FOV of the mirrors, only the effective area reduces significantly for off-axis sources (see Figure 68).

There were problems with failing drive electronics of two CCDs (CCD 4 in RGS-2, covering the wavelength range from 20.1 to 23.9 Å and CCD 7 in RGS-1, 10.5 to 14.0 Å). Hence the total effective area is reduced by a factor 2 in these wavelength bands. Although the built differences between the two RGS units are small, the energy resolution of the

---

[5] The formula for conversion of wavelengths into energies is λ [Å] $\times$ E [keV] = 12.3985.

two instruments is slightly different due to slightly different focusing properties of the instruments (as shown in Fig. 64). Observers should make sure that there is still sufficient exposure and wavelength coverage for the measurement of important spectral features of their sources, such that these are not lost because of the two RGS CCD chain failures.

The performance of the RGS instruments is explained in detail in the following sections. Key performance parameters are summarized in Table 6.

Table 6: *The* **RGS** *key performance parameters*

Parameter	value	comment
A_{eff}	140 cm^2	peak effective area (at 15Å)
λ	5–38 Å	wavelength range first order
E	0.35–2.5 keV	energy range first order
$\lambda/\Delta\lambda$ *FWHM*	100–500	resolution (line separation)
$\lambda/\Delta\lambda$ *HEW*	100–800	resolution (weak line detection)
$\delta\lambda$	±8 mÅ p.p	wavelength accuracy
bin size (3 × 3 pix.)	$2''.5$	cross dispersion
	7–14 mÅ	dispersion, 1st order

3.4.1 Diffraction geometry

The diffraction geometry of the reflection gratings is illustrated in Fig. 57. Light strikes the gratings at an angle of incidence α with respect to the plane of the grating, and is dispersed into dispersion angle β, which are related by the dispersion equation,

$$\cos\beta = \cos\alpha + m\lambda/d \tag{1}$$

with λ the radiation wavelength, d the grating period, and m the spectral order (RGS is designed for orders $m < 0$, *i.e.* $\beta \geq \alpha$).

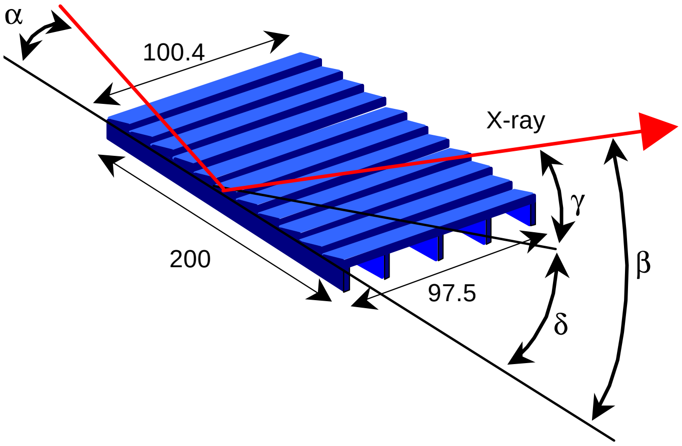

Figure 57: *Schematic drawing of a grating, including some of the key dispersion angles.*

3.4.2 RFC chip arrays

Figure 58 displays a sketch of the chip geometry in an RFC. The two RFCs are offset with respect to each other along their dispersion direction so as to fill the gaps in between each other chips (i.e., providing continuous coverage along the dispersion direction). The interchip gap between two adjacent CCDs is about 0.5 mm (corresponding to ~ 85 mÅ and ~ 45 mÅ at short and long wavelengths respectively). The dispersion direction is along the spacecraft "Z" axis. Higher energies, shorter wavelengths, are dispersed to higher values in Z and to lower dispersion angles (BETA values) .

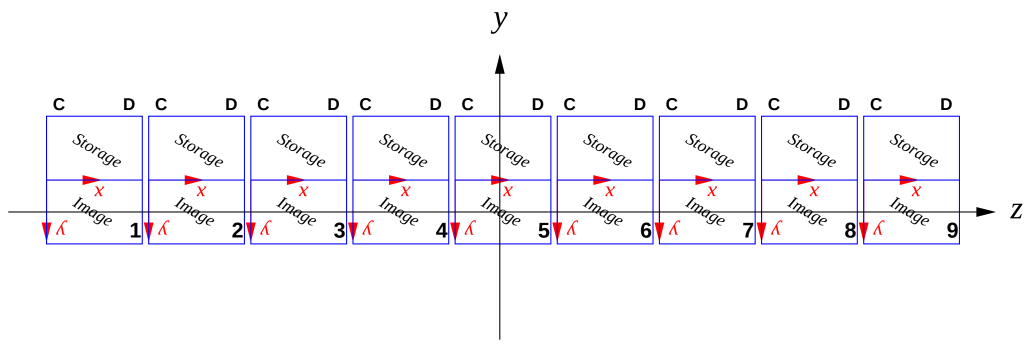

Figure 58: *Sketch of an RFC chip array, with 9 MOS CCDs. The half of each CCD at large camera-y coordinates is exposed to the sky, the other half is used as a storage area. The dispersion direction is along the "Z" axis, so that higher energies (shorter wavelengths) are dispersed to higher values in Z. Using the spacecraft axis, the BETA value (dispersion direction) is antiparallel to Z, and the cross-dispersion is parallel to Y. This translates onto the sky such that cross-dispersion is antiparallel to Y, and BETA is antiparallel to Z.*

The chip on the left side of Fig. 58 has number 1 (the low Z end of the coordinate scale), the one on the right is number 9 (largest Z value, smallest dispersion angle and highest energy or smallest wavelength). The user is referred to the **XMM-Newton** Calibration Access and Data Handbook (`http://xmm.vilspa.esa.es/calibration/docs/general/calhb_2.0.ps.gz`) for a more complete description of the coordinate systems. For an on-axis source with RGS as prime instrument, the individual chips cover approximately the energy ranges listed in Table 7. The numbers tabulated there relate to a nominal case.

After the first week of operations, an electronic component in the clock driver of CCD4 in RGS-2. failed. A similar problem occurred in early September, 2000, on CCD7 of RGS-1. The affected wavelengths are shown in Table 7.

Detailed simulations should be performed in case the user is interested in lines that are close to the chip boundaries (see Table 7 for the location of these boundaries). To shift important lines away from chip boundaries or non operating CCDs, users may want to consider changing the pointing (boresight coordinates) accordingly and observing with a fixed position angle. For this purpose the task *rgslinepos* is provided as part of the **XMM-Newton** science analysis system (SAS). Large offsets in the dispersion direction are not recommended as this reduces the overall effective area significantly (see Figure 68). Another, undesired, side-effect of an offset pointing could be the displacement of the source close or to an EPIC CCD boundary, users should check that this is not happening for their observations. Last, the fact that offset pointing requires a particular position angle implies a smaller visibility window for the observation.

Table 7: *The wavelength and energy ranges*[1] *covered by the chips of* **RGS** *-1 and* **RGS** *-2 for an on-axis source*

Chip no.	**RGS-1**		**RGS-2**	
	Energy [keV]	**Wavelength** [Å]	**Energy** [keV]	**Wavelength** [Å]
1	0.33–0.37	33.2–38.0	0.33–0.37	33.5–37.1
2	0.37–0.43	28.9–33.2	0.37–0.44	28.0–33.3
3	0.43–0.50	24.8–28.9	0.44–0.50	24.9–28.0
4	0.50–0.60	20.8–24.8	(0.50–0.62[2])	(19.9–24.9[2])
5	0.60–0.73	17.0–20.8	0.62–0.77	16.2–19.9
6	0.73–0.91	13.6–17.0	0.77–0.95	13.0–16.2
7	(0.91–1.2[2])	(10.3–13.6[2])	0.95–1.25	9.90–13.0
8	1.20– 1.70	7.5 –10.3	1.25–1.80	7.0 –9.90
9	1.70– 2.50	5.0 – 7.5	1.80–2.50	5.0 – 7.0

Notes to Table 7:
1) Due to the scattering, the chip boundaries are not sharp features of the effective area (see § 3.4.5), but some non-zero effective area is also present at wavelengths that correspond to gaps but which are sufficiently close to a CCD chip.
2) non-operational chain (electronics/chip)

3.4.3 RGS grating orders

X-rays are reflected into spectral orders –1 and –2 with the highest efficiency, so these are the orders expected to produce useful data in the majority of observations. Count rates in the –3 order are about 8 times lower than in the –2. Depending on grating order, the RGS covers the energy ranges listed in Table 8.

The exact location of a source spectrum on the RGS CCD chips depends on the source's location within the field of view of the X-ray telescopes. For a target on-axis the observed spectrum is well centered on the RFC chips in the cross-dispersion direction. The wavelength scale for sources off-axis in the cross-dispersion direction is the same as for those on-axis, but will be different for sources off-axis in the dispersion direction. Currently the achieved accuracy of the wavelength scale is ±10 mÅ (peak-to-peak). This accuracy can probably be improved with further, ongoing analysis. The offline data analysis with SAS takes care of the shifts of the wavelength as function of source position in the dispersion direction.

Figures 59 and 60 show the residuals of the RGS measured versus nominal positions for certain emission lines and a set of observations of coronal sources. The nominal wavelengths are indicated in each frame. The abscissa shows the index number of the observation (see key at the bottom right). Residuals from first order spectra are indicated by circles, those for second order spectra, by squares. Error bars are smaller than the size of the symbols in most cases. Note that in the case of RGS-1 (Fig. 59) the Fe XVII line at

Table 8: *The energy ranges covered by the* **RGS** *in different grating orders*

Order	Energy range [keV]
–1	0.35 – 2.5[1]
–2	0.62 – 2.5[1]
–3	1.20 – 2.5[1]

Note to Table 8:
1) Practical limitation due to very low effective area above 2.5 keV. The theoretical upper limit is 2.5 keV × -m, where m is the order number.

17.05 Å and the N-Lyα line are at inter-chip gap for the first order spectra, and therefore the residuals are systematically too high, as the wavelength cannot be accurately be determined in these cases by the method used. For RGS-2 (Fig. 60) none of the lines falls at an inter-chip gap. For further reading on the RGS wavelength scale monitoring, the user should take note of the SOC document XMM-SOC-CAL-TN-0020 (available from `http://xmm.vilspa.esa.es/docs/documents/CAL-TN-0020-1-0.ps.gz`).

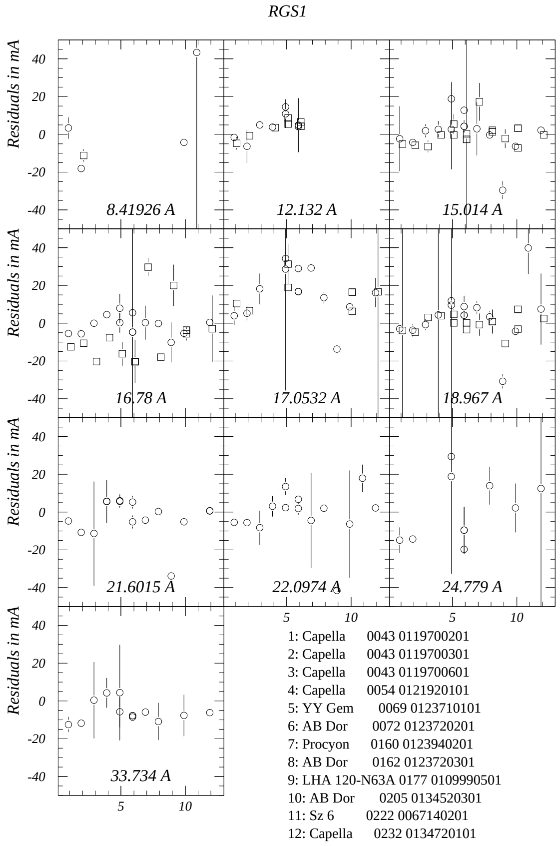

Figure 59: **RGS** *-1 wavelength scale accuracy. See text for details.*

Due to the grating relation (§ 3.4.1, equation 1), the orders overlap spatially on the CCD detectors of the RFC (see Fig. 61, top panel). Separation of the spectral orders is achieved by using the CCDs' intrinsic energy resolution (~ 160 eV, *FWHM*, at 2 keV). The

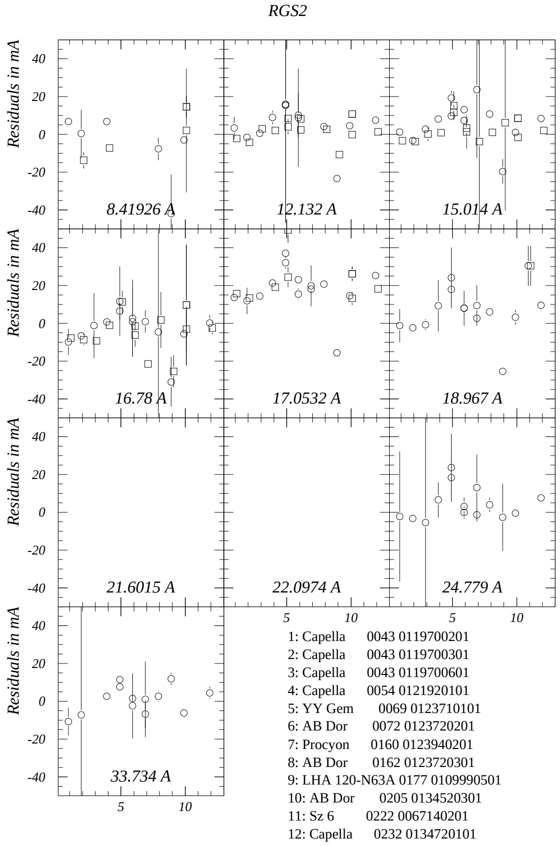

Figure 60: **RGS** *-2 wavelength scale accuracy. See text for details.*

dispersion of a spectrum onto an RFC array is shown in the bottom panel of Fig. 61. The –1 (lower) and –2 order (next) are very prominent and are clearly separated in the vertical direction (i.e., in CCD energy, or PI, space). Photons of higher orders are also visible for brighter sources. The signal from the calibration sources is also seen in the bottom panel as short horizontal features.

3.4.4 RGS spectral resolution

The two RGS units operate independently of one another. Their Line Spread Function, LSF, is a convolution of the mirror response and the grating response, and it depends on the proper alignment of these units.

The mirror responses, or telescope PSFs, are presented above (§ 3.2.1.1). Each mirror response impacts on the width of the LSF core of the RGS unit located behind it. The grating response depends on the co-alignment and flatness of the 182 gratings that are integrated per RGA. In addition there is also a significant (but well calibrated) component due to scattering on the surfaces of the mirrors and the gratings (seen as the horizontal distribution of events in the bottom panel of Fig. 61). Pointing stability of **XMM-Newton**, which affects the resolving power through variations of the angle of incidence on the gratings has proven to be negligible.

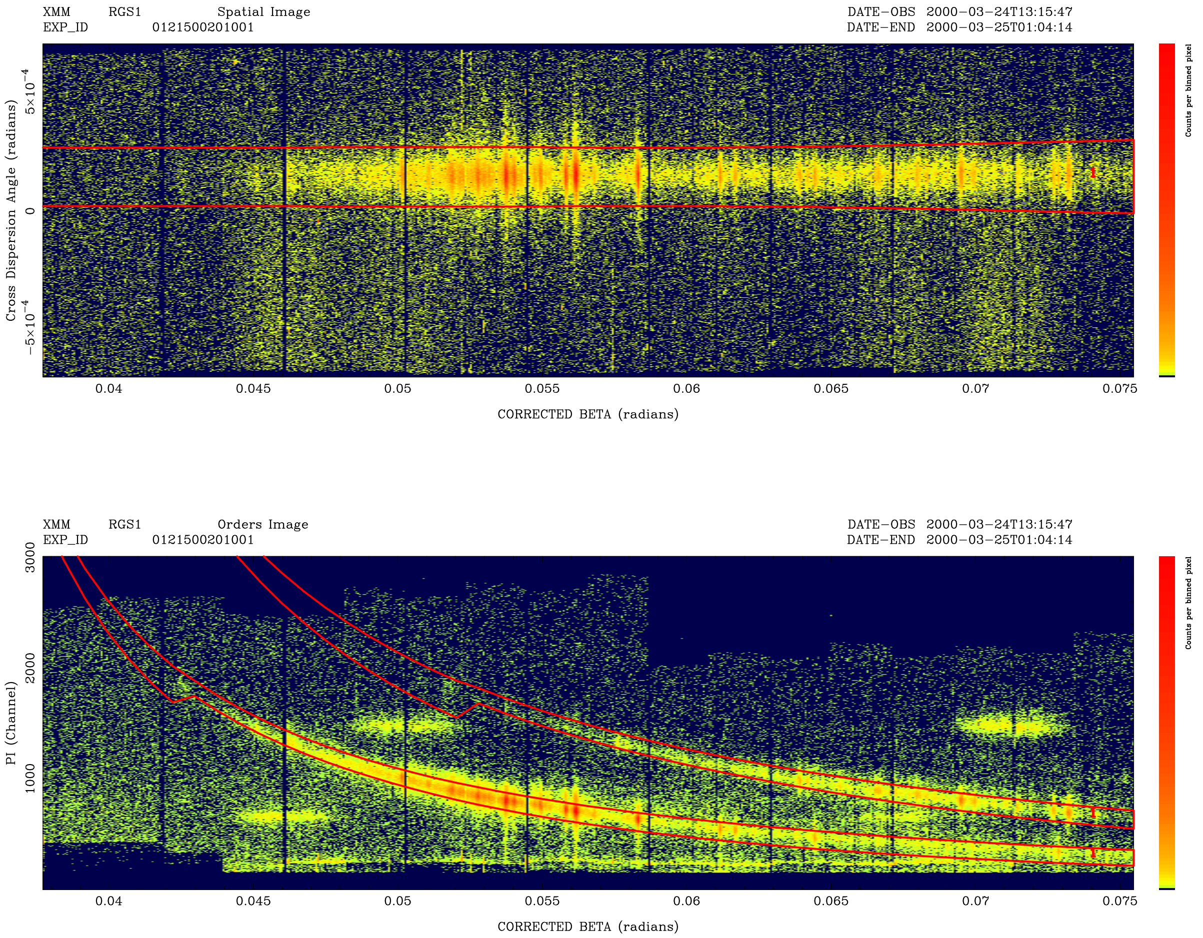

Figure 61: *Example of* **RGS** *data for one calibration observation (id: 0121500201001) of Capella. The color scale represents a logarithmic intensity scale. The dispersion axis runs horizontally and increases to the right. Low dispersion angle corresponds to shorter wavelengths, higher energies and therefore a higher signal in the CCD's. The top panel shows the image of the dispersed light on the detector (the cross dispersion is along the vertical axis). The bottom panel shows the order selection plane, with the CCD's energy or PI information on the ordinate. This also illustrates the mechanism used for separating* -1 *and* -2 *grating orders onto the* **RGS** *focal cameras. In the bottom panel the low and high level thresholds are visible. Standard data selections are indicated by the red curves. In the top panel effects of fixed pattern noise at the long wavelength side of the RGS band are seen.*

An example for an individual line, the first order OVIII Lyα (λ = 18.97Å) emission line, along the dispersion direction, is displayed in Fig. 62. The measured data are compared with simulations using SciSim. There is excellent agreement between the measured performance of the LSF and the predicted by SciSim which is based on pre-flight calibrations. This proves that the predicted resolving power can be achieved. The same line, perpendicular to the dispersion direction, is presented in Fig. 63.

The shape of the LSF core largely determines the ability of the spectrometer to separate

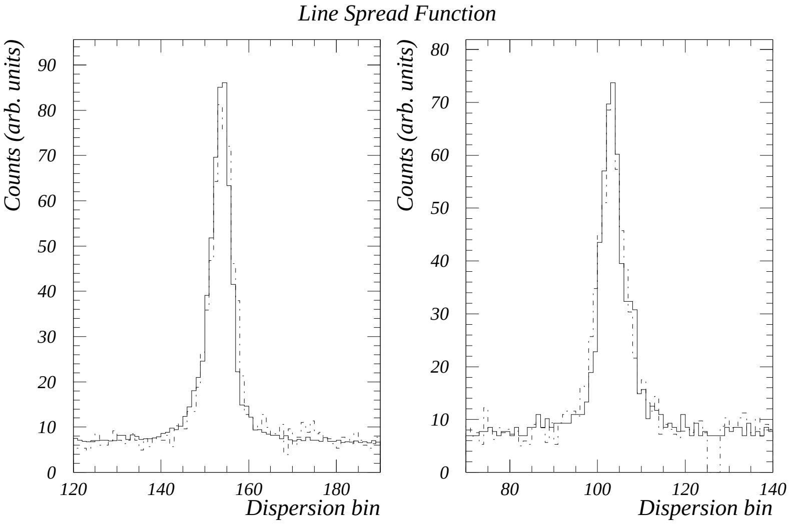

Figure 62: *Comparison of Line Spread Functions with pre-flight simulations. The O*VIII *Ly*α *(*$\lambda = 18.97$ *Å) line was used to compare data with simulations with* **SciSim**. *Data are shown with solid lines, simulations are show with dash-dotted lines. The LSF for* **RGS** *-1 is plotted left, that for* **RGS** *-2 on the right.*

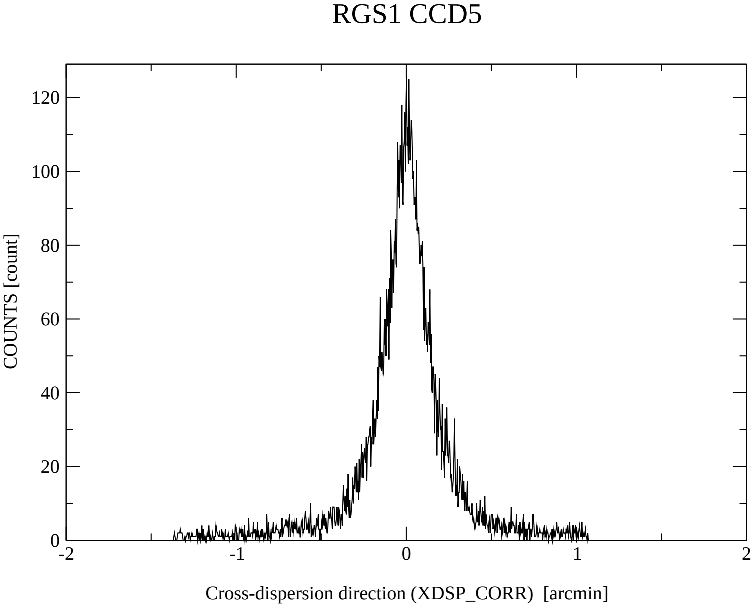

Figure 63: *A close-up view of the O*VIII *Ly*$\alpha\lambda 18.97$*Å line, along the cross-dispersion direction.*

closely spaced emission lines. The various components scale differently with wavelength, which gives rise to a composite line shape which can not easily be characterized in terms of a simple analytical function. The telescope blur contributes a constant term to the spectrometer line width, while misalignments and flatness errors of the gratings contribute a term which slowly increases with increasing wavelength. The scattering component is most significant at the shortest wavelengths and the highest diffraction orders. This is illustrated in Fig. 64 where the predicted resolution (the *FWHM* of the LSF) for the two RGS s are shown in the second and forth panels (the steep rise below 7Å is due to the scattering component of the gratings). Also shown are the measurements, which are deduced from a few narrow, bright emission lines in HR1099 (Lyα lines of Ne (m=–1, –2), O, N and C). Fig. 65 shows the predicted spectral resolving power ($\lambda/\Delta\lambda_{\rm FWHM}$ = E/Δ E) as a function of wavelength and measurements from Capella, Procyon, HR1099, AT Mic and λ And. The measured values of $\lambda/\Delta\lambda_{\rm FWHM}$ may be slightly affected by line blending or velocity broadening in some cases. As an example, the Capella spectrum used to measure some line widths is shown in §3.4.9.2, Fig. 71. Figures 64 and 65 demonstrate again that the instrument resolving power is close to expectations. The explicit spectrometer line response is close to predictions based on a raytrace model for the spectrometer.

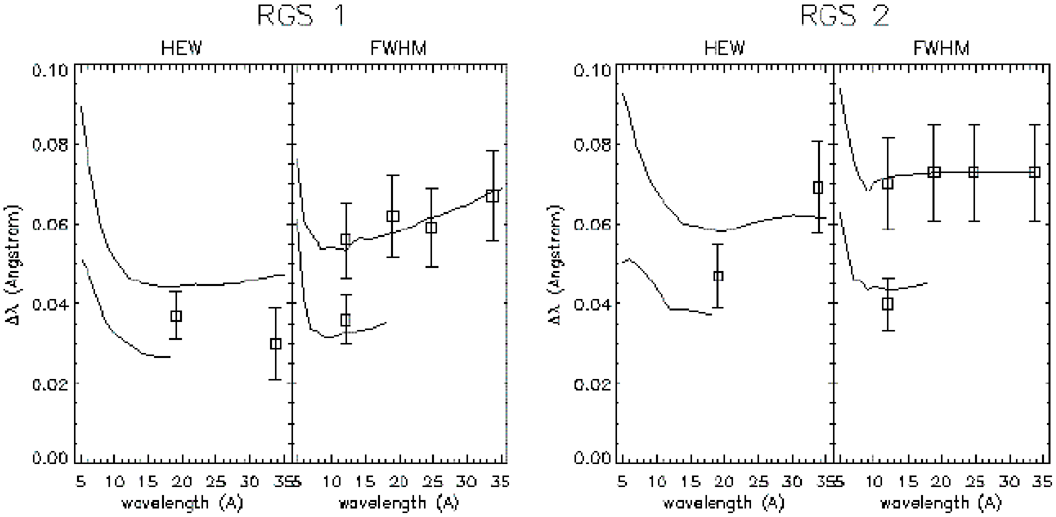

Figure 64: *The resolving power (*HEW *and* FWHM*) of* **RGS** *-1 (left) and* **RGS** *-2 (right) in the –1 and –2 grating orders.* HEW *indicates the detectability of a weak feature against a strong continuum and* FWHM *whether two closely spaced spectral lines can be resolved.*

The ability to detect weak emission lines above the background or the continuum is better measured by the half energy width (*HEW*) of the profile. This width, especially at short wavelengths, is more dependent on the amplitude and width of the scattering wings. Again, the data agree with the predictions and in the *HEW* sense the resolving power goes to ∼ 800 at the longest wavelengths. The first and third panels of Fig. 64 display the *HEW* as a function of wavelength, for both RGS units separately.

3.4.4.1 RGS spectral resolution for extended sources

The RGS spectral resolution depends on the angular extent of the observed source. For an extended source ($\geq 30''$), emission lines are broadened according to the relation

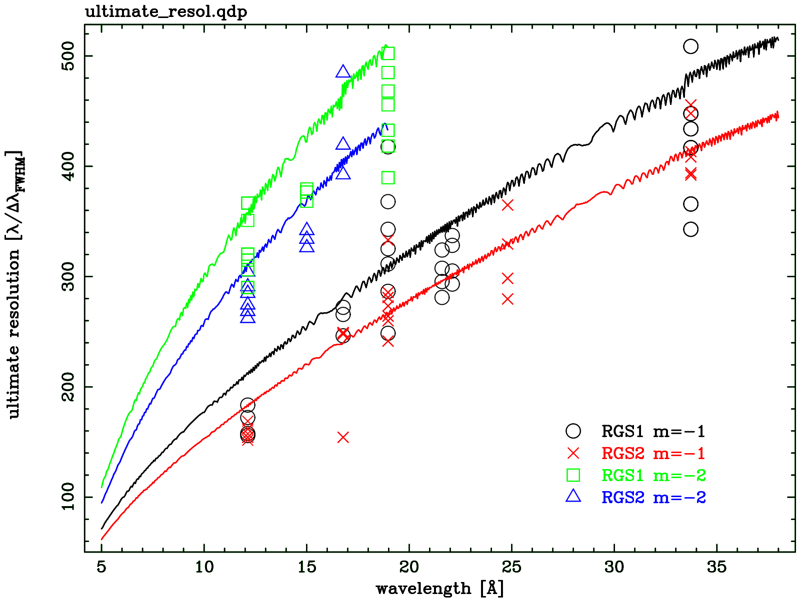

Figure 65: *The predicted resolving power* ($\lambda/\Delta\lambda_{\rm FWHM}$ = E/Δ E) *of both* **RGS** *-1 and* **RGS** *-2, first and second grating order. Measured individual lines for a variety of targets and spectral order extractions are also shown for comparison. The different instruments and extraction orders are color and symbol coded. Some of the measured values may have significant line velocity broadening.*

$$\Delta\lambda(ext) = 0.124/m \times \ \theta(ext), \tag{2}$$

where $\Delta\lambda$(ext) is the resolution (in Å) in case of an extended source, for the spectral order m and a source extent of θ(ext), in arcmin. This illustrates that, for a source extent of order $1'$, RGS still clearly outperforms EPIC in terms of spectral resolution. This is demonstrated by, e.g., the observed spectra of a moderately extended source like 1E 0102.2-7219. This target is a supernova remnant in the Small Magellanic Cloud with an angular extent of $\Delta\theta \sim 2'$. The first and second order spectra of 1E 0102.2-7219 are shown in § 3.4.9.2, Figs. 74, 75 and 76.

3.4.5 RGS effective area for dispersive spectroscopy

Several parameters determine the RGS effective area per dispersion order: the properties of all optical components in the light path, the CCD quantum efficiency and on source and order filtering criteria.

The following optical components are contributing:

- The effective area of the mirror modules (see § 3.2.2).
- The reflection grating arrays: how much of the light from the mirrors is diffracted to the different spectral orders and then absorbed on the RFCs. This is determined by: the amount of collimated light that is intercepted by the grating arrays, the reflectivity of the gratings into the dispersion order

and the effective surface of the gratings that provides useful dispersed light (since the gratings are mounted relatively close together, about 1 cm spacing, light with large dispersion angles is vignetted by the back of the neighboring grating, thus reducing the surface area that provides useful intensity to the camera at these dispersion angles).

- RGS focal camera CCD's quantum efficiency, this varies from 70% to 95% over the RGS passband from 0.35 to 2.5 keV.

Additionally these components are functions of energy (wavelength) and also source position angle.

Finally data selections in the RFC, amongst others used to separate orders and to suppress the scattering, will determine the effective area.

To assess the total efficiency of the RGS instrument per spectral order, the efficiency with which the background is rejected and different spectral orders can be selected must also be taken into account. This is performed by filtering in the imaging domain (cross-dispersion versus dispersion angles) and in the domain CCD-PI versus dispersion angle. Standard data selections are indicated by the red curves in Fig. 61. In the cross-dispersion direction a filter is applied which includes typically 90–97% of the total intensity. One can see in Fig. 61 that the RGAs' spectral orders spatially overlap in the dispersion direction. However, the intrinsic energy resolution of the CCDs allows the separation of X-ray photons in different orders, i.e., photons which are of different energies, but have the same position along the dispersion direction. Default masks for the spatial extraction of photons from the different orders (using PHA or PI-energy channel vs. dispersion coordinate plots, as in Fig. 61), are created by the offline analysis SAS tasks for each **XMM-Newton** RGS instrument. The user can also modify the extraction masks as described in the SAS User's Guide. In addition the exposure time per wavelength bin is calculated taking into account the data selections, rejected columns and pixels and the dead space between CCDs. The expected efficiency in the post-observation RGS order selection with the SAS is ca. 81% (0.9×0.9). This is a function of wavelength and is less at shorter wavelengths, due to additional loss of scatter outside of the extracted (dispersion-PI) region.

Fig. 66 displays the calculated effective area of both RGS units together, and Fig. 67 the individual RGS -1 and -2 overlayed one on top of the other. The calculations have been performed taking into account all the factors listed above. Some clear features can be identified from these figures:

- the effective area has broad gaps at the locations corresponding to the non-operational CCD's
- the efficiency function around dead spaces (e.g. chip boundaries) and at the edges of the non-operational CCD chains does not drop sharply nor completely decreases to zero. This is due to the scattering causing photons with wavelengths corresponding to the passive areas being redistributed into non-passive areas (the amplitude of this sensitivity is strongly dependent on the selection mask in CCD PI versus dispersion coordinate space)

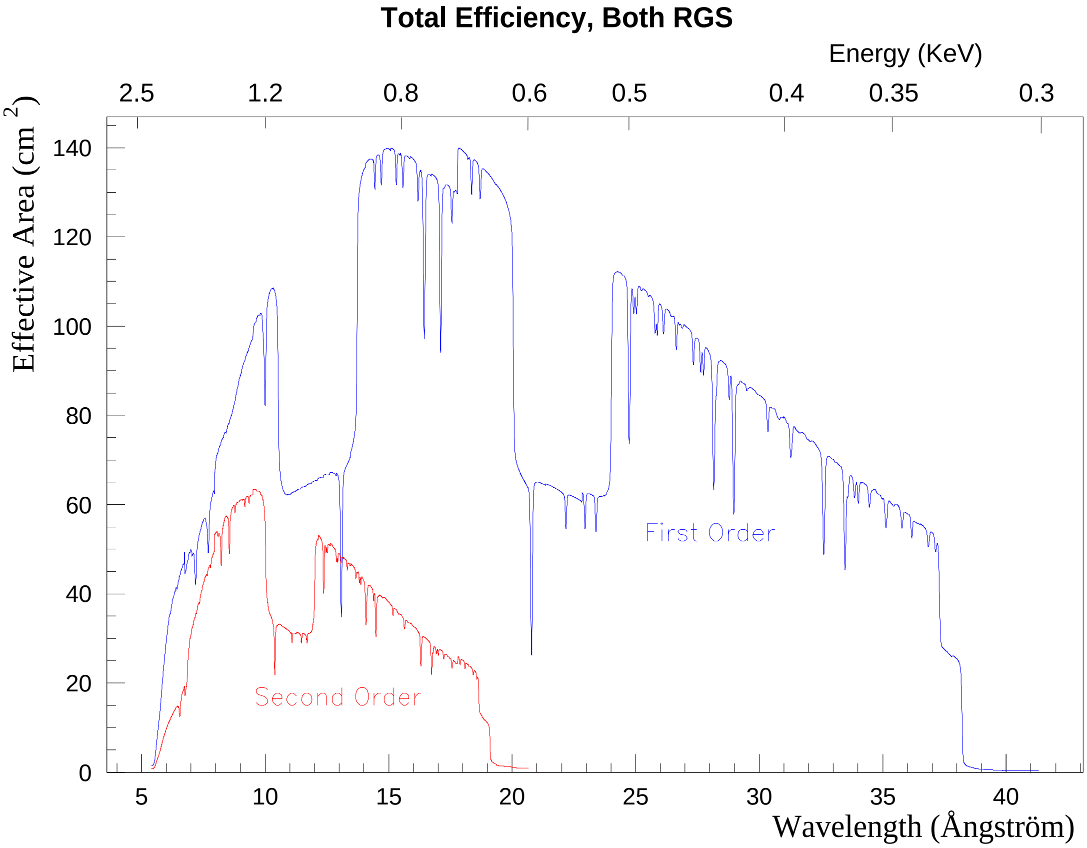

Figure 66: *The effective area of both* **RGS** *units combined as a function of energy and wavelength (top and bottom horizontal scale, respectively) See text for detailed explanations*

- the total effective area (both RGS added, Fig. 66), shows several of these chip boundaries, as the alignment of the RGS cameras is such that the inter-chip gaps do not coincide in wavelength.
- a similar effect of lower area as with the inter-chip gaps can be seen at wavelengths equivalent to bad columns, but there it is less pronounced
- absorption edges area are due to the existence of passive layers in the X-ray path consisting of the following atoms: Si ($\lambda = 6.74\,\text{Å}$), Al ($\lambda = 7.95\,\text{Å}$), Mg ($\lambda = 9.51\,\text{Å}$), F ($\lambda = 17.80\,\text{Å}$), O ($\lambda = 22.83\,\text{Å}$)
- apparent oscillations with small amplitude of the effective area are due to data selections by regions that are defined as polygons across the surface of binned two dimensional data (cross dispersion versus dispersion angle and CCD energy versus dispersion angle). The fact that pixels of these binned images are selected discretely, gives rise to small scale variations of the selected area within the region. This is seen as oscillations of the detection efficiency. This is not a problem, nor is it an additional uncertainty of the response, as these data selection effects are properly included in the response generation.

Fig. 68 shows the effective area as a function of off-axis angles. The ratio of the median

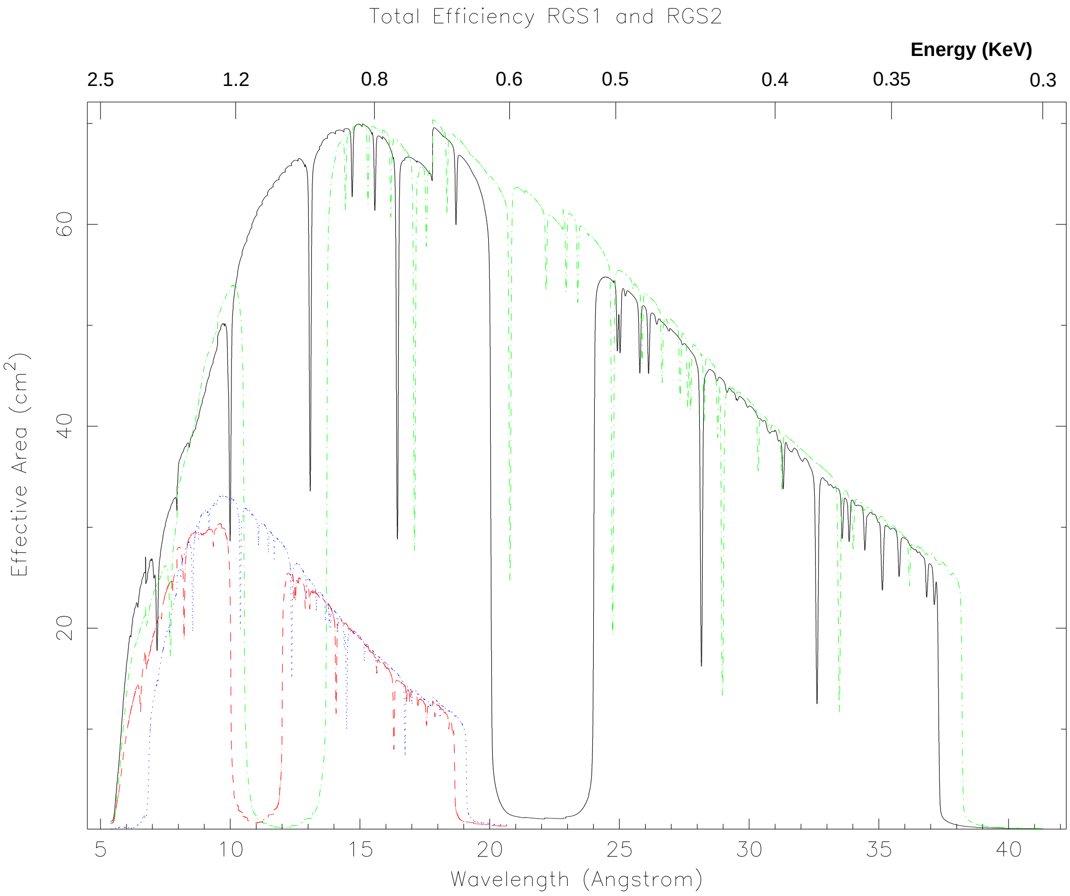

Figure 67: *The effective areas of both* **RGS** *units separately as a function of energy and wavelength (top and bottom horizontal scale, respectively). See text for detailed explanations.*

off-axis effective area to the on axis values decreases from 0.996 at ± 0'.5 to 0.89 and 0.82 at -2'and $+2$', respectively.

3.4.6 RGS sensitivity limits

The main point of the RGS sensitivity is the line detection threshold. To get an estimate of the exposure time necessary to detect a line above a certain underlying continuum (at a given significance level) detailed simulations can be performed using SciSim. Then the line flux integrated over the *HEW* of the line profile should be evaluated. For such an estimate, four contributing components must be considered:

1. the flux of the line,
2. the flux of the underlying continuum of the source,
3. the X-ray background and
4. the particle background.

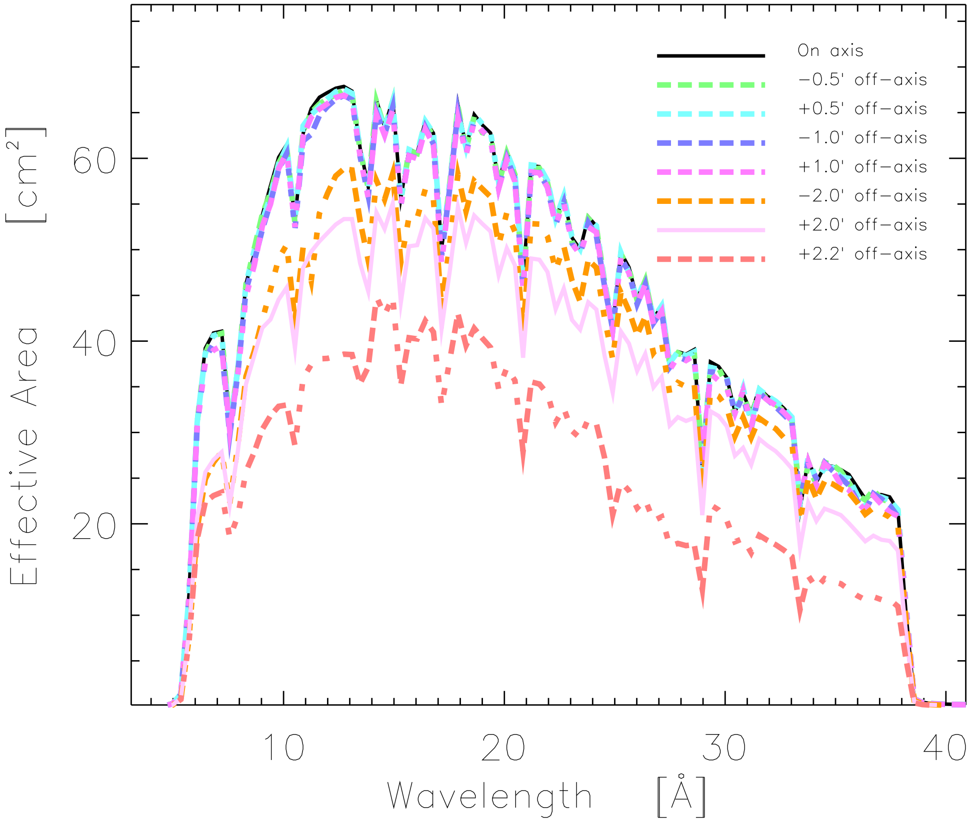

Figure 68: *The* **RGS** *-1 effective area as a function of off-axis angle. The gap due to the non-operational CCD is not included in this plot to allow quick extrapolation to* **RGS** *-2.*

The X-ray background varies over the sky. At the discussed energies the extragalactic X-ray background can be well reproduced by a power-law spectrum. This allows us to consider the X-ray background simply by adding an additional component to the continuum flux of the source.

The RGS instrument background has different components, each with its own characteristics and time dependency. The main components are listed below. The background characterization has been performed with in-flight data by analysing clear sky images (where there is no source emission) and fitting a model.

- particle background (minimum ionizing particles, protons and ions). These particles deposit most of their energy outside the 0.35 to 2.5 keV energy band and can thus mostly be rejected by the on-board software. There is an additional on-board rejection based on the spatial shape of the events. Except for the period when the spacecraft is passing through the radiation belts (i.e. for spacecraft altitude above 35000 km) and occasional solar storms, the in-flight measured particle background is quite stable. Typically it produces 2.7 ± 1 events cm^{-2} s^{-1}, which is a factor 2 higher than expected pre-launch. This number applies for event rates before any on-board selection and across the whole field of view. The quoted variation is larger than the statistical one and is due to variations in solar background.

- low energy electrons which enter through the telescope. Electrons with energies up to 20 keV are rejected by the electron deflector at the exit plane of the mirrors. Higher energy electrons create secondary radiation in the spacecraft and detector shielding.
- fluorescence lines in the detector housing due to interactions with the electron and other minimum ionizing particles. The expected strong fluorescence from the detector housing material, Al, is strongly suppressed by a Au coating. One still expects to see Al Kα and Au-M emission in the RGS energy band. These lines are indeed observed at a very low intensity ($\leq 10^{-3}$ counts cm^{-2} s^{-1}).
- calibration sources, they can easily be modeled. Nevertheless, the fraction spilling into the standard event selection regions is very small, since these are offset in the cross dispersion direction and additionally placed at locations where their energy signal is outside the order selection regions.
- read-out noise: although strictly speaking this is not a background component, the noise characteristics of each CCD has a tail which cannot be distinguished from proper X rays. It is roughly constant in dispersion and cross dispersion directions (with $\sim$ 0.67 counts s^{-1} in the whole detector, i.e. before any spectral extraction), and can be modeled by an exponential pulse height dependency. The typical detector noise count rate is 1×10^{-3} counts s^{-1} Å^{-1}, for the background in the extracted spectrum.
- soft protons entering through the mirrors: it has been found to be consistent with distributions coming from two different components, one distribution originating from protons being reflected off the grating array that results in a beam centered on the zero-order position and the other distribution having a much larger angular spread consistent with a diffuse non-scattered component. While the widths of these two distributions appear to be fixed, the overall count rate and shape are clearly variable with time. Overall particle count rates variations by a factor 20 have been measured for similar length observations. The changes in the background shape are related, according to the models, to changes in the input particle energy spectrum and on the fraction of protons that are reflected by the gratings. It is found that this fraction is correlated with the overall count rate. Quiescent background periods seem to be dominated by the diffuse component. The count rate in quiet periods is $1 - 5 \times 10^{-3}$ counts s^{-1} Å^{-1}. It should also be noted that background fluence is generally higher on the CCD's that are closer to the primary focus (CCD8 & 9).

The average background spectrum has been analyzed for quiet-time periods. This has been performed using clear sky images (or "blank" images) and selecting low background periods (after inspection of the light curves). The average first and second order RGS-1. and RGS-2. background spectra are shown in Fig. 69. The total exposure time is about 220 ks. The spectra have been extracted in a standard way for the energy (90% beta-PI window), but with a large cross-dispersion window (3.'4 field of view). The background count rate in the quiet period is $1-5 \times 10^{-3}$ counts s^{-1} Å^{-1}. This corresponds to $1-5 \times 10^{-5}$ counts s^{-1} per RGS resolution element for a point source.

The fraction of the total exposure time which corresponds to quiet background periods is, right now, unpredictable, as it is basically linked to the solar activity itself. During the first year of **XMM-Newton** operations there have been both "active" and "quiet" background epochs, during which about 50% and nearly 100% (respectively) of most exposures where taken with quiet background. A significant fraction of the data collected so far has much higher background than the one shown in Fig. 69. This should be taken into account for exposure time estimates, specially if detection of weak features is the main objective of the observations.

Each of these background component has a very different impact on the RGS sensitivity. The first four are either rejected on board or have low intensity. The major constituents are therefore a tail on the CCD response due to readout noise, and the soft proton radiation.

Examples of RGS dispersed spectra are given in figures Figs. 71–79. Details of a few weak lines are shown in Figs. 73 and 75. Detailed simulations with realistic spectra with SciSim should be performed for sources where a detection and/or separation of one or more emission lines is the main scientific goal. The background model in SciSim has been updated based on the above description.

3.4.7 RGS response

Various components may feature in the data from RGS observations, such as:

- Internal X-ray calibration source background:

  Four calibration sources permanently illuminate the CCD of the RFC. The emission is primarily in F-K and Al-K and care has been taken such that the energies of these lines do not coincide spatially with the equivalent energies in the diffracted spectrum (they are evident as four horizontal distributions in the bottom panel of Fig. 61). The source intensity is 0.1 counts $\mathrm{cm}^{-2}\ \mathrm{s}^{-1}$. Using both spatial and energy information, their contribution to the celestial spectra can be estimated.

- Optical load on the CCDs:

  This is caused by various optical straylight components. Detected optical photons will modify the gain calibration of the CCDs through an introduction of an additional energy offset. Using diagnostic mode data, these offsets can be measured.

- Background:

  This component is explained in detail in § 3.4.6. The diffuse cosmic X-ray background can be modeled assuming an isotropic spatial distribution. The soft-protons induced background is more difficult to remove, for point sources, it can be estimated by selecting a region on the CCDs in the cross dispersion direction and using the same windows in the CCD pulse height as for the source. The background estimation for spatially extended sources or low surface brightness sources (like clusters) is more problematic as it is not so simple to select an acceptable "empty" region in the cross dispersion direction. The average background described in section § 3.4.6 could be used for quiet periods, however, as some of the components (or model parameters) are

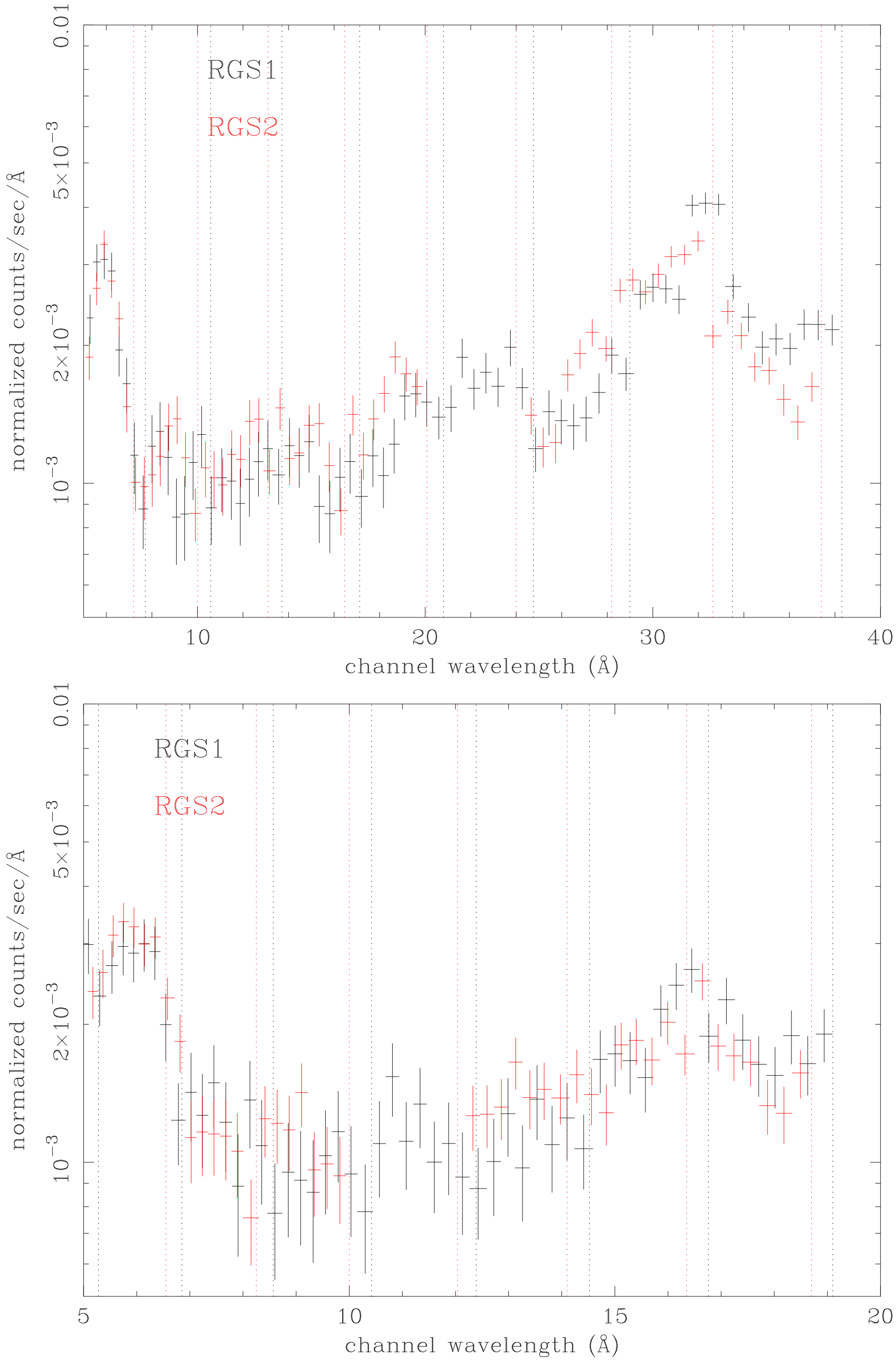

Figure 69: *The average quiet background spectra from first (top) and second (bottom) order regions.* **RGS** *-1. is shown in black,* **RGS** *-2 in red. Large errors in some channels are presumably due to small number of non-bad pixels within those beta channels. An enhancement of the count rate below 7 Å in each* **RGS** *is due to a change in the width of the pulse height filter at that wavelength. There are bumps around* ∼ 32 *Å in both* **RGS** *spectra. The origin(s) have not been fully understood but the most likely explanation is a somewhat higher dark current for CCD2 in both* **RGS** *instruments (they are the only two devices from an early lot).*

clearly variable, this is not a trivial task. The uncertainty of this method is estimated comparing the different "blank-sky" exposures used to obtain the average spectrum and it is about 30%. In some cases, EPIC data could be used to directly measure the background. As a different alternative, for extended, irregular, sources the user may consider the need for a particular position angle that could guarantee an "empty" background region in the cross dispersion direction.

- Apparent cross-talk between orders:

  The CCD response includes a low energy tail due to a finite number of photons producing anomalously low energy signatures. In the case of bright emission feature being measured in the second order spectrum, the intensity of this tail may become significant, as it may produce counts in the co-located first order spectrum. These effects can be easily identified in PHA or PI energy versus dispersion plane. (cf. Fig. 61).

- Effects of scattering by the gratings:

  Due to X-ray scattering off the gratings (about 20% at mid band), there is an additional tail of the LSF. While true source continuum emission follows the dispersion equation (the inverse relation between photon energy and wavelength), scattered light appears as an horizontal distribution in the pulse height versus dispersion plot (cf. Fig. 61). This effect can be modeled and is included in the response generator of the SAS and also in SciSim.

3.4.8 Operating modes of the RGS

All RGS CCDs are operated in the so-called "frame store" mode, in which half of each CCD is exposed to celestial radiation. The contents of this half is transferred to the second (shielded) half, which works as a storage area before readout, while the first half is acquiring the next frame. Thereby, the two-dimensional dispersed photon distribution is stored.

The standard science (data acquisition) mode of operation of the RGS instrument is called "**spectroscopy**". It consists on a 2-dimensional readout of up to all 9 CCDs over the full energy range resulting in an accumulation time of about 5.7 s (0.6 s per CCD). Currently, due to the operational failures of two CCD chains (i.e. RGS -1. CCD7 and RGS -2. CCD4), only up to 8 CCDs are readout per RGS instrument, with an accumulation time of about 4.8 s. Each RGS CCD is read out via two nodes.

Each individual chip (and any combination of chips) can be read out. The energy range covered depends on which CCDs are read out and on the position of the source within the field of view. A rough estimate of which energies are sampled if a given CCD (or combination of CCDs) is (or is not) read out is provided in § 3.4.2, Table 8 (e.g. the energy/wavelength ranges affected by the lost CCDs).

The on-chip binning (OCB) factor in this mode is 3×3 pixels. Then, a few more operations are performed on board to reduce the data rates to within the RGS telemetry bandwidth. After applying a low signal threshold, hot columns and hot pixels are rejected (defined by a look up table). The remaining pixels are treated by a programmable processor (DPP).

Pixels exceeding an upper signal threshold and pixels with too complex structures are rejected (these are due to cosmic rays), and only events which fit in a 2 × 2 pattern are transferred to the ground (including information on their shape).

For extremely bright sources, non-standard read out schemes can be employed, such as reading only a limited set of CCDs to reduce the pile-up or using a read out sequence like CCD 1, 3, 2, 3, 4, 3 etc. for some special timing purposes.

In parallel to the recording of science data, diagnostic images are transferred to the ground. One complete CCD of each RGS is read in this way every 1500 s. Then the on-board data processing is bypassed, and the entire CCD image (or "Q-dump") is transferred to ground. These data are used by the instrument and calibration teams for dark current and system noise level verification with the aim to identify possible instrument degradation with time and/ or changes affecting the health of the RGS instruments. The XMM-Newton guest observer has the possibility to use these frames to improve the calibration of the CCD offsets, e.g. in the case of visual light background.

The mode described so far is used for almost all the observations and it is the recommended configuration. However, for extraordinarily bright celestial sources with an expected RGS count rate larger than 70 counts s^{-1}, the **spectroscopy HCR** (High Count Rate) mode should be used. This mode is the same as the spectroscopy mode but without diagnostic frames being taken in parallel to reduce the telemetry rate.
Some basic characteristics of the RGS science modes are listed in Table 9.

3.4.9 RGS specific proposal submission information

In the preparation of RGS observing proposals, the following information should be taken into account. A few more instrumental effects, which partly also affect instruments other than the RGS, are listed in § 4.8.

Table 9: *The* **RGS** *science data acquisition modes*

Mode	**Description**
Spectroscopy	2-D readout of up to all 9 CCDs over the full energy range with a long duty cycle (5.7 s readout time); each CCD readout takes 0.6 s. 3 × 3 pixel OCB is applied. Some events are rejected on-board. See text for details. Diagnostic images are taken in parallel
Spectroscopy HCR	High count rate (i.e > 70 c/s). Similar to spectroscopy but no diagnostic images recorded

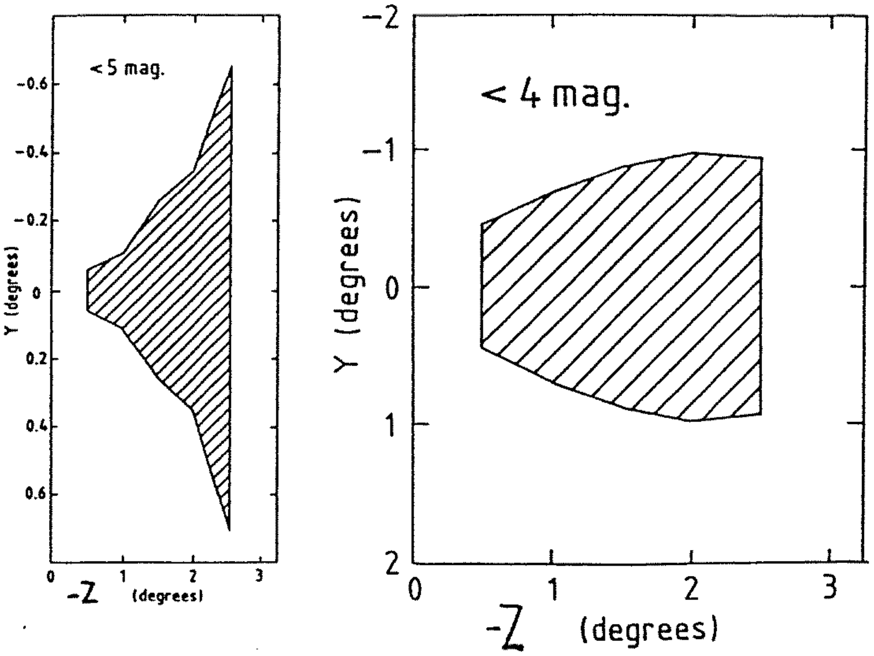

Figure 70: **RGS** *avoidance angles for sources brighter than 4 (5) optical magnitudes (right/left panel). -Z is the dispersion direction of* **RGS***, Y is the cross-dispersion direction.*

3.4.9.1 RGS avoidance angles

Visual light from bright sources can enter the RGS under certain angles. To avoid contamination of RGS observations, such sources must be avoided, with approximate avoidance angles as displayed in Fig. 70. Nearby (within 10′) bright X-ray sources should also not be located along the dispersion direction of the RGS during an observation in order to avoid spectral overlaps. Information on how to choose a position angle using SciSim in order to avoid bright sources is provided in § 4.4.

The choice of avoidance angles is entirely at the responsibility of the GO. Should an observation become too constrained due to these avoidance angles, GOs may consider violating these regions, depending on the scientific impact on their proposal.

3.4.9.2 RGS spectral quality

Examples of dispersed RGS spectra of are given in Figs. 71–79. A few of the main emission lines are indicated in some plots. A significant fraction of the apparent continuum background measured underneath the Fe-L forest, is due to scattered light. This is included in the response matrix of the instrument, which has to be used to determine the underlying spectral properties.

3.4.9.3 RGS flux to count rate conversion

For the conversion of flux to RGS count rates or of count rates from other X-ray satellites to count rates expected for the different **XMM-Newton** detectors, we recommend

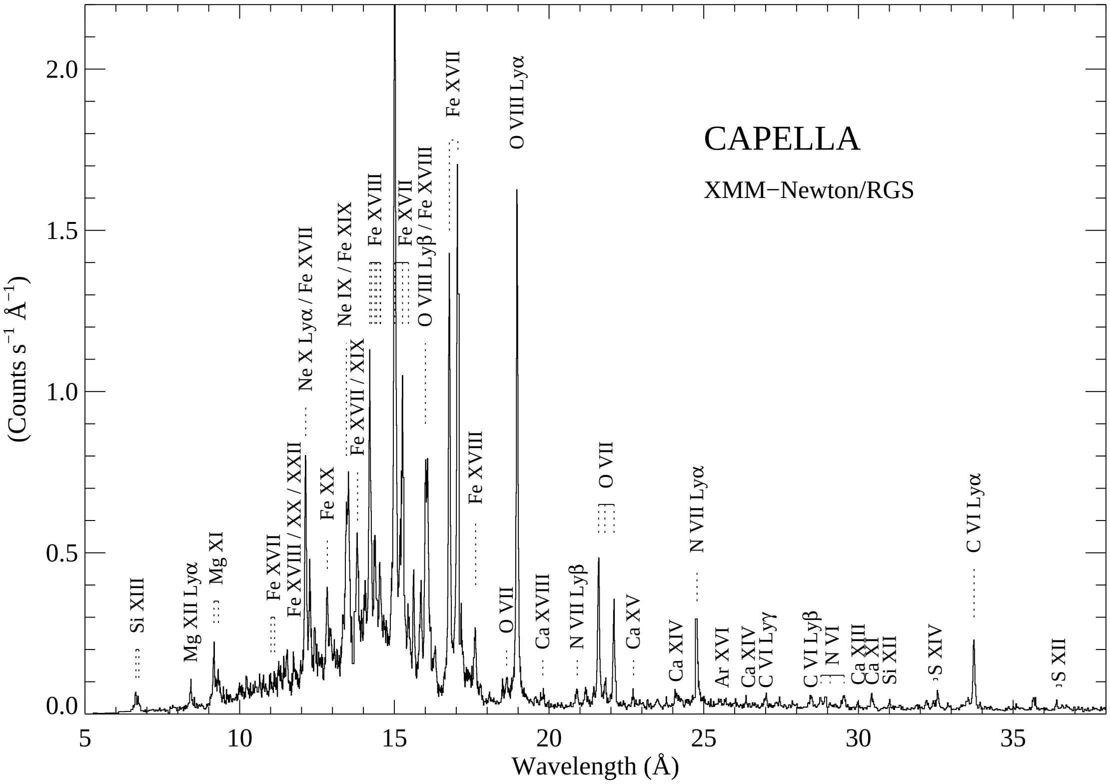

Figure 71: *Coronal spectrum of the binary star Capella. The* **RGS** *-1 first order spectrum is shown with some line identification labels. The total exposure time is 53 ks (adapted from Audard et al. 2001, A&A 365, L329)*

the use of the SAS task rgsrmfgen to generate a response matrix (rmf) to be used for simulations and /or the use of the *PIMMS* software at NASA's HEASARC (at the URL `http://heasarc.gsfc.nasa.gov/Tools/w3pimms.html`).

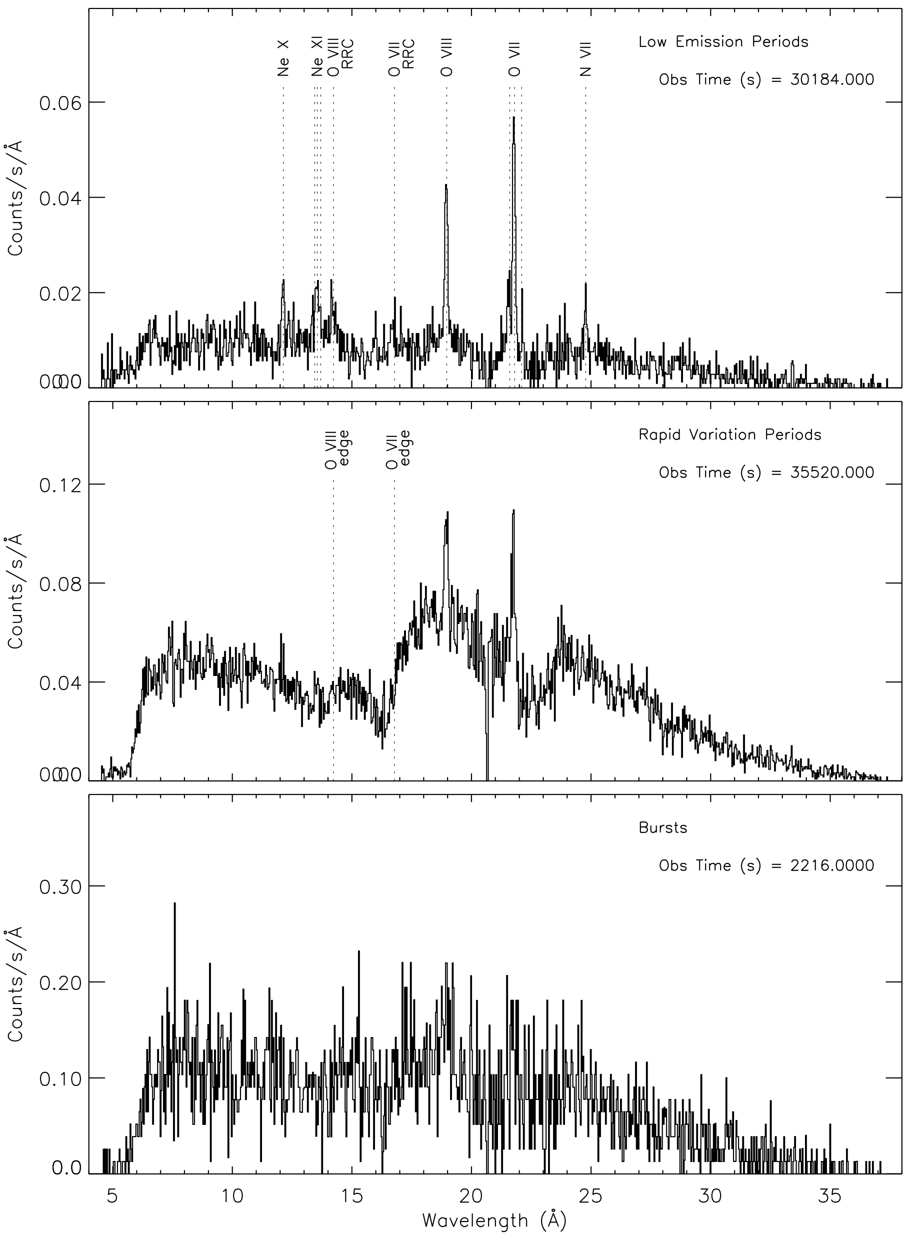

Figure 72: **RGS** *spectra of the highly variable low-mass X-ray binary EXO 0748-67. The three panels show the spectra for three different activity states (low emission, active variation and burst). The spectra are binned to 0.035 Å per bin. The cumulative exposure time for each spectrum is indicated (Cottam et al. 2001, A&A 365, L277)*

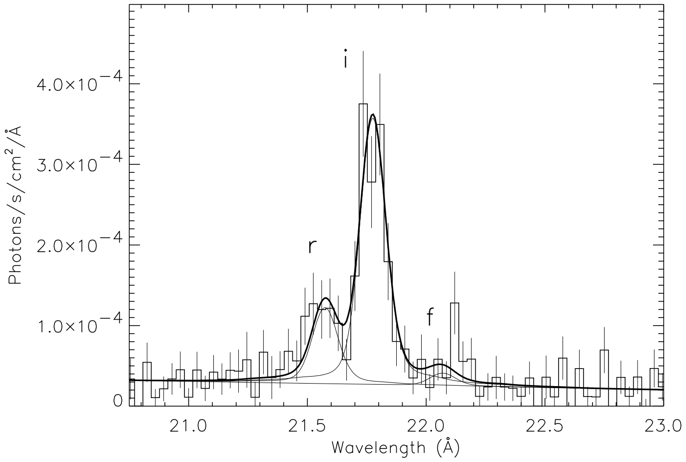

Figure 73: *Detail of the EXO 0748-67* **RGS** *spectrum. The* O VII *He-like lines are shown overlaid with the instrument line spread function, broadened to account for a 1390 km* s^{-1} *velocity field. The contributions from the resonance line (r), intercombination lines (i), and forbidden line (f) are shown with thin lines. The thick line shows the combined fit (Cottam et al. 2001, A&A 365, L277)*

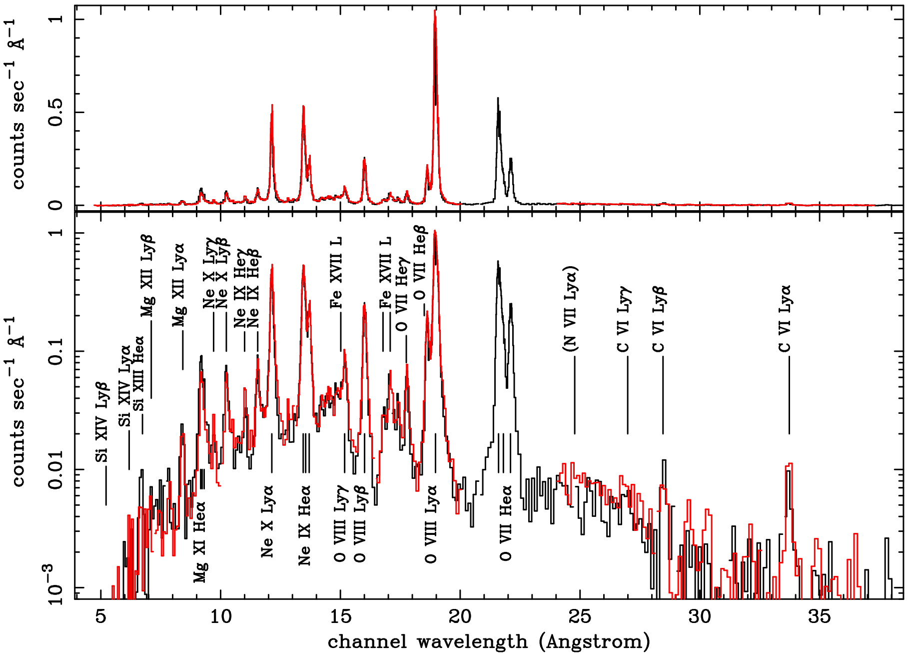

Figure 74: *The first order* **RGS** *spectrum of the supernova remnant 1E 0102.2-7219, located in the Small Magellanic Cloud. The effective exposure time is 29.7 ks for each* **RGS** *, after selection of low background periods in a 37.9 ks exposure.* **RGS** *-1 is plotted in black,* **RGS** *-2 in red. The data are provided in both linear and logarithmic scales. This figure and the next one show that almost the nominal* **RGS** *spectral resolution can be achieved even for moderately extended ($\Delta\theta \sim 2'$) objects (Rasmussen et al. 2001, A&A 365, L231)*

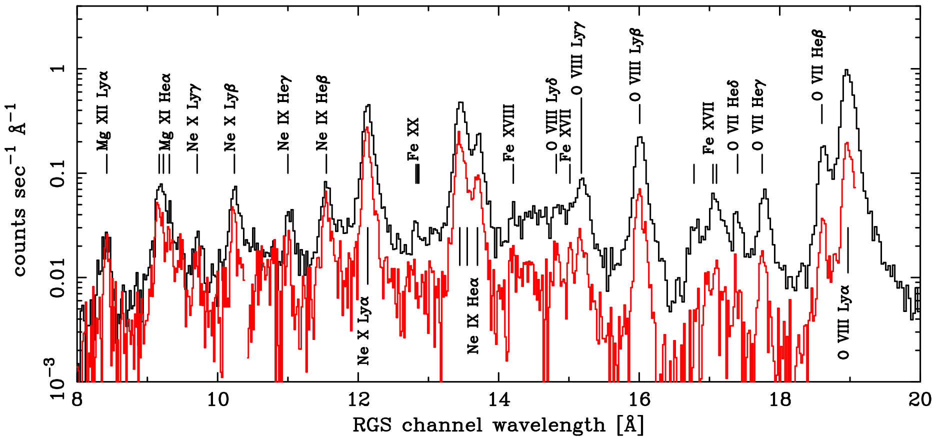

Figure 75: *Detail of the 8–20 Å region of the spectrum shown in the previous figure. First (black) and second (red) order are plotted separately. The data from the two spectrometers have been averaged for each order extraction. The higher spectral resolution and resilience to source extent is clearly seen in second order, where some line complexes blended in first order are resolved (Rasmussen et al. 2001, A&A 365, L231)*

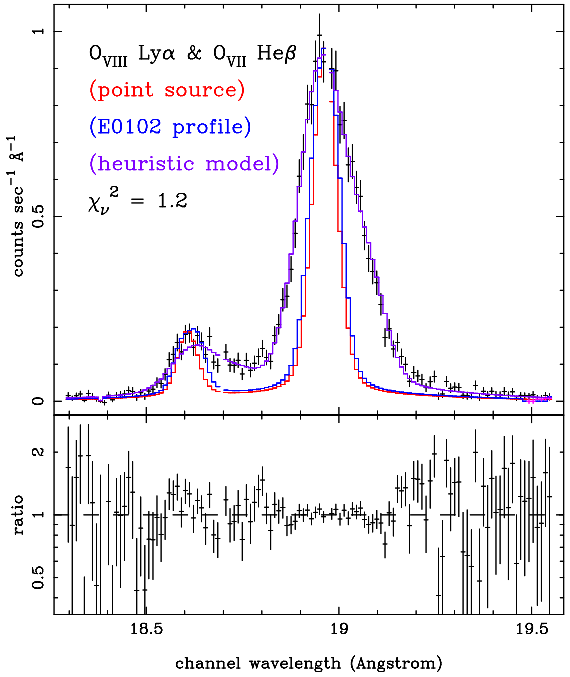

Figure 76: *Detail of the oxygen line profile in the 1E 0102.2-7219 spectrum (cp previous two figures) The plot compares the point source line spread function for* **RGS** *-1, the approximate monochromatic line profile based on the target's angular distribution and an heuristic wavelength broadening template function that is applied in addition to the angular distribution (Rasmussen et al. 2001, A&A 365, L231)*

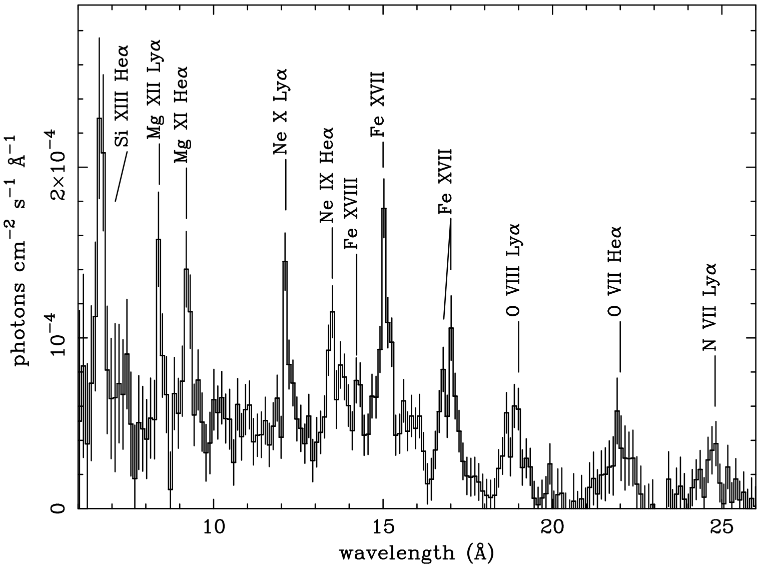

Figure 77: *The* **RGS** *spectrum of the bright starburst nucleus of the nearby edge-on galaxy NGC 253, binned to 0.07Å per bin. The effective exposure time is* ~ 53.4*ks for each spectrograph, after selection of low background periods. The extraction region is 1′ along the minor disk axis. (Pietsch et al. 2001, A&A 365, L174)*

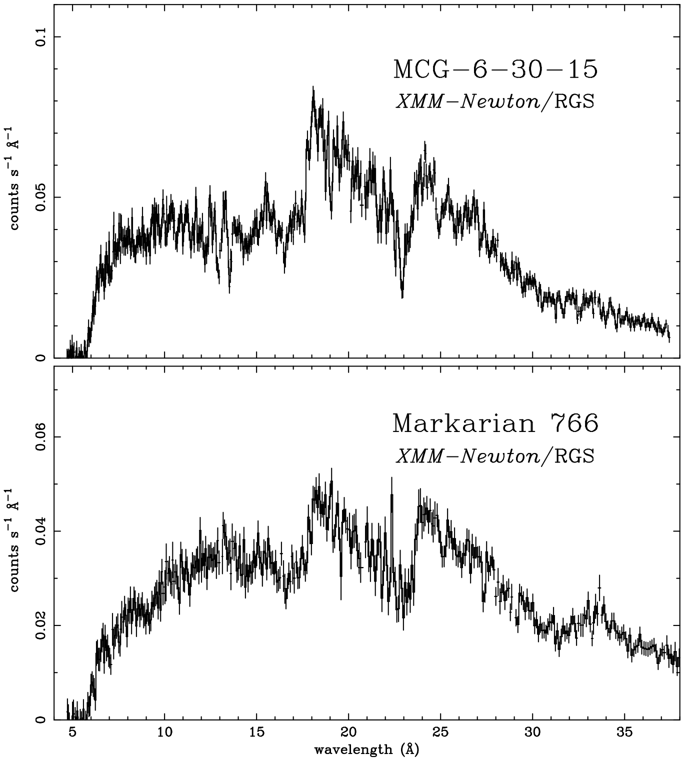

Figure 78: *The* **RGS** *spectra of two bright, nearby, Narrow Line Seyfert 1 galaxies. MCG–6–30–15 (top) was observed for a total of 120 ks while Mrk 766 (bottom) exposure time is 55 ks. (Branduardi-Raymont et al. 2001, A&A 365, L140)*

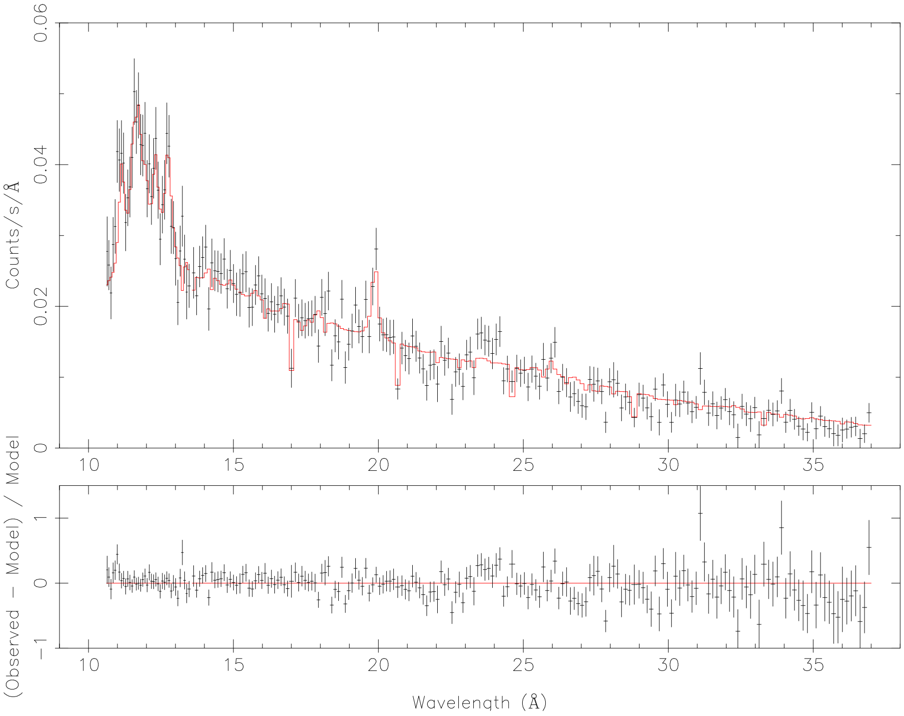

Figure 79: **RGS** *spectrum of the rich cluster of galaxies Sérsic 159-03 (Abell S 1101). The effective exposure time is 36 ks. The plot also shows in red a fit with a two components cooling flow model. Note the redshifted O*VIII *Lyα line at 20.0Å and the Fe* XXIV*, Fe* XXIII *and Ne* X *lines between 11.2 and 12.8 Å(Kaastra et al. 2001, A&A 365, L99)*

3.5 OPTICAL MONITOR (OM)

Besides its three X-ray telescopes, **XMM-Newton** also has a co-aligned 30-cm optical/UV telescope (OM), providing for the first time the possibility to observe simultaneously in the X-ray **and** optical/UV regime from a single platform. A summary of OM's salient properties is provided in Tab. 10. Although small in size, the OM is a powerful instrument because of the absence of atmospheric extinction, diffraction and background. It can obtain simultaneous optical/UV observations of sources in the field of view in the waveband from 160 to 600 nm. Imaging over the central part of the X-ray field of view with a resolution of ca. $1''$ (depending on instrument configuration), low-resolution grism spectra of X-ray sources optical counterparts or high time-resolution photometry can be obtained. Due to the extreme sensitivity of its detectors, the OM cannot be used for observations of optically bright sources ($m_V \leq$ ca. 7.4 mag, for an A0 star with the V filter).

3.5.1 OM telescope

The OM telescope consists of an $f/12.7$ modified Ritchey Chrétien optics (see schematic in Fig. 80). From the primary mirror incoming light is reflected onto a secondary, from where it is reflected onto a rotatable 45° flat mirror located behind the primary, which can direct the beam onto one of two detector assemblies operated in cold redundancy.

Table 10: *OM characteristics – an overview*

Total bandwidth^1	160 – 600 nm
Spectral bandwidth^2	160 – 550 nm
Sensitivity limit^3	23.5 mag
Field of view	ca. $17'$
PSF (*FWHM*)	$1.6''$–$2.3''^4$
Timing resolution^5	0.5 s
Spectral resolution^6	0.5/1.0 nm
Spatial resolution	0.5/2.0"
Brightness limit^7	$m_V = 7.4$ mag

Notes to Table 10:
1) See Fig. 85 for filter bandpasses.
2) Covered by two grisms.
3) 6-σ detection of an A0 star in 1000 seconds; see Table 17 for expected integration times on three stellar types.
4) Depending on the filter
5) In the Fast Mode.
6) With the UV and optical grism, respectively.
7) Highest magnitude of a star, which can be observed with the OM without exceeding the instantaneous maximum flux. This *brightness limit* is dependent on the filter and the spectra type. The number quoted in Tab. 10 refers to an A0 star with the V filter; see also Tab. 20. The *dose limit* is instead related to the total amount of photons detected during a whole exposure.

3.5.2 OM detector

The OM is operated as a photon-counting instrument. Each of the (redundant) OM detectors has a format of 2048×2048 pixels, each about $0.5'' \times 0.5''$ on the sky. The field of view is therefore $1024''$ on a side, or $17' \times 17'$. The light-sensitive surface is an S20 photocathode optimized for the UV and blue. This provides sensitivity from 160 nm (set by the detector window) to 600 nm.
The internal noise (dark noise) of the detectors is extremely low. However, in the UV the Galactic diffuse background amounts at about 7% of the rate seen in darkframes. It can generally be ignored by comparison with other, cosmic sources of background, although it may play a rôle for diffuse faint sources (*e.g.*: diffuse galactic light).
The OM detectors consist of a micro-channel plate (MCP) intensified CCD (MICs) with 384×288 pixels, 256^2 of which are usable for science observations. Each CCD pixel has a size of $4'' \times 4''$ on the sky. Photons coming from the 45°-mirror enter the detector and hit the photo-cathode, from where electrons are pre-amplified by three successive MCPs (Fig. 81). This leads to an amplification of the signal by a factor of ca. 10^5. The detector achieves a large format through a centroiding technique, subsampling the 256^2 CCD pixels into 8×8 pixels each, as described in the following.

3.5.2.1 Imaging with OM

As mentioned above and shown in Fig. 81, photons entering the OM detector hit a photocathode, which is located at the backside of the detector entrance window. Electrons emanating from the photo-cathode are amplified by the MCPs, creating photon splashes at the location of the OM CCD. The detection of a photon entering the detector is performed by reading out the CCD and determining the photon splash's centre position using a centroiding algorithm, which is part of the onboard software. In the process of centroiding a grid of 8×8 "in-memory" pixels is defined, leading to an array of 2048×2048 in-memory pixels with an approximate size of $0.5''$ on the sky. In the resulting images at some level there is always a pattern repeating on an 8×8 grid, resulting from a limitation in the algorithm. This can be removed by subsequent processing on ground.
As with all photon-counting detectors, there is a limit to the maximum count rate achievable before saturation sets in. The frame time[6] of the OM detectors is about 13 ms at slowest, so a linearity correction must be applied in the offline data processing for count rates above ca. 10 counts/s for point sources. Both *deadtime* and *coincidence losses* contribute to the non-linearity of the OM detector. Deadtime losses are due to the lack of instrumental response during a frame transfer. Coincidence loss is observed whenever the count rate is such that more than one photon arrive in the same pixel within a given readout frame. Deadtime becomes important for short framerate. On the other hand, longer framerates are more likely affected by coincidence losses. These effects are quantitatively described in § 3.5.6.
In addition, sources which are too bright can depress the local sensitivity of the photocathode: this is a cumulative effect, so that fainter sources observed for long times have the

---

[6] It is defined *frametransfer time* the time needed to transfer the charge accumulated on the continuously exposed CCD during an integration time into the storage area. It amounts to $\simeq$0.1728 ms. The sum of the frametransfer time and of the time needed to read out all the pixels in the storage area is the *frametime*. The frametime depends on the sizes, shapes and positions of the windows. For a full frame it amounts to about 11 ms. The only time when source photons are not properly recorded by the detector is during charge transfer. Therefore, the *deadtime* is equal to the frametransfer time.

Table 11: *The science data acquisition modes of OM*

Mode[1]	**Special feature**
Imaging	Mosaic of 2-D imaging windows with long exposure times (> 800 s)
Fast	High time resolution, providing 2-D time-sliced images over small areas.

Notes to Table 11:
1) Both modes can be used simultaneously, as long as total memory capacity and telemetry bandwidth are not exceeded.

same effect as brighter sources observed for shorter periods. This places some operational constraints on the instrument. Pointing of bright sources may also yield ghost images in subsequent observations due to fluorescence.

Cosmetically, the OM detectors are good, with few hot or dead pixels, and little global variation in quantum efficiency. There is a small-scale granularity on the photocathode, which can be removed by flat-fielding in the ground processing. To some extent, the granularity (and the 8×8 pattern mentioned above) is smoothed by the spacecraft drift.

3.5.3 OM windows and field of view

While the OM can access a large part of the field viewed by EPIC, there are limitations on what can be observed in an exposure. These limitations are set in the first place by the amount of on-board memory, and secondly by the telemetry rate allocated to the instrument. Because of constraints on the telemetry rate available, it is not possible to transmit the full data on every photon that the OM detects. Instead a choice has to be made between image coverage and time resolution. The observer can therefore choose up to 5 "windows", of which up to two may be operated in the "fast" mode (see § 3.5.3.1, below). These can be placed where required, with restrictions as identified in § 3.5.10.

In addition to these windows, the instrument assigns itself several small windows for tracking guide stars (§ 3.5.10). The tracking information is included with the other science data.

In general, an observation with the OM will consist of a sequence of exposures in different filters and/or with a sequence of different window setups to cover the full field of view.

A set of default OM window configurations is available: these will generally be satisfactory for most proposals.

For details on the intricacies of non-default OM window choice and the applicable restrictions, please refer to § 3.5.10.2.

3.5.3.1 OM operating modes

The OM can operate in the two modes listed in Table 11. These allow either imaging or fast photometry or both simultaneously.

- Imaging mode

  The *Image Mode* emphasizes spatial coverage at the expense of timing information. Imaging can be performed with different pixel sizes. The tradeoff is that the images with unbinned pixels take more memory and more telemetry, and therefore the windows must be small or the subsequent exposure long in order to allow the instrument memory to empty. Images can be taken at the full sampling of the instrument or binned by a factor of 2 or 4, to yield a resolution element on the sky of approximately 0.5, 1.0 or 2.0 arc seconds. The maximum total size of the science windows is determined by the memory available in the DPU. A single Image Mode window binned by a factor 2×2 can be up to 976×960 detector pixels, which results in a 488×480 binned pixel image being stored in the DPU. At full sampling (with no binning) the window can be up to 652×652 pixels. Any drift in the pointing direction of the spacecraft is corrected in the image by tracking guide stars.

The maximum allowed integration time for an OM imaging mode exposure is 5 ks. Since the OM in its imaging mode produces accumulated images, there is no timing information attached to individual incoming photons.

- Fast mode

  The *Fast Mode* emphasizes timing information at the expense of spatial coverage. In its Fast Mode, the OM does not produce accumulated two-dimensional images, but instead produces event lists like the X-ray instruments. This mode is useful for monitoring rapidly variable sources, for example AGN or accreting binaries. Two small windows can be assigned, each of a maximum of 512 pixels only. Thus the maximum size of an approximately square window would be 22×23 pixels (= 506 total). There is no binning within a Fast Mode window. The pixel locations of individual photons within the window are recorded and assigned a time tag, which has a user-specified integration time of between 500 ms and the tracking frame duration (10–20 s). No tracking correction is applied to Fast Mode data. This can be applied on the ground, from the drift history supplied by the OM. The data are obtained by default in 0.5 s time slices, each preserving the pixel information. Shorter times are in principle possible, but at the risk of overloading the DPU (*e.g.* when two Fast Mode windows are operated), and are therefore discouraged.

  The maximum allowed integration time for one fast mode window is 4.4 ks, and 2.2 ks each if two are used simultaneously.

Each mode has a specific **overhead**, *i.e.* time needed for the instrument set-up, before the actual science exposure can start. For both the above OM modes this overhead includes also the reference frame exposure. The reader is referred to § 4.5.2 for a general discussion of the impact of instrumental overheads on the planning of an **XMM-Newton** observation.

3.5.3.2 OM default configurations

To ease the use of the OM and to maximize the scientific yield of observations in cases when no particular instrument configuration is requested, OM default configurations have been defined. There is one type of default configuration per OM observing mode, thus one for the imaging mode and one for the fast mode (§ 3.5.3.1). Moreover, two additional full frame mode will be available starting from the AO2, which allow imaging observation of the whole OM field of view. Finally, default windows for the grisms have been defined.

The default configurations are as follows:

1. Imaging Mode default (`EPIC/RGS Image` in the RPS)

   - Imaging with (default) 2 × 2 in-memory pixel binning ($1.0''$ pixels).
   - A setup of 5 consecutive exposures per filter, covering 92% of the total ($17' \times 17'$) OM FOV.
   - In each of the 5 exposures per filter a large fraction of the FOV will be covered by one large window, while a second, smaller imaging mode window at 0.5"×0.5" spatial resolution ensures continuous monitoring of the prime target (at the centre of the FOV; see Fig. 82).

   An example of the configuration corresponding to this mode is shown in Fig 83.

2. Fast Mode default (`EPIC/RGS Image Fast` in the RPS)

   - Window configuration as under 1.
   - An additional central window is operated in the OM fast mode. Its size is 22 × 23 in-memory pixels ($11'' \times 11.5''$). The user is recommended to carefully check the accuracy of the target coordinates, to avoid substantial flux losses.

3. Full-Frame imaging modes (`Full Frame High/Low Resolution` in the RPS)

   New modes will be available starting from the AO2 to obtain images of the whole OM field of view in full (high) or 2×2 binned (low) resolution. These modes do not allow tracking, and have higher instrumental overheads than the Imaging Mode default. However, they allow an homogeneous sampling of the whole OM field of view. They are therefore particularly well suited for survey studies, to obtain multiobject grism spectroscopy in a wide field, or if time resolution is not a critical issue in a given OM observation. They cannot be combined with other windows (either in image of fast mode) within the same exposure. They *can* be combined with modes requiring tracking in the same OM observation, but if and only if the Full-Frame exposure is performed *after* all the exposures which need tracking (see Sect. 3.5.7), because Full-Frame modes annihilate the results of tracking.

4. Default grism configurations

   Two default configurations will be available for a user interested to use OM optical or UV grism:

   - a predefined window, which contains the spectrum of the target (with its 0th order) at full detector resolution (`TBN` in RSP)
   - a Full Frame Low Resolution exposure, which provides the spectra of all the targets in the OM FOV, with degraded spatial (and hence spectral) resolution

   It will still possible for OM users to define customized windows (see § 3.5.10.2)

Within a default configuration observation, OM users can specify their choice of filter(s) and exposure times.

3.5.3.3 Integration time for exposures

To achieve the best possible efficiency in the use of the limited hardware capabilities, **an integration time of at least about 1 ks is recommended for each exposure**. With a setup of 5 exposures per filter, this leads to 5 ks duration per default observation with one given filter. Note that longer integration times per exposure are allowed (§ 3.5.3.1). We remind, however, that the maximum allowed exposure times per exposure are: 2.2 ks for the Fast Mode, if two Fast Mode windows are in use; 4.4 ks for the Fast Mode, if one Fast Mode window is in use; 5 ks for the Image Mode. Shorter exposure times are limited by the OM telemetry allocation vs. required downlink time as described in § 3.5.10.2. The current limits are: 800 s for the Image Mode and 1200 s for the Fast Mode.
There are in principle no constraints on the exposure time in Full Frame Low/High Resolution Modes. However, it is advisable not to exceed 5000 seconds, to avoid potential onboard memory corruption after interaction of cosmic rays with the camera, or counter wraparound. Tab. 12 summarizes the integration time constraints:

3.5.3.4 Filter choice

For maximum scientific yield (including the consideration of creating a useful archival database), **the use of the following filters is recommended**:

1. B (first choice)
2. UVW2 (second choice)
3. U (third choice)
4. UVW1 (fourth choice)

A different set of filters for observations in the OM default configuration may be chosen by the user based on scientific considerations. However, **the sequence in which the filters are used must comply with the instructions provided in § 3.5.5.1**. The four filters listed above would be used in the sequence U, B, UVW1 and UVW2.

3.5.3.5 Some examples

Example 1: With an exposure time of 1 ks, an observation using the imaging default mode (with 5 exposures) takes 5 ks (per filter). To this number an overhead of ∼1.7 ks must be added. In order to be able to use two filters, at least 13.4 ks of total observing time (as determined by the feasibility of the planned X-ray observations) are needed. Conversely, if 10 ks are available, only one filter can be used. In facts, even if the available integration time were equally distributed between two filters, each exposure should have an exposure time of ∼660 seconds, which is below the minimum allowed (cf. Tab. 12).

Table 12: *OM exposure time constraints*

Science window configuration	Minimum (s)	Maximum (s)
Only Image Mode windows	800	5000
Image Mode + 1 Fast Mode windows	1200	4400
Image Mode + 2 Fast Mode windows	1200	2200

Table 13: *OM on-board PSF FWHM in different lenticular filters*

Filter	FWHM (″)
V	1.6
B	2.0
U	2.3
UVW1	1.7
UVM2	2.0
UVW2	2.3

Example 2: A 20 ks X-ray observation allows the usage of four imaging default mode OM exposures, only if the overheads associated with the X-ray cameras are longer then 2.8 ks: [(800 s×5)+1700 s]×4 = 22800 s. In this case the preferable filter choice is: U, B, UVW1 and UVW2, unless science needs suggest otherwise

Example 3: the overhead for an exposure in Full Frame High Resolution Mode is 2600 s. Within 20 ks of available elapsed time, at most 3 exposures of ∼4050 s each can be accommodated: [3×(4050 s+2600 s)]≃19950 s.

Example 4: Users interested in U, B, V photometry would choose the filters in the order V, U and B. In order to reach similar limiting magnitudes within a total observing time of 20 ks, two default mode imaging observations with the V filter (requiring 10 ks) and one each with the U and B filter (in that order) can be chosen (cf. § 3.5.5.1). Even better, instead of choosing two 1 ks integrations in the V filter, 2 ks exposures may be defined. This choice actually minimizes the instrumental overheads.

3.5.4 Optical/UV point spread function of the OM and tracking

The OM telescope produces images on the detector which are nominally diffraction-limited over the field of view (ca. 0.35″ at 400 nm, decreasing with increasing wavelength). However, this is convolved with the somewhat larger detector resolution. Nonetheless, this image quality is much better than that obtained with the X-ray instrumentation. The OM onboard software calculates the spacecraft drift from guide stars in the tracking windows and continually corrects the incoming photons from the detector to register them correctly in the accumulating image ("shift & add" in-memory). This can be done only in steps of an integral number of pixels, so some further broadening (on the scale of another 0.5″) still occurs.
The on-board measurement of the PSF for different filters is shown in Fig. 84 and Tab. 13. Measurements are based on the observation of the GD153 field, performed during revolution #90. The FWHM values refer to a fit with a single Gaussian.

3.5.5 OM optical elements

The OM is equipped with a filter wheel holding several optical elements that can be moved into the light path. These elements, which are described here, comprise not only lenticular filters, but also two grisms. The complete set of optical elements is collected in Tab. 14. Their arrangement on the OM filter wheel is indicated by the position number on the filter wheel. **Sequences of exposures using different optical elements must**

always have increasing filter wheel position numbers. Observations with the three optical broad-band filters U, B and V, for example, must always be conducted in the order V, U and B (positions 1, 3 and 4).

Table 14: *OM optical elements*

Filter wheel position number	**Filter name**
0	Blocked
1	V
3	U
4	B
5	White
6	Grism 2 (visible)
7	UVW1
8	UVM2
9	UVW2
10	Grism 1 (UV)

3.5.5.1 OM filter bandpasses

The OM is equipped with a set of filters with bandpasses covering part of the UV and optical range. The filter throughput curves are displayed in Fig. 85. The plotted quantity is the OM effective area for a given filter including the entire telescope response based on inflight measurements. Aperture radius is 6" for the optical, and 17.5" for the UV filter. Preliminary zeropoints are listed in Tab. 15.
The Magnifier filter will **not be available** in AO2.

3.5.5.2 OM grisms

In addition to the filters, the OM filter wheel holds two grisms. The throughput of the OM grisms depends on wavelength. This, folded with the OM detector response, is displayed in Fig. 86. Only one grism can be used at any time, because they are mounted – together with the other optical elements (see Table 14) – on the OM filter wheel.

Table 15: *Zeropoints for various OM filters*

Filter	Zeropoint (Magnitudes)
V	18.1071
B	19.2761
U	18.2389
UVW1	17.3716
UVM2	16.0169
UVW2	15.1650

The spectral resolution of the grisms is almost constant over their wavelength ranges. The UV grism has a spectral resolution of ca. 0.5 nm per 1″ pixel, the optical one of 1 nm per pixel. The grisms can thus be used for moderate resolution optical and UV spectroscopy in conjunction with the X-ray observations. As an example of the visual grism flight performances, the spectrum of the white dwarf BPM 16274 is shown in Fig. 87. An image of the target area should be taken for identification of spectral sources prior to or after obtaining spectroscopic exposures with a grism.

The optical grism is blazed and the zeroth order image are relatively weak. The UV grism is not blazed, however, and ca. 1/3 of the light is expected to go into the zeroth order image, which is expected to be visible near the edge of the FOV when the first order spectrum is centered.

3.5.6 OM sensitivity and detection limits

Both Fig. 88 and Tab. 16 provide the expected count rate of the OM, in counts per second, for $m_V = 20$ mag stars of various types, with the different filters introduced above. These numbers were obtained under the assumption of a perfect, i.e., deadtime-free and coincidence loss-free, detector, and with an aperture radius of 6” (17.5”) for optical (UV) filters.

Table 16: *OM count rates [10^{-4} counts/s] as function of spectral type for stars with $m_V =$ 20 mag under the assumption of a zero deadtime detector*

Filter	**B0V**	**A0V**	**F0III**	**G0III**	**G2I**	**K0III**	**M0III**
V	1759	1748	1730	1698	1689	1677	1642
B	6896	4933	3856	2636	2091	1979	1102
U	9327	2030	1410	889	498	385	85.4
UVW1	6972	864	395	198	91.6	61.5	10.4
UVM2	2973	230	45.3	8.72	2.59	0.52	0.058
UVW2	1493	105	16.9	2.85	1.02	0.46	0.21

The numbers listed in Tab. 16 can be used to calculate the expected count rates of stars of given magnitude, C_{mag}, by the formula

$$C_{mag} = C_{20} \times 10^{0.4\times(20-b_{mag})} \quad , \tag{3}$$

where C_{20} is the count rate of an $m_V = 20$ mag star, b_{mag} is the magnitude of the target of interest and C_{mag} is the count rate of a star with $m_V = b_{mag}$.
However, OM deadtime and coincidence losses must be taken into account. The correction is approximated by the following formula:

$$C_{mag} = \frac{\log(1 - C_{det} * T)}{T_{ft} - T} \tag{4}$$

where C_{mag} is the count rate of incident photons from equation (3), C_{det} is the actual measured count rate, T is the CCD frametime in units of seconds and T_{ft} the frame-transfer time in the same units. The frame time is a function of the OM science window configuration, as described in § 3.5.3. In this context a conservative value for the OM

Table 17: *Required exposure times for different types of stars with* $m_V = 23$ *mag*[1]

Filter	**Spectral type**		
	B0	**A0**	**G0**
U	548	2068	4609
B	858	1027	1792
V	4421	4531	4707
UVW1	702	4207	17786

Notes to Table 17:
1) In seconds, for a 5-σ detection. Numbers obtained adopting a zodiacal light level of 100 S10 units, where S10 is the brightness of one $m_V = 10$ mag A0 star per square degree.

CCD frametime is 12.9 ms. An optimum aperture radius of 6″ was found to be the radius at which the loss correction formula is self consistent. At this radius its accuracy is at a level of 5% between different frame times.
In Fig. 89 a comparison between formula (4) and the inflight instrument performance is shown. The ratio between the theoretical curve (*red*) and the best fit (*blue*) can be parameterized as a 4^{th} order polynomial function in $x \equiv C_{det} \times T$: $1 - 0.076x + 0.144x^2 - 0.64x^3 + 0.57x^4$.
For the 20th magnitude stars in Fig. 88 and Tab. 16, OM coincidence losses are negligible. Losses become significant for a point source at a count rate of about 10 counts s^{-1} (about 10% coincidence).
In Tab. 17 estimates of required OM integration times for 23rd magnitude stars are provided. The values listed are the integration times, in seconds, for a 5-σ detection.
Tab. 18 tabulates the limiting magnitudes that can be detected by OM in an integration time of 1000 s at the 5-σ confidence level.

Table 18: *Limiting magnitudes for a 5-σ detection in 1000 s*[1]

Filter	**Spectral type**			
	B0	**A0**	**G0**	**K0**
V	21.4	21.4	21.3	21.3
B	23.2	23.0	22.4	22.1
U	23.7	22.2	21.4	20.5
UVW1	23.4	21.4	19.9	17.8

Notes to Table 18:
1) Numbers obtained adopting a zodiacal light level of 100 S10 units.

The expected levels of different external background radiation processes in the optical/UV are tabulated in Table 19. The background count rate in the OM is dominated by the zodiacal light in the optical. In the far UV the intrinsic detector background becomes important. Images are regularly taken with the blocked filter and no LED illumination to measure the detector dark counts. The mean OM dark count rate is 2.56×10^{-4} counts s^{-1} pixel^{-1}. The variation across the detector is ±9%, with a mainly radial dependence, being highest in an annulus of about 8″ radius and lowest at the center. Variation as a function of time are ±7%, without any apparent trend. However, if a very bright star is in the field of view the dark rate can be up to ≃60% higher than normal,

despite the use of the Blocked filter.
Artifacts can appear in the **XMM-Newton** OM images due to light being scattered within the detector. These have two causes: internal reflection of light within the detector window and reflection of the off-axis starlight and background light from part of the detector housing.
The first of these causes a faint, out of focus ghost image of a bright star, displaced in the radial direction away from the primary image (see Fig. 90). The second effect is due to light reflecting off a chamfer in the detector window housing. Bright stars that happen to fall in a narrow annulus $12.1'$ to $13'$ off axis shine on the reflective ring and form extended loops of emission radiating from the center of the detector (see Fig. 91). Similarly, there is an enhanced "ring" of emission near the center of the detector due to diffuse background light falling on the ring.
These features are less prominent when using UV filters, due to the lower throughput.

3.5.7 OM Field Acquisition

At the start of each science observation a 20 seconds V-filter image is taken to allow proper identification of the field stars with respect to the uploaded guide stars. Shifts are applied on board, whenever necessary, to align the guide star and the OM detected star patterns. This short exposure is defined *Field AcQuisition* (FAQ). A correct (*i.e.*: within a few arcseconds) FAQ is indispensable for, *e.g.*, a proper placing of the Fast Mode windows.
On-flight experience demonstrates that the FAQ is properly working on the overwhelming majority of the fields. However, a few cases have been observed, where the FAQ fails, and no shift is consequently applied. On "pathological" fields as crowded areas (clusters, groups) or fields with only a few uploaded guide stars the FAQ is more likely to fail.
The *XMM-Newton* PIs must be aware that no compensation is granted if the FAQ failure yields an impact on the scientific outcome of a given observation.

3.5.8 OM distortion

The **XMM-Newton** OM optics, filters and (primarily) the detector system result in a certain amount of image distortion. This effect can be corrected with a "distortion map", by comparing the expected position with the measured position for a large number of stars in the OM field of view. A V-filter analysis has been performed on the LMC pointing. The effect of applying this correction is shown in Fig. 92. A positional r.m.s. accuracy

Table 19: *Levels of different OM background contributors*

Background source	**Occurrence**	**Count rate range**[1]
Diffuse Galactic	all directions	0.072–0.0006
Zodiacal[2]	longitude 90° ± 20°	$0.212–2.6\times10^{-5}$
Average dark count rate[3]	all directions	2.56×10^{-4}

Notes to Table 19:
1) In units of [counts s^{-1} arcsec^{-2}].
2) In differential ecliptic coordinates, i.e., the angle between the Sun and the pointing position of **XMM-Newton**. Maximum is for l,b = 70,0 in the white filter, minimum is for l,b = 110,70 in the UVW2 filter.
3) In units of [counts s^{-1} pixel^{-1}]

Table 20: *The m_V brightness limits for all OM filters. An A0 type star spectrum is assumed*

Filter	Max. m_V
V	7.4
U	7.6
B	8.5
White	9.7
UVW1	6.6
UVM2	5.2
UVW2	4.4
Grism 2 (opt.)	9.6
Grism 1 (UV)	8.7

of 1″ is obtained. The preliminary distortion map has been entered into the appropriate CCF file and can be used in conjunction with SAS.

3.5.9 OM brightness and dose limits

To avoid damage of the OM photocathode, the maximum allowed source brightness is set to a count rate of ∼ 19000 photons/s, corresponding to an m_V= 7.4 mag A0 star in the V filter. The equivalent brightness limits for the other filters and optical elements are tabulated in Table 20. For calculating the brightness limits an A0 type spectrum was assumed. Similarly, a maximum count rate of 190000 photons/s is allowed during the V-filter field acquisition at the start of observation. Moreover, the maximum allowed dose during an OM exposure is 10^9 photons in the innermost 2", and 5×10^9 photons outside. This puts some constraints not only on the properties of the sources in the OM field but also on the maximum exposure time. The expected dose can be calculated making use of the count rates listed in Tab. 16. These values are conservatively calculated according to the pre-flight values.

In case an optically bright source beyond these limits is in the OM FOV (not just within an active science window!), users must specify in their proposals that the OM will be in the "GO-off" position. It is the user's responsibility to check for the presence of such bright sources. The user is recommended to check the Guide Star Catalogue (at the URL: `http://archive.eso.org/gsc/gsc`).

The **XMM-Newton** AO2 proposer will be able to check the impact of the sources present in a given field with respect to the OM brightness and dose limits through the function "Technical Evaluation" in XRPS.

3.5.10 OM specific proposal submission information

In the preparation of OM observing proposals, the following information should be taken into account.

3.5.10.1 OM star tracking windows

Before each OM science exposure a reference tracking frame is obtained (FAQ). The tracking stars are used to calculate the OM attitude solution for the process of shift & add of the tracking frames of the science windows. The reference tracking frame taken first provides the coordinate reference point. OM tracking star windows are small windows (64×64 in-memory pixels), defined as such so as to read out a minimum of data as fast as possible and take away a minimum of OM's processing capacity from the science observations. Images of tracking windows are not down-linked to the ground, but processed onboard. Only the x and y position of the tracking stars in units of in-memory pixels, the number of counts from the stars per tracking frame and the pointing offset information is transmitted as part of the telemetry stream. The number and the properties of OM tracking windows for a science observation are determined by an onboard algorithm and therefore **not** user-selectable.

3.5.10.2 Choice of non-default OM science windows

For OM observations more than one science window may be defined. There are several boundary conditions that limit the user's choice and which **must** be taken in account properly if a non-default instrument configuration is to be used.

- Maximum number of windows

  Up to five science windows in total (of which up to two in the fast mode) are allowed (Fig. 93).

- Allowed science window locations and sizes

  The size of an OM science window must be integer multiples of 16 in-memory (0.5″) centroiding pixels, i.e., 2×2 CCD pixels.

  Science windows must start at an even pixel number in both the horizontal (x-) and the vertical (y-) direction [*e.g.*: (16,16), (32,32)], and end at (n×16,n×16), where n is an integer number. Starting at pixel coordinate (0,0) is not possible because of the necessity to allocate a 16 pixel wide margin to accommodate spacecraft drift.

  The maximum size for a single user defined Image Mode window is:

  - full resolution: 652×652
  - 2×2 binning: 488×480 binned pixels

  or any rectangular size with a total equivalent number of pixels. If more than one image window is defined, the sum of the number of pixels (binned or not) of all windows should not exceed 432698. A maximum of five windows is allowed, out of which one or two can be used in Fast Mode.

  The maximum size of a Fast Mode window is 512 pixels in full resolution, equivalent to 22×23 pixels.

- Science window overlaps

  Different scenarios for OM science window configurations are displayed in Figs. 93 and 94. **OM science windows must overlap either entirely or not at all**. This must be true for all satellite position angles allowed by the specifications made during proposal submission, in particular if the windows are specified in celestial coordinates (Fig. 94).

Particular care must be employed if windows are defined partly in pixels and partly in sky coordinates within the same exposure. *It is responsibility of the PI to ensure that these windows do not overlap for any position angle.* Violation of this constraint can lead to unrecoverable loss of science exposures.

- Fast Mode slice duration constraints

  The minimum fast mode time slice duration for a fast mode window is 0.5 s. Shorter times are in principle possible, but discouraged.

For a more detailed explanation the reader may refer to the technical note on Constraints on the OM Window Configuration and Definition of the OM Default Configurations (§ 7).

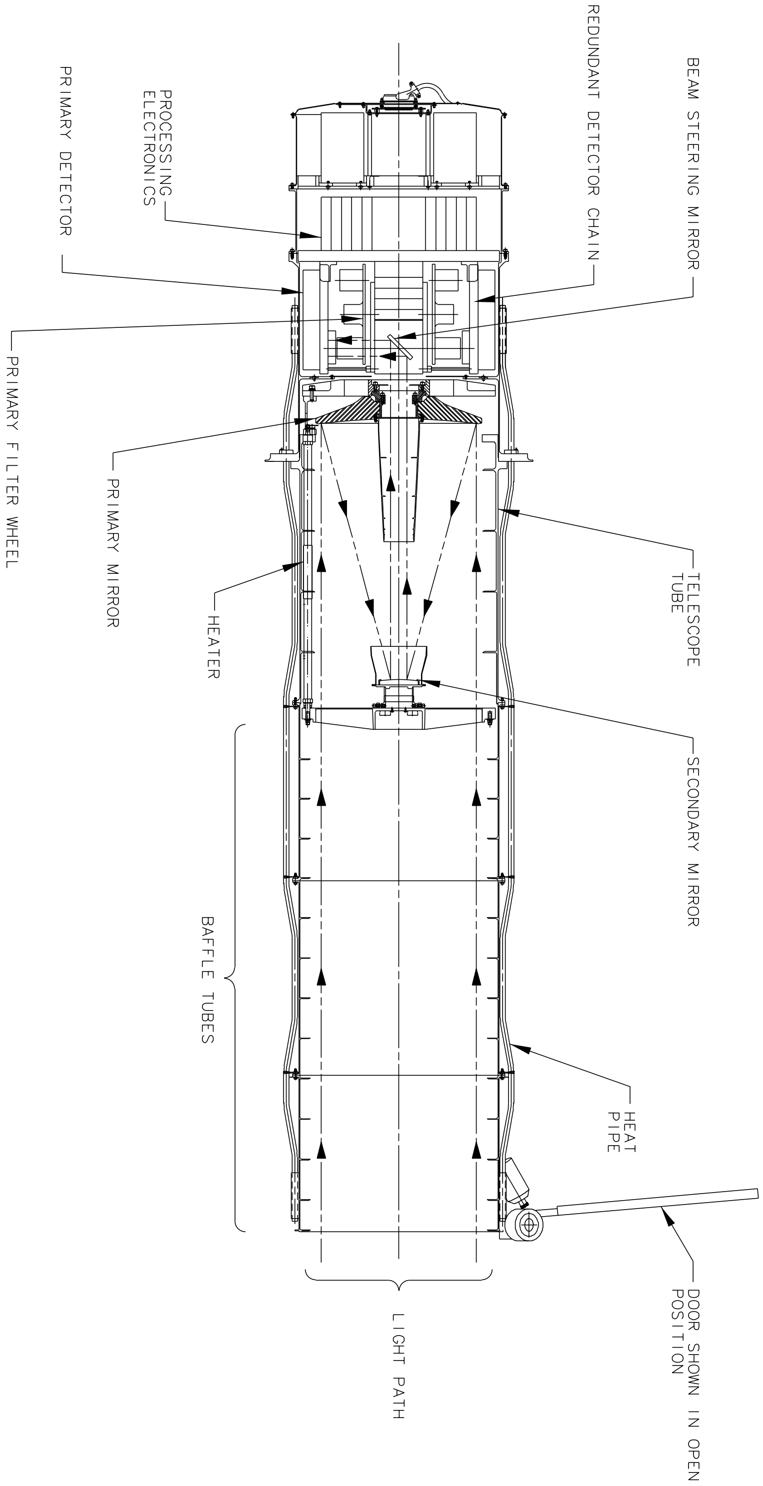

Figure 80: *The light path in* **XMM-Newton's** *optical/UV telescope, OM.*

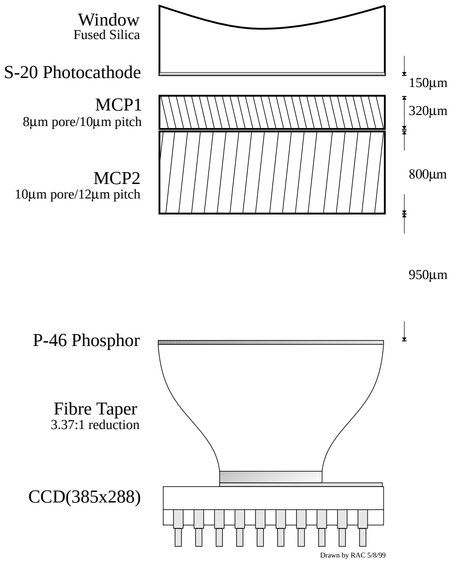

Drawn by RAC 5/8/99

Schematic Structure of Detector Head

Figure 81: *Sketch of the OM micro-channel plate intensified CCD (MIC) detector.*

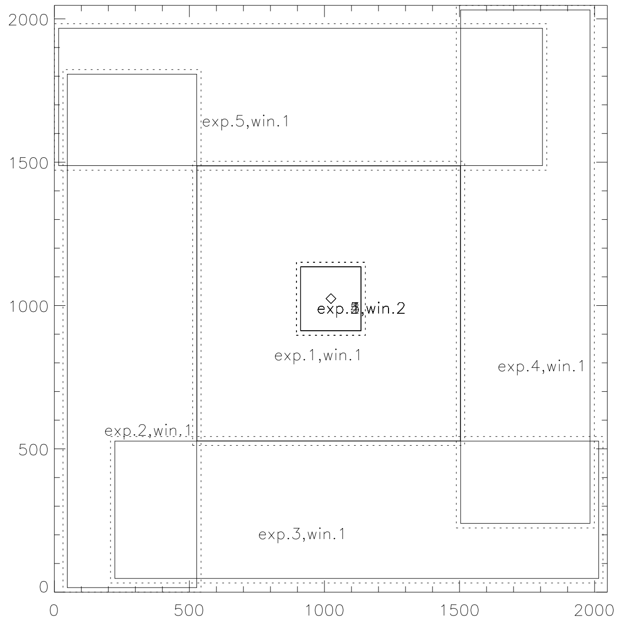

Figure 82: *Setup of OM imaging mode default mode observations consisting of a sequence of 5 exposures. The science windows are indicated by solid lines, the detector windows by dashed lines. A 16 in-memory pixel margin around the science window is allocated to accommodate spacecraft drifts.*

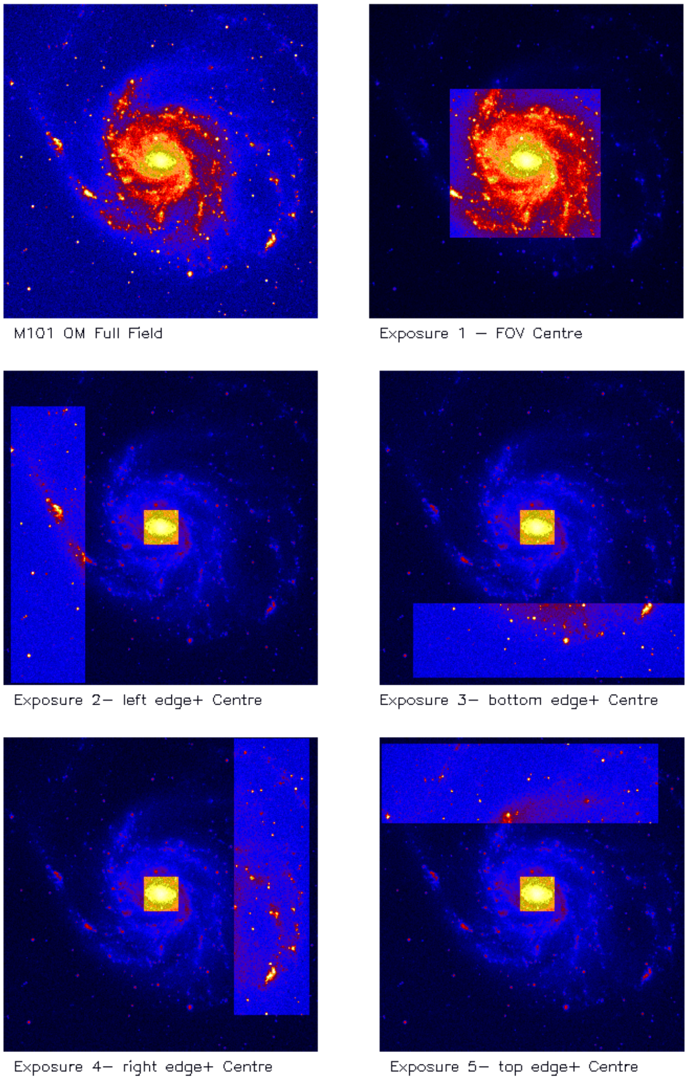
M101 OM Full Field

Exposure 1 – FOV Centre

Exposure 2– left edge+ Centre

Exposure 3– bottom edge+ Centre

Exposure 4– right edge+ Centre

Exposure 5– top edge+ Centre

Figure 83: *Example of a field imaged with the default Image Mode configuration.*

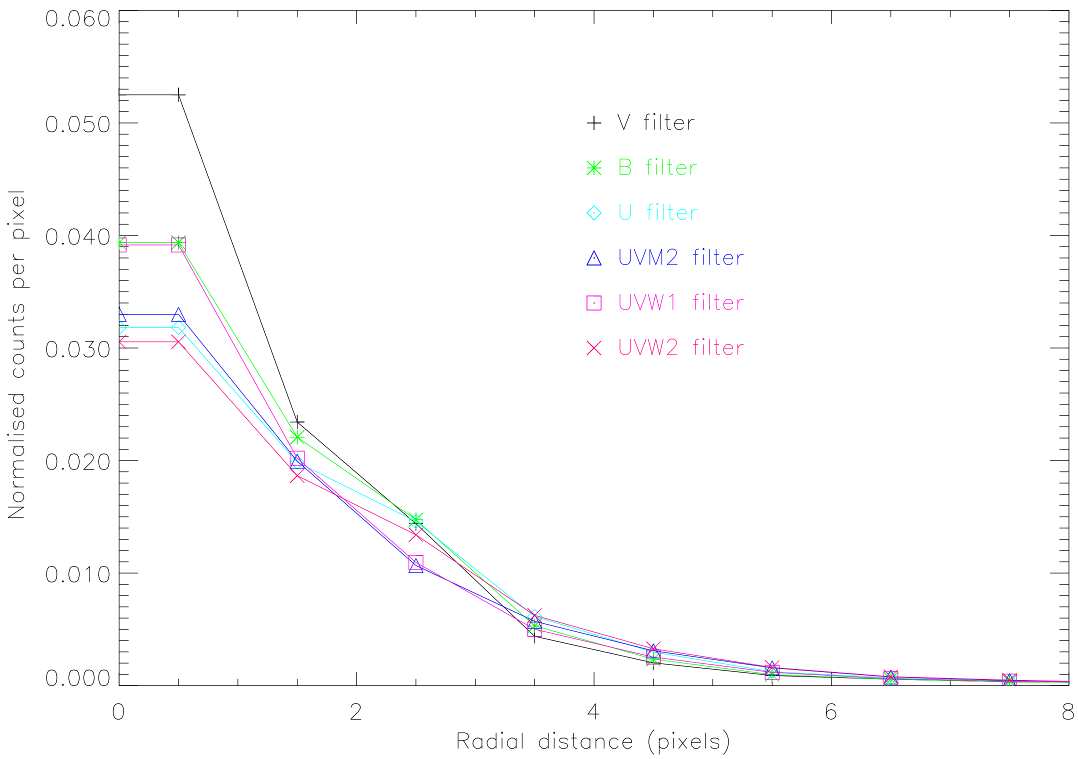

Figure 84: *Optics+detector OM PSF in different filters*

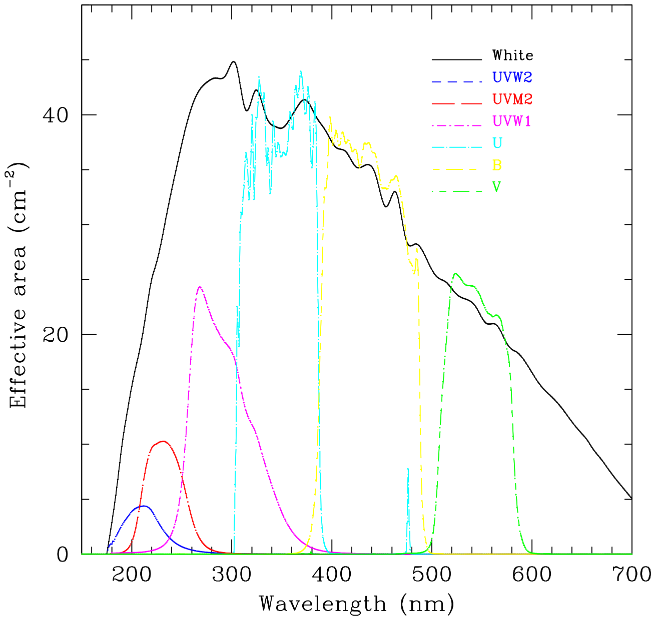

Figure 85: *Throughput curves for the OM filters, folded with the detector sensitivity.*

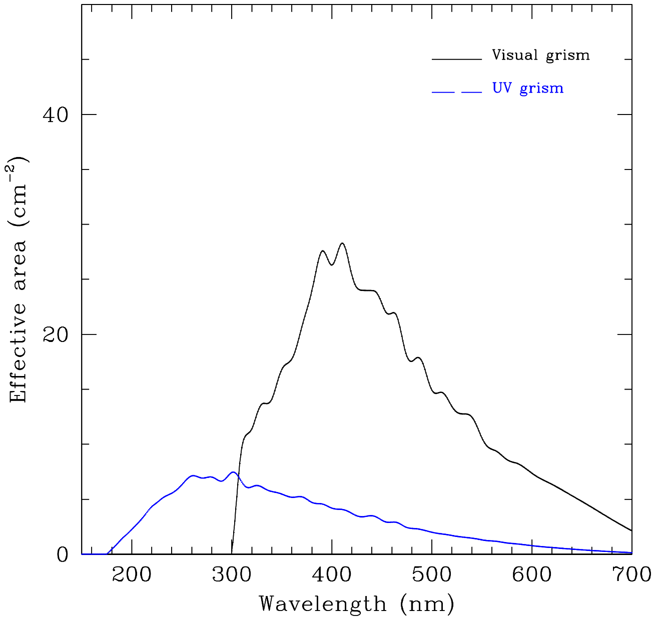

Figure 86: *The OM grism throughput, folded with the detector response.*

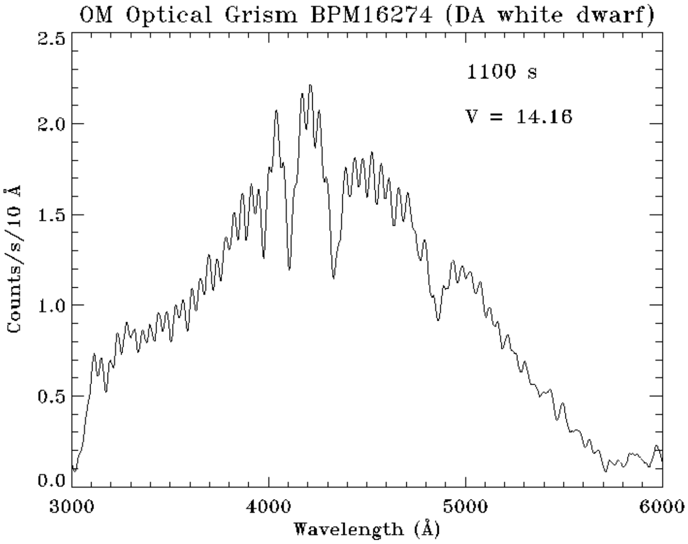

Figure 87: *Spectrum of the white dwarf BPM 16274, obtained with the OM visual grism. The deep absorption features are H-absorption. The semi-periodic fluctuations are due to fixed pattern noise.*

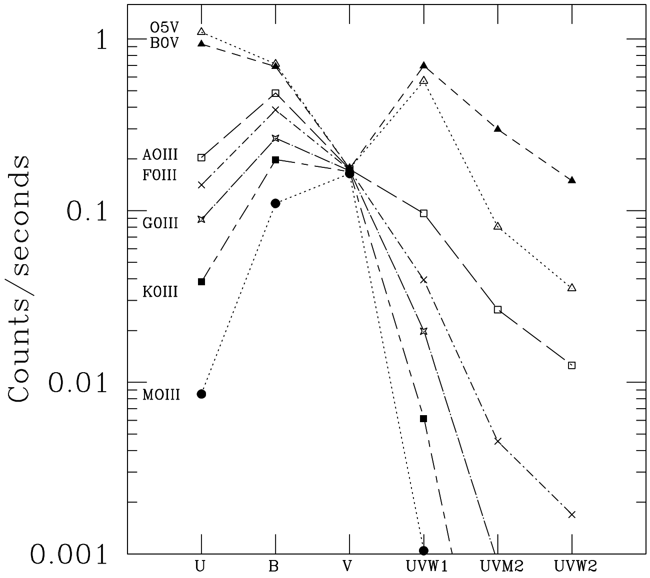

Figure 88: *OM count rates vs. filter selection for stars of different spectral type with* $m_v = 20$ *mag.*

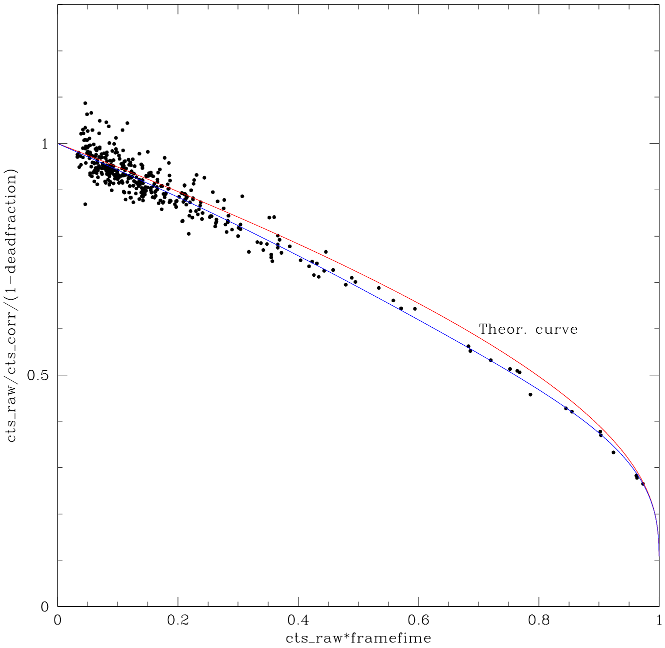

Figure 89: *Theoretical (red line) and empirical (blue line) coincidence loss correction curves superposed to flight data*

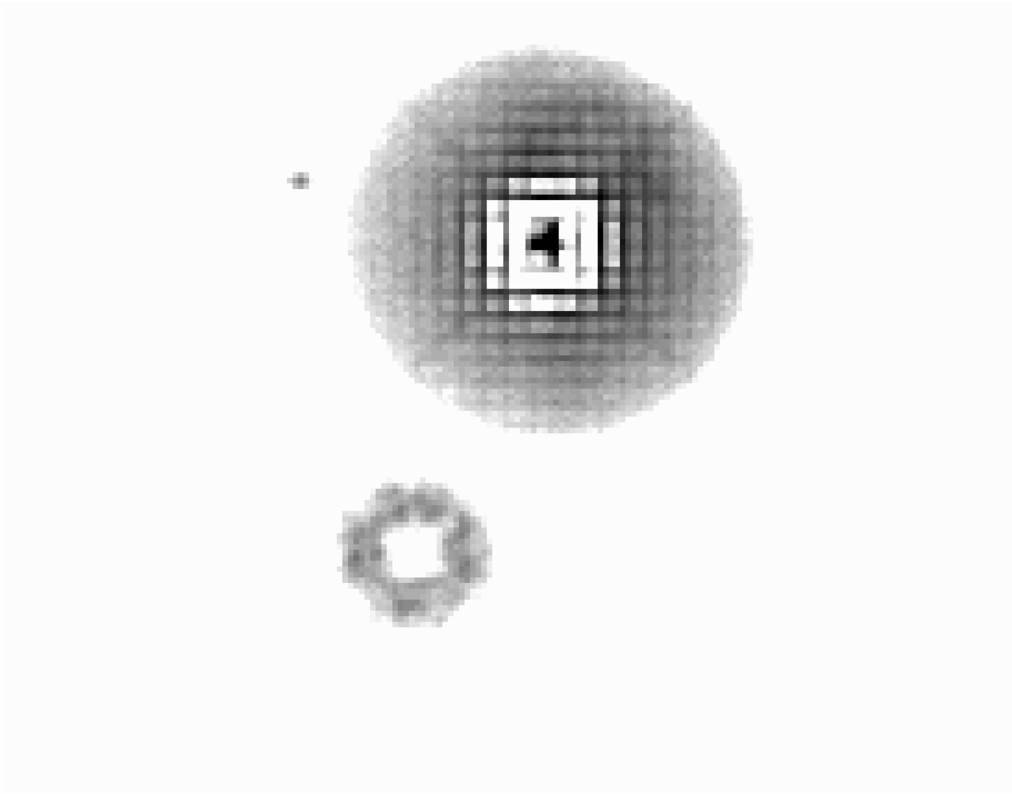

Figure 90: *Out-of-focus ghost image ("smoke ring") of a bright field star, during a 3C273 observation. Clearly visible is the strong fixed pattern noise around the bright source*

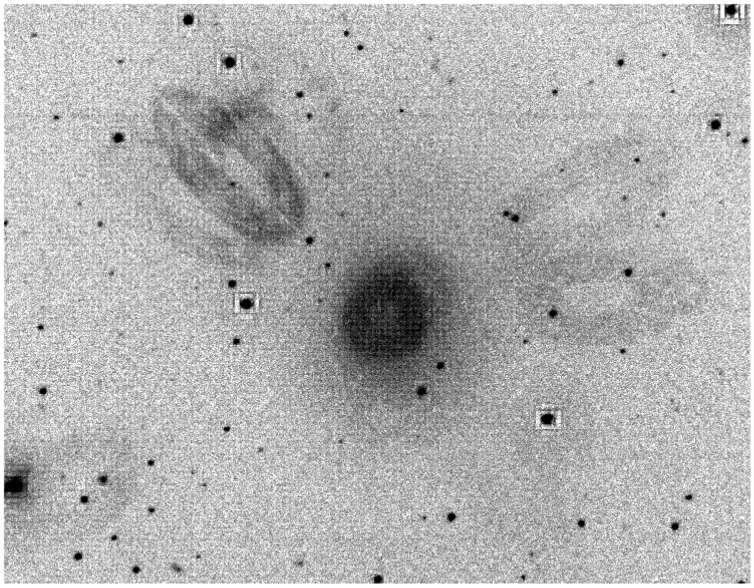

Figure 91: *Straylight ellipses caused by reflection of a star outside the field of view, taken from the PKS 0312 offset 6 field (V filter in use). The average background rate is 15 counts pixel*$^{-1}$ *per exposure; in the bright straylight loop is 30 counts pixel*$^{-1}$*. The background is also enhanced in the central region due to reflection of the diffuse sky light from outside the field. In the center it rises to ≃3 times the average background rate.*

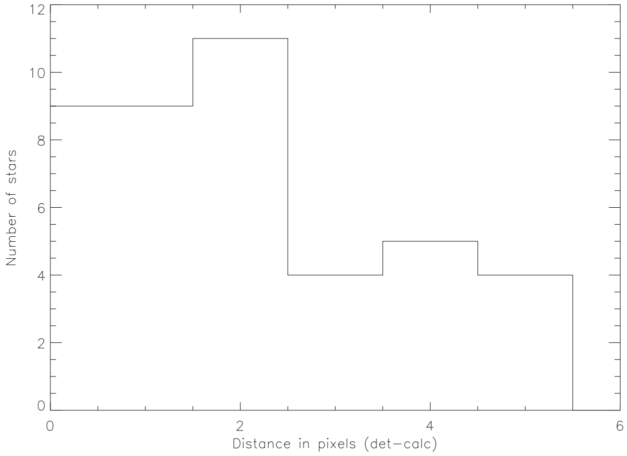

Figure 92: *Positional error of sources in a field of view, where the distortion map has been applied. The histogram was made using sources from the 3C273 field fitted to a map derived from the LMC field*

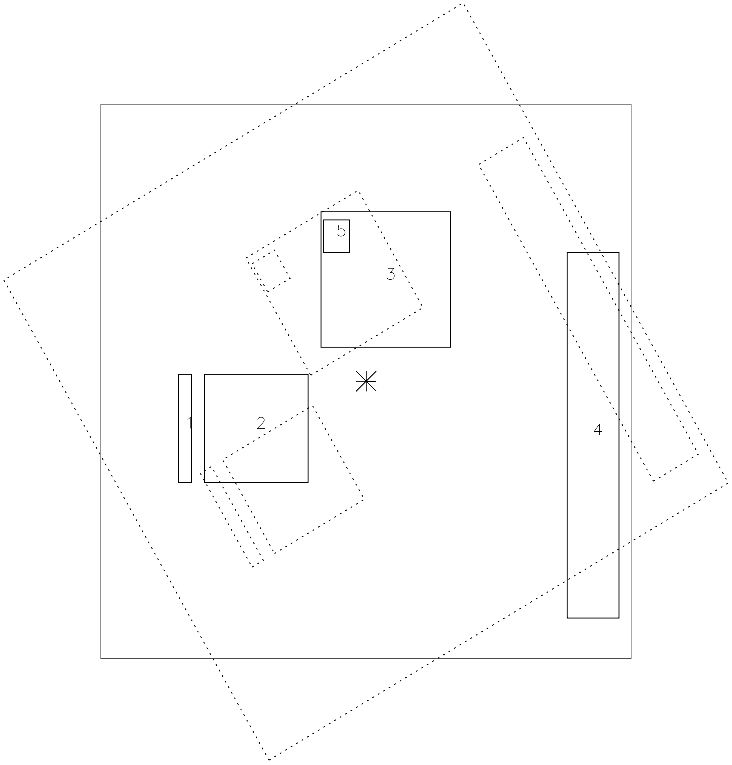

Figure 93: *When the boundaries of OM science windows are defined in detector pixel coordinates, the relative location of the windows with respect to each other does not change. However, different areas on the sky are imaged under different position angles.*

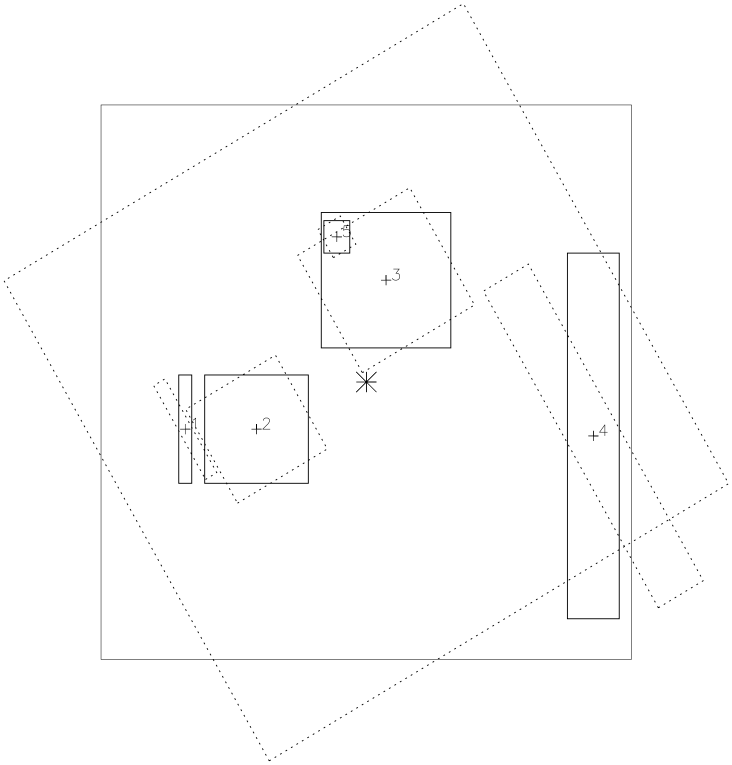

Figure 94: *Defining the locations of OM science windows in sky coordinates one makes sure that (approximately) the same area of the sky is imaged under different position angles. Now, however, the OM science windows can change their relative locations. Windows 3 and 5 (which used to be in the upper left corner of window 3, see previous figure) are now partially overlapping, which is not allowed and window 4 is now partly outside the OM FOV (which is also not allowed).*

3.6 XMM-Newton support instruments

The so-called "non-science" instruments onboard **XMM-Newton** are the EPIC Radiation Monitor System (ERMS) and the Attitude and Orbital Control System (AOCS).

3.6.1 EPIC Radiation Monitor Subsystem (ERMS)

The ERMS registers the total count rate and also basic spectral information on the background radiation impinging on **XMM-Newton** and its science instruments. This is done not only during science observations, but during the entire lifetime of the mission.
Depending on the mode in which the ERMS is operated, it updates background radiation information once in 512 seconds (slow mode) or 4 seconds (fast mode). The ERMS is normally working in slow mode.
The ERMS data consist of three measurements per readout, two spectra from the High Energy Detectors (HEDs) and one from the Low Energy Detector (LED). 256 spectral bins each will be available in the LED and HED. The HEDs are sensitive to electrons above 200 keV and protons above 10 MeV, while the LED is sensitive to electrons with energies above 50 keV.
The two high energy spectra are the "HE detector spectrum", with events from either one or both HE detectors, and the "coincidence HE spectrum", in which only events detected by both HEDs will be recorded.
The data from the ERMS comprise the following quantities:

- one header keyword (warning flag),
- seven broad-band count rates, three from the LED, four from the HEDs,
- LE detector spectrum (256 channels),
- HE detector spectrum (256 channels),
- HE coincidence spectrum.

In this way, the ERMS monitors the total radiation dose that **XMM-Newton** is exposed to. When the level of radiation intensity exceeds a certain threshold, the ERMS issues a warning to the ground for the Spacecraft Operator to safe the instruments.
ERMS data are not delivered to the PI as part of the **XMM-Newton** science data but can be obtained from the SOC on request. Note that these data are not properly calibrated and therefore are not suitable for general scientific use.

3.6.2 Attitude & Orbit Control Subsystem (AOCS)

The AOCS determines the attitude of the **XMM-Newton** spacecraft while in orbit, based on the information from one of **XMM-Newton**'s two star trackers (which are operated in cold redundancy) and its "Fine Sun Sensors". During slews and the post-slew phase (comprising attitude determination, trim, and settling of the spacecraft), entries are made into the Attitude History File (AHF) every 10 seconds. Note that during slews the AHF will not contain attitudes reconstructed from actual AOCS telemetry, but the results of a slew time/path predictor, based on the actually observed slew start/end times and attitudes. The accuracy of the attitude reconstruction during slews is expected to be better than $1'$.

In the “stable pointing mode” (i.e., after the slews and the post-slew phase), the conditions under which entries into the AHF are made are optimized parameters. An entry is made into the AHF only in case of Relative Pointing Errors (RPEs) exceeding the programmed limit. The minimal programmable limit (i.e., the smallest programmable deviation from the nominal boresight) is $1''$. The minimal time resolution with which entries into the AHF can be made in case of such instantaneous excursions is 2 seconds. For a single nominal pointing entry, only a mean RPE will be provided.

The AOCS attitude information is independent of that from the OM’s star tracking windows (§ 3.5.3).

The AHF is a file containing processed AOCS telemetry. Clipped to the start/end times of an observation or slew, the complete AHF for the relevant revolution becomes an ODF or SDF component which is delivered to the observer. For “stable pointing periods” the data records identify intervals of time during which the spacecraft’s boresight did not deviate by more than a configurable limit from the mean boresight during that period. For open loop slews and post-slew attitude trims, the AHF provides the instantaneous boresight at equidistant points in time (typically 10 seconds). It should be noted that attitudes for open loop slews are derived from a “slew model” into which the boundary conditions (actual start/end times and attitudes) have been entered, i.e., the intermediate attitudes provided for slews are not based on sensor data telemetered during the slews.

It should be noted that there is an additional file that holds attitude data, which is the only one being used by the SAS definitively from AO-2 onwards. This is the so called Raw Attitude File (RAF) which provides the attitude information at the maximum possible rate (one entry every 0.5 s). The AHF is in fact a smoothed and filtered version of the RAF.

3.7 Comparison with other X-ray satellites

A basic comparison of **XMM-Newton**'s properties with those of *Chandra*, *ROSAT* and *ASCA* is given in Tab. 21. It is visible immediately that *Chandra* and **XMM-Newton** have complementary characteristics and that both constitute a new generation of X-ray missions, with enormously improved capabilities compared to their predecessors.

Table 21: *Comparison of* **XMM-Newton** *with other X-ray satellites*

Satellite	**Mirror PSF *FWHM* [″]**	**Mirror PSF *HEW* [″]**	**E range [keV]**	**A_e at 1 keV [cm^2]^a**	**Orbital target visibility [hr]**
XMM-Newton	6	15	0.15 – 15	4650^b	40^c
Chandra	0.2	0.5	0.1 – 10	800	50
ROSAT	3.5	7	0.1 – 2.4	400	1.3^d
ASCA	73	174	0.5 – 10	350	0.9^d

Notes to Table 21:
a) Mirror effective area.
b) Note that Figs. 10 and 11 do not just show the mirror effective areas but have the EPIC detector responses included as well.
c) Orbital visibility (above 46,000 km).
d) Low orbit with Earth occultation.

Some special strengths of **XMM-Newton** are e.g.:

- The high time resolution of **XMM-Newton** with the EPIC pn camera.
- The high sensitivity of **XMM-Newton** + EPIC pn at high energies.
- Excellent low energy response down to 0.15 keV.
- Extreme sensitivity to extended emission.
- High-resolution spectroscopy (RGS) with **simultaneous** medium-resolution spectroscopy and imaging (EPIC) and optical/UV observations (OM).

3.7.1 A comparison of XMM-Newton vs. Chandra

The basic difference in instrument operation between **XMM-Newton** and *Chandra* is that on **XMM-Newton** all instruments, unless prohibited by constraints (§ 4.2), operate simultaneously, while science instruments on *Chandra* are alternated.

Several figures have already been shown above comparing the characteristics of **XMM-Newton**'s science instruments with those of *Chandra*, namely:

- Mirror effective area and PSF: Table 21.
- Imaging effective area: Fig. 28 and Fig. 29.

A few more examples are collected here.

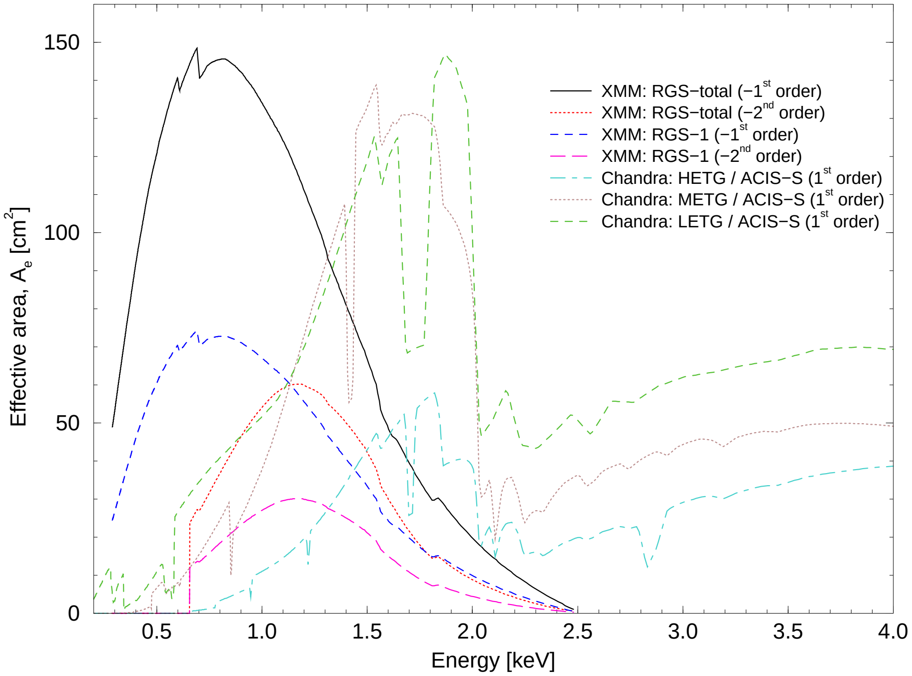

Figure 95: *The effective area of both RGS units combined and RGS-1 (linear scale), compared with Chandra's ACIS-S instrument with various transmission gratings.*

3.7.1.1 Effective area for dispersive spectroscopy

Fig. 95 displays the effective area of both RGS units together (from Fig. 66), compared with different *Chandra* instrument combinations. In order to avoid overcrowding the figure, the combination of *Chandra* HRC+LETG is not shown.

3.7.1.2 Non-dispersive spectroscopy: an example

For illustrative purposes, we add here a direct comparison of an **XMM-Newton** EPIC and an *Chandra* ACIS-I observation of a cluster with a 6 keV thermal plasma spectrum, 0.3 solar metallicity, a redshift of 0.3 and an X-ray flux in the 0.1–10 keV band of 10^{-12} erg cm^{-2} s^{-1} (thus a fairly luminous system). Such a comparison gives a good feel for the capabilities of both instruments for performing studies of faint objects. We simulated the response of the *Chandra* ACIS front-illuminated CCD imaging instrument, using the response matrices supplied for the guest observer proposal submission. With a 30 ksec observation ACIS is able to measure the temperature of the cluster to about 10% accuracy (assuming only poissonian noise and neglecting systematic effects).
For comparison, we simulated (using SciSim) the combined response of the 3 EPIC focal plane cameras on **XMM-Newton**, using the same input spectrum and observing time. Using a preliminary response matrix for EPIC, we estimate a temperature measurement accuracy of order 2.5% (neglecting systematic effects).

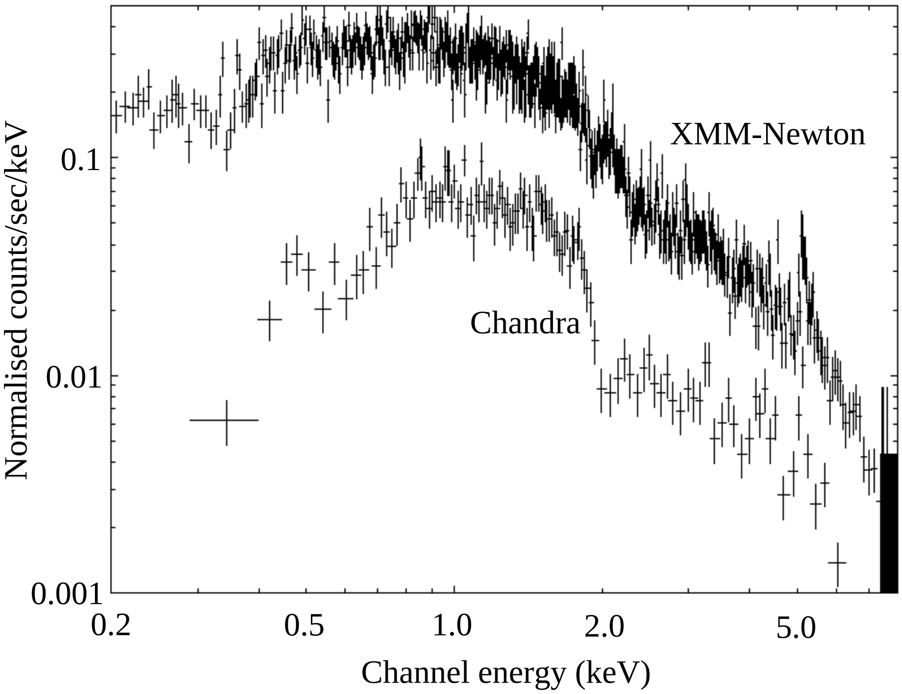

Figure 96: *Comparison of a 30 ks observation of a cluster with a 6 keV thermal plasma spectrum with Chandra ACIS-I (bottom) and* **XMM-Newton** *EPIC (top). Normalised counts are counts per spectral bin.*

3.7.1.3 XMM-Newton EPIC vs. Chandra ACIS-I pile-up comparison

It has been shown above (§ 3.3.9) how pile-up affects the accuracy of spectral fits and the shape of the X-ray PSF. Figs. 97 and 98 show the fraction of piled-up events for different numbers of counts per CCD frame (in full window imaging mode). One can see in Fig. 98 that pile-up effects for given source fluxes are more severe for ACIS-I by more than an order of magnitude compared to EPIC MOS and even by two orders of magnitude compared to EPIC pn.

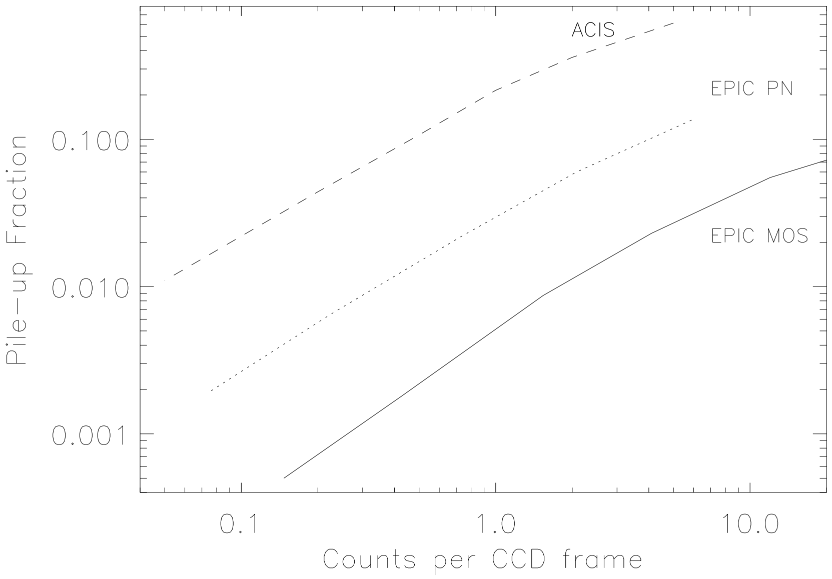

Figure 97: *Comparison of Chandra ACIS-I vs.* **XMM-Newton** *EPIC (pn and MOS) pile-up for different total frame count rates. The frame times are 3.3, 2.8 and 0.07 seconds for ACIS-I, MOS and pn, respectively.*

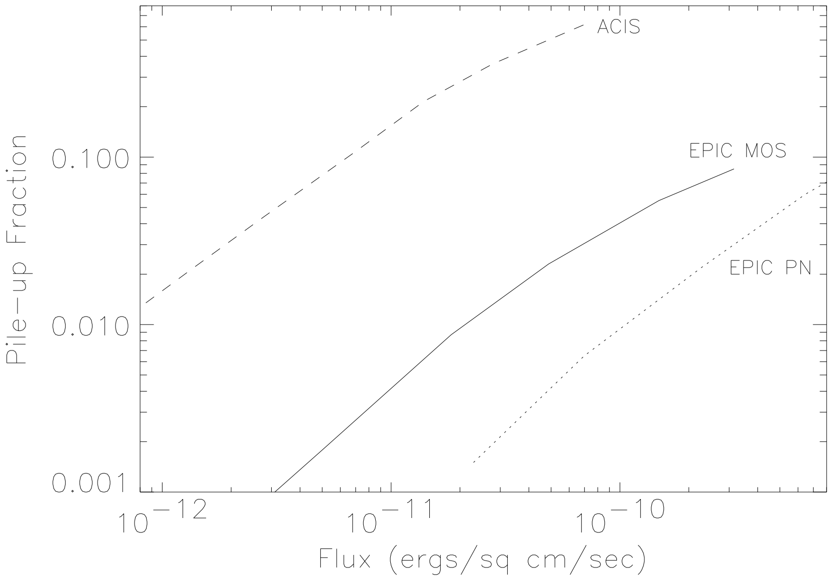

Figure 98: *Comparison of Chandra ACIS-I vs.* **XMM-Newton** *EPIC (pn and MOS) pile-up for different incident source fluxes, after conversion of counts per frame to flux units, adopting an $\alpha = -1.7$ power law spectrum with an absorbing hydrogen column density of 3×10^{20} cm^{-2}.*

4 Observing with XMM-Newton

XMM-Newton observes with all instruments simultaneously, brightness limits and other constraints permitting. All instruments can be operated independently (i.e., the exposure times of individual instruments are not coupled to each other) and observers will receive the science data of all science instruments operating during an observation.

When planning **XMM-Newton** observations several boundary conditions must be taken into account. The constraining parameters are listed in this section.

4.1 XMM-Newton orbit

XMM-Newton was launched on the 10th December 1999 by an Ariane 5 launcher into a highly elliptical orbit, with an apogee of about 115,000 km and a perigee of ca. 6000 km (the minimum elevation for science observations is 46,000 km; see Fig. 99 . The orbital inclination is 33°, the right ascension of the ascending node is 195° and the argument of perigee 89°. Such an orbit provides the best visibility in the southern celestial sky.

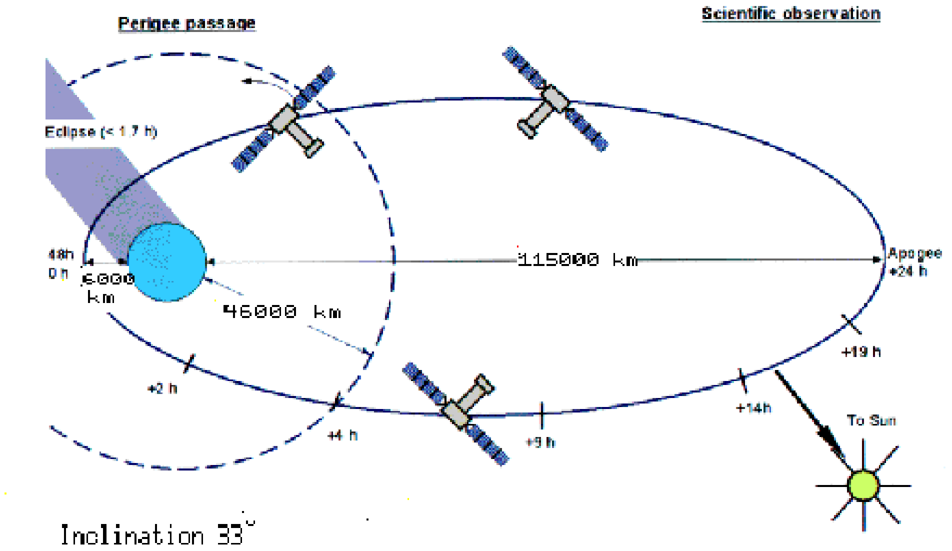

Figure 99: *Sketch of the highly elliptical* **XMM-Newton** *orbit. Figure provided by Dornier Satellitensysteme GmbH.*

Objects are continuously observable during the entire visibility period in an orbit, as **XMM-Newton** is operated with three ground stations, located at Perth, Kourou and Santiago. Thus, the complete visibility period (145 ks) is available for continuous observations.

4.2 XMM-Newton observing constraints

For the individual instruments, and also for the **XMM-Newton** observatory in general, different observing constraints apply, which may affect the scheduleablity of targets significantly. These are:

4.2.1 Radiation belts

The radiation background is variable around the **XMM-Newton** operational orbit, depending on the satellite's location with respect to Earth's magnetosphere. For useful **XMM-Newton** science observations to be conducted, the minimum satellite elevation is 46,000 km. At this height, the instruments OM and RGS can start to perform scientific observations. The EPIC cameras, which are much more sensitive to the particle background, can only start to perform scientific observations three hours later. Closer to Earth, the background is prohibitively high. Because of this, about 145 ks of the 48-hour orbital period can be used for science observations with RGS and OM and about 135 ks can be used to perform scientific observations with the EPIC cameras. The particle background outside the belts is dominated by the solar particle emission. The incident flux is therefore coupled to the level of solar activity. During intense solar flares the **XMM-Newton** payload instruments will be switched off.

4.2.2 Bright source avoidance

In both the X-ray (EPIC/RGS) and the optical/UV regime (OM) there are restrictions with respect to the brightness of sources within the field of view, albeit of a different nature.

- OM bright optical/UV source avoidance

  With the increasing count rate of a target, the science quality of OM data for that source is compromised by deadtime effects. The effect is of the order of 5% for a source with a count rate of 10 counts/s, increasing to approximately 30% for sources with count rates of 50 counts/s (assuming in both cases a CCD framerate of 100 Hz).

  A different kind of limitation is imposed on science observations by the OM detector photocathode. MCP-based intensifier tubes show localised gain depressions caused by bright point sources. The main cause of the sensitivity loss is related to the defects in the photocathode. From measurements made with OM test tubes, a non-linear relationship between the local sensitivity loss with accumulated count dosage was established. The brightness limits for all OM filters are tabulated in Table 20 in § 3.5.9.

  OM observations of sources beyond these brightness limits are not allowed. **These limits hold for any source in the OM FOV, even if it resides outside an active OM window.**

  Since the above refers to point source limits, the quantity to be specified in **XMM-Newton** observing proposals for extended sources, like e.g. galaxies with active nuclei, is the maximum surface brightness (in most cases of the central object) in V magnitudes per square arcsec. The limits (at the position of the brightest emission) are the same as for point sources (see Tab. 20).

In addition, the following solar system sources must be avoided by the OM, with avoidance angles as listed:

- Moon – 35°
- Mars – 3.5°
- Jupiter – 4.5°
- Saturn – 2°
- Uranus – 0.4°
- Neptune – 0.4°

Avoidance of planets will be ensured by the SOC and is thus not a concern to the user.

- RGS bright optical/UV source avoidance

  Bright optical/UV light entering the RGS under certain angles can deteriorate the quality of the science observations. This is described in § 3.4.9.1.

- EPIC bright X-ray source avoidance

  The **X-ray** count rate must be kept below a threshold (as quantified in Tab. 3) in order to keep pile-up below 1%). Otherwise the energy resolution and the quality of spectro-photometry could be compromised in the case of extended sources. For point sources, the effect is not so important and, even if the pile-up is over the threshold indicated above, good results on spectral shape and absolute flux can be obtained by excising the core of the PSF, what will obviously produce some loss of signal.

  Observations with an expected high level of photon pile-up are not *per se* disallowed, but a special scientific justification is expected stating why and how the scientific goals of the proposal can be achieved despite the expected pile-up (and thus the deteriorated spectral response and PSF quality; §§ 3.3.9 and 3.7.1.3).

  Bright optical off-axis objects can leak through the filters and generate false X-ray events that can contribute to the degrading of the telemetry bandwidth. This effect becomes important if the off-axis source is 50 times brighter than the on-axis limit, i.e. 4 or 5 magnitudes brighter.

The EPIC telemetry limits are not hard-wired, making it difficult to provide universal guidelines. For EPIC MOS imaging modes the baseline count rate allowed is about 150 photons/s. For EPIC pn it is about 300 photons/s and therefore observations of single bright point sources at the pile-up limit are not constrained by telemetry. The brightest extended objects, such as the Cas A supernova remnant approach the telemetry limits, and can be accommodated by limited change of telemetry allocation depending on instrument usage, or by graceful loss of data frames. For timing modes the event rates are limited to about 1500 events per second by both the camera and telemetry constraints.

- No RGS bright X-ray source avoidance

  Due to the much smaller effective area of RGS compared to EPIC and the dispersion of the source spectra over many detector pixels, the source count rates per pixel are much lower. Therefore, photon pile-up in RGS is negligible. Only optically bright sources can impose constraints on RGS observations, as mentioned above. However, radiation of nearby X-ray sources should not fall on the dispersed spectrum of the program source (§ 4.4).

4.2.3 Celestial constraints

The visibility of sources on the sky depends on several constraints, including avoidance of solar system sources. These are:

- Earth limb avoidance

  Minimum avoidance angle: 47°.

- Solar avoidance

  A solar aspect angle within the range $70^\circ - 110^\circ$ must be maintained at all times. Note that this is not a bright source avoidance cone, but driven by requirements on the spacecraft's alignment with respect to the Sun to ensure sufficient energy supply.

- Lunar avoidance

  Minimum avoidance angle: 22°.

The numbers listed here coincide with the avoidance angles used by the **XMM-Newton** Target Visibility Tool.

4.2.4 Position angle constraints

In particular the RGS, but also the OM with its grisms, can place position angle constraints on observations, if one wants to avoid spatial overlaps of the dispersed spectra of adjacent sources. Therefore, adjacent sources should not be aligned with the dispersion direction. In the case of RGS, avoidance of bright sources outside the field of view, as described in § 3.4.9.1, can also lead to position angle constraints. A description of how to avoid such sources is provided in § 4.4).
If nothing is specified during proposal submission, there is by default no orientation constraint on **XMM-Newton** observations. Note that any constraint imposed on an observation makes it "time-critical" and thereby more difficult to schedule.
Observations with position angle constraints need a special justification stating why a given orientation in needed. Observations whose allowed position angle range is less than 10° will be considered "time-critical" will need a high rating from the OTAC in order to be performed. If the position angle needs to be constrained, then the observer can use the **XMM-Newton** Target Visibility Tool provided at the URL `http://xmm.vilspa.esa.es/user/vis/vis_top.html` to find out during which revolutions the source will be visible for a user-selectable minimum observing time. The nominal satellite position angle is provided for each of the revolutions with target visibility as specified by the user.

4.2.5 Raster observing mode

XMM-Newton does not have any capability to create a "raster" of nearby pointings via small aspect motions in an automatic fashion. Each observation must be requested individually (via XRPS) and will be handled separately. This implies that each observation has the full operational overheads (see § 4.5.1) and that such observations will not automatically be scheduled within one or consecutive orbits.

4.2.6 Dithering mode

XMM-Newton does not require a dithering mode (because of the large pixel size of it's EPIC CCD cameras) and hence such a mode is not supported. This means that users must, in order to overcome inhomogeneities in the coverage of a FOV (different net exposure times, e.g., because of chip boundaries), conduct observations of slightly offset positions on the sky. However, since **XMM-Newton** does not have a raster observing mode either (see above), this leads to a sequence of separate observations that are, from the standpoint of scheduling, treated as independent and might thus not be scheduled back-to-back.

As a secondary point, users should be aware that when proposing such partly overlapping observations to cover a field of view larger than $30'$, one should make sure that within a single observation the required OM filter coverage is achieved (because the position angle of the spacecraft might have changed by the time a neighbouring observation is scheduled, which would lead to different coverages on the sky).

4.2.7 Tracking mode

PIs interested in observing a moving (solar system) target should take into consideration that **XMM-Newton** does not support tracking the path of such sources on the sky in an automatic fashion. **XMM-Newton** has, however, already successfully been used to observe a few comets. The method to perform such kind of observations is that the spacecraft is pointed in a way that the target crosses the instrument's field of view. If the required exposure time is longer than the time in which the target passes through the field of view, the total integration time must be split into several observations, with the subsequent increase in overhead time.

The analysis of the data also will need some especial handling. The spatial and timing information for each EPIC event must be used later on-ground to restore the image and spectrum of the target.

4.3 Sky visibility during the XMM-Newton mission

Target visibility should **always** be checked using the **XMM-Newton** Target Visibility Tool, which is located at the URL `http://xmm.vilspa.esa.es/user/vis/vis_top.html`. Currently, it contains information for the time period of AO-2 observations. Fig. 100 displays only a first-order approximation of the sky visibility during this time. It is shown for illustrative purposes and should be used only as a rough guideline to assess whether any visibility problem, in particular in the dark area around Cyg X-1, exists, but not for quantitative statements. The map is not accurate, because it is based on $10° \times 10°$ bins. Since a whole bin is rejected even if only a tiny fraction of it is affected by an observing constraint (like e.g., bright source avoidance), the actual visibility is underestimated.

The **XMM-Newton** Target Visibility Tool determines the visibility, if any, for certain target coordinates under configurable conditions. Note that basic parameters, like e.g., avoidance angles, should not be changed when running it. The defaults represent the values that are actually used for satellite operation. More details are provided by the **XMM-Newton** Target Visibility Tool online help.

Fig. 101 is a complementary representation of those areas on the sky for which there is **no** adequate visibility during the period of time corresponding to revolutions 400-600 of the **XMM-Newton** mission. Note that, despite its appearance, this is not just an inverted version of Fig. 100. It shows areas for which a certain maximum continuous target visibility is not reached in any orbit (up to orbit 600). It must be taken into account that the target visibility is affected by the differences between the long term predicted orbit and the real orbit. It means that targets in regions of the sky for which a minimum visibility is not reached in a long term evaluation could become visible taking into account short term predictions of the orbit. Again, this image is only a first-order approximation, based on a 10° grid. For more accurate information for given target coordinates, the **XMM-Newton** Target Visibility Tool **must** be used.

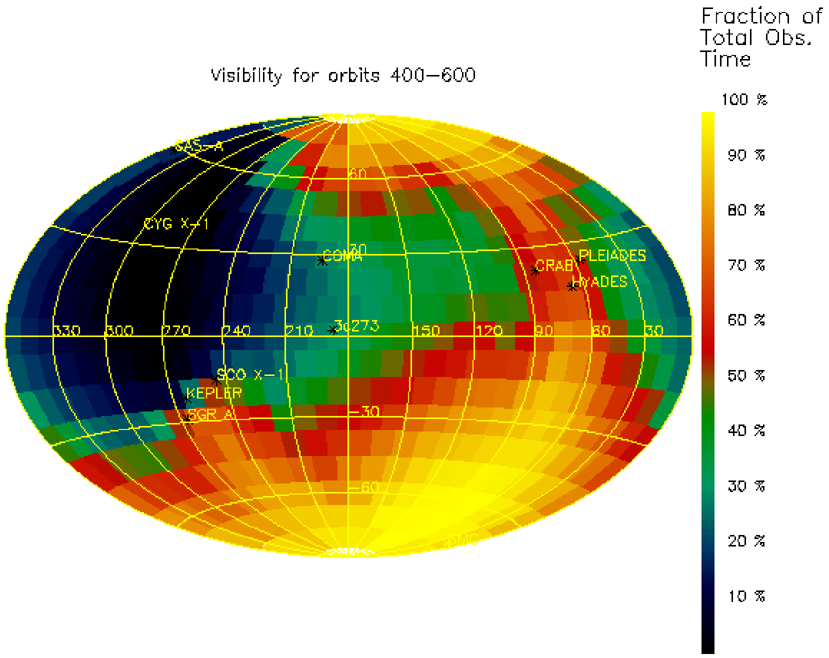

Figure 100: *Approximate sky visibility (in % of the total theoretically available time) during orbits 400–600 of* **XMM-Newton** *operation. Coordinates are equatorial, in units of degrees, centred on (180,0).*

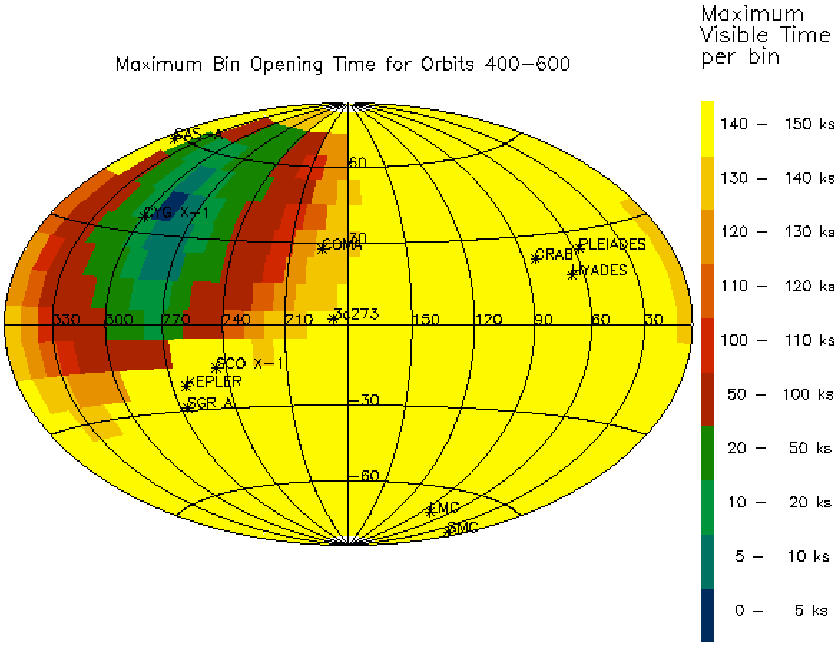

Figure 101: *Sky areas for which a given maximum target visibility is not reached during orbits 400–600 of* **XMM-Newton** *operation. Same coordinates as in Fig. 100.*

4.4 Position angle determination for XMM-Newton observations

First a few words on **XMM-Newton** nomenclature: the **XMM-Newton** “roll angle” is defined as the rotation angle between the plane defined by the major rotation axis of the spacecraft (the spacecraft X-axis) and the spacecraft Z-axis, to that defined by the spacecraft X-axis and the spacecraft-Sun direction. The roll angle increases in a clockwise direction with respect to the positive X-axis.
The “position angle”, on the other hand, is defined as the rotation between the spacecraft X-Z plane and the plane defined by the spacecraft X-axis and celestial North. Again, the position angle increases in a clockwise direction with respect to the positive X-axis. Note that the satellite's –Z-axis, which is also the RGS dispersion axis, is North-aligned under a position angle of 0°, i.e. the declination axis.

Users can determine the best position angle at which to obtain their planned observations, while avoiding nearby bright sources, using SciSim (Appendix A) as follows.
The SciSim GUI (Appendix A.2, Fig. 102) shows the field of view (FOV) of the spacecraft when viewed along the -X axis of the spacecraft, i.e., from the focal plane towards the mirrors and outwards. The coordinates convention do not follow the optical path, i.e., there is no mirror inversion of the the image of the detectors on the sky. The tool also

displays the RGS dispersion axis, in the form of two blue horizontal lines, the separation of these lines representing the cross-dispersion direction extent of the illuminated part of the CCD chip array. This view can be rotated in terms of the position angle of the spacecraft. It is therefore a simple matter of creating a model field in SciSim containing the sources which could potentially cause confusion, and finding a suitable position angle value for which these sources are **not** aligned along the RGS dispersion axis. Sources can be defined in SciSim by clicking on "Sources" and using the Source editor GUI, which, amongst other properties, allows the user to enter target coordinates.

After having chosen the most appropriate position angle for a given observation, the user can introduce that position angle constraints in the Target Visibility Tool and check when that observation is feasible

The observer should notice that a source is visible twice a year with a 180° difference in the position angle.

4.5 XMM-Newton observation overheads

As for all telescopes, **XMM-Newton** observations are also affected by operational overheads. We outline here which overheads apply to **XMM-Newton** observation for the users' information only. **Some of these overheads need to be taken into account in XMM-Newton observing proposals**, and they will be added on top of the requested science duration as warranted.

There are two categories of overheads:

1. Operational overheads and
2. instrument and setup overheads.

4.5.1 Operational overheads

XMM-Newton operational overheads are:

- Slew time to move to the target coordinates: variable, depending on the relative target position with respect to the starting spacecraft attitude; the **XMM-Newton** slew rate (except for the first slew after perigee passage and the last slew before perigee passage) is 90°/h.
- AOCS reference star acquisition time and fine trim to the actual target position after a slew – about half an hour per observation.

Operational overheads do not need to be taken into account in XMM-Newton observing proposals.

4.5.2 Instrument and setup overheads

The following instrument and setup overheads apply to **XMM-Newton** science observations. Note that some of them will occur simultaneously, at the start of an observation.

- EPIC setup time is mainly due to the upload (in the case of the MOS cameras) or the calculation (in the case of the pn camera) of the offset tables needed to compute the amount of the optical loading of the CCD chips, i.e., the charges that must be subtracted to set the correct zero level for X-ray observations. The overhead of each pn exposure due to the offset calculation is about one hour. The overhead of each MOS exposure due to the offset table upload is about 10 minutes.
- The overhead of RGS exposures is about one minute and a half.
- The overheads of the OM exposures are mainly due to the setup of the instrument and the field acquisition driven by the guide star recognition (cp. § 3.5.7). The total overhead time is of the order of 30 minutes.

Instrument and setup overheads need to be taken into account in **XMM-Newton** observing proposals. A detailed description of the instrument and setup overheads can be found in the **XRPS Users' Manual**.

4.5.3 Special science exposures

Optimal scientific usage of the **XMM-Newton** instruments sometimes requires special (science) exposures. These are **not** overheads and therefore part of the requested science observing time:

- An OM image should be acquired before every grism exposure.
- OM fast mode images should be embedded in an image mode science window. This will help with the fixed pattern noise correction, as it provides a template at the proper count rate level.

Consequently, the observer should specify such additional exposures in the proposal.

4.6 Instrument alignment

XMM-Newton has three independent X-ray telescopes and an optical/UV telescope, with a total of six science instruments. Neither the telescopes' optical axes nor the centre positions of the detector FOVs are aligned perfectly. Thus, radiation from sources in the spacecraft's boresight direction does not fall onto the nominal on-axis position of all detectors simultaneously. Since the start of the PV phase of mission operations, the instrument boresights have been accommodated via individual calibrations which allow placement of the target at the preferred location for either the RGS or the EPIC instruments. For virtually all cases this represents an acceptable compromise, except that for RGS some Ne lines fall on or near the gap between CCDs, and for EPIC a point source can be located closer to the edge of a window than would be preferred for the maximum encircled energy coverage.

For AO-2 the intention is to improve the situation by implementing a single boresight choice for all observations. This will minimise the loss of line features on dead RGS areas, and move the target slightly away from the pn inter-CCD gap. At the same time the MOS window clocking sequences will be shifted to centre the target better for Small Window and Timing observations.

The user can, in principle, always choose for an off-axis pointing but this requires specification of a roll angle which implies reduced visibility. The user can use the SAS task srcinfov and/or SciSim to determine these choices.

4.7 Absolute and relative pointing accuracy

The Absolute Measurement Accuracy (AMA) is the error on the **XMM-Newton** boresight, after application of all the corrections on-ground. The absolute measurement accuracy of the pointing direction of the spacecraft is limited by the information reported by the AOCS. However, after the examination of some fields with secure cross-identification of field stars, it is concluded that the value of the AMA is, on average, $4''$.
The value of the Absolute Pointing error (APE), i.e., the offset between the actual and required pointing direction, achieved when the guide stars are correctly found, is of about $10''$.
The Relative Pointing Error has originally been defined as the spacecraft jitter over periods of 2 minutes. The Absolute Position Drift has been defined as the change in reference axis over a period of 16 hours. In general, it is found that the spacecraft is more stable that the measurement accuracy ($2''$) on timescales of minutes and that there is also a long term drift over hours of typically $2'' - 3''$, which is measurable and correctable.

4.8 Points of concern

Some more parameters that might influence certain **XMM-Newton** observations, and should therefore be taken into account, are:

- Seam losses between abutted CCDs

  Although small, there **are** gaps between the chips of the different X-ray detectors onboard **XMM-Newton**. The two EPIC MOS cameras are mounted orthogonal with respect to each other, so that in final images, after adding up the data from two X-ray telescopes, the gaps should not be visible after correction for exposure. There will only be a reduced total integration time in areas imaged at the location of chip boundaries. The pn camera has a different chip pattern, leading to minimal losses in other areas of the field of view. It is also offset with respect to the X-ray telescope's optical axis so that the central chip boundary does not coincide with the on-axis position. The inter-CCD gaps of the EPIC MOS chip array are 400 μm ($11''$) wide. Those between neighbouring CCDs within one quadrant of the pn chip array are 40 μm ($1.1''$) wide, the gaps between quadrants about 150 μm ($4.1''$).

  The nine CCDs in each RGS also have gaps of about 0.5 mm in between them. Table 7 lists the energies affected by the gaps in RGS-1. However, the two RGS units will be offset with respect to each other along the dispersion direction to ensure uninterrupted energy coverage over the passband. Due to operational problems with two CCDs there are two additional gaps, one on each RGS unit. The wavelength ranges affected are from 10.5 to 14.0 Å and from 20.1 to 23.9 Å in RGS-1 and RGS-2, respectively.

  By choosing the instrument that is most important for the planned research as the primary instrument, **XMM-Newton** users can ensure that the programme source is placed properly, away from chip boundaries.

- Charge transfer efficiency (CTE)

  While being transported from their original location to the readout nodes, the charges of CCD pixels are transferred from pixel to pixel up to several hundred times. During each transfer, a small fraction of the charge (which depends mostly on impurities in the semi-conducting layer) can be lost. This effect can be quantified and corrected for in the offline data calibration process.

- "Out of time" events

  The **XMM-Newton** X-ray detectors do not have shutters and are therefore at all times exposed to incoming radiation from the sky. Trying to prevent photon pile-up (see above), the CCDs are read out frequently. During readout, photons can still be received. However, they hit pixels while their charges are being transferred to the readout nodes, i.e., when they are not imaging the location on the sky they would normally observe during the exposure. Thus, events hitting them during readout are "out of time" (and also "out of place"). One cannot correct for this effect in individual cases, but only account for it statistically.

  The MOS CCDs have frame store areas, which helps suppress the effect of out-of-time events. The frame shift times of a few ms are much shorter than the maximum frame integration time of 2.8 s. Therefore, the surface brightness background of smeared photons is only a fraction of a percent divided by the ratio of the PSF size to the CCD column height.

  For pn the percentage of "out of time" events is 6.2% for the full frame mode, 2.3% for the extended full frame mode, 0.15% for the large window mode and 1.1% for the small window mode. The large window mode has a smaller fraction of "out of time" events because half the image height is used as a storage area, but the reduced smear is penalised by a loss in live time.

- RGA rib scattering

  Light scattered off the stiffening ribs of the grating plates of the RGAs produces diffuse ghost images in the EPIC MOS FOV in the ±Y direction (i.e., the RGS cross-dispersion direction). The intensity of these images is of the order of 10^{-4} relative to the intensity of the focused image. For off-axis sources at azimuth angles corresponding to the ±Y direction, the intensity of the ghost images increases to a few times 10^{-4}.

  Rib reflection is currently implemented in SciSim (v. 2.0.1), but the reflection coefficient is too high, and the diffuse nature of the scattered light ghosts is not modeled. Simulations with SciSim will therefore overestimate the surface brightnesses of RGA scattered light due to this effect.

- OM exposures

  When using `FAST` mode the target coordinate must be accurate at better than a few arcseconds to fit the target in the ±10" wide windows.

  `FAST` mode OM exposures require a successful Field Acquisition. FAQ could fail in crowded fields, where many extended objects are present. This limits

> the possibility of performing - *e.g.* - high resolution OM timing of active galactic nuclei in clusters.
>
> Ring-like loops due to scattering of out-of-field bright stars (see Fig. 91) can heavily affect the detection of faint or extended sources at the boresight. This effect is mainly due to bright stars that happen to fall in a narrow annulus $12.1'$ to $13'$ off-axis.

Except for event selection, which is performed onboard for EPIC MOS and rib reflection effects in EPIC, the above effects are dealt with in the offline data analysis with the SAS.

4.9 XMM-Newton slew observations

XMM-Newton conducts EPIC and OM science and/or calibration observations during slews from one target to another. **Slew observations cannot be proposed.** The data obtained during slews are stored in so-called "Slew Data Files" (SDFs). Slew data are processed by the PPS pipeline and the resulting data files put into the **XMM-Newton** science archive (**XMM-Newton** Science Archive; § 6.4).

5 XMM-Newton Guest Observer Program (AO-2)

5.1 XMM-Newton proposal preparation and submission

The **ESA** Director of Science will issue a call for proposals in "Announcements of Opportunity" (AOs). Policies concerning, e.g., duplication avoidance, proposal categories or target categories are described in the AO-2 documentation.

5.1.1 XMM-Newton proposal preparation

In order to estimate the feasibility of an **XMM-Newton** observing proposal, users will need information from the following sources:

1. For all observations of targets with "simple" spectral characteristics, i.e., observations of point source targets with spectra that can be approximated by simple, single-component models to estimate the expected count rate for a given flux (as used for the production of the figures displaying the expected flux to count rate conversion factors above), the information contained in the instrument-specific chapters of this document should suffice.
2. For more complicated source geometries and/or spectra, modeling with *PIMMS*, *XSPEC* or SciSim might be required.
3. To scale count rates from previous X-ray satellite missions to **XMM-Newton**, it is recommended to use *PIMMS*.
4. Target visibility can be assessed using the **XMM-Newton** Target Visibility Tool.
5. To check during which **XMM-Newton** orbits a certain position angle can be achieved in order to avoid nearby sources during RGS (or OM grism) observations, see § 4.4.

5.1.2 XMM-Newton proposal submission

XMM-Newton proposal submission is facilitated via the **XMM-Newton** Remote Proposal Submission software (XRPS). The required inputs into the XRPS forms are described in the XRPS Users' Manual.

Every XMM-Newton proposer must first register as an XRPS user.

5.1.2.1 XMM-Newton Remote Proposal Submission (XRPS)

XRPS is a software package interfacing with the **XMM-Newton** Archival Management Subsystem (AMS), the Proposal Handling Subsystem (PHS) and the archival data base, developed by Logica UK Limited. It is part of the **XMM-Newton** PHS and as such located under the PHS on the web server. Proposal submission is facilitated via a web interface.

5.1.2.2 How to fill out the RPS online forms

An XRPS Users' Manual is available to guide users through the online XRPS. It is highly recommended to **follow exactly the procedures outlined in the XRPS Users' Manual to ease the interaction with the software**.

5.2 Technical proposal optimisation

Upon successful receipt of a proposal by the SOC, the PI will receive an acknowledgement that it has been entered into the system. In the process of proposal preparation for OTAC review, potential conflicts will be identified. Then the proposal will undergo review by the OTAC. Parallel to OTAC review, proposals will be subjected to a technical review by SOC personnel. Note that **it is the proposer's responsibility to ensure that the target coordinates (and, if necessary, the satellite position angle) are correct.** After OTAC acceptance, successful proposals will be technically optimised for implementation in the **XMM-Newton** observing program. Technical optimisation of proposals will consider the following points:

- EPIC
    1. EPIC expected X-ray counts
       Calculating the expected X-ray counts for the specified target for each filter of each EPIC instrument.
    2. EPIC expected optical count rate
       Calculating the expected optical counts for each specified target for each filter of each EPIC instrument.
    3. EPIC telemetry bandwidth
       Calculating the expected telemetry bandwidth for each EPIC exposure.
    4. EPIC signal to noise ratio
       Calculating the expected signal to noise ratio for each EPIC exposure.
    5. EPIC science parameter
       Calculating for each EPIC exposure the:
        - expected pile-up
        - fraction of smeared photons
        - duty cycle
        - total number of counts
        - total area of the chosen field of view
        - counts per frame
- RGS
    1. RGS expected X-ray count rate
       Calculating the expected X-ray counts for the specified target for each RGS instrument.
    2. RGS expected optical count rate
       Calculating the expected optical counts for the specified target for each RGS instrument.

3. RGS telemetry bandwidth
   Calculating the expected telemetry bandwidth for each RGS exposure.
4. RGS diagnostic downlink time estimation
   Calculating the downlink time associated with the diagnostic data when the RGS instrument is operating in spectroscopy mode.

- OM

1. OM image mode count rate estimation
   Calculating the counts expected in each imaging mode window of each OM exposure.
2. OM fast mode count rate estimation
   Calculating the counts expected in each fast mode window of each OM exposure.
3. OM fast mode time slice estimation
   Calculating the fast mode time slice duration, for each fast mode window, in units of the MIC frame time. GOs originally specify the time slice duration of each fast mode window in ms.
4. OM tracking frame time estimation
   Calculating the OM tracking frame time, for each exposure, in units of the DPU cycle. The exposure duration, originally specified by GOs in seconds, is then calculated as an integer multiple of this tracking frame time.
5. OM science windows
   - Calculating the size of the window, in detector pixels, for each science window that is specified by the GO in arc-seconds. If the GO has specified a window in detector pixels then this value is output.
   - Assigning a blue fast mode area (1 or 2) to each fast mode window.
   - Calculating the number of memory windows required to enclose the specified science windows and their details (position and size).
6. OM telemetry bandwidth
   Calculating whether the data generated during an exposure can be downlinked during the next exposure using the telemetry bandwidths available to the OM instrument. The tool also indicates the actual bandwidth which can be used and the time taken to downlink the data with this bandwidth.
7. OM bright object and guide stars
   For each observation indicating:
   - whether the observation is possible with any filter (not just those specified by the GO).
   - for which filters there are potential bright sources in the field of view.
   - the position angle constraints, if any, which would ensure that these bright sources do not appear in the field of view.
   - the potential guide stars for the observation. The right ascension, declination and visible magnitude of up to 32 stars are generated.

8. OM science parameters
   Calculating for each OM exposure the:
   - total count rate
   - source count rate
   - signal to noise ratio

- General

  1. Assign telemetry look-up table
     Identifying a telemetry allocation table for the observation, using the telemetry bandwidths calculated for each instrument.
  2. View information file
     Allowing the Proposal Handler to view the information file.

Based on the evaluation described above the SOC will recommend an “optimal” instrument setup for every observation accepted by the OTAC. PIs will always be informed about all changes of observation parameters of a proposal.

6 Analysing XMM-Newton data

6.1 XMM-Newton analysis software – the Science Analysis Subsystem (SAS)

In this Section some information related to the scientific analysis of **XMM-Newton** data are briefly outlined. The reader is referred to the documentation available on-line for a more detailed description of the **XMM-Newton** data format and reduction/analysis software.

6.1.1 XMM-Newton data: the Observation/Slew Data Files (ODF/SDF)

XMM-Newton reformatted telemetry is organized in the Observation/Slew Data Files (ODF/SDF). Most of the ODF/SDF files have a FITS format. An ASCII summary file provides the user with some general information on the observation (pointing, proposal, data quality records), as well as an index of the files contained in the ODF. A more detailed ASCII summary file - including a description of the instrumental configuration for all the exposures - can be created through a SAS task (cf. the on-line SAS Documentation).
ODF/SDF contain uncalibrated science files, which cannot be directly used for scientific data analysis. Their content is described in the **XMM-Newton** Data Files Handbook and in the **XMM-Newton** ODF/SDF Interface Control Document.

6.1.2 The Science Analysis System (SAS)

The Science Analysis System (SAS) is the software package to reduce and analyze the **XMM-Newton** science data. It broadly consists of two main blocks:

- reduction pipelines, which apply the calibrations to the ODF/SDF science files, and produce calibrated and concatenated event lists (for the X-ray cameras) and flatfielded OM sky images.
- a set of file manipulation tools. Such tools allow also the extraction of spectra, light curves, (pseudo-)images and source lists from the X-ray event lists, as well as the generation of the appropriate instrument response matrices.

The user is referred to the SAS User's Guide for a general description of the SAS, as well as to the on-line available SAS Documentation.

6.1.3 XMM-Newton data: the Processing Pipeline Subsystem (pipeline) products (PPS)

The SSC (see Appendix B) runs the SAS reduction pipelines on all the **XMM-Newton** ODF/SDF. Each dataset is screened to verify its scientific quality and identify potential processing problems The SSC pipeline (PPS) output includes a wide range of top level scientific products, such as source lists, multiband images, and spectra and light curves for all the detected sources in the EPIC field of view, as well as the results of cross-calibrations with a wide sample of source catalogues and with the matching ROSAT field. Results of the XID program will be incorporated as well, whenever relevant. The PPS products are shipped to the PI of an **XMM-Newton** proposal together with the ODF/SDF files of her/his observation.

The user is referred to **XMM-Newton** Data Products Interface Control Document and **XMM-Newton** Data Products Specification Document for a detailed description of the PPS products content and format.

6.2 XMM-Newton Calibration data

All the **XMM-Newton** calibration data are organized in a "Current Calibration File" (CCF). Each constituent of the CCF is uniquely identified by its (progressive) issue number and date of validity. Access to the CCF is based on the Calibration Index File.(CIF), which must be generated by the user through a specific SAS task at the beginning of an analysis session.

CCF constituents are available from the **XMM-Newton** Calibration Page. This directory is frequently updated. The **XMM-Newton** user may consider subscribing the CCF mailing list, which notifies in real-time all changes in the CCF content.

The user is referred to **XMM-Newton** Calibration Access and Data Handbook for more information about the calibration files, and the SAS infrastructure to access/visualize the content of the CCF constituents (Calibration Access Layer, CAL). The CCF *release notes* (accessible also through the **XMM-Newton** Calibration Page) provide information on the accuracy of the **XMM-Newton** calibrations.

6.3 The XMM-Newton data CD-ROM

Once the PPS products have been successfully generated, a CD including the ODF/SDF and PPS products is burnt and shipped to the PI of the relevant **XMM-Newton** observation. The CD contains all the files needed to perform a scientific analysis of the **XMM-Newton** data, except the CCF, which needs to be downloaded from the **XMM-Newton** Calibration Page.

The regular distribution of **XMM-Newton** data CD-ROMs started on February 16, 2001. The shipping of the **XMM-Newton** data CD-ROM corresponding to the observations later than this date is baselined to occur no later than 30 days from the observation date. Earlier observations are currently being reprocessed. The reprocessing is expected to have been completed when the current issue of the UHB will be published.

6.4 The XMM-Newton Science Archive (XSA)

The first interface to the **XMM-Newton** Science Archive (XSA) will be publicly available in March 2002, when the proprietary period on the first shipped **XMM-Newton** data expires.

In the meanwhile, publicly available data (*e.g.*: calibration and Performance Verification phase data) can be retrieved from the SAS Scientific Validation and the **XMM-Newton** Performance Verification Data Summary pages (see § 7 for URL addresses). The SAS Scientific Validation page contains also the results of the scientific validation of the currently available SAS version. It reflects therefore the data reduction and analysis software state-of-the-art, and provides additional and frequently updated information on the accuracy of the **XMM-Newton** calibrations.

7 Documentation

We compile here links and references of additional sources of information on **XMM-Newton**.

1. SOC services related to observations
   - **XMM-Newton** Remote Proposal Submission (XRPS)
     `http://xmm.vilspa.esa.es/user/rpsman_top.html`
   - **XMM-Newton** Target of Opportunity Notification
     `http://xmm.vilspa.esa.es/user/too/too_alert_top.html`
   - **XMM-Newton** Target Visibility Tool
     `http://xmm.vilspa.esa.es/user/vis/vis_top.html`
   - **XMM-Newton** Observation Search Page (PROTOTYPE)
     `http://xmm.vilspa.esa.es/cgi-bin/obs_search/selectobs`
   - **XMM-Newton** Observation Status Log
     `http://xmm.vilspa.esa.es/user/mplan/`
   - **XMM-Newton** Performance Verification Data Summary
     `http://xmm.vilspa.esa.es/user/mplan/XMM-Newton/public_list.html`
   - **XMM-Newton** Guaranteed Time Program
     `http://xmm.vilspa.esa.es/user/uhb/gto_top1.html`
   - **XMM-Newton** First Cycle: Approved GO Observations
     `http://xmm.vilspa.esa.es/news/AO/ao1_top.html`
   - **XMM-Newton** SOC Advanced Planning
     `http://xmm.vilspa.esa.es/news/advance_plan1.html`
2. SOC services related to the SAS
   - SAS
     `http://xmm.vilspa.esa.es/sas/`
   - SAS Documentation (including the Users' Guide)
     `http://xmm.vilspa.esa.es/sas/documentation/`
   - SAS Scientific Validation
     `http://xmm.vilspa.esa.es/public/xmm_sas_sv.html`
   - SAS Observation Report
     `http://xmm.vilspa.esa.es/sas-cgi/or.cgi`
   - SAS User Requirements Document
     `ftp://astro.estec.esa.nl/pub/XMM/documents/XMM-PS-GM-12_i1.0.ps.gz`
   - SAS Software Specification Document
     `ftp://astro.estec.esa.nl/pub/XMM/documents/sas_ssd_issue2.0.ps.gz`
   - **XMM-Newton** Calibration
     `http://xmm.vilspa.esa.es/user/calib_top.html`
3. Other online SOC services

   - The **XMM-Newton** Science Simulator (SciSim)
     `http://xmm.vilspa.esa.es/scisim/scisim.html`
   - **XMM-Newton** Proposal Handling Subsystem (PHS; in preparation)
     `http:/xmm.vilspa.esa.es/`
   - **XMM-Newton** Archive Management Subsystem (AMS; in preparation)
     `http://xmm.vilspa.esa.es/`
   - **XMM-Newton** Glossary
     `http://xmm.vilspa.esa.es/tech/socdoc/glossary.html`
   - "Building **XMM-Newton**" – an online picture gallery
     `http://xmm.vilspa.esa.es/user/build/buildxmm_top.html`
   - **XMM-Newton** Personnel
     `http://xmm.vilspa.esa.es/user/personnel_top.html`

4. **XMM-Newton** Mailing lists

   - **XMM-Newton** helpdesk
     `http://xmm.vilspa.esa.es/xmmhelp/`
   - **XMM-Newton** News Mailing List
     `http://xmm.vilspa.esa.es/news/xmm_news_signup.html`
   - Announcements about the **XMM-Newton** SAS
     `http://xmm.vilspa.esa.es/mailman/listinfo/sas-announce/`
   - List for the users of the **XMM-Newton** SAS
     `http://xmm.vilspa.esa.es/mailman/listinfo/sas-user/`
   - CCF mailing list
     `http://xmm.vilspa.esa.es/mailman/listinfo/ccf/`

5. Online **XMM-Newton** documents

   - Call for Proposals (AO-2; in preparation)
     `http://xmm.vilspa.esa.es/news/AO/`
   - **XMM-Newton** Data Files Handbook
     `ftp://xmm.vilspa.esa.es/pub/odf/data/sv/docs/datafileshb_2_0.ps.gz`
   - **XMM-Newton** Calibration Access and Data Handbook
     `ftp://xmm.vilspa.esa.es/calibration/docs/general/calhb_2.0.ps.gz`
   - **XMM-Newton** Routine Calibration Plan
     `http://xmm.vilspa.esa.es/docs/documents/CAL-PL-0001-2-0.ps.gz`
   - **XMM-Newton** ODF/SDF Interface Control Document
     `ftp://xmm.vilspa.esa.es/pub/odf/data/sv/docs/xmm-soc-icd-0004-ssd-2_8.ps.gz`
   - **XMM-Newton** Data Products Interface Control Document
     `ftp://xmm.vilspa.esa.es/pub/odf/data/sv/docs/xmm-soc-icd-0006-ssc-2_1.ps.gz`
   - **XMM-Newton** Data Products Specification Document
     `ftp://xmm.vilspa.esa.es/pub/odf/data/sv/docs/ssc-lux-sp-0004-1_1.ps.gz`

6. Documents that are available as paper copies only

- **XMM-Newton** Science Management Plan ESA/SPC(88)20

7. Documents related to sections of the UHB

   - § 3, **XMM-Newton** – a concise overview:
     - Jansen et al., 2001, A&A, 365, L1
   - § 3.2, X-ray telescopes:
     - Aschenbach et al., 2000, in X-Ray Optics, Instruments, and Missions III, J.Trümper and B.Aschenbach, eds., SPIE 4012, p.731
     - Gondoin et al., 2000, in X-Ray and Gamma-Ray Instrumentation for Astronomy XI, K.A.Flanagan, O.H.Siegmund, eds., SPIE 4140, p.1
   - § 3.3, EUROPEAN PHOTON IMAGING CAMERA (EPIC):
     - Strüder et al., 2001, A&A, 365, L18
     - Turner et al., 2001, A&A, 365, L27
     - Lumb et al., 2000, in X-Ray and Gamma-Ray Instrumentation for Astronomy XI, K.A.Flanagan, O.H.Siegmund, eds., SPIE 4140
     - Pizzolato, 2001, *On the long term behaviour of the MOS instruments quiescient background*, available at `http://www.ifctr.mi.cnr.it/~fabio/public/background.ps`
   - § 3.4, REFLECTION GRATING SPECTROMETER (RGS):
     - den Herder et al., 2001, A&A, 365, L7
     - Erd et al., 2000, in X-Ray and Gamma-Ray Instrumentation for Astronomy XI, K.A.Flanagan, O.H.Siegmund, eds., SPIE 4140, p.13
   - § 3.5, OPTICAL MONITOR (OM):
     - Mason et al., 2001, A&A, 365, L36
     - Constraints on the OM Window Configuration and Definition of the OM Default Configurations `ftp://astro.estec.esa.nl/pub/XMM/documents/xmm_ps_tn_026.ps.gz`
   - Appendix B, **XMM-Newton** Survey Science Centre (SSC):
     - Watson et al., 2001, A&A, 365, L51

8. External links

   - X-ray telescopes at the Max-Planck-Institut für extraterrestrische Physik `http://wave.xray.mpe.mpg.de/xmm`
   - EPIC at the Physics Department, Leicester University `http://www.src.le.ac.uk/xmm/`
   - EPIC at the Max-Planck-Institut für extraterrestrische Physik `http://wave.xray.mpe.mpg.de/xmm`
   - RGS at the Space Research Organization Netherlands `http://www.sron.nl/divisions/hea/xmm/`
   - OM at the Mullard Space Science Laboratory `http://mssls7.mssl.ucl.ac.uk/`

- SSC
`http://xmmssc-www.star.le.ac.uk/`
- AXIS: An **XMM-Newton** International Survey
`http://www.ifca.unican.es/~xray/AXIS/`
- UK **XMM-Newton** Information Centre
`http://www.xmm.ac.uk/`
- NASA's **XMM-Newton** Guest Observer Facility
`http://heasarc.gsfc.nasa.gov/docs/xmm/xmmgof.html`
- *PIMMS* (HEASARC)
`http://heasarc.gsfc.nasa.gov/Tools/w3pimms.html`
- *XSPEC* (HEASARC)
`http://heasarc.gsfc.nasa.gov/docs/xanadu/xspec/`

Additional information on **XMM-Newton** can always be obtained from other locations under the SOC home page, at `http://xmm.vilspa.esa.es/`.

A XMM-Newton Science Simulator (SciSim)

SciSim is the tool developed by the SOC for modeling **XMM-Newton** observations. It can be downloaded by **XMM-Newton** users for modeling sources and observation scenarios that are not described in this document. SciSim (v. 2.0 and higher) is capable of creating output files in the Observation Data File (ODF) format. For the conversion of the output files (described in the following) to ODFs, SciSim contains so-called ODF converters (see the SciSim online help, under "Users Guide", "Detailed Users Guide", "ODF converters" for details). ODFs can be analyzed using the SAS software (§ 6.1), making a direct comparison between models and observations possible. SciSim v2.1 maintains some tools (Appendix A.4) to convert SciSim output to other formats.

In order to make this document self-contained, we include here a general description of SciSim. Note that this is meant to be only a short introduction. The following is not a complete description of SciSim. **For the most up-to-date information the SciSim online help should be consulted.** (`http://xmm.vilspa.esa.es/user/scisim_top.html`)

A.1 SciSim – a brief general introduction

SciSim is a collection of programmes that can model **XMM-Newton** observations. Rays can be generated using a random generator and injected into the **XMM-Newton** telescope optics. Although all **XMM-Newton** instruments normally operate simultaneously, each can be excluded from SciSim model runs for the sole purpose of cutting back on processing time.

The individual SciSim components model one part of **XMM-Newton** each. Starting with the cosmic simulator (CSim), the space-craft (S/C) simulator (Appendix A.3.1.1) and the ray generator, which produce the input radiation (Appendix A.3.1), the propagation of the incoming radiation through the different parts of **XMM-Newton** is modeled, first through the mirrors (Appendix A.3.2) and then either directly onto the EPIC pn camera or onto the RGAs (Appendix A.3.4) and then onto either the EPIC MOS cameras (Appendix A.3.3) in the prime focus or the RFCs in the secondaries of two out of three **XMM-Newton** telescopes (Appendix A.3.4). Two examples of SciSim runs are presented in Appendix A.5.

SciSim has been programmed to resemble the scientific instruments on-board **XMM-Newton** as closely as possible. Missing items are listed in Appendix A.6. SciSim tools presented in Appendix A.4 can be used to convert SciSim output to formats that can be read by other software packages.

A.2 SciSim Graphical User Interface

SciSim can be executed from both the command line and from a specially developed set of GUIs. These GUIs pop-up parameters dialogs for the different components of SciSim.

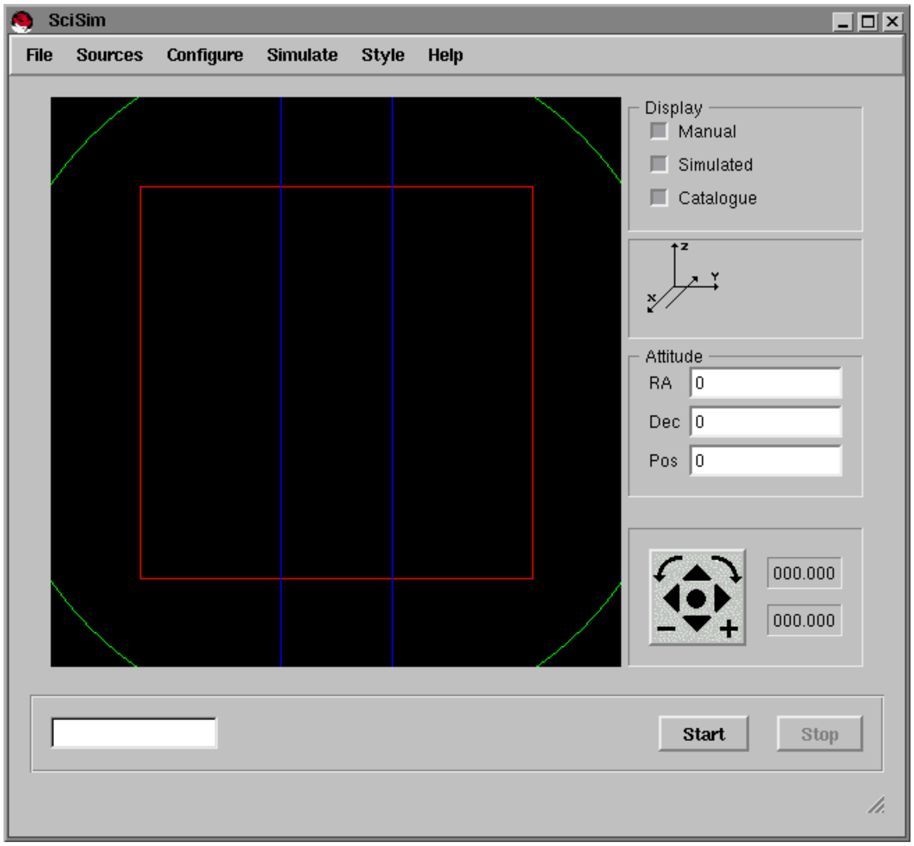

RA 0
Dec 0
Pos 0

Figure 102: *The top-level GUI of the* **XMM-Newton** *Science Simulator (SciSim), presenting a field of view on the sky that will display any emitting sources that can be chosen from catalogues or defined by the user.*

The top-level SciSim GUI is presented in Fig. 102. It offers several click-on buttons for choosing operations.

- "File"

  This offers various options to import or save source, configuration and default parameters. In particular, the default configurations for the three **XMM-Newton** X-ray telescopes (XRT1, 2 and 3) can be accessed under this pull-down menu. These default configurations are recommended for general users and standard simulations (see A.5)

- "Sources"

  Under this option the user manually edit model sources, simulate a random source distribution, import sources from catalogues and influence the properties of the modeled background.

- "Configure"

  This spawns the instrument configuration GUI, which is used for configuring SciSim, see below.

- "Simulate"

  Start/stop a simulation.

- "Help"

  Information on the SciSim release version and the online help. Note that, in order to use the online help facility of SciSim from the GUI, a Netscape Browser must be running.

A.2.1 SciSim configuration GUI

A particularly important GUI is the configuration GUI. This allows the user to choose which parts of **XMM-Newton** are to be modeled, i.e., which sub-units of SciSim are to be executed. A screen capture of this GUI is provided in Fig. 103.

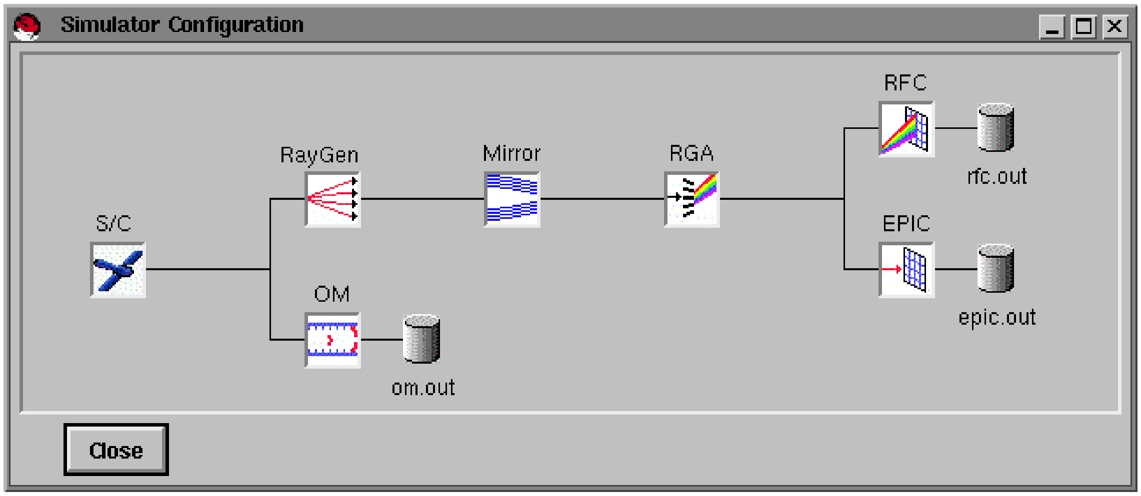

Figure 103: *The configuration GUI of SciSim, displaying which parts of* **XMM-Newton** *will be modeled. In the setup shown, all instruments will be modeled and the data will be stored in the files om.out (OM), epic.out (EPIC) and rfc.out (RGS).*

Components of SciSim are switched on/off by clicking on an icon in the configuration GUI with the left mouse button. The name of the output data file for the chosen configuration will always be displayed.

By clicking on any of the icons in the configuration GUI with the right mouse button, a menu will pop up to configure that particular sub-unit of SciSim. These will be introduced briefly in the following.

A.3 SciSim components

SciSim consists of several parts, which simulate different entities. Each can be controlled via its own GUI. As an example, the GUI of the Ray Generator component of the Cosmic Simulator, CSim, is presented below.

The different simulators contained in SciSim are:

- CSim – Cosmic Simulator
- SPSim – S/C Simulator
- GSim – Ray Generator
- MSim – Mirror Simulator
- ESim – EPIC Simulator
- RSim – RGS Simulator
  RSim consists of the following subunits:
  - RGASim – Reflection Grating Array Simulator
  - RFCSim – RGS Focal Camera Simulator
- OSim – OM Simulator

A.3.1 CSim – The Cosmic Simulator

CSim is that part of SciSim creating a simulated piece of sky, with sources with user-specified properties. It includes a Ray Generator, called GSim. Csim can produce astronomical model data for subsequent processing by the other simulators within SciSim.

X-ray sources can be created interactively or by using source lists. The results from interactive sessions can be written into output files, which can later be reused as inputs to CSim.

The following source parameters can at present be defined in CSim:

- Spatial distribution
- Spectral distribution
- Optical Counterpart
- Field Coordinates
- Source Position Selection

- Source Database
- Artificial Stellar Distribution
- X-ray background
- Saving and loading the source list

All these parameters are selected either directly from the appropriate fields in the SciSim GUI or by clicking the "Sources" button. The details of the parameters to choose can be found in the CSim online help.

Special parts of CSim are the S/C Simulator (SPSim) and the Ray Generator (GSim).

SPSim sets a number of important parameters for the simulation as the observation duration and telescope pointing. Some S/C effects can be modeled (jitter, drift, slew) for instrument calibration purposes but not for general **XMM-Newton** users.

GSim simulates the distribution of incoming photons from a given source (distribution). These rays are propagated later, by other parts of SciSim, through the telescope assemblies and into the detectors, thereby imaging the artificial view of the sky onto the detector plane.

A.3.1.1 The SPSim GUI

The integration time in seconds is entered from the "Simulation" folder of the SPSim GUI (Fig. 104). The parameters in the "Proposal" folder are not critical for the simulation, but useful to show the actual data structure and naming conventions for **XMM-Newton** data products as well as to organize the simulations by using different observation identifiers for different runs. After the high pointing stability proved in orbit, spacecraft effects will not need to be modeled by general **XMM-Newton** users.

A.3.1.2 The GSim GUI

The CSim GUI is displayed in Fig. 105. It allows users to specify the details of the simulation as listed above, by opening the different folders that are visible in the screen shot.

- Instrument

  Here the user can enter the upper and lower boundary for the energy spectrum of the simulated radiation (these are not the energy thresholds for the bandpasses of the instruments!).

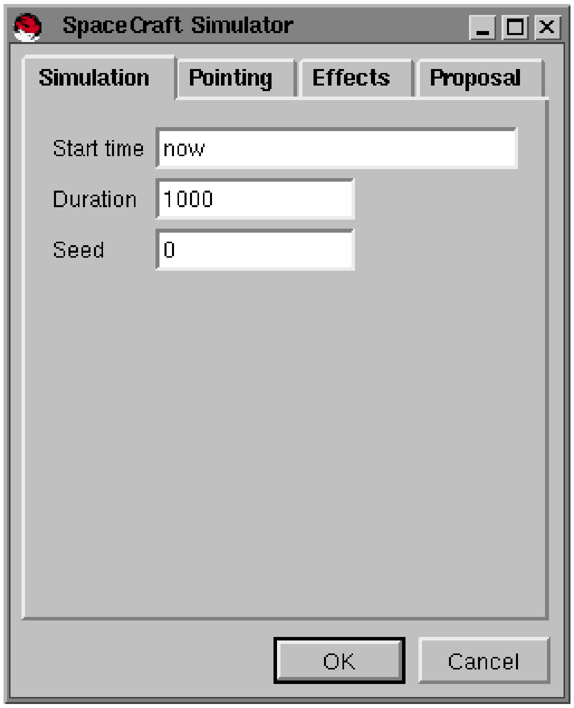

Start time: now
Duration: 1000
Seed: 0

Figure 104: *The GUI of SciSim's Space Craft Simulator.*

- Illumination

  This is the input field to vary the illumination over the FOV. These input parameters should not be changed for astronomical simulations.

The GUIs for the other components of SciSim are designed very similarly and therefore not shown here.

A.3.2 MSim – The Mirror Simulator

MSim simulates the X-ray response of **XMM-Newton**'s mirror modules. Therefore, it can also be called a "ray tracer". Not only the imaging characteristics of the mirrors, but also losses on the way from the entrance aperture to the detector surfaces are modeled.

MSim is an important part of the **XMM-Newton** calibration activities, because it is the software module producing the empirical descriptions of such basic quantities as the mirror PSF and the effective area, A_e. MSim is a highly configurable software module that allows to take into account many free parameters. There is a number of mirror models included, but the default telescopes configurations mentioned above (A.2) are recommended for standard simulations.

MSim simulates the following features:

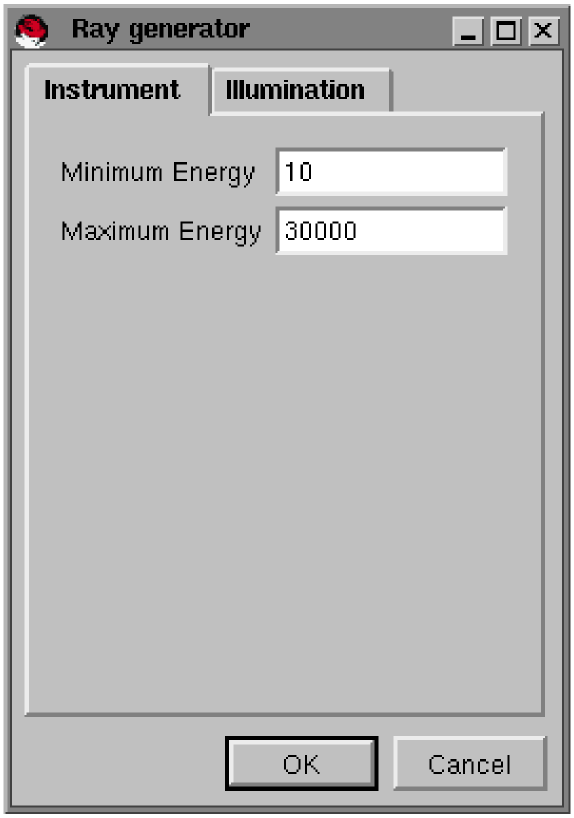

Minimum Energy: 10
Maximum Energy: 30000

Figure 105: *The GUI of SciSim's Ray Generator.*

- X-ray baffle plates with tolerancing on the centering and radii
- spider with tapered spokes
- nest with deformed mirror shells; included are Fourier-Legendre deformations, roll-off, polynomial distortions, spider fixation distortions, non-uniform thickness, tilt and decentre.
- reflection coefficients of nickel and gold, taking into account the density, dust contamination and energy and angle dependent absorption.
- scattering of gold and nickel surfaces, modeled with a power-law power spectral density of the surface roughness, a tabular specification of the PSD or Gaussian scattering.
- electron deflector
- misalignment of all parts of the module
- misalignment of the entire module with respect to the satellite

A.3.3 ESim – The EPIC Simulator

ESim simulates the properties of both types of EPIC cameras, MOS and pn.

The two camera types are fundamentally different, the MOS chips, e.g., being front-illuminated, while the pn CCDs are back-illuminated. ESim models the interaction of X-ray photons with the CCDs and records the results in output files. These output files contain event lists, as they would also be obtained during real observations.

ESim, as the other instrument simulators, is capable of simulating all science data acquisition modes of the detectors. Other parts of ESim simulate event recognition patterns, etc., including parts of the **XMM-Newton** onboard software.

ESim comprises routines to model the following features:

- Camera (mis-)alignment;
- CCD (mis-)alignment;
- Filter transmission, including pinholes (applicable to EPIC);
- Stacked surface (dead layers) of materials that either make up the gates (front illumination) or the back-layers (back illumination) of the CCDs of a camera;
- Charge Collection Efficiency (CCE) in sensitive layers (e.g. field free regions,high doping implants or surface losses);
- Photon shot noise;
- Absorption depth;
- Depletion depth due to doping profiles, temperature and voltages applied;
- Frame timing due to clocking schemes;
- Sequential read-out of CCDs;
- Image dark noise and amplifier characteristics of multiple read-out nodes of a CCD;
- Charge Transfer Efficiency;
- Frame read-out effects like smearing of pixels;
- Event reconstruction.

A.3.4 RSim – The RGS Simulator

RSim consists of two major parts, RGASim and RFCSim. The former simulates the physical properties of the RGAs, the latter those of the RFCs.

RGASim represents the continuation of the ray tracing that is performed by MSim. Multiple reflections are allowed, so that every ray that enters RGASim either leaves the module or is absorbed. Those rays leaving the RGAs in the direction of the RFCs are picked up by RFCSim and projected on the 9 CCD surfaces.

The features contained in RGASim are:

- 3D model of grating array
- trapezium shaped grating plates
- ribs on grating back
- the support braces placed in between some of the gratings (including holes).
- missing gratings, allow for partly filled RGA.
- blocking of rays by the walls separating the grating rows.
- scattering off the grating surface.
- grating positioning and alignment errors.
- grating non-flatness (bow, warp).
- variable line density groove spacing and additional random spacing errors.
- tabulated grating efficiency (from the Columbia EM code).
- reflections on grating back, ribs and SiC support structure (specular only).
- multiple reflections in between two grating plates and/or braces.
- misalignment of the RGA relative to telescope and detectors.

Rays can be produced in individual spectral orders in order to speed up the calculations.

A.3.5 OSim – The OM Simulator

OSim is a partly independent simulator, because the OM has its own telescope. The commonality with the other subunits of SciSim is only in the relative alignment of the different telescopes with respect to each other on the spacecraft.

OSim contains the optical/UV ray tracer and it simulates the behaviour of the detector itself. The following features are currently supported:

- Imaging (coordinate transformation) by telescope and channel
- Count rate for each pixel

- Sky background
- Source spectra
- Gaussian Point Spread Function (PSF) of optics
- Reflectance of primary and secondary mirrors
- Reflectance of selector (dichroic)
- Transmittance of various filters
- Magnification by magnifier
- Transmittance of magnifier
- Transmittance of detector window
- Photocathode quantum efficiency
- FWHM of detector
- Sampling by CCD pixels

Additional features are planned for the next release of OSim.

A.4 SciSim tools

The XMM-Newton Science Analysis Subsystem is the package to analyze the data generated by XMM-Newton satellite and SciSim ODF files. In addition, some intermediate Utilities are developed.

- *reporter2fits*

  converts SciSim output into FITS format

- *reporter2pha*

  converts the output binary output of RFCSIM and ESIM to the OGIP PHA format.

- *image2sources*

  converts the specified image array (the default is the primary array) of the input FITS file into a list of SciSim-compatible sources. The produced list of sources can then be fed into GSIM.

A.5 Examples for the use of SciSim for proposal preparation

Here we present two examples of the use of SciSim in the preparation of an **XMM-Newton** observing proposal, one each for EPIC and RGS. Note that the SciSim online help also contains two tutorials for source simulations.

CAVEAT 1: When importing model spectra created in *XSPEC* into SciSim(from the SciSim on-line help, see "Importing spectra from *XSPEC*" in the "Cosmic Simulator" chapter of the "Detailed Guide"), these spectra **must** be created with an energy grid that is dense enough so as to be smaller than the energy resolution of the instruments (in particular RGS)! Otherwise, the input spectrum will already determine the "resolution" of the output "model". A 0.1 eV energy grid is sufficient to sample RGS spectra adequately. For EPIC simulations a spectral bin width of 10 eV should suffice. The energy grid should best be defined using the available response matrices (see http://xmm.vilspa.esa.es/CCF and the SAS tasks *rgsrmfgen* and *rmfgen*). Alternatively, the grid can be defined in the *XSPEC* task *dummyrsp* as the increment parameter.

A.5.1 Example for simulating EPIC observations

To produce the EPIC spectrum shown in Fig. 106, a 6 keV Raymond-Smith thermal plasma model spectrum created with *XSPEC* was imported into SciSim. The energy resolution of the *XSPEC* input model was chosen to be 1 eV, i.e. higher than the energy resolution of EPIC. The adopted source flux is 10^{-12} erg s^{-1} cm^{-2} in the energy band from 0.5–4.5 keV. To import the spectrum from the SciSim GUI, users must choose option "Sources" in the top menu, then "new" in the source editor, then click on "Spectrum" and choose the option "*XSPEC*" from the menu. This will prompt the user for the input file name (FILENAME.DAT) from the current directory. The absorbing column density can also be provided in the source editor of SciSim (in units of 10^{24} atoms cm^{-2}); thus, no absorbing column density needs to be modeled in *XSPEC*.

The different components of the simulator can be configured through their corresponding GUIs. There are some pre-defined "default" specific configurations for standard simulations, i.e., simulations not intended for calibration or test purposes. These default configurations can be loaded from the "File" click-on button on the top-level SciSim GUI.

"Telescope 3" option loads a configuration appropriate for EPIC-pn simulations. Once it is been loaded, the top-level GUI option "Configure", spawns the configuration GUI, the "S/C", "RayGen", "Mirror", "RGA" and "EPIC" modules are switched on. Clicking with left mouse button on the "RFC" and "OM" icons will switch off these modules. Clicking on the S/C icon with the right mouse button, the integration time was in the current example set to 30000 [s]. Clicking on the mirror module icon (with the right mouse button), one can choose between different mirror modules. The same procedure can be followed to choose a particular EPIC-pn filter and observing mode by clicking on the EPIC

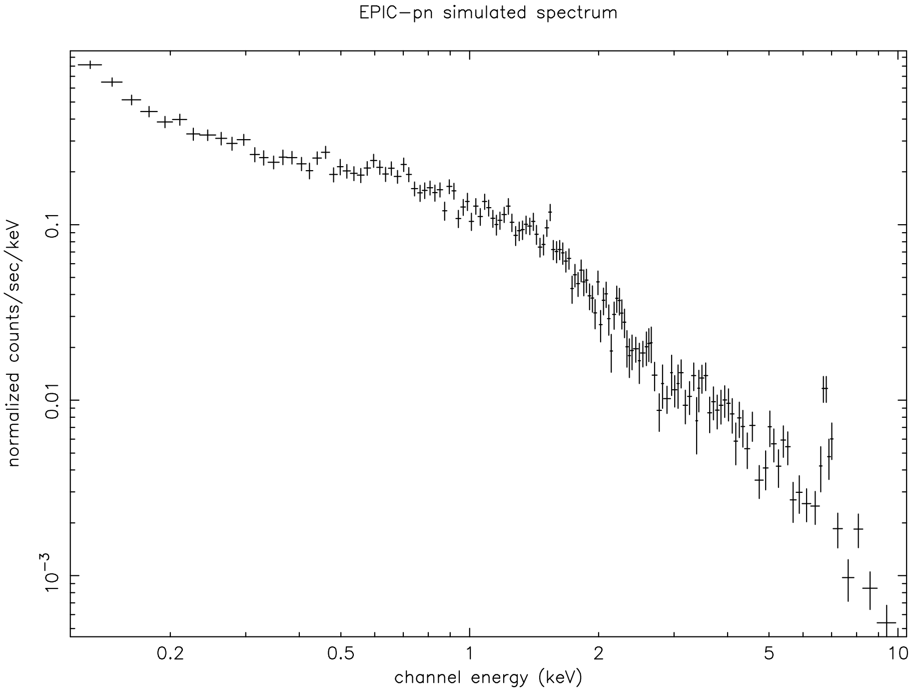

Figure 106: *Simulation of a 30 ks observation of a cluster with a 6 keV thermal plasma spectrum with* **XMM-Newton** *EPIC-pn (thin filter). Normalised counts are counts per spectral bin.*

icon. Note that RGA is already set to "none" since there is no grating in front of this camera. For a "standard" model simulation neither spacecraft effects nor other options regarding the mirrors and instruments need to be specified.

Once all inputs are specified, the simulation is started by clicking on the "start" button at the bottom of the GUI (or "Simulate" "Start" in the top menu). While the simulation is running, a performance bar will inform the user of its progress.

Upon successful completion the results of the model run are contained in a file named, by default, "epic.out", which is created in the current directory (i.e., the one from which SciSim has been started). The contents of this binary file can be viewed by converting them to ASCII (*ssimascii*), OGIP-PHA (*reporter2pha*) or FITS (*reporter2fits*) formats. The "epic.out" file can also be converted to an Observation Data File (*podf*), and then be analysed with the SAS package.

Extended sources can be modeled either by using an input image and using the tool *image2sources* described above or by using the top-level GUI menu option "Sources", choosing option "Edit" and then specifying in the folder "Shape" an ellipsoidal (either uniformly or non-uniformly emitting) shape (only options available), instead of the default ("point").

Note: Default configuration files, which have been derived from the best information available before the current release of SciSim, were used exclusively for the plots in this document. Users should be aware that a number of simple changes to the configuration files might be used either to aid some simple scenario modeling, or to investigate more practical problems of science analyses. The scope of data items that might be modifiable seems at first daunting, but we note a few here that are easily changed:

- The charge transfer efficiency (CTE) should be set to 1.0 if spatially variable spectra are to be analysed. On the other hand, if the observer wants to investigate likely errors involved due to such CTE changes and the minor effect on the energy resolution the data values need not be modified. Users should also be aware of possible incorrect energy scales in the SciSim output spectra due to differences between the CTE used in the simulation and the CTE correction implemented in the SAS version in use.
- The dead spaces between EPIC CCDs have been set to representative values in order to demonstrate the cosmetic effect on focal plane coverage. Users requiring to utilize 100% field coverage in order to estimate diffuse fluxes could run simulations with dead space modified to 0.0.
- The simulation assumes perfect set-up of offset tables within the camera, so that there is no gain and offset error predicted for optically bright targets. If users should wish to simulate the effect of a "thin" filter position with some light leakage loading, then this is best obtained by modifying the value of system noise. For example, based on the suggestions of maximum visible brightness usable per filter, one can estimate the additional light loading by the following method: For the thin filter, where $m_V = 17$ is a typical limiting magnitude (for 1 electron per pixel), the observation of an $m_V = 12$ target would produce a peak signal of about 100 electrons per pixel per full frame in MOS (16 in pn). Therefore, the additional shot noise is 10 (4) electrons rms. This should be added in quadrature to the existing noise and consequently the noise field in the configuration file should be amended to 11 (6) electrons, and the resulting effect on resolution noted. Unfortunately, this does not correctly simulate the energy offset, nor the spatial variation of optical loading.

A.5.2 Example for an RGS simulation

To produce the RGS spectrum shown in Fig. 107 , a two-component Raymond-Smith thermal plasma model spectrum was created with *XSPEC* and imported into SciSim. The model consists of a 0.35 keV and a 2.0 keV component of equal flux. The adopted source intensity is 2.6×10^{-9} erg s^{-1} cm^{-2} in the RGS band (0.35–2.5 keV). The resolution of the *XSPEC*-created input model was chosen to be 0.1 eV, i.e., higher than the RGS's energy resolution. Importing the spectrum from the SciSim GUI works as described above in the example for an EPIC simulation.

Under the top-level GUI option "File", "Telescope 1" loads a configuration appropriate for

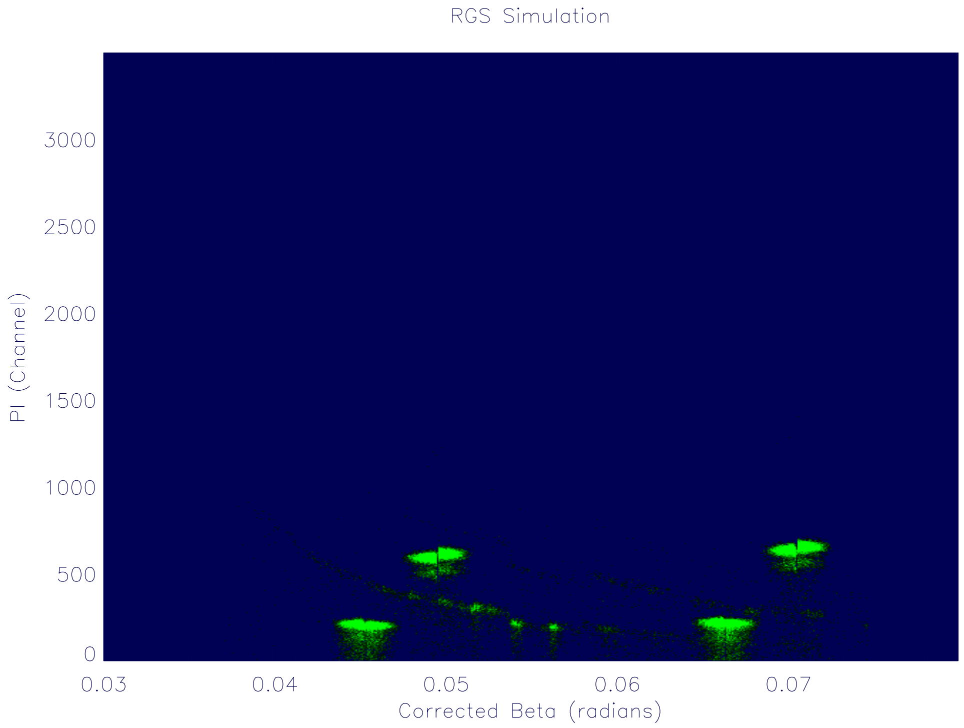

Figure 107: *The dispersion along the dispersion coordinate, Z (in mm), vs. CCD PHA-channel output of an RGS spectrum in –1. and –2. grating orders onto the RGS focal cameras, assuming equal gains of all CCD output nodes. This also illustrates the mechanism used for separating spectral orders.*

RGS1/MOS1 simulations while “Telescope 2” is suited for RGS2/MOS2. Then, the option “Configure” spawns the configuration GUI, from which the “OM” and “EPIC” modules were switched off by clicking on the icons with the left mouse button. Clicking on the S/C icon with the right mouse button, the integration time was set to 60000 [s]. Again, as for EPIC simulations, for a “standard” model simulation neither spacecraft effects nor other options regarding the mirrors and instruments need to be specified.

Once all inputs are specified, the simulation is started by clicking on the “start” button at the bottom of the GUI (or “Simulate” “Start” in the top menu). While the simulation is running, a performance bar will inform the user of its progress.

Upon successful completion the results of the model run are contained in a file named “rfc.out”, which is created on the current directory (i.e., the one from which SciSim has been started). The data can be converted to an ODF readable by the SAS software through the tool *rodf*. Note that to obtain the final 1-D spectrum with the *rgsproc* SAS task, the option *category=SCISIMCCF* should be used within the *cifbuild* SAS task.

A.6 SciSim performance issues

Several features of **XMM-Newton** are currently not included in SciSim. The most important are:

1. General
    - SciSim run times for large numbers of rays or complicated input scenarios (as e.g., an input spectrum produced with *XSPEC* can be very long (up to orders of hours).
    - Input of a sky image (emission distribution) is via a tool, which is at present still rudimentary and causes extremely long run times of the simulations.
2. EPIC
    - SciSim does not account for pn columns that might be discarded because of the hit of a minimum ionising particle (MIP; i.e., a cosmic particle).
    - There is no SciSim routine to handle optical/UV loading of the EPIC cameras and, accordingly, also none to perform EPIC MOS offset calculation to correct for this effect.
3. RGS
    - The scattering model that is used has not yet been optimized for the high energy end of the bandpass, which causes an overestimation of the amount of scattered light. The instrument's performance with respect to scattering wings at these energies is slightly better than predicted by SciSim.
4. OM
    - OSim cannot simulate OM grism observations.
    - OSim does not allow the modeling OM fast mode observations.
    - There is no OM window selection option.
    - OM detector distortion is not taken into account.
    - OM detector response non-linearity is not included.

B XMM-Newton Survey Science Centre (SSC)

The **XMM-Newton** Survey Science Centre (SSC) is an international collaboration involving a consortium of 9 institutions in the UK, France, Germany and Spain together with associate scientists in Italy, Belgium, Japan, USA and the UK. The major roles of the SSC in the **XMM-Newton** project are:

- the coordination of the **XMM-Newton** serendipitous survey via a ground-based follow-up/identification programme (the SSC 'XID Programme');
- the development, with the **XMM-Newton** SOC, of the **XMM-Newton** science analysis software (SAS);
- the routine pipeline processing of all **XMM-Newton** observations.

These activities are briefly summarised here with greater emphasis on the XID Programme as this is not described elsewhere in any detail. The XID Programme will also be of interest as potential **XMM-Newton** observers are requested to consider agreeing to the serendipitous content of their **XMM-Newton** observations being used in the context of this programme.

Further information on the **XMM-Newton** SSC and its role in the project is available from `http://xmmssc-www.star.le.ac.uk/`.

B.1 The SSC Follow-up Programme: the XID Programme

Because of its large throughput and good spatial resolution, pointed observations with the **XMM-Newton** EPIC X-ray cameras reach very faint X-ray flux limits ($\approx$ a few $\times 10^{-15}$ erg cm^{-2} s^{-1}, 0.15–10 keV, in typical observations). At these fluxes, each **XMM-Newton** EPIC field at both high and low galactic latitudes contains substantial numbers of "serendipitous" X-ray sources. Pointed **XMM-Newton** observations thus provide a "serendipitous" X-ray survey (the "**XMM-Newton** Serendipitous Sky Survey", see Watson et al., 2001, A&A, 365, L51 and Watson, 1998, Astr. Nach., 319, 117) which, like previous surveys, is expected to make a major impact in a number of front-line areas of astrophysics, a fact that provided one of the original motivations for the SSC concept within the **XMM-Newton** project.

The role of the SSC in this area is to coordinate the follow-up of the serendipitous content of **XMM-Newton** observations in order to ensure that this valuable resource can be exploited effectively by the community. The key initial step is the 'identification' of the X-ray sources, i.e., classification into different object types. Literally identifying every **XMM-Newton** serendipitous source is not a realistic task, nor a sensible approach. Instead, the emphasis of the SSC XID Programme is on the characterisation of the **XMM-Newton** source population through the detailed follow-up of well-defined, small subsamples (as outlined below). The XID Programme thus aims to bring together the **XMM-Newton** data themselves, existing catalogue and archival material and new ground-based observational data in an integrated fashion.

The overall XID Programme has two main components:

The "Core Programme" consisting of complete identifications of selected high galactic latitude X-ray samples based primarily on optical imaging and spectroscopy. The results from this programme are being used to "characterize" the content of the **XMM-Newton** serendipitous survey. The Core Programme also includes a parallel study for the low galactic latitude sky.

The "Imaging Programme" which aims to obtain optical photometry and colours for a substantial fraction of all **XMM-Newton** fields. The rationale is based on the fact that a combination of X-ray flux and X-ray colours (from the **XMM-Newton** data) and optical magnitude and optical colours (e.g. from new ground-based observations) provide the key parameters which make possible an accurate 'probabilistic' identification of the **XMM-Newton** sources. This is possible using the results from the Core Programme which characterise the **XMM-Newton** source populations, thus providing the link, in a statistical sense, between the source identification and properties and these basic parameters.

The entire programme is based on samples of serendipitous X-ray sources drawn from pointed **XMM-Newton** observations that are in the public domain, or are made available to the SSC by the observation PI.

The initial phase of the XID Programme is now well underway. A substantial allocation of observing time has been gained by the SSC Consortium to provide the ground-based optical/IR imaging and spectroscopy required. The largest allocation of telescope time has been made available through the Canary Islands 'International Time Programme' to the 'AXIS' project which represents a substantial subset of the XID Programme goals. The AXIS project is led by Dr Xavier Barcons, Santander. Over half of the total allocation to the AXIS project in 2000/2001 has already been used for the programme. Additional telescope time allocations have been made on the ESO/MPG 2.2m (for southern hemisphere imaging), on the INT 2.5 m (for a long-term imaging programme) as well as a number of smaller allocations.

Some preliminary results from the XID Programme are included in Watson et al., 2001, A&A, 365, L51, whilst more up-to-date status information etc. can be found on:
`http://xmmssc-www.star.le.ac.uk/` for the XID Programme overall;
`http://www.ifca.unican.es/~xray/AXIS/` for the AXIS project.

The XID programme is designed to support the community's access to, and exploitation of, the serendipitous data from **XMM-Newton**, and as such all the results will be made public through the **XMM-Newton** Science Archive. The SSC intends to make some preliminary data from the XID programme public in the near future, in advance of the opening of the **XMM-Newton** Science Archive which is not planned until March 2002. This will be announced via the SSC web page at `http://xmmssc-www.star.le.ac.uk/`.

B.2 Pipeline processing of XMM-Newton science data

The SSC is responsible for the task of processing all **XMM-Newton** observations to produce data products for the three scientific instruments. This processing uses the same SAS software modules that are available for users' interactive analysis of **XMM-Newton** data, but the infrastructure required to carry out the processing has been developed by the SSC. Each dataset processed is subject to a screening process by the SSC team which aims at verifying the quality of the processing and the identification of any processing problems.

The aim of the pipeline processing is to provide a set of data products which will be of immediate value for the **XMM-Newton** observer as well as for the **XMM-Newton** Science Archive where they will also be stored for eventual public release. The pipeline products, together with the ODF (see § 6.1.1), are distributed to observers by the **XMM-Newton** SOC.

The **XMM-Newton** data products include calibrated, "cleaned" event lists which are intended to provide the starting point for most interactive analysis of the data as well as a number of secondary high-level products such as sky images, source lists, cross-correlations with archival catalogues, source spectra and time series. These provide a useful overview of the observation for the **XMM-Newton** observer as well as constituting key archival resources.

B.3 Science analysis software development

In collaboration with the SOC, the SSC has made a major contribution to the development of the **XMM-Newton** Science Analysis System (SAS, see § 6.1) provided by the SOC to the community to enable **XMM-Newton** data analysis to be carried out by **XMM-Newton** observers. The SAS provides **XMM-Newton**-specific software tools for all **XMM-Newton** science data. It allows the processing of the Observation Data Files (ODFs, see § 6.1.1) sent to the observer through to high-level science products, but does not, in general, aim to provide the high-level analysis tools (e.g. spectral fitting) themselves.

C XMM-Newton Routine Calibration Program

To monitor the performance of the **XMM-Newton** science instruments, regular observations on a number of targets are performed during the routine phase that started after the end of the Calibration & Performance Verification Phase (CALPV) (July 1, 2000, revolution 103).

Such observations are defined in the **XMM-Newton** Routine Calibration Plan (available at `http://xmm.vilspa.esa.es/docs/documents/CAL-PL-0001-2-0.ps.gz`) and are used to update the Current Calibration Files (CCFs, see § 6.2) whenever necessary.

The following routine calibrations are foreseen:

- EPIC
    - CTI, Gain and bright Pixel Monitoring: with filter closed or cal-closed during the ascending parts of a revolution when scientific observations are not yet possible due to the high radiation in the belts.
    - Effective Area, Gain & Offset Monitoring
    - Stability of the boresight: to be monitored once after an eclipse season.
    - Monitoring of Spectral Capabilities and Contamination
- RGS
    - Confirmation of the Wavelength Scale
    - Monitoring of Effective Area: once during each period 3C273 or Mkn421 become visible. 3C273 is variable and cross-calibration with other observatories is done whenever possible.
    - Gain and CTI monitoring
    - Diagnostic Frames: these are performed once per month in parallel with EPIC cal-closed observations after perigee exit.
- OM
    - Monitoring of the Spectrophotometric Grism Calibration
    - Monitoring of the Visual and UV Grism Grism Calibration
    - Monitoring of the Photometric Calibration
    - Contamination Monitoring
    - Engineering Mode Observations: are performed whenever OM does not allow any filter observations but needs to be blocked because of bright optical sources.